

E.L. Theuws

# Analyzing reconstruction scenarios for dolmen D14 using non-destructive, digital methods

With a focus on the dislocated capstone





# Analyzing reconstruction scenarios for dolmen D14 using non-destructive, digital methods

With a focus on the dislocated capstone

by

E.L. Theuws

to obtain the degree of Master of Science

at the Delft University of Technology,

to be defended publicly on Monday December 20, 2021 at 16:00 PM.

Student number: 5134528

Project duration: February 1, 2021 - December 20, 2021

Thesis committee: Dr. Ir. D.J.M. Ngan-Tillard, TU Delft  
Dr. L. Truong-Hong, TU Delft  
Dr. A.A. Mehrotra, TU Delft  
Dr. R.C. Lindenbergh, TU Delft  
Dr. G. Giardina, TU Delft

An electronic version of this thesis is available at <http://repository.tudelft.nl>.

Cover image is a picture from dolmen D14 (RTV Drenthe, 2019).





# Thesis summary

Dolmens are monuments constructed from large megalithic boulders that were built thousands of years BCE. In the Netherlands, 54 dolmens remain, mostly located in the province of Drenthe. Over the years, some of these monuments have been damaged by people. This is also the case for dolmen D14, which had one of the capstones dislocated in 2019. Damage to the dolmen caused by people has led dolmen management agencies to face dilemmas over if and how these monuments should be reconstructed. In order to make a more informed decision, it is important to understand the stability of potential reconstruction scenarios, without performing invasive tests that could damage the structure. Therefore, this research focuses on non-destructive, digital methods to analyze potential reconstruction scenarios for dolmen D14 in the Netherlands. The methods comprise of three parts: 1) creating geometrical models, 2) estimating the relevant rock parameters that contribute to the shear strength of the rock contact surfaces and 3) digitally analyzing the stability of reconstruction scenarios.

Geometrical models are required as input for the digital stability analyses. A 3D model was previously made by the Groningen Institute of Archaeology using photogrammetry. However, this model was found to contain a lot of faulty data and was not sufficiently refined. Therefore, new geometrical models were developed in four steps: 1) acquiring point-cloud data using laser scanners, 2) point cloud pre-processing, 3) mesh generation and 4) mesh evaluation. Point cloud data was acquired with two scanners, a large and very accurate terrestrial laser scanner (TLS) and a small and slightly less accurate laser scanner (BLK). Nonetheless, not all rock surfaces could be captured with sufficient detail. Throughout the modelling process, it was found that it is best to minimize the overlap between the datasets from the two scanners, since overlap creates inaccuracies in the resulting mesh. Furthermore, it was found that subsampling is required for mesh generation due to computational limitations. Meshing was only possible with a minimum subsampling distance of 1mm for the point clouds. However, due to even more stringent computational limitations from the stability analysis software, the most detailed geometrical models were developed based on a subsampling distance of 50mm. Furthermore, it was found that the average point-to-mesh distance of the rocks throughout the meshing process is in the order of 0.1-1mm, which is deemed sufficiently accurate for the purpose of this research.

Apart from the geometrical models, the rock parameters also need to be determined in order to be able to conduct digital stability analyses. In this part, the focus was on the shear strength parameters as specified in the failure criterion of Zhao (1997b). The Joint Roughness Coefficient (JRC) was determined with a carpenter's comb to be on average 9.2 for the rocks. The Joint Matching Coefficient (JMC) was set to 0.3, in line with the recommendations made by Zhao (1997b). The Joint wall Compressive Strength (JCS) was found to be 41 MPa, with an Equotip. This is lower than expected based on the literature, so a value of 50 MPa was assumed. The normal stress ( $\sigma_n$ ) on the rock contact areas was calculated based on the volume and weight of Rock 3, as well as the assumed contact surface area. Lastly, the residual friction angle ( $\varphi_r$ ) was estimated based on analog rock samples to the rocks in the field. The tilt test gives a basic friction angle of 33°, which indicates that the residual friction angle should be slightly lower. The residual friction angle was also estimated using a Golder shear box test. This test was performed on two different types of samples: a flat, sand-blasted sample and a rough, tensile-split sample. The result for the flat, sand-blasted sample was a residual friction angle of 30°, which is in line with literature. The rough, tensile-split sample results were deemed unreliable. Based on all shear strength parameters, it was concluded that the influence of the residual friction angle is by far the greatest on the shear strength. Therefore, it was decided to adopt a simple Mohr-Coulomb shear strength criterion for the joint in the digital stability analysis, with a friction angle of 30°.

The third research part is concerned with the digital analysis of potential reconstruction scenarios. These analyses were performed numerically using 3DEC software. Two reconstruction scenarios were evaluated on their stability. Model 1 was based on the rock configuration of dolmen D14 as it was in 2019, right before the dislocation of the capstone. Model 2 was based on the rock configuration as it was in 1925, right before a major reconstruction of the monument. The stability was evaluated by checking what the minimum pushing force was to reach instability of the model. Instability, in this case, was defined as the non-convergence of the model in terms of the unbalanced force ratio within the specified number of cycles. It was found that for Model 1, a pushing force of only 2 kN is required to create instability, whereas this was 94 kN for Model 2. However, it should be noted that this pushing force was only evaluated at one location and in one direction. For the same model but another pushing force location or direction, the model results can therefore be very different. Lastly, a sensitivity analysis was done for the number of cycles within which convergence should be reached, the mesh coarseness and the friction angle of the joint. It was found that for a greater number of cycles within which convergence should be reached, the minimum force for model non-convergence is increased. For the mesh coarseness, there was no clear trend in the data for the meshes with an average mesh edge length (AMEL) of 0.10, 0.15 and 0.20 m. However, the minimum force for model non-convergence was very high for the mesh with an AMEL of 0.05 m. This is caused by small differences in the geometry, which influence the rock configuration and thereby the failure mode. Furthermore, it was found that the minimum force for model non-convergence was slightly higher for normal meshes compared to smart meshes, which were produced with coarser elements on the inside of the rocks and equally detailed elements on the outside of the rocks. This can be explained by that convergence is determined based on the unbalanced force ratio that is calculated for all grid points. For different grid points, the unbalanced force ratio will also be different. The friction angle was also found to have a significant impact on the results. For a higher joint friction angle, the minimum force for non-convergence was also found to be higher.

The findings of this research indicate that even though some difficulties can arise when adopting non-destructive, digital methods, there is great potential for this type of stability analysis of reconstruction scenarios for megalithic monuments.

# Preface

This thesis was written to fulfill the graduation requirements of the MSc Civil Engineering, with a specialization in Geo-Engineering, at the Delft University of Technology. I was engaged in researching and writing this thesis from February to December 2021.

I am grateful to be able to conclude my time as a student with a research that really characterizes my study interests, as this research was the perfect combination between my passion for engineering and my fascination for history. This research would not have been possible without the help and support received from many people around me. In many ways, a thesis is actually more a team effort than it is individual work and I greatly appreciate everybody's help.

First and foremost, I would like to thank D. Ngan-Tillard for introducing this topic to me and providing me with great guidance. I am thankful for your feedback and I greatly appreciate all the help that you gave me throughout this project. I would also like to express my appreciation to my other supervisors L. Truong-Hong, A. Mehrotra, R. Lindenberg and G. Giardina from TU Delft for your involvement in the project and assistance when I needed help. Your help has been invaluable, especially due to the interdisciplinary nature of this research. Also, I would like to thank C. Carranza-Torres from the University of Minnesota, Duluth Campus for your help, especially at the start of the modelling but also when interpreting the results at a later stage. It was very valuable to learn about 3DEC from you. Moreover, I would like to thank the Cultural Heritage Agency of the Netherlands (Rijksdienst Cultureel Erfgoed) and J. Schreurs, together with Stichting het Drentse Landschap and T. Bezuijen and R. Huizing for proposing this interesting research topic. Additionally, I would like to thank H. Huisman, for his help with the determination of the rock types of dolmen D14. Last but not least, I would like to thank my parents and sisters, as well as all friends and my roommates, who gave me unconditional support for the entirety of this journey.

*E.L. Theuws,  
Delft, December 2021*

# Contents

<b>1</b>	<b>Introduction</b>	<b>1</b>
1.1	Background . . . . .	1
1.2	Problem statement . . . . .	2
1.3	Research questions . . . . .	3
1.4	Objective and scope of the study . . . . .	3
1.5	Reconstruction guidelines . . . . .	4
1.6	Thesis outline . . . . .	7
<b>2</b>	<b>Creating geometrically accurate 3D meshes</b>	<b>8</b>
2.1	Introduction . . . . .	8
2.2	Literature . . . . .	9
2.3	Methods . . . . .	11
2.4	Results . . . . .	18
2.5	Discussion . . . . .	35
2.6	Conclusion . . . . .	36
<b>3</b>	<b>Non-destructive examination of rock contact surface parameters</b>	<b>39</b>
3.1	Introduction . . . . .	39
3.2	Literature . . . . .	39
3.3	Methods . . . . .	49
3.4	Results . . . . .	56
3.5	Discussion . . . . .	60
3.6	Conclusion . . . . .	62
<b>4</b>	<b>Numerical stability analyses</b>	<b>64</b>
4.1	Introduction . . . . .	64
4.2	Literature . . . . .	64
4.3	Methods . . . . .	68
4.4	Results and discussion . . . . .	75
4.5	Conclusion . . . . .	86
<b>5</b>	<b>Conclusion</b>	<b>88</b>
5.1	Creating geometrically accurate 3D meshes . . . . .	88
5.2	Non-destructive examination of rock contact surface parameters . . . . .	89
5.3	Numerical stability analyses . . . . .	90
<b>6</b>	<b>Recommendations</b>	<b>92</b>
6.1	Creating geometrically accurate 3D meshes . . . . .	92
6.2	Non-destructive examination of rock contact surface parameters . . . . .	92
6.3	Numerical stability analyses . . . . .	93

<b>Appendices</b>	<b>99</b>
<b>A Leica scanners product specifications</b>	<b>99</b>
<b>B Figures of modelling Step 2: Point cloud pre-processing</b>	<b>100</b>
<b>C Figures of modelling Step 3: Mesh generation</b>	<b>108</b>
<b>D Griddle meshing settings</b>	<b>111</b>
<b>E Areas with sparse point density in the point cloud models</b>	<b>112</b>
<b>F Mesh faces and sampling distance</b>	<b>115</b>
<b>G PMD analyses</b>	<b>116</b>
<b>H JRC determination guidelines</b>	<b>122</b>
<b>I JRC values in the field</b>	<b>124</b>
<b>J JCS values in the field</b>	<b>128</b>
<b>K Tilt test results</b>	<b>131</b>
<b>L JCS, JRC and JMC values in the lab</b>	<b>132</b>
<b>M Golder shear box results</b>	<b>138</b>
<b>N 3DEC scripts</b>	<b>145</b>
<b>O Comparison analytical and numerical results, rectangular block on slope</b>	<b>149</b>
<b>P Comparison analytical and numerical results, rectangular block on two rectangular supports</b>	<b>151</b>
<b>Q Comparison analytical and numerical results, dolmen in 2D</b>	<b>153</b>
<b>R Numerical results for dolmen stability analysis</b>	<b>156</b>

# List of Tables

2.1	Characteristics of Leica scanners . . . . .	11
2.2	Specifics of the point cloud . . . . .	18
2.3	Number of points for the point clouds, divided per data set . . . . .	19
2.4	Number of points for a defined area of Rock 3, divided per data set . . . . .	20
2.5	Number of points for detailed and subsampled point clouds . . . . .	22
2.6	Area size for the areas of uncertainty . . . . .	22
2.7	Comparison between the number of points of Rock 4, for TLS and BLK data sets . . . . .	32
2.8	Comparison between the number of points of Rock 3, with and without GIA data set . . . . .	33
3.1	JRC values for each rock and average value for all rocks . . . . .	56
3.2	JCS values for each rock . . . . .	57
3.3	Average JCS values for all rocks . . . . .	57
3.4	Tilt test results . . . . .	57
3.5	JRC results for the laboratory samples . . . . .	58
3.6	JCS results for the laboratory samples . . . . .	58
3.7	JMC results for the laboratory samples. . . . .	58
3.8	Residual friction angle results for the Golder shear box test . . . . .	58
4.1	Model parameters used for the sensitivity analysis . . . . .	73
4.2	Analytical results of the 2D megalith models . . . . .	77
4.3	Numerical results of the 2D megalith models . . . . .	78
4.4	Number of cycles before convergence is reached in modelling Phase 1, for different AMELs and mesh types . . . . .	82

# List of Figures

1.1	Map of megalithic monument D14 . . . . .	2
1.2	Pictures of dislocated Rock 3 . . . . .	2
1.3	Structural elements of a dolmen . . . . .	5
1.4	Pictures of dolmen D14 in 1927 . . . . .	6
1.5	Picture of metal pin connecting Rock 3 to Rock 2 . . . . .	6
2.1	Close-up of 3D model made by GIA . . . . .	8
2.2	Total 3D model made by GIA . . . . .	9
2.3	Mesh elements . . . . .	10
2.4	General workflow for creating 3D meshes . . . . .	11
2.5	Workflow of point cloud pre-processing . . . . .	12
2.6	Workflow for mesh generation . . . . .	14
2.7	PMD calculation . . . . .	17
2.8	Signed distances of a rock mesh . . . . .	17
2.9	Images of the point cloud models . . . . .	19
2.10	Area of Rock 3 used for density comparison . . . . .	20
2.11	Point cloud of Rock 1, differentiated by point cloud data set . . . . .	21
2.12	Point cloud of Rock 3, differentiated by point cloud data set . . . . .	21
2.13	Rock surface with low density: Rock 1 North . . . . .	23
2.14	Rock surface with low density: Rock 5 . . . . .	23
2.15	Rock surface with anomaly: Rock 1 top . . . . .	24
2.16	Subsampling and the number of mesh faces . . . . .	24
2.17	Element size for a subsampling distance of 1 mm . . . . .	25
2.18	Element size for a subsampling distance of 50 mm . . . . .	26
2.19	Mesh differences for different AMELs . . . . .	26
2.20	Mesh differences for smart and normal meshes . . . . .	27
2.21	Signed PMD of Rock 4 expressed as a histogram after meshing Step 3.1. . . . .	28
2.22	Signed PMD for all seven rocks after meshing Step 3.1 . . . . .	28
2.23	Signed PMD for Rock 4 after meshing Step 3.1 . . . . .	28
2.24	Euclidean PMD of Rock 4 expressed as a histogram. . . . .	29
2.25	Euclidean PMD for all seven rocks after meshing Step 3.1 . . . . .	29
2.26	Euclidean PMD for Rock 4 after meshing Step 3.1 . . . . .	30
2.27	Signed PMD for different rocks after meshing Step 3.1 and Step 3.4 . . . . .	31
2.28	Euclidean PMD for different rocks after meshing Step 3.1 and Step 3.4 . . . . .	31
2.29	Signed PMD for Rock 4 compared to TLS and BLK data sets . . . . .	32
2.30	Euclidean PMD for Rock 4 compared to TLS and BLK data sets . . . . .	33
2.31	Signed PMD for Rock 3 compared for including and excluding the GIA data set . . . . .	34
2.32	Euclidean PMD for Rock 3 compared for including and excluding the GIA data set . . . . .	34
3.1	Rock types of the rocks in the zone of interest . . . . .	40
3.2	Grey and red Våxjö granite . . . . .	41

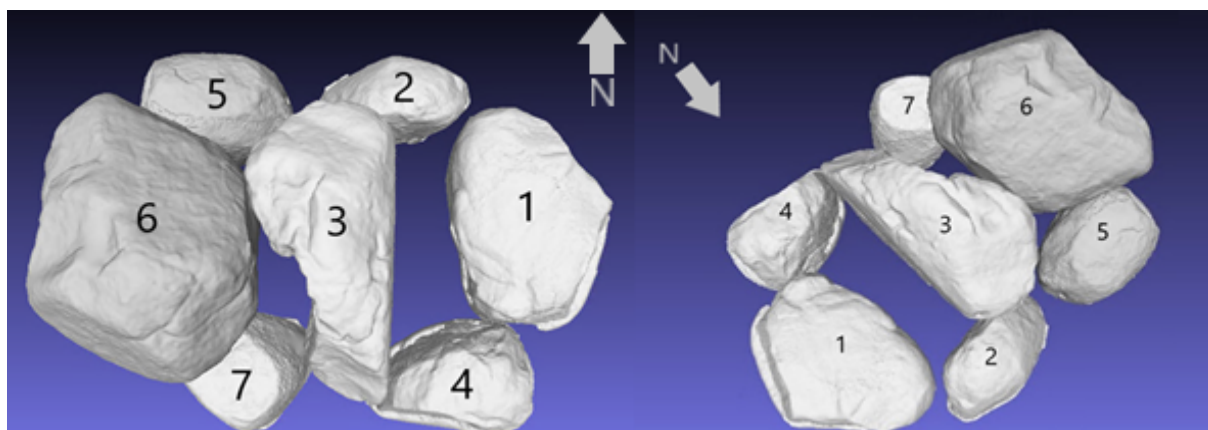
3.3	Map of the origins of the rocks in the zone of interest . . . . .	42
3.4	Patton's bilinear model sample shape . . . . .	43
3.5	Patton's bilinear model for joint shear behavior . . . . .	43
3.6	Peak and residual shear strength characteristics . . . . .	45
3.7	Rock contact zone between Rock 5 and Rock 6 . . . . .	47
3.8	Rock contact zone between Rock 6 and Rock 7 . . . . .	47
3.9	Tilt test procedure . . . . .	48
3.10	Field locations for JRC and JCS . . . . .	49
3.11	Carpenter's comb . . . . .	50
3.12	Tilt test sample . . . . .	51
3.13	Tilt test apparatus . . . . .	52
3.14	Rock sample before and after sandblasting . . . . .	53
3.15	Producing a rough joint . . . . .	53
3.16	Rough, tensile-split sample . . . . .	54
3.17	Sample preparation . . . . .	54
3.18	Golder shear box test setup . . . . .	56
3.19	Shear stress vs. normal stress plots . . . . .	59
4.1	Stability of a rectangular block on a slope . . . . .	65
4.2	Cycle of mechanical calculations . . . . .	67
4.3	Rectangular block on a slope models . . . . .	69
4.4	Rectangular block on two rectangular supports models . . . . .	69
4.5	Dolmen D14 in 2D at the Northern contact point . . . . .	70
4.6	Dolmen D14 in 2D at the Southern contact point . . . . .	70
4.7	Pictures of the dolmen as positioned in 2019 . . . . .	71
4.8	Model 1 rock configuration . . . . .	71
4.9	Pictures of the dolmen as positioned in 1925 . . . . .	72
4.10	Model 2 rock configuration . . . . .	72
4.11	Coulomb joint model in 3DEC . . . . .	73
4.12	Schematic of pushing force location and direction . . . . .	74
4.13	Rock configuration before and after modelling Phase 1 . . . . .	75
4.14	Rock configuration before and after modelling Phase 2 . . . . .	75
4.15	Results of the rectangular block on a slope . . . . .	76
4.16	Influence of the mesh coarseness on the model results for the rectangular block on two rectangular supports . . . . .	77
4.17	Rock configuration of Model 1 after 200000 cycles . . . . .	78
4.18	Rock configuration of Model 2 200000 cycles . . . . .	79
4.19	Effect of the number of cycles on the minimum force for model non-convergence . . . . .	80
4.20	Effect of the number of cycles on the calculation time . . . . .	80
4.21	Effect of the mesh coarseness on the minimum force for model non-convergence . . . . .	81
4.22	Meshes before and after modelling Phase 1 for normal and smart meshes . . . . .	82
4.23	Meshes before and after Phase 1, and after Phase 2 . . . . .	83
4.24	Meshes with AMEL 0.05 m and 0.20 m after Phase 1 . . . . .	83
4.25	Figures of the failure mode of the models with an AMEL of 0.05 m . . . . .	84
4.26	Effect of the mesh coarseness on the calculation time . . . . .	85
4.27	Effect of the friction angle of the interfaces between the rock blocks on the minimum force for model non-convergence . . . . .	85

# List of abbreviations

AMEL	Average Mesh Edge Length
BLK	Leica BLK360 scanner
CHA	Cultural Heritage Agency
FOS	Factor Of Safety
GIA	Groningen Institute of Archaeology
JCS	Joint wall Compressive Strength
JMC	Joint Matching Coefficient
JRC	Joint Roughness Coefficient
PMD	Point-to-Mesh Distance
TLS	Terrestrial Laser Scanner (Leica P40 scanner)
ZOI	Zone Of Interest

## Definitions

For the sake of clarity, the separate rocks within the zone of interest (ZOI) of the megalithic monument have been given numbers. The numbers were awarded from east to west and from north to south. In other literature, the dislocated capstone is also referred to as capstone D9. In this report, it will be referred to as Rock 3.



Definitions for the numbers of the rocks in the zone of interest.

# Chapter 1

## Introduction

### 1.1 Background

Dolmens are megalithic monuments, which were typically built a few thousands of years BCE and can be found all over the world. Some thousands of dolmens were built in Europe, of which 54 have been preserved in the Netherlands. The Dutch dolmens were built with rocks that came with glaciers in the second to last ice age in the Netherlands, the Saalian, which lasted from 300 000 to 130 000 years ago. During this ice age, the glaciers transported rocks from Scandinavia to large areas in North-West Europe. Although the rocks were deposited in the Netherlands only a few hundred thousand years ago, the rocks themselves can be millions of years of age. Dutch dolmens are all located in the provinces of Drenthe (52) and Groningen (2), in or close to a geographical area called the Hondsrug. The dolmens were built by a people called the funnel beaker culture, after the distinct type of pottery that they left behind. The purpose of their megalithic structures remains largely unresolved, although there have been clues that they were used as burial sites and as a place for gatherings and rituals (Bakker, 2010).

The dolmen of interest, D14, owes its name to the province in which it is located, Drenthe. The dolmen is located in a rural area in the small village of Eext. With around 18 meters in length, it is one of the largest dolmens in the Netherlands. The dolmen consists of 18 support stones, 8 capstones, 2 keystones, 2 gate stones and 8 stones demarcating the outskirts of the dolmen. The configuration of rocks of the dolmen is very distinct. Dolmens consist of support stones that are nowadays often partly buried in the soil and capstones that lie on top of these support stones. This configuration of three stones with one stone on the top is called a trilithon. A dolmen generally consists of multiple trilithons in a row, such that an open space is created on the inside. At the ends of these rows, keystones are placed. This can be seen for dolmen D14 in Figure 1.1, in which the support stones are referred to with Z and Z', the capstones are denoted as D and the keystones can be found at Sl. Another feature of the dolmen is the original entrance to the chamber. The entrance is surrounded by gate stones, which are denoted with P. The rocks on the outskirts of a sandhill, which covered the dolmen in the past, are referred to with K.

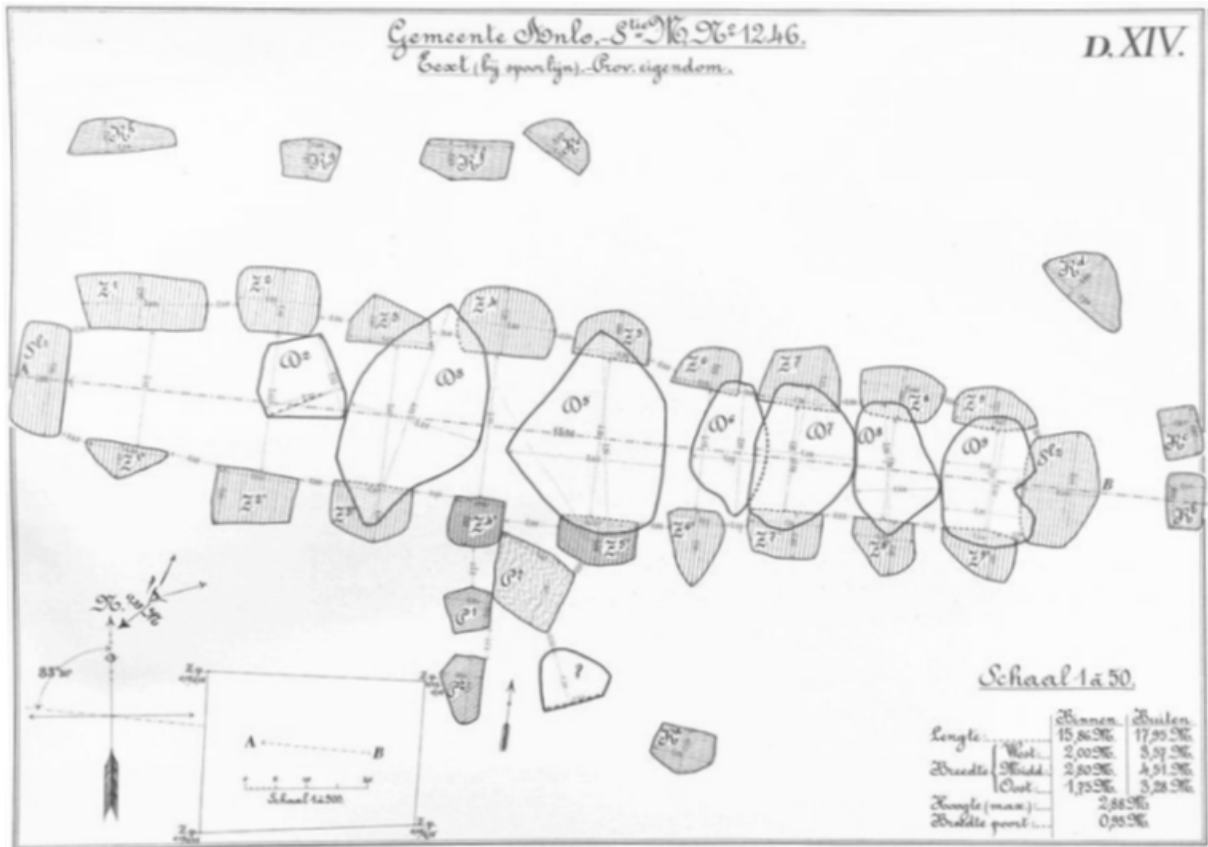


Figure 1.1: Map of megalithic monument D14, made by Van Giffen in 1925. Adapted from RAAP 4112, 2020.

## 1.2 Problem statement

In the spring of 2019, the capstone Rock 3 of dolmen D14 was dislocated. It is suspected that this rock was pushed off its two support stones. Since this incident, the rock has been lying on its side (see Figure 1.2).



Figure 1.2: Dislocation of capstone 3, view from the South (left) and East (right).

Cultural Heritage Agency (CHA) of the Netherlands has asked TU Delft to digitally investigate potential reconstruction scenarios for the dolmen in the neighborhood of Rock 3. This thesis does not focus on a multitude of potential reconstruction scenarios. Instead, it focuses on the methods for investigating potential reconstruction scenarios. Future decisions on whether the dolmen will actually be reconstructed can then be supported by stability analyses of potential reconstruction scenarios.

## 1.3 Research questions

Based on the problem description, the main research question was formulated as follows:

*How can dolmen D14, focusing around the dislocated capstone Rock 3, be reconstructed to a stable configuration of rocks while also conforming to the demands from the relevant dolmen management agencies?*

This research question contains two elements. Firstly, there is the question of how the dolmen can be reconstructed to a structurally stable configuration of rocks. Structurally stable, in this sense, means the immobility of the construction. Even when people with bad intentions would try to push against a rock in order to dislocate it, it should cause little to no displacement of the assemblage of rocks. The other element of this research question is that the rock configuration should conform to the demands from the relevant dolmen management agencies. The demands regarding the reconstruction scenarios were specified by the relevant dolmen management agencies, which are the Cultural Heritage Agency (CHA) of the Netherlands and the Stichting Drentse Landschap, see Section 1.5. The CHA implements policies regarding cultural heritage, amongst which dolmen, from the Ministry of Education, Culture and Science and the Stichting Drentse Landschap is more specifically committed to the sustainable conservation and management of the Dutch dolmen.

In order to answer the main research question, three sub-questions were formulated.

1. How can a model be created, which (1) accurately documents the geometry of all individual rocks in the zone of interest and (2) is suitable for digital stability analysis?
2. How can the relevant rock parameters, contributing to the shear strength of the rock contact surfaces between the rocks, be determined?
3. How can potential reconstruction scenarios be digitally assessed on their stability, while considering the limitations inherent to digital analyses?

## 1.4 Objective and scope of the study

The main objective of this research is to investigate new methods to assess the stability of a dolmen, and specifically dolmen D14 around the dislocated Rock 3. In the past, dolmens were reconstructed using a trial-and-error approach in the field. It can be very hard to find a stable configuration in the field, as the rocks have small contact areas and very irregular geometry. For this reason, past reconstructions have resulted in some unstable rock configurations. The dislocation of (cap)stones can result in splitting of the rocks. This should be prevented in order to preserve these cultural heritage sites for generations to come. When digital, non-destructive stability analyses are performed before the physical reconstruction of the dolmen, one can have a better view of whether it will be a lasting solution to the problem.

Since this is such a broad research field, combining many disciplines, the scope of the work should be defined beforehand. The research will focus on three parts, based on the three research sub-questions. These parts will be illustrated below.

*Part 1. Developing geometrical models that accurately document all independent rocks and are suitable for digital stability analyses.*

Part 1 will focus on developing digital geometrical models for all of the rock surfaces in the zone of interest. The models will only be made for Rock 1-7 as these are thought to be most useful for the digital stability analyses of Part 3. The focus will only be on the visible parts of the rocks of the dolmen, not the buried part of the support rocks. Furthermore, a recommendation should be made

regarding the point cloud requirements, such as density and accuracy of the point cloud, to create 3D models for documentation and numerical stability analysis.

*Part 2. Determining relevant rock parameters, contributing to the shear strength of the rock contact surfaces between the rocks.*

Part 2 focuses on the shear strength of the rock contact surfaces, only using non-destructive methods in the field or tests on analog samples in the laboratory. The main focus will be on the determination of the residual friction angle, since this parameter was found to have the biggest influence on the shear strength of the interface between non-matching rock surfaces.

*Part 3. Evaluating how the stability of reconstruction scenarios for dolmen D14 can be digitally analyzed, while considering its limitations.*

As for Part 3, the focus will mostly be on how potential reconstruction scenarios should be analyzed, and less so on which reconstruction scenarios would be most stable. With the methods as explained in this part, the analysis can be done for a multitude of scenarios. The reconstruction scenarios will only include Rock 1-7 and will be defined in accordance with the guidelines for reconstruction scenarios of the dolmen.

## **1.5 Reconstruction guidelines**

Reconstruction is rebuilding a monument to its state at a specific time in its past. However, the precise state and configuration of dolmen D14 has been changed many times in its past (RAAP 4112, 2020). For this reason, this section will look at the requirements for the reconstruction of dolmen D14 as stipulated by the relevant management agencies. As an extension thereof, the general structural elements of a dolmen and, more specifically, the structural history of dolmen D14 will also be presented.

### **1.5.1 Requirements from the relevant management agencies**

The relevant management agencies involved in the project are the Cultural Heritage Agency (CHA) of the Netherlands and the Stichting Drentse Landschap. It was desired that potential reconstruction scenarios would be in line with the general configuration of rocks that is typical for dolmens, as well as with the reconstruction history of dolmen D14. Furthermore, dolmens with a large space between trilithic elements would be more attractive in the eyes of tourists. Apart from these two guidelines, the agencies have stipulated that the reconstruction should be done without any damage to the monument. Not only the rocks may not be damaged, the mosses that grow on the surface of some of the rocks should also not be harmed. Lastly, it is desired that no artificial elements be added to the structure, such as metal pins or mortar.

### **1.5.2 Structural elements of a dolmen**

Dolmens have a very distinct rock configuration. Currently, dolmens look a lot different from what they looked like when they were originally constructed. The large rocks, nowadays the only remaining elements of the dolmen, used to be part of a much larger structure. These large rocks served as a skeleton to create an open room within a small hill of sand (see Figure 1.3). This room could be accessed from the outside via a gate. On the outskirts of the small hill were other rocks to demarcate the end of the hill and support the sand. In between the large rocks, some smaller rocks were placed that were used to fill up the smaller gaps and keep the sand from entering the room. One feature that stands out in this configuration, is that the rocks that are part of the room are placed in such a way that the inner space becomes rectangular. This means that the rocks were placed with their flat surfaces as walls of the room and that their more rounded or bulky surfaces were pointed away.

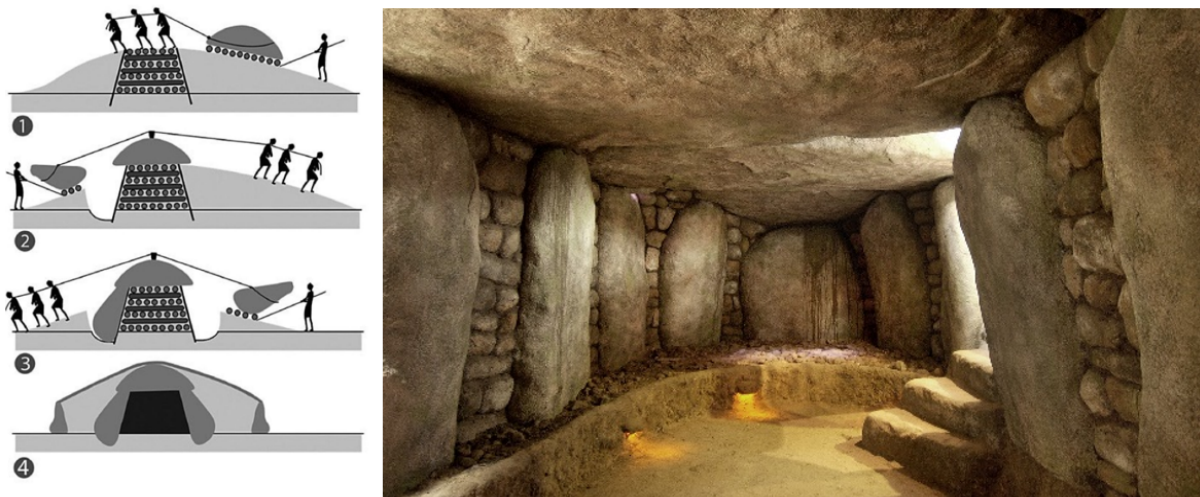


Figure 1.3: Reconstruction of a dolmen profile cross-section (left) and an inside chamber of a dolmen (right). Adapted from Clerinx, 2017 (left) and Hunebeddencentrum, 2018 (right).

### 1.5.3 Structural history of dolmen D14

In the past, dolmens have been modified many times. For instance, large quantities of megalith rocks have been transported to the Western part of the Netherlands in order to create dykes. Also, amateur archaeologists have adapted the configuration of the rocks to their taste. A very brief reconstruction history of dolmen D14 will be presented here, based on RAAP 4112, 2020. The focus of this structural history will be on Rock 1 and Rock 3 since these rocks are most relevant for the reconstruction of the dolmen in the zone of interest.

The earliest documents of dolmen D14 date back to the eighteenth century (RAAP 4112, 2020). In the earliest documents, it is found that Rock 3 was located in a different position than it was in 2019, namely with its low side facing north. Another rock that was clearly in a different position in 1925 compared to 2019 is Rock 1. Compared to the situation in 2019, it appears that Rock 1 was rotated by approximately 90 degrees in 1925. The face that was once facing the west is currently the top of the rock. In 1925, Van Giffen published a map of monument D14, from which the position of Rock 1 can be deduced (Figure 1.1). The orientation of Rock 3 can be derived from the direction of the triangular notch, which is in the east in Figure 1.1, while it is in the west in the configuration of 2019. Furthermore, the orientation of Rock 1 and 3 is clearly visible in the pictures that Van Giffen took in 1927 (see Figure 1.4). At that time, Rock 1 played the role of a keystone, interlocking Rock 3 between itself and Rock 6.

In 1957, there were reports that Rock 3 had fallen off its base stones and was split in two (RAAP 4112, 2020). Afterwards, it was decided to construct a pillar made of fieldstones, to support the capstone while it was still in two pieces. Only in 1965, the rock was mended with mortar and placed back. This time, Rock 3 is placed in contact with only Rock 2 and 4, not with the keystone Rock 1. This is also the moment when Rock 3 is shifted 180 degrees to the position that it was in right before its fall in 2019. Rock 1 was rotated and tilted at the same time to the position it is currently in. The reason to change the orientation of both rocks remains unclear. In 1996, the fieldstone pillar was removed. To ensure the stability of Rock 3, a metal pin was inserted (see Figure 1.5) and resin was applied to connect Rock 3 and 2. Furthermore, a cement-like mixture was used to attach Rock 3 to Rock 2 and 4.

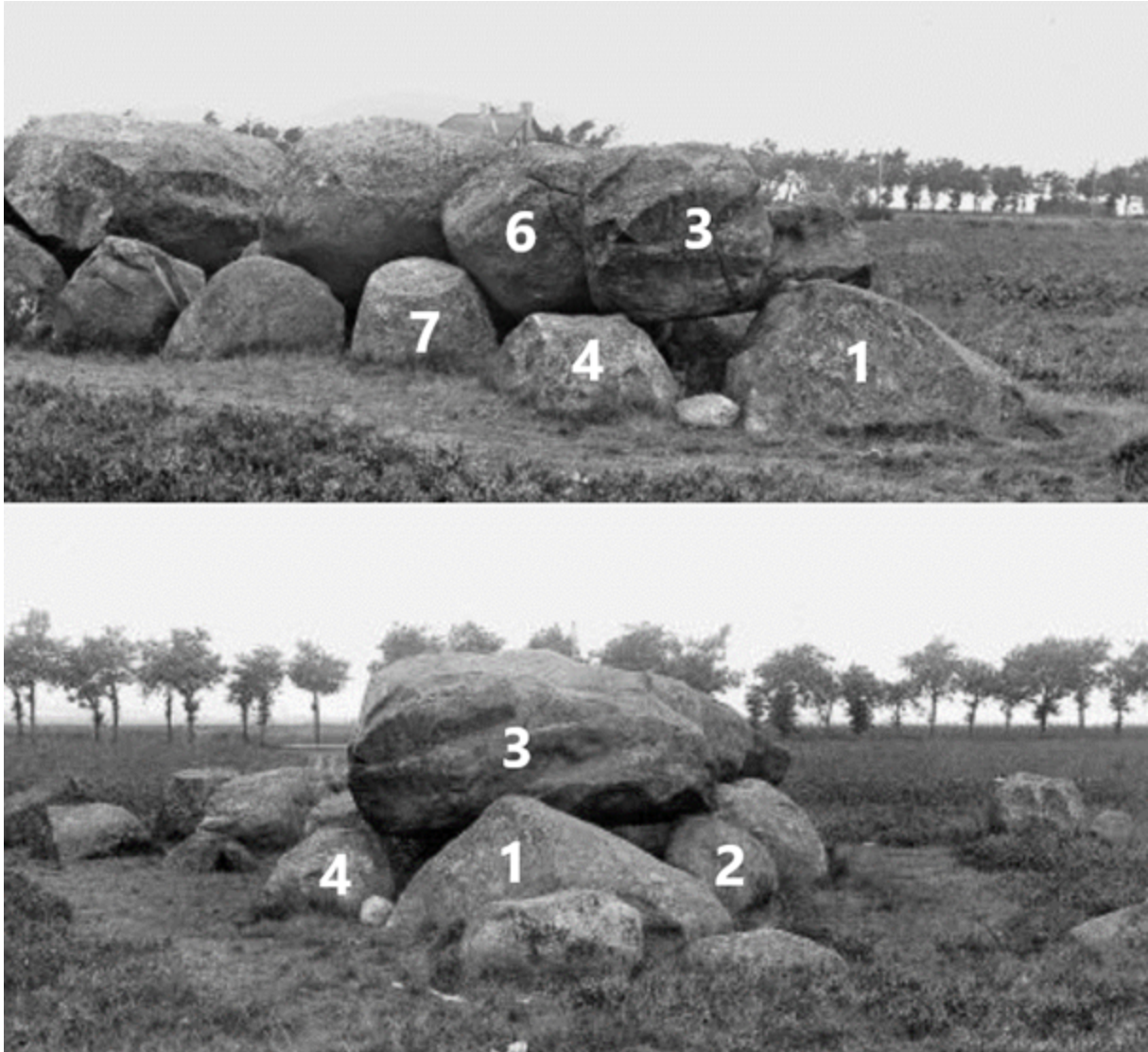


Figure 1.4: Pictures of dolmen D14 in 1927, adopted from RAAP 4112, 2020.



Figure 1.5: Picture of metal pin connecting Rock 3 to Rock 2 (n.d.). Adapted from RAAP 4112, 2020.

## **1.6 Thesis outline**

This research is split up in three parts. These parts will be dealt with in separate chapters. The first part (Chapter 2) concerns the development of a geometrically accurate 3D models of the rocks in the zone of interest, using laser scanning equipment. The second part (Chapter 3) concerns non-destructive methods for rock joint parameter determination that are required for the stability analyses. The third part (Chapter 4) deals with the actual stability analyses and the factors that influence their results. In Chapter 5, a conclusion will be presented for each of the three parts, as well as their linkages and the recommendations for future research can be found in Chapter 6.

## Chapter 2

# Creating geometrically accurate 3D meshes

This chapter starts with an introduction in which the need for accurate 3D models is explained (Section 2.1). In the following Section (2.2), some terminology and literature on this topic will be introduced. In Section 2.3, the methods will be further explained, after which its results will be presented (Section 2.4) and discussed (Section 2.5). Lastly, conclusions on this topic can be found in Section 2.6.

### 2.1 Introduction

In 2017, a 3D model of dolmen D14 was made by the Groningen Institute of Archaeology (GIA, 2017). This 3D model, however, is not very suitable to be used for the stability analyses. First of all, it contains a lot of noisy data points (see Figure 2.1). This is especially true for the narrow spaces near the contact areas of the rocks and underneath the capstones. A noisy data set is likely to produce a 3D mesh model with a low accuracy. Therefore, results of stability analyses based on this GIA model may not correctly reflect the behavior of the dolmen

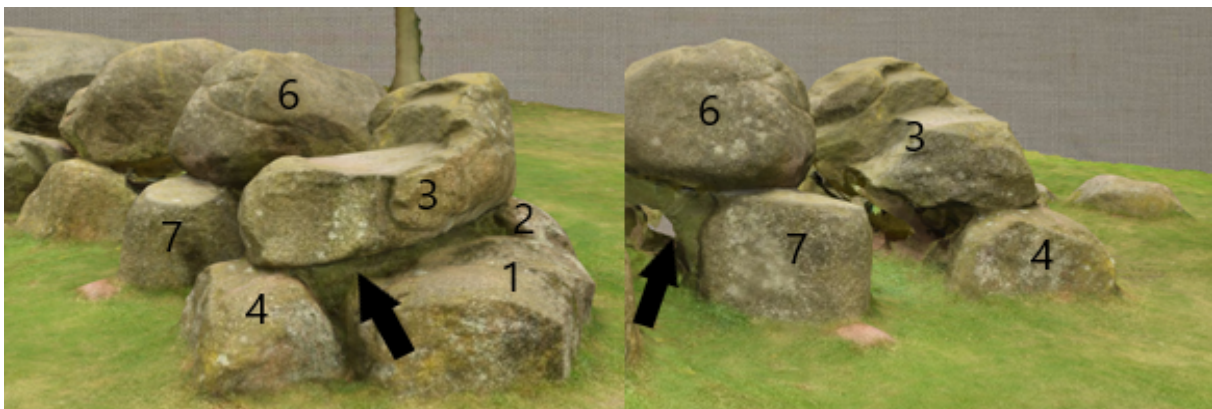


Figure 2.1: Modified captures of the 3D model made by GIA, 2017. The arrows point to noise in the model.

The second major disadvantage is that the mesh of the model is very coarse. The total number of faces is 199,999, for an area of 28x21m (see Figure 2.2).

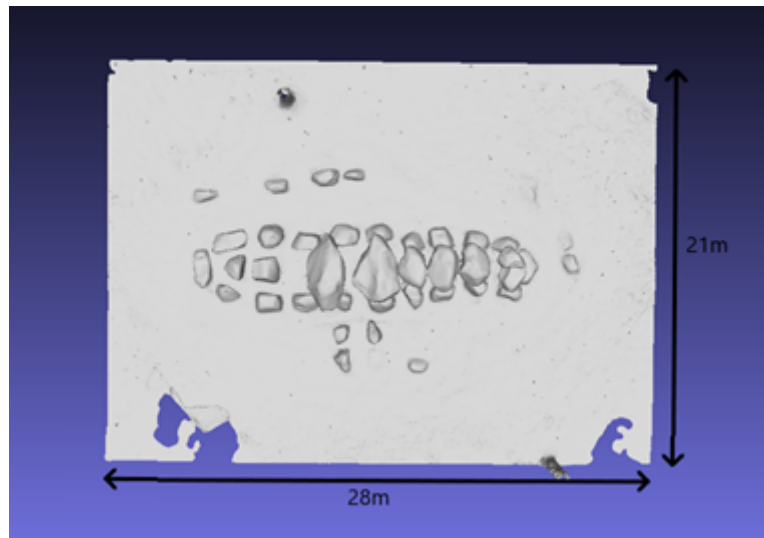


Figure 2.2: Total 3D model made by GIA, 2017. Modified with dimensions.

Due to these disadvantages, it was decided to create new 3D meshes that are more detailed and have a higher accuracy. These new models were created with two purposes:

1. to document the geometry of the rocks so that it can be used for consultation in the future.
2. to be used for digital stability analyses of the dolmen.

When creating models for documentation, the aim is to make a model that is as accurate and detailed as possible. The model can be a surface mesh. However, when creating a model to be used for the digital stability analyses, the meshes should be sufficiently detailed as to represent the rocks surfaces with enough detail, but the level of detail, and thereby file size, should also not be too large. Detailed, complicated meshes that require a lot of memory can not be used for numerical calculations, since there are limitations with regards to memory when using a common desktop. This model should be a volume mesh in a format that is compatible with the numerical analysis software (3DEC).

## 2.2 Literature

This section will start off with some information on how LiDAR technology works (Section 2.2.1). Then, basic terminology will be provided on meshes (Section 2.2.2) and a selection of studies will be presented on laser scanning and its applications to document and assess the stability of archaeological rock structures (Section 2.2.3).

### 2.2.1 LiDAR and point clouds

LiDAR (Light Detection And Ranging) technology is used to acquire point cloud data. A point cloud is a set of discrete points with x-, y-, z-coordinates of points in a 3D space. Moreover, the point cloud may have other attributes such as the Red-Green-Blue (RGB) color of points. LiDAR technology revolves around laser beams (Vosselman & Maas, 2010). The laser scanner emits a laser beam, and when it hits an object, some of this energy bounces back to the scanner. This return signal is then detected by the scanner. A timer, built into the scanner, detects how much time has passed since the signal was emitted. The distance between the object and the scanner can then be calculated by multiplying half the time period with the speed of light. The output of a laser scanner is called a point cloud, that consists of a multitude of points in a 3D space. By combining the distance between the scanner and an object with the horizontal and vertical angle at which the measurement was taken, the 3D space can be filled with points. Laser beams do not travel through objects. Therefore, multiple

scanning positions should be used to fully capture a site. These scans can be aligned with each other to create a full 3D model.

## 2.2.2 Terminology on meshes

A model is, simply put, a representation of an object. However, 3D models come in different forms. In this research, the starting point for the geometrical models were point cloud models. Based on a point cloud, a mesh can be generated by using appropriate surface reconstruction methods. There are two different types of meshes: surface and volume meshes. A surface mesh consists of vertices, edges and faces that together represent the shape of an object's surface (see Figure 2.3). A volume mesh solely consists of 3D elements, consisting of vertices, faces and volume elements.

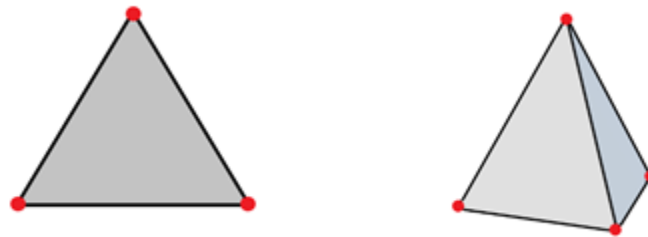


Figure 2.3: Mesh elements consisting of faces (grey), edges (black) and vertices (red). The left element is a surface element and the right element is a volumetric element.

## 2.2.3 Application of laser scanning to document and assess the stability of archaeological rock structures

Laser scanning is increasingly applied to document archaeological sites (Vosselman & Maas, 2010). Laser scanning technology is very useful, since it can document the state of the site and produce dense 3D information on its geometry. Oftentimes, the combination of laser scanning with pictures, videos and drawings provides the best documentation of an archaeological site. Laser scanning for documentation of archaeological sites has, for example, been done on the great pyramid of Giza, Egypt (Neubauer, Doneus, Studnicka, & Riegl, 2005), Al-Deir monument in Petra, Jordan (Alshawabkeh, Bal'awi, & Haala, 2010) and the Byzantine land walls in Istanbul, Turkey (Bayram et al., 2015).

Other laser scanning uses include capturing the geometry with the purpose of assessing the stability of a monument or potential reconstructions. This was done for several monuments including the middle stoa in the Agora in Athens, Greece (Georgopoulos, 2014), A'Famosa fortress in Malacca, Malaysia (Wei, Chin, Majid, & Setan, 2010) and the Domus Tibernia on the Roman Forum, Italy (Tapete et al., 2013). More specifically for megalith monuments, Rodríguez-Miranda et al. (2017) researched the Alto de la Huesera dolmen in Spain. In this research, laser scanning was used to document the changes of the rocks of the dolmen during a reconstruction, which lasted from 2010 to 2014. Specifics of the point cloud cannot be found in the article. The only information that is provided is that the mesh elements of the rocks in the 3D model were 3 cm in length, which is not very detailed. The meshing software was not documented. Although the above studies have used laser scanning for stability assessments or potential reconstruction scenarios, none of these used numerical methods for their calculations.

Two instances were found in which digital geometrical models were made of a dolmen using laser scanners, with which stability analyses were performed using numerical methods. Muñoz-Menéndez et al. (2020) did a stability analysis on a large boulder, balancing on top of another large boulder.

In this research, terrestrial laser scanning and photogrammetry were used to capture the geometry. Consequently, AutoCAD and Rhinoceros were used to create meshes from a point cloud that consisted of 6.1 million points. Another study was conducted by Motsa et al. (2020), which was a structural investigation of the Mnajdra megalithic monument in Malta. In this study, terrestrial laser scanning equipment was used to capture the geometry of the structure, after which parametric eigenvalue analysis was conducted using the finite element method. No specifics are provided regarding the density of the point clouds, as well as on the density of the meshes used in the numerical calculations. The meshes were made in Autocad and then imported in the numerical stability software Abacus.

## 2.3 Methods for 3D mesh generation

3D models were developed in four steps. Firstly, laser scanning equipment was used to acquire point cloud data of the geometry of the rocks. Secondly, this point cloud data was pre-processed, which can include data cleaning, point cloud alignment and removing irrelevant points, so that the 3D meshes could be generated in the third step. Lastly, the meshes were evaluated on their fit and completeness. The steps of the workflow will be elaborately discussed in this section. The general workflow for creating 3D models can be summarized by four steps (see Figure 2.4).

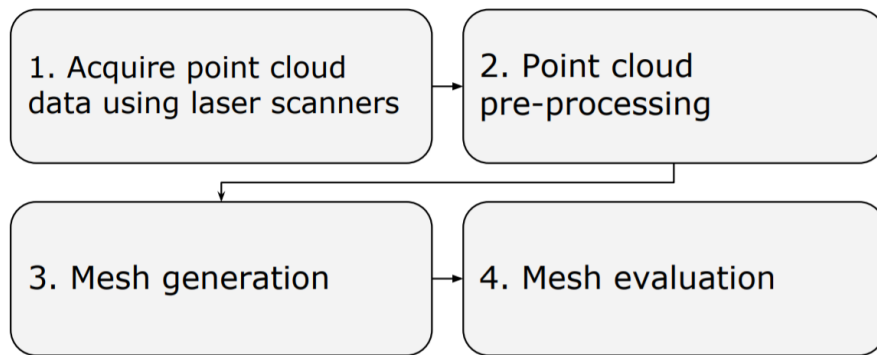


Figure 2.4: General workflow for creating 3D meshes.

### 2.3.1 Acquiring point cloud data

A site investigation was conducted on the site of the dolmen. The main goal of this fieldwork was to use laser scanners to capture geometrical surface data of the rocks. Special interest was paid to the zone around the dislocated Rock 3. Two laser scanners were used: (1) a Leica P40 terrestrial laser scanner (TLS) owned by TU Delft, and (2) the Leica BLK360 scanner (BLK) borrowed from Leica. Both scanners are able to capture high-resolution scans, although with different accuracies (see Table 2.1, Appendix A). The TLS was used to acquire data points of the rocks, but was too large in size and not sufficiently adjustable in height to reach all surfaces of the rocks, since the rocks were located in a narrow area. Therefore, the smaller BLK was also used to provide complement data, where TLS data is not available.

	Leica P40 (Leica Geosystems, 2017b)	Leica BLK360 scanner (Leica Geosystems, 2017a)
Range	Up to 270 m	0.6 – 60 m
3D point accuracy	3mm @ 50m / 6mm @ 100m	6mm @ 10m / 8mm @ 20m

Table 2.1: Characteristics of Leica scanners used to capture point cloud data.

### 2.3.2 Point cloud pre-processing

The second step in creating 3D meshes is to create point cloud models from the raw data. The main objectives are to remove outliers and combine the TLS and BLK datasets in order to create a point cloud model with the highest possible data coverage and accuracy. This process was divided into 8 modelling sub-steps (see Figure 2.5) and will be described in detail in this section. Figures to illustrate each sub-step can be found in Appendix B.

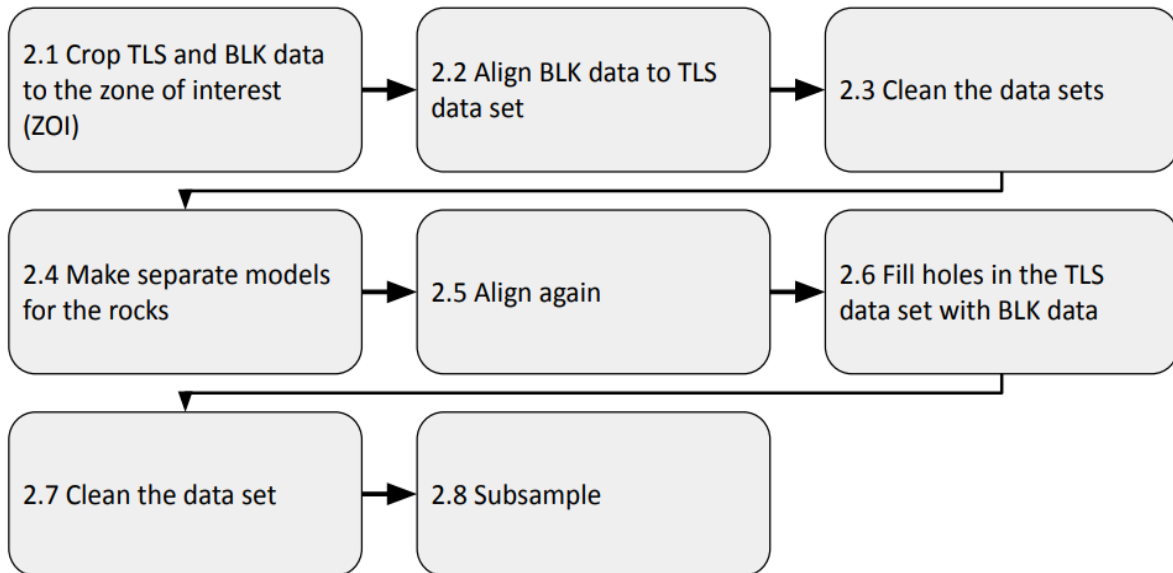


Figure 2.5: Workflow of point cloud pre-processing Step 2.

Pre-processing steps were performed with CloudCompare (CloudCompare, version 2.11.3, 2021; CloudCompare, version 2.12.alpha, 2021), which is open-source software that is used for registration and analysis of point cloud data. Below, the steps of the point cloud modelling process are explained in further detail.

#### 2.1 Crop TLS and BLK data to the zone of interest (ZOI).

In order to develop point cloud models that capture the complete surfaces of all rocks, two different datasets were used. One dataset was acquired with the TLS and the other with the BLK scanner. As these data sets contained many points, which can cause difficulty to manage in a common desktop, the datasets must be reduced to only the points in the Zone of Interest (ZOI), which comprises of Rock 1-7.

#### 2.2 Align BLK data to TLS data set.

Since the point clouds from the BLK and TLS were in different coordinate systems, the point clouds must be aligned to the same coordinate system. The TLS data set was kept as a reference and the BLK data set was aligned. This was done in two steps. In the first step, the BLK data set was roughly aligned. Rough alignment is done by picking at least three point pairs. A point pair consists of one point in the reference point cloud and one point in the point cloud that is to be aligned. The new alignment of the point cloud will be estimated by minimizing the distance between the point pairs. In the second step, fine alignment was done. Fine alignment can be done automatically without picking point pairs. Using an iterative closest point (ICP) algorithm (Vosselman & Maas, 2010), the root mean square distance between the reference cloud and the aligned cloud is continuously calculated to determine a transformation matrix for the point cloud that is to be aligned. This distance between the

clouds is computed from subsampled point clouds that are randomly created from the reference and aligned point clouds. The process iteratively estimates the optimal transformation matrix between the two clouds and is terminated when either the maximum number of iterations, or the root mean square difference (RMSD) reaches a predefined threshold.

### 2.3 Clean the data sets.

The first cleaning sub-step is to remove a significant part of the outliers and irrelevant points. These points can be caused by undesirable objects near the rocks, such as equipment or tree leaves, or sensor deficiencies, such as faulty time measurements and multi-path reflections.

### 2.4 Make separate models for the rocks.

So far, all pre-processing sub-steps were applied to one large dataset, consisting of the data point of all rocks. During this sub-step, separate point clouds were created for each rock. In total, 14 different files were produced. 1 file for each rock, 7 rocks per data set and two data sets.

### 2.5 Align again.

Further alignment of the TLS dataset to the BLK dataset was required for each rock individually. This is necessary because the initial alignment can still be off by a couple of centimeters. In this process, the TLS data set was kept as the reference and the BLK data set were aligned. The offset of the TLS and BLK datasets was now reduced to a couple of millimeters.

### 2.6 Fill the sparse point cloud zones in the TLS data set with BLK data.

The next step was to combine the TLS and BLK data. This was done by looking at the offset between the TLS and BLK data. Whenever the datasets were visually found to be not very well matching, the BLK point cloud was removed. It was decided to remove the BLK data because the TLS data should have a higher accuracy compared to the BLK data, according to Leica's own publishing (see Appendix A). For example, for Rock 3 the TLS and BLK data were used over the whole rock surface, while Rock 2 consists of TLS data for one half of the rock surface and BLK data for the other. For Rock 3, not only data from the TLS and BLK scanner was used, but also from the 3D model of the dolmen published by Groningen Institute of Archaeology (Groningen Institute of Archaeology (GIA), 2017). This data was necessary after the dislocation of Rock 3, because one side of the rock is not visible anymore since it is resting on the ground surface. The GIA data was acquired before 2019, and therefore shows the side of the rock that is currently laying on the ground, however in lower resolution. The original GIA data was a .obj mesh and not a point cloud. Therefore, the mesh data had to be converted to point cloud data by means of taking sample points from the mesh.

### 2.7 Clean the data set.

Additional cleaning of the data set was required.

### 2.8 Subsample.

The last step to make appropriate point cloud models is subsampling. This is done in order to reduce the file size of the data, which makes the data easier to be handled with a common desktop. Subsampling is necessary because the program that is used to create the meshes, MeshLab, cannot run too large files. Subsampling is creating a subset of the points of the point cloud by a certain requirement. In this research, this requirement was set to 'space'. This means that the minimum distance between two neighboring points is never smaller than the specified space. For example, for a subsampling distance of 5 mm, the minimum distance between the points should be no smaller than 5 mm. During the subsampling process, no new points are created. Points are only discarded when they are too close to each other.

### 2.3.3 Mesh generation

Several meshing steps have been taken to develop the point cloud models of Rocks 1-7 into 3D meshes. The steps are illustrated in Figure 2.6 and are further elaborated upon in this section. Figures of the different steps within the workflow can be found in Appendix C.

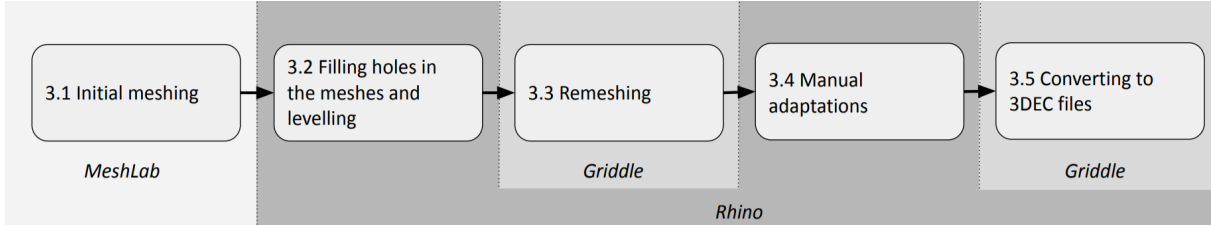


Figure 2.6: Steps in developing the 3D meshes from point cloud models.

#### 3.1 Initial meshing in MeshLab.

The 3D meshes were created in MeshLab (Meshlab, version 2020.12, 2020), which is open-source software designed to calculate, process and edit 3D meshes. There are several methods for doing this (Kazhdan, Bolitho, & Hoppe, 2006; Lim & Haron, 2014), but one of the most well-known is the Poisson surface reconstruction method. This method was chosen because it was found to give good results for noisy data (Kazhdan et al., 2006) and because it can be easily applied using free software such as Meshlab. This method requires two steps: the calculation of the normal vectors for all points and the surface reconstruction.

First, the normals of all points need to be estimated. This is done based on the principle of tangent plane estimation (Hoppe, DeRose, Duchamp, McDonald, & Stuetzle, 1992). The tangent plane is a plane fitted to a number ( $k$ ) of neighboring points. The plane is fitted to a point using principal component analysis, based on analyzing a covariance matrix  $C$  which is constructed based on the  $k$  nearest neighboring points. The covariance matrix is expressed in Equation 2.1 (Nurunnabi, West, & Belton, 2015).

$$C = \frac{1}{k} \sum_{i=1}^k (p_i - \bar{p})(p_i - \bar{p})^T \quad (2.1)$$

In this formula,

- $k$  = number of neighboring points
- $p_i$  = point of interest
- $\bar{p}$  = center point in the data

From this covariance matrix, the eigenvalues and eigenvectors can be calculated. The normal of the point is the eigenvector, corresponding to the smallest eigenvalue. The normals were estimated within Meshlab using default input values for the option 'compute normals for point sets', which means that 10 neighboring points were used.

The second step of the Poisson reconstruction method is the actual surface reconstruction. Poisson surface reconstruction is an implicit surface reconstruction method using an indicator function. This means that there is an interpolation between the points of the point cloud to find a function that represents the surface, which best fits the points. This function should give a result of 1 for the points inside the surface, and 0 for the points outside the surface. This 3D indicator function  $\tilde{\chi}$ , can be

expressed as follows:

$$\Delta \tilde{\chi} = \nabla \cdot \vec{V} \quad (2.2)$$

In this formula,

$\tilde{\chi}$  = indicator function for the implicit surface  
 $\vec{V}$  = oriented normals of the points

This is a standard Poisson problem. The Laplacian of the function  $\tilde{\chi}$  is equal to the divergent of the normals. It should be solved to find the function  $\tilde{\chi}$ , which gradient best matches the oriented normals of the points  $\vec{V}$ .

Poisson surface reconstruction results in watertight, triangulated meshes. The meshes are generally smooth, which is suitable for noisy data (Kazhdan et al., 2006). However, the Poisson surface reconstruction method has a tendency to over-smooth the data when it is applied to very sparse or very anisotropic point clouds. In the latter case, the main issue is with determining the directions of the normals. In an effort to improve the Poisson surface reconstruction method, the screened Poisson surface reconstruction method was developed (Kazhdan & Hoppe, 2013). With this method, positional constraints are added to the calculations, in order to prohibit an over-smoothing of the data.

### 3.2 Filling holes in the meshes and levelling in Rhino.

Since the laser scanners could not acquire any data of the rocks beneath the ground, the point clouds only consisted of points of the visible surfaces of the rocks. Therefore, the meshes were also only fitted to the visible surfaces of the rocks, causing them to contain holes at the bottoms of the rocks. This means that there is no information about what the rock looks like beneath the ground. It was decided to construct flat surfaces on the ground level in order to produce 'watertight' meshes. This was necessary, since the stability analysis software 3DEC requires volumetric meshes and therefore the surface meshes needed to be 'watertight'. This closing of the meshes was done in Rhino (Rhinceros, version 6.34.21034.7001, 2021). At the same time as closing the meshes, the meshes were also levelled to each other, meaning that the flat bottom was set at the same depth for all rocks.

### 3.3 Griddle remeshing in Rhino.

Within Rhino, the Itasca plug-in Griddle (Griddle, version 2.00.8, 2020) was used to re-mesh the surfaces. The Gsurf tool was used to create a mesh containing elements of more regular size. Important remeshing setting options will be discussed in this section. First of all, the element *mode* can be decided. It was chosen to select the quadrilateral dominated option. In the meshing process, the preference will be given to quadrilateral elements, but when this proves too difficult some triangles will also be allowed. Another important setting is the *minimum* and *maximum edge length*. These numbers specify the target range in which the element edges should lie. If given the same value for both parameters, the mesher will aim for an average edge of that length with less variation in size. The *ridge angle* denotes the level of detail in the mesh. It ranges from 0 to 90 and it states what angle is allowed between two mesh faces that share an edge. All advanced parameters were kept at their default values. All meshing values for Griddle can be found in Appendix D.

### 3.4 Manual adaptations in Rhino.

In this meshing step, the mesh was visually inspected in Rhino. Small mesh elements were replaced for larger ones and the mesh was reconstructed. This is done, because small elements can cause problems in stability analysis software. Other adaptations in Rhino include moving and tilting of rocks. This is necessary to create new configurations of the rocks, based on the specified scenarios to be analyzed.

When creating the rock configurations for the sensitivity analysis regarding the mesh coarseness, the rocks were placed in exactly the same positions using Rhino commands.

### 3.5 Converting Rhino to 3DEC files.

The last step of the meshing process is to convert the Rhino files to 3DEC files. This was done using the Griddle extension with the GVol tool. This tool creates a volume mesh from a surface mesh. The default parameter values can be found in Appendix D. With GVol, local mesh refinement can be done. This was also done for the rocks in order to reduce the calculation time in 3DEC. This was done by creating larger blocks on the inside of the rocks and smaller elements on the outside of the rocks. Furthermore, Griddle allows for direct conversion of a Rhino mesh to a 3DEC mesh and results in a .3dgrid file type. This file type can be loaded directly into 3DEC.

## 2.3.4 Mesh evaluation

The mesh evaluation methods consist of qualitative mesh observations (Section 2.3.4.1) and quantitative point-to-mesh distance (PMD) analyses (Section 2.3.4.2).

### Qualitative mesh evaluation

The point clouds and resulting meshes are visually inspected to evaluate the quality of the meshes.

### Quantitative mesh evaluation

Point to mesh distance (PMD) analyses were conducted in CloudCompare (CloudCompare, version 2.12.alpha, 2021) to check how the meshes fit the point cloud. The point-to-mesh distance calculation was done to measure the fit of the mesh to the point cloud. Point-to-mesh distance (PMD) is defined as the minimum distance between a point and the mesh it is compared to. This way, PMD can give an indication of how well the mesh fits the point cloud. In theory, this is calculated by finding the minimum distance between a point  $P$  and a triangle  $T(s,t)$  from the mesh (see Figure 2.7). First, the squared distance  $Q(s,t)$  between the point  $P$  and the nearest point on the triangle should be found (Eberly, 1999). This is calculated using the following formula:

$$Q(s,t) = |T(s,t) - P|^2 = as^2 + 2bst + ct^2 + 2ds + 2et + f \quad (2.3)$$

In this formula,

$$a = E_0 * E_0$$

$$b = E_0 * E_1$$

$$c = E_1 * E_1$$

$$d = E_0 * (B - P)$$

$$e = E_1 * (B - P)$$

$$f = (B - P) * (B - P)$$

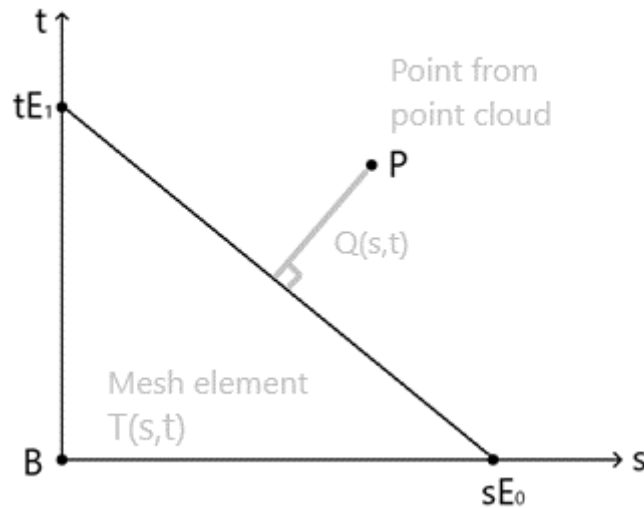


Figure 2.7: Illustration of PMD calculation. Point P represents a point of the point cloud and triangle  $T(s,t)$  represents an element of the mesh.

The goal is to minimize the distance  $Q(s,t)$ . This can either occur for a point on the boundary of the triangle, or in the interior of the triangle, when the gradient of  $Q$ ,  $\nabla Q(s,t) = 0$ .

The results of the minimum distance between a point and the mesh can be given in terms of Signed and Euclidean distances. The Signed distance is the distance from a point to the mesh, with a sign indicating the position of the point with respect to the mesh surface. This Signed distance can be either positive for points inside the mesh or negative for points outside the mesh (see Figure 2.8). It can be seen that the colors of the points in the figure indicate the distance between the point and the mesh. Red and yellow indicate positive values, lying inside the mesh, while green and blue values indicate negative values, lying outside the mesh. The Signed distance can be used in analyses to investigate the distribution of points laying inside and outside the mesh. The other type of distance is the Euclidean distance. The Euclidean distance is the absolute value of the Signed distance and does therefore not differentiate between points laying inside or outside the mesh surface. The Euclidean distance is commonly used as a measure of the mesh fit to the point cloud.

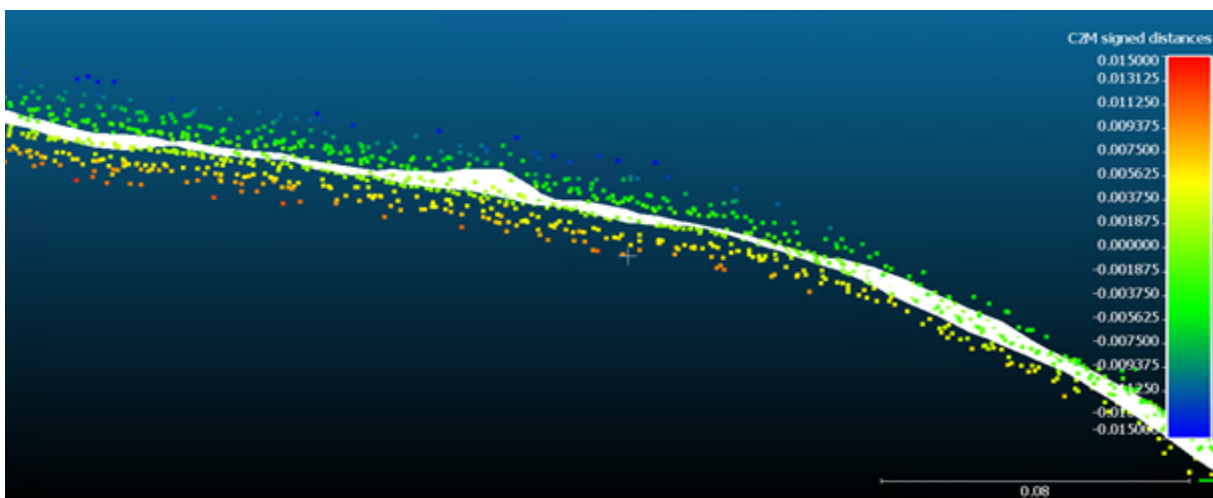


Figure 2.8: Signed distances of a rock mesh. Red/yellow for positive points and green/blue for negative points. The mesh is displayed in white.

In total, four different analyses were done:

1. PMD analysis between the original detailed point cloud and meshes made with subsampled point clouds, after meshing Step 3.1. In this analysis, the PMD was calculated for Rock 1-7.
2. PMD analysis between the original detailed point cloud and meshes made with subsampled point clouds, after meshing Step 3.4. In this analysis, the PMD was calculated for Rock 1-7. The final 3DEC mesh cannot be compared, since its format is not recognized by CloudCompare.
3. PMD analysis between the TLS and BLK point clouds and meshes made from the two data sets combined that were subsampled, after meshing Step 3.1. This analysis was done to quantify the difference between the two data sets used in this research. In this analysis, the PMD was calculated only for Rock 4.
4. PMD analysis between the original detailed point cloud and meshes made with subsampled point clouds using either only TLS and BLK data or TLS, BLK and GIA data, after meshing Step 3.1. In this analysis, the PMD was calculated only for Rock 3.

All analyses have been done for Signed distances and Euclidean distances. The mean values, standard deviation and 90<sup>th</sup> percentile values were investigated.

## 2.4 Results

The results will be discussed for each of the four modelling steps: acquiring point cloud data, point cloud pre-processing, mesh generation and mesh evaluation.

### 2.4.1 Acquiring point cloud data

A total of 51 scans was used to capture the geometry of the rocks. A scan is a capture of the surrounding geometry at one scanning location. The details of the total point cloud, as well as the point cloud cut to the zone of interest (ZOI), can be found in Table 2.2. Most of the BLK scans were taken around the ZOI, and the TLS scanner collected data spread out more evenly around the dolmen.

	Total point cloud (before pre-processing)		Point cloud cut to the ZOI (before pre-processing)	
	TLS	BLK	TLS	BLK
Number of points (-)	411 million	417 million	102 million	125 million
Number of scans (-)	20	31	18	26
File size (GB)	6.4	8.1	1.6	2.8

Table 2.2: Specifics of the total point cloud and for the point cloud cut to the ZOI.

### 2.4.2 Point cloud pre-processing

The result of the point cloud pre-processing step was a total of 28 point clouds. 4 separate point clouds were created for each of the seven rocks. All rocks used data from both the TLS and the BLK scanner, and GIA data was also used for Rock 3. Some images of the detailed point clouds can be found below (Figure 2.9). Several aspects of the point clouds will be discussed, such as the use of the different datasets, the subsampling step and some surfaces of interest in the final point cloud models.

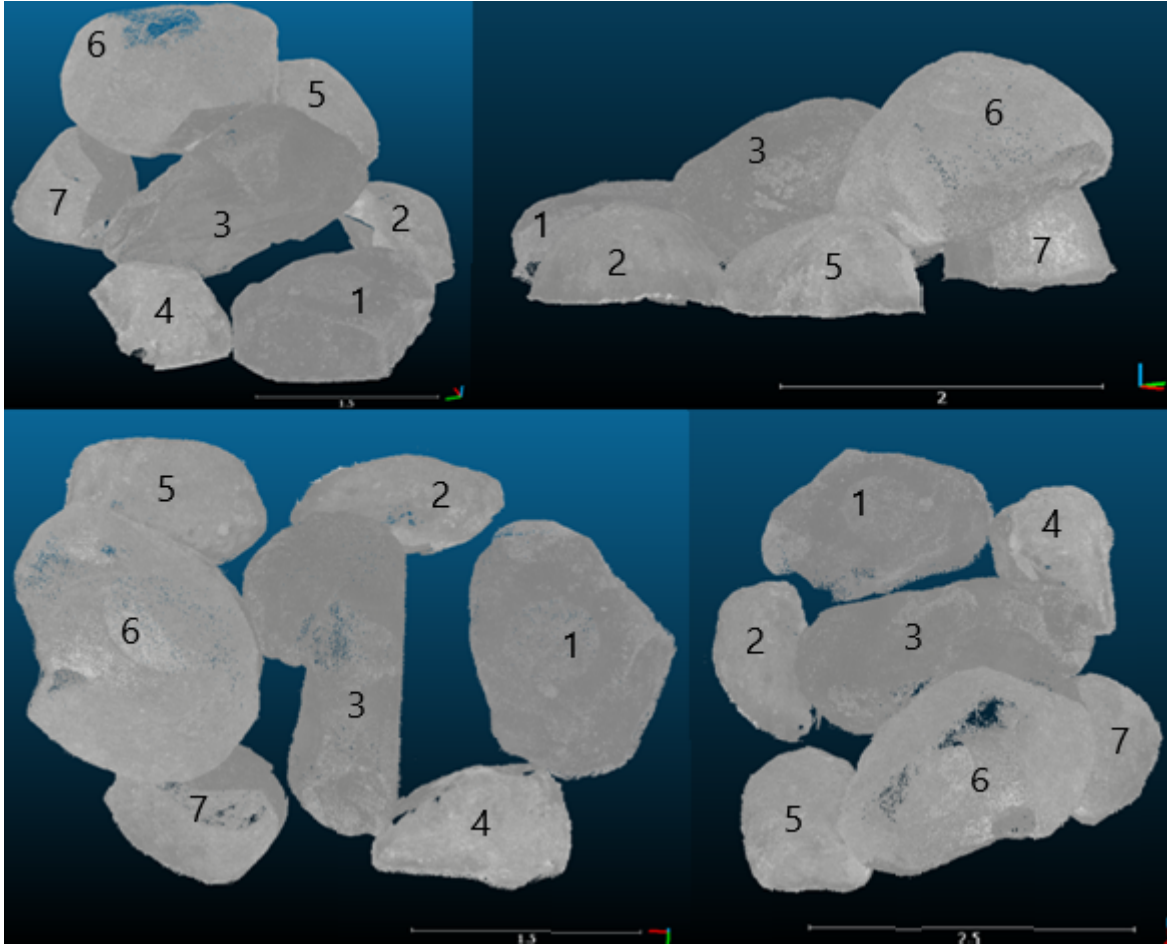


Figure 2.9: Images of the point cloud models. The scale of the figure is indicated in meters.

### Datasets

Data from the TLS and the BLK scanners, as well as GIA data for Rock 3, was used to create the point cloud models for all rocks. The number of points of the detailed point cloud is split out between all data sets for each rock in Table 2.3.

Number of points	Total number of points	Number of points from TLS data	Number of points from BLK data	Number of points from GIA data
Rock 1	23,145,530	15,219,233	7,926,297	
Rock 2	4,001,152	3,747,129	254,023	
Rock 3	43,707,784	12,215,219	31,287,409	1,983
Rock 4	5,570,129	4,846,237	723,892	
Rock 5	6,166,669	5,393,247	773,422	
Rock 6	25,439,980	20,666,917	4,773,063	
Rock 7	10,281,916	4,763,913	5,518,003	

Table 2.3: Number of points for the point clouds, divided per data set and documented after pre-processing.

The number of points was compared on a small area of approximately  $0.47\text{m}^2$  of Rock 3 (see Figure 2.10) to compare the point density of the TLS, BLK and GIA datasets. The corresponding number of

points can be found in Table 2.4. It can be seen that for this rock area, the density of the BLK dataset is the highest, and almost double the density of the TLS dataset. Furthermore, the GIA density is a lot lower, with only 1413 points per square meter. Although this example of density difference gives an indication of the magnitude in which the densities can differ between the different datasets, it should be noted that this density differs greatly between each rock and even for each surface of each rock.

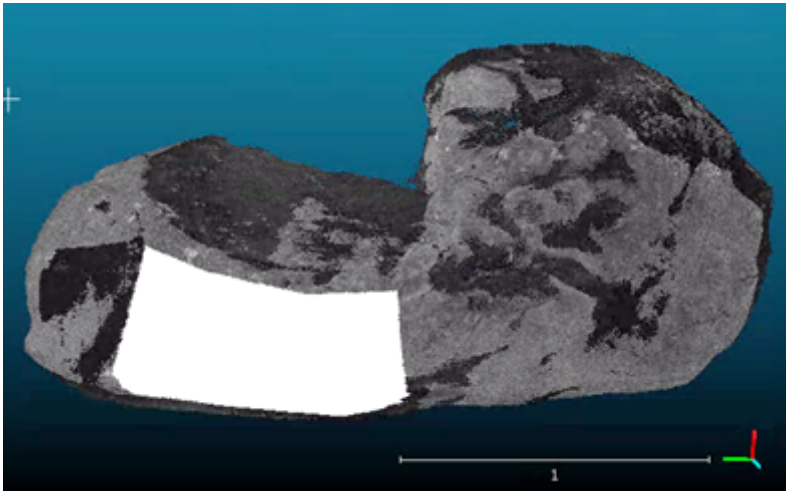


Figure 2.10: Area of Rock 3 (depicted in white) used for density comparison. The scale of the figure is indicated in meters.

	TLS	BLK	GIA
Number of points	1,678,758	2,949,527	664
Points/m2	3,571,826	6,275,589	1,413

Table 2.4: Number of points for a defined area of Rock 3, divided per data set.

The point clouds from the different datasets were joined together to create point cloud models with the highest possible accuracy and density. This means that combinations of datasets had to be used. To illustrate these combinations, the original dataset of the points for the point cloud of Rock 1 and Rock 3 can be found in Figures 2.11 and 2.12. For these rocks, there are significant parts of overlap between the TLS and BLK datasets.

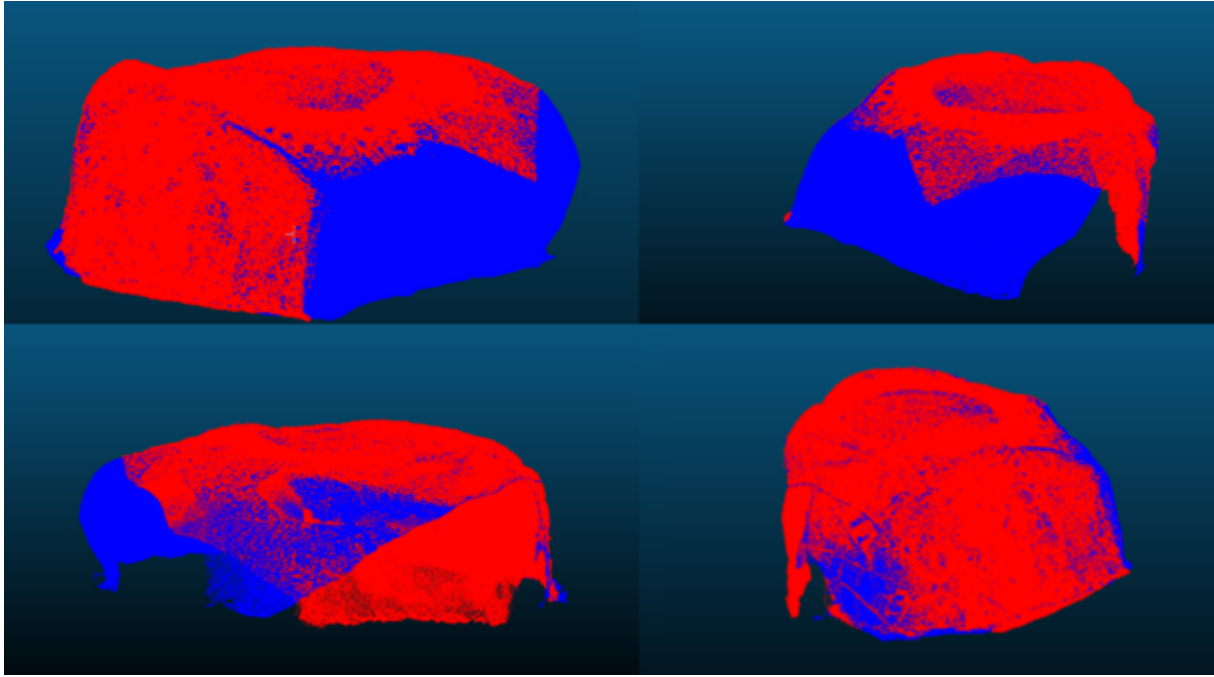


Figure 2.11: Point cloud of Rock 1, differentiated by point cloud data set. TLS in blue and BLK in red. Views from the east (left top), north (right top), west (left bottom) and south (right bottom).

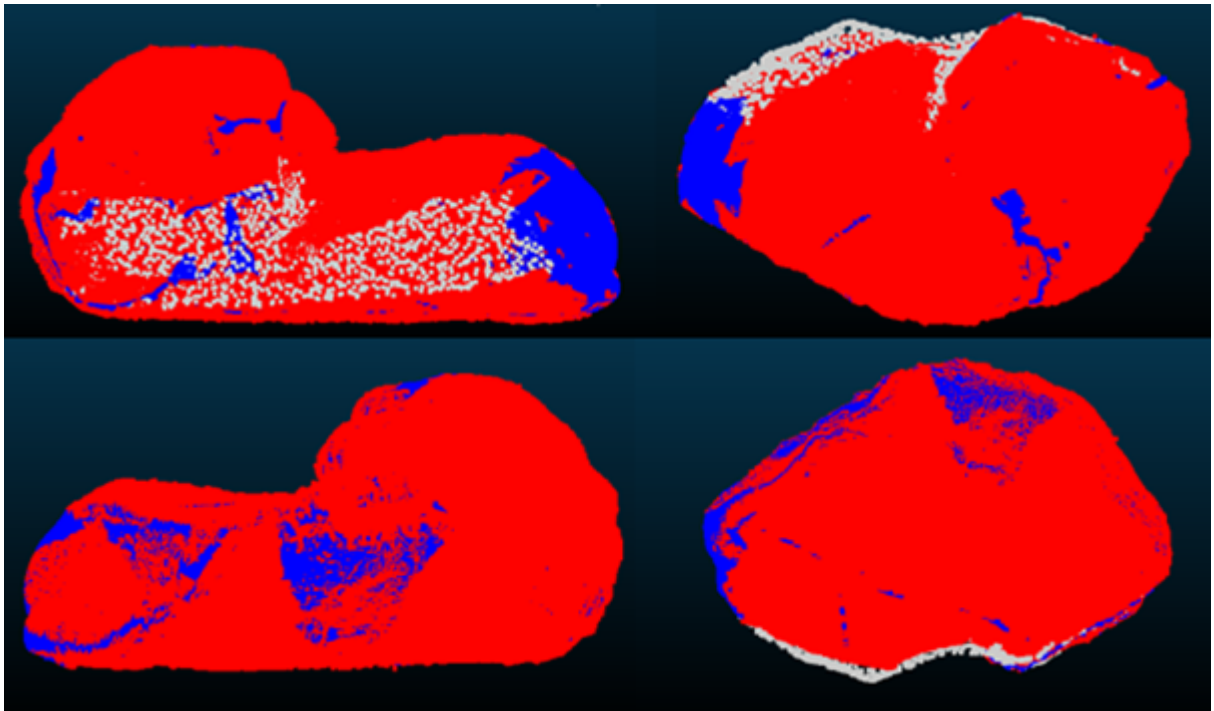


Figure 2.12: Point cloud of Rock 3, differentiated by point cloud data set. TLS in blue, BLK in red and GIA in white. Views from the bottom (left top), east (right top), top (left bottom) and west (right bottom).

### Subsampling

During the meshing stage, it was found that it was only possible to fit a mesh to the cloud when the number of points was sufficiently low. Using a trial and error approach, it was found that the lowest

possible subsampling distance, which resulted in point clouds that could be meshed, was 1 mm. Documentation requires a point cloud that is as detailed as possible. Therefore, this number was taken as the lowest value for subsampling. The other three subsampling values were 5 mm, 10 mm and 50 mm. These values were chosen, since the lowest subsampling distance for which the model could run in 3DEC was 50 mm. The model for stability analyses should be sufficiently detailed, while also coarse enough that the file size is sufficiently small so that it can be run in 3DEC. The number of points of each point cloud can be found in Table 2.5. Another secondary advantage of subsampling is that some noise is reduced. This is especially true for subsampling with a large distance, such as 10 mm.

	Number of points (-)				
	Detailed point cloud	Sampling distance 1 mm	Sampling distance 5 mm	Sampling distance 10 mm	Sampling distance 50 mm
Rock 1	23,145,530	6,261,140	204,225	40,465	1,466
Rock 2	4,001,152	1,424,406	70,647	19,039	822
Rock 3	43,707,784	16,541,732	617,951	117,860	3,089
Rock 4	5,570,129	1,780,954	85,988	21,519	843
Rock 5	6,166,669	1,946,233	94,971	24,869	1,042
Rock 6	25,439,980	6,580,220	282,256	74,315	3,097
Rock 7	10,281,916	2,773,590	108,582	26,418	1,042

Table 2.5: Number of points for detailed and subsampled point clouds.

### Point cloud surfaces of interest

Even though data was used from two scanners as well as the addition for Rock 3 with GIA data, still some rock surfaces lacked data (of sufficient density). The largest rock surface areas with little data are Rock 1 (North), Rock 1 (South), Rock 2 (South), Rock 5 (South) and Rock 7 (North). Apart from that, Rock 1 (top) was found to have a circular abnormality in the point cloud model. The approximate area sizes of these areas can be found in Table 2.6. Figures of these rocks can be found in Appendix E. Rock 1 (North), Rock 1 (top) and Rock 7 (North) will be discussed below to highlight the different causes of uncertainty.

Areas of uncertainty	Area size (m <sup>2</sup> )
Rock 1 (North)	0.17
Rock 1 (South)	0.04
Rock 1 (top)	0.29
Rock 2 (South)	0.06
Rock 5 (South)	0.08
Rock 7 (North)	0.12

Table 2.6: Area size for the areas of uncertainty.

In Figure 2.13, the missing data of the point cloud of Rock 1 (North) can be seen. This data is missing, because the Northside of Rock 1 was so close to Rock 2 that the scanner could not capture the surface of this rock. This is also what happened for Rock 5 (South) because Rock 5 was in contact with Rock 6, so there was a very narrow space which resulted in that the scanner could not capture the whole

surface of Rock 5 (see Figure 2.14). For Rock 1 (top), the cause of the area of uncertainty is not a lack of data, but rather an abundance. The circle that is visible on the top of the point cloud is caused by the BLK data (see Figure 2.15). The BLK scanner was placed on a tripod on top of Rock 1. The scanner scanned the area around it, but was not able to scan the surface area beneath it. Since there is a little bit of offset between the TLS and BLK datasets, this circle is visible on the point cloud models.

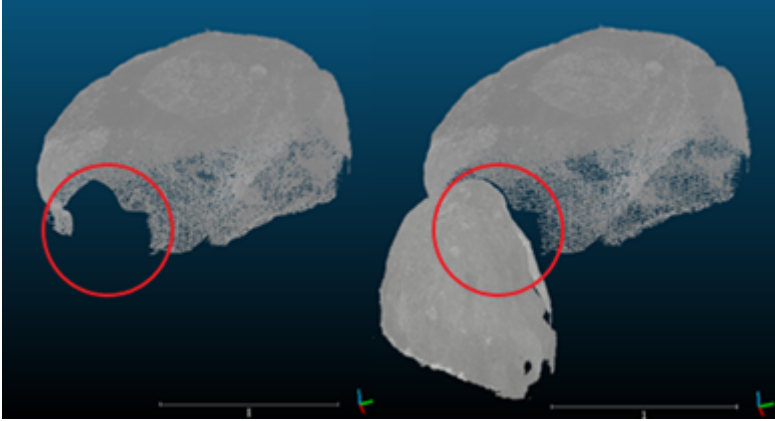


Figure 2.13: Rock 1 (left) and Rock 1 and Rock 2 (right). There is little data on the Northside of Rock 1 near Rock 2. The scale of the figure is indicated in meters. The red ellipses indicate the zone with missing data.

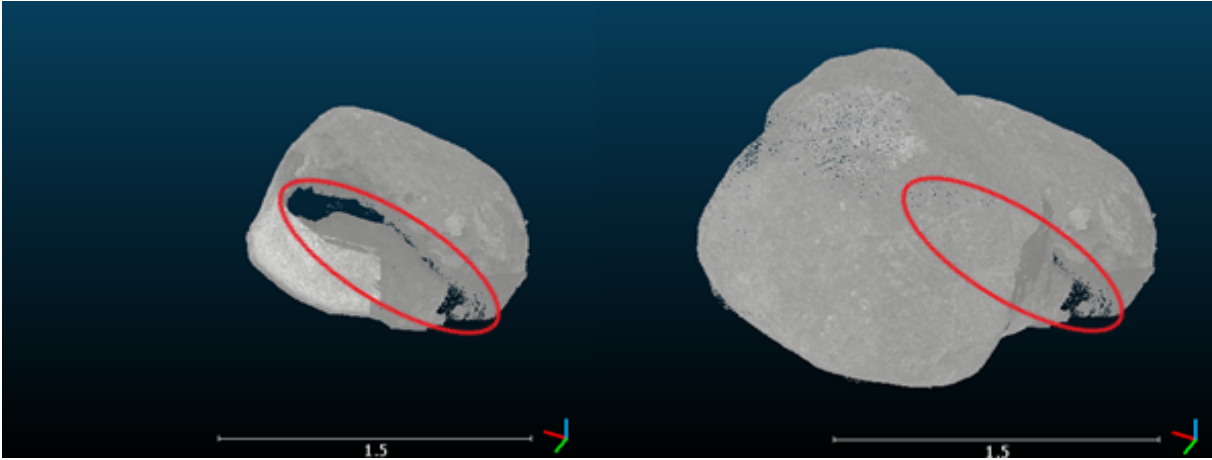


Figure 2.14: Rock 5 (left) and Rock 5 and Rock 6 (right). There is little data on the Southside of Rock 5 near Rock 6. The scale of the figure is indicated in meters. The red ellipses indicate the zone with missing data.

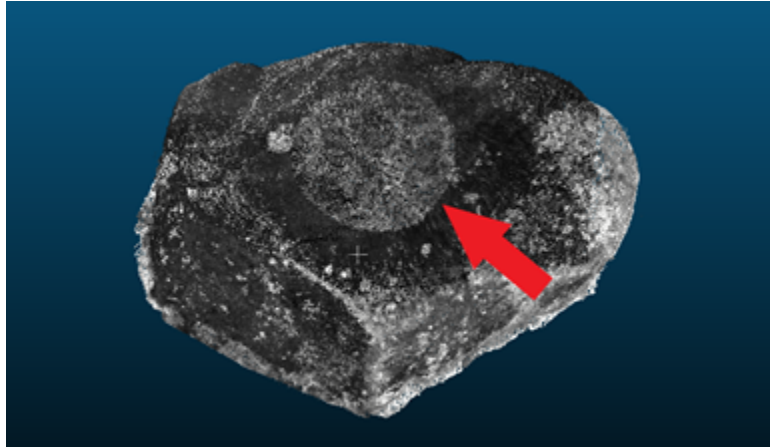


Figure 2.15: Rock 1 as seen from the top. It can be seen that there is a circle, indicated with the red arrow, on the top of the point cloud. This circle was created by the overlap between the TLS and BLK datasets. The BLK scanner was positioned on top of Rock 1 for one scan, and did not capture the circular surface beneath the scanner.

### 2.4.3 Mesh generation

From 35 point clouds, 21 meshes were produced, since only the subsampled point clouds by space of 5 mm, 10 mm and 50 mm could be meshed for the seven rocks. The number of mesh faces as a function of the subsampling distance can be found in Figure 2.16 (see also Appendix F). It can be seen that the number of faces decreases approximately linearly with the subsampling distance.

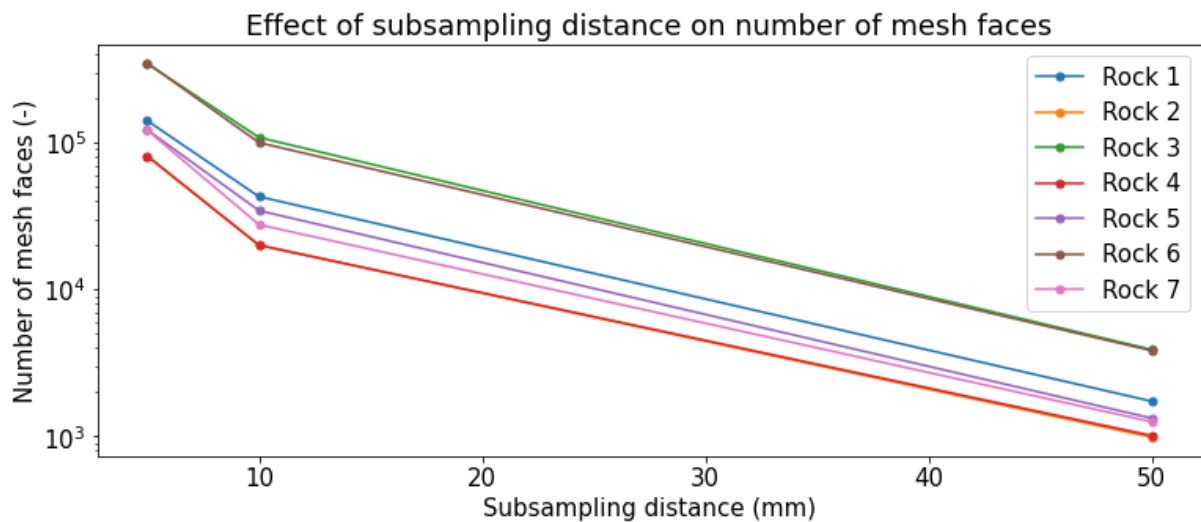


Figure 2.16: Effect of subsampling on the number of faces of the mesh for the surface meshes, after meshing Step 3.4.

### 2.4.4 Mesh evaluation

The mesh was evaluated using qualitative observations (Section 2.4.4.1) and quantitative analyses (Section 2.4.4.2).

## Qualitative mesh evaluation

From visual inspection, a couple of observations were made. Firstly, it was found that the areas with sparse point cloud data give coarser elements after initial meshing. This can be explained by that when fewer points are available, the mesh elements fitted to the point cloud will also be larger. For example, when looking at the mesh of Rock 1 after meshing Step 3.1, the area on the North (which was indicated as a surface of interest in Section 2.4.2.3) contains much larger elements than for neighboring surface areas where more point cloud data was available (see Figure 2.17). Secondly, for point cloud areas with large overlap and offset between the TLS and BLK data, the mesh showed inaccuracies. For example, the offset between the TLS and BLK data on top of Rock 1 caused inaccuracies on the top surface of Rock 1.

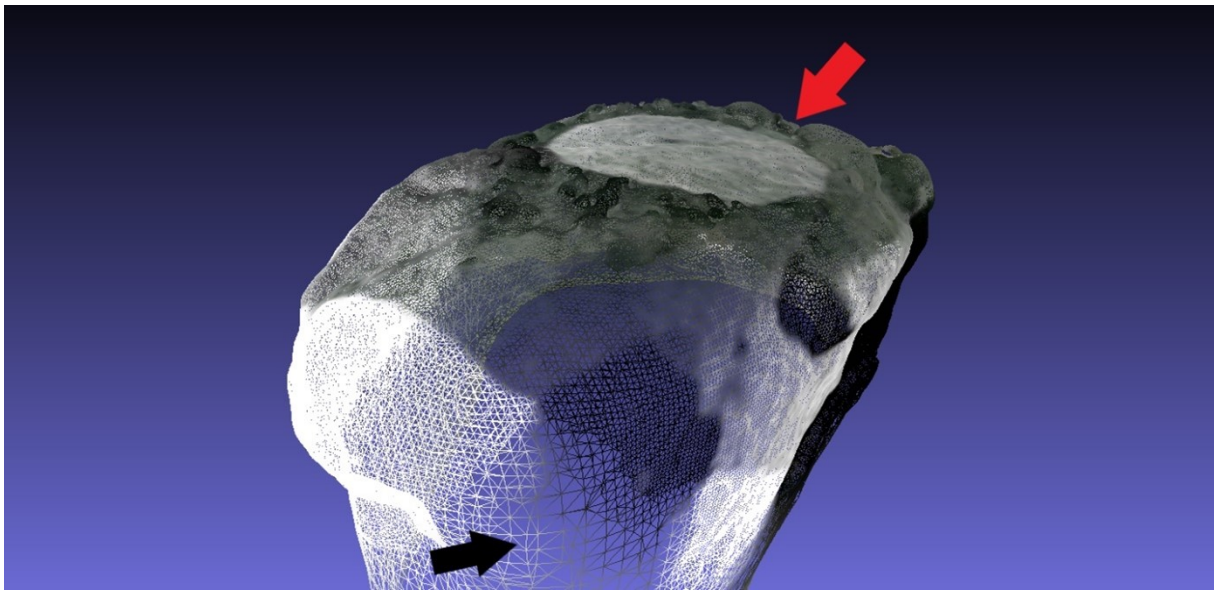


Figure 2.17: Mesh of Rock 1, based on the point cloud with 1 mm subsampling distance. The larger elements on the Northside of the rock can be found near the black arrow and the inaccuracies in the top surface of the mesh can be found near the red arrow.

When checking the meshes based on a larger subsampling distance, such as 50 mm, it was found that these observations change (see Figure 2.18). The areas with a sparse point density were found to result in approximately the same size of elements as before. However, their size with respect to the surrounding elements was now larger, since the surrounding elements were larger. As for the inaccuracies that were caused by the offset between the TLS and BLK data, these were a lot less profound for the coarser meshes. This is because when using fewer points, the mesh becomes more smooth.

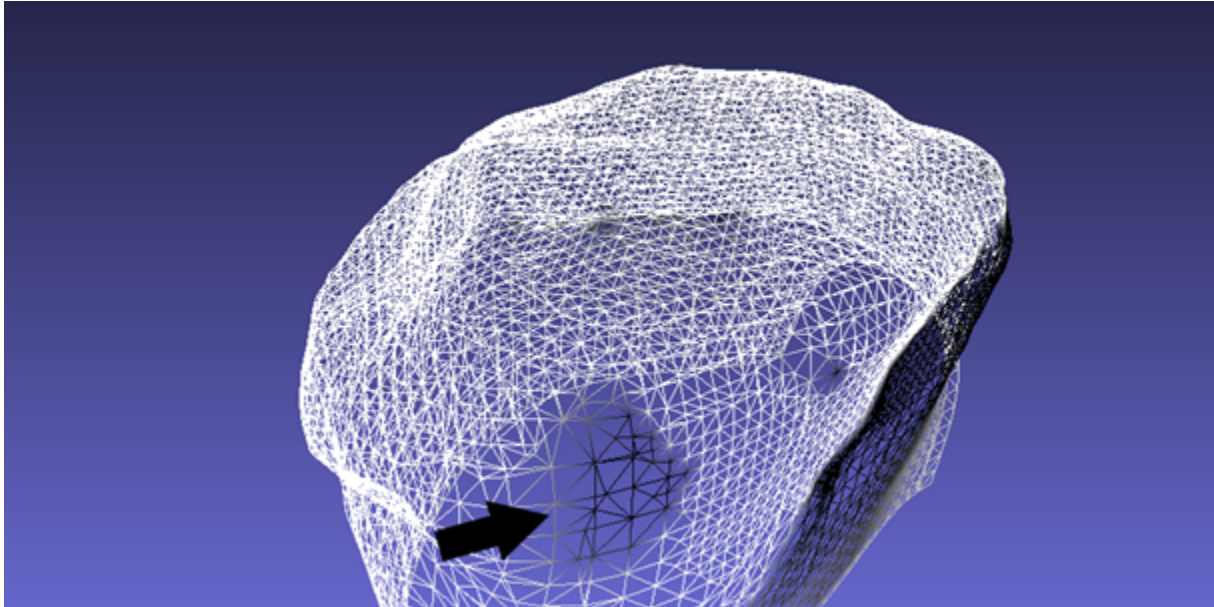


Figure 2.18: Mesh of Rock 1, based on the point cloud with 50 mm subsampling distance. The larger elements on the Northside of the rock can be found near the black arrow. The inaccuracies at the top surface are much smaller.

The volume meshes could not be quantitatively evaluated after meshing Step 3.5. However, some qualitative observations were made. First of all, there is the difference between meshes with an average mesh edge length (AMEL) of 0.15 m and 0.20 m, which can be seen in Figure 2.19. It can be observed that the shape of the meshes is slightly different. Since these meshes were made based on different point clouds, the mesh vertices are different for the two meshes. This, consequently, also results in different mesh edges and faces.

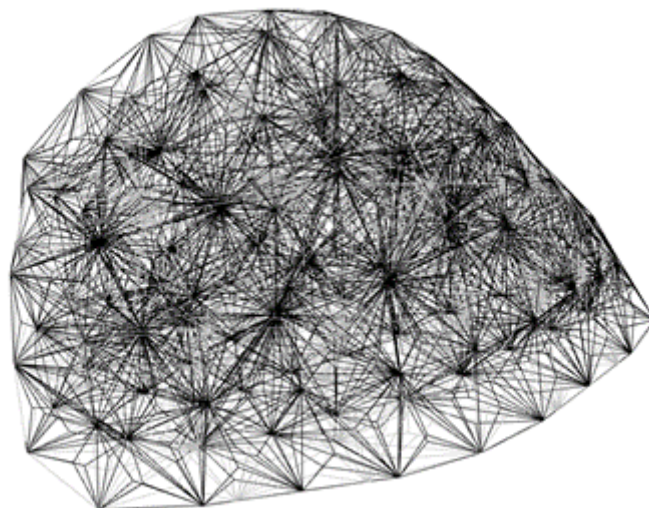


Figure 2.19: Mesh of Rock 2 after Meshing Step 3.5, for an AMEL of 0.15 and 0.20 m. Black indicates the mesh with an AMEL of 0.15 m and grey indicates the mesh with an AMEL of 0.20 m.

Another point to note is the difference between the normal mesh and the smart mesh (see Figure 2.20). The normal mesh has elements that are of approximately the same size near the surface as on

the inside of the volume mesh, while the smart mesh has coarser elements on the inside compared to the outside. The outside vertices, as well as mesh edges and faces, are the same for the two meshes, while the main difference can be found inside the mesh.

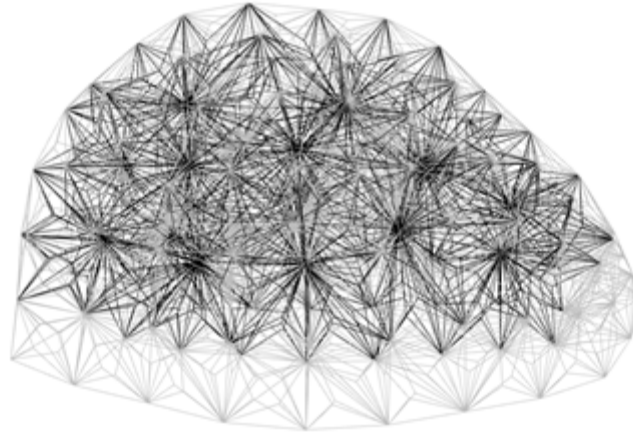


Figure 2.20: Mesh of Rock 2 after meshing Step 3.5, for an AMEL of 0.15 m. Grey indicates the mesh of the normal mesh and black the mesh of the smart mesh. Whenever the mesh edges are the same, grey is depicted.

### Quantitative mesh evaluation

The mesh to point cloud fit was quantitatively evaluated by using point-to-mesh distance (PMD) analyses. These analyses were done after meshing Step 3.1 and 3.4 in order to evaluate the influence of the meshing steps on the mesh to point cloud fit. The PMD analysis was also done to compare the difference between the TLS and BLK on Rock 4 and between including or excluding the GIA dataset for Rock 3.

#### PMD after meshing Step 3.1

Point-to-mesh distance (PMD) from the final (merged TLS and BLK) point cloud was compared for the meshes after meshing Step 3.1, which is the initial meshing step in Meshlab, made based on subsampled point clouds with a minimum distance between two adjacent points no smaller than 1 mm, 5 mm, 10 mm and 50 mm. The PMD was calculated between these meshes made with subsampled point clouds and the detailed point clouds, without any subsampling.

Signed distances

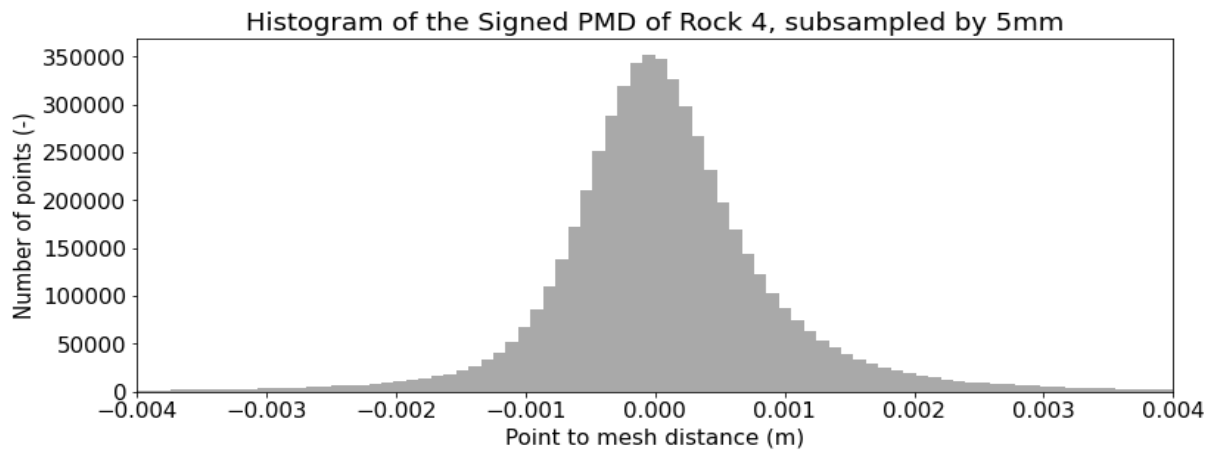


Figure 2.21: Signed PMD of Rock 4 expressed as a histogram after meshing Step 3.1.

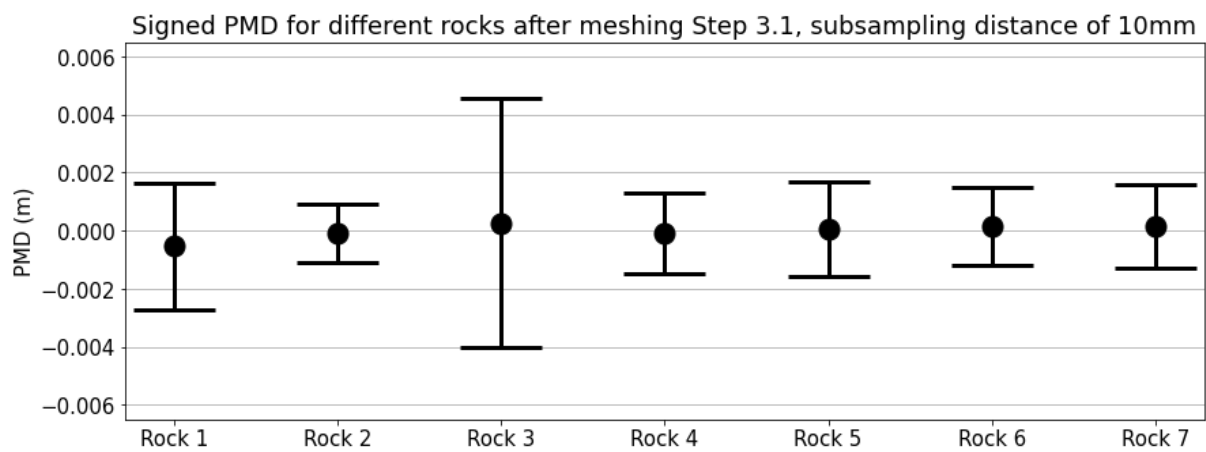


Figure 2.22: Signed PMD mean value and range of one standard deviation for all seven rocks after meshing Step 3.1, created from point clouds that were subsampled with a distance of 10 mm.

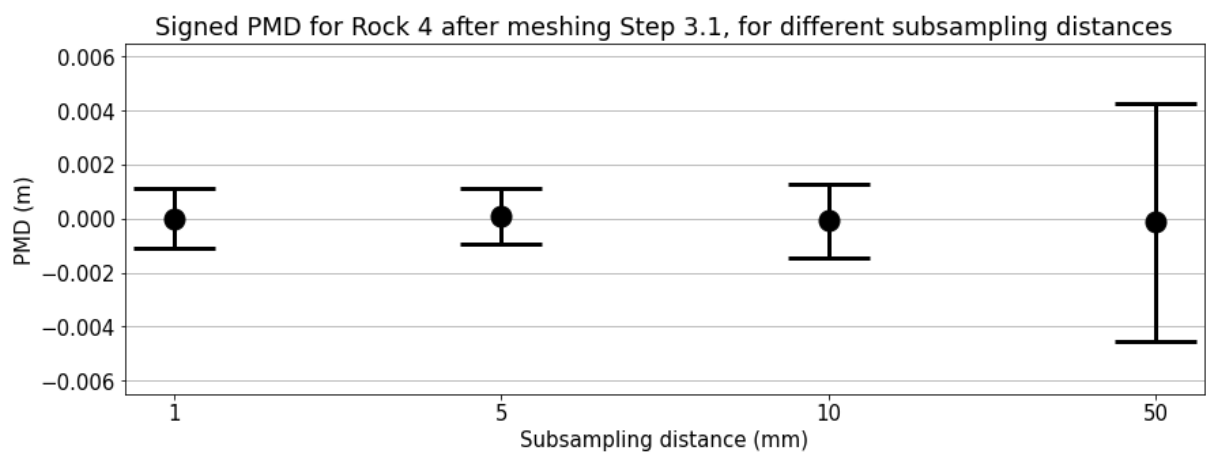


Figure 2.23: Signed PMD mean value and range of one standard deviation for Rock 4 after meshing Step 3.1, created from point clouds that were subsampled with different distances.

The histogram depicting the number of points as a function of the Signed distance can be found in Figure 2.21. It can be seen that most of the points are located close to the mesh. Based on the distribution of the PMD of all points, the mean and standard deviation can be calculated. This was done for all seven rocks for subsampling distances of 1, 5, 10 and 50 mm. The results for all rocks can be found in Appendix G. For the Signed PMD, it can be found that the mean PMD is generally in the order of 10-100 micrometer. The standard deviation is in the order of 100-1000 micrometer. It was found that there can be large variations for the PMD between the different rocks (see Figure 2.22). Rock 3 was found to have the largest range of PMD values, followed by Rock 1. However, the subsampling distance also has a significant effect on the PMD. In general, the range of PMD values increases with increasing subsampling distance (see Figure 2.23).

### Euclidean distances

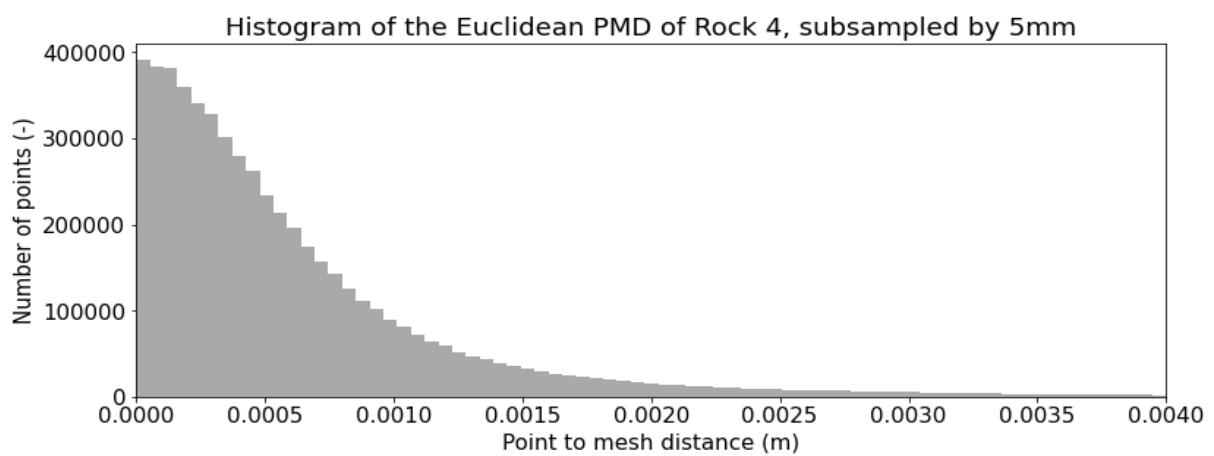


Figure 2.24: Euclidean PMD of Rock 4 expressed as a histogram.

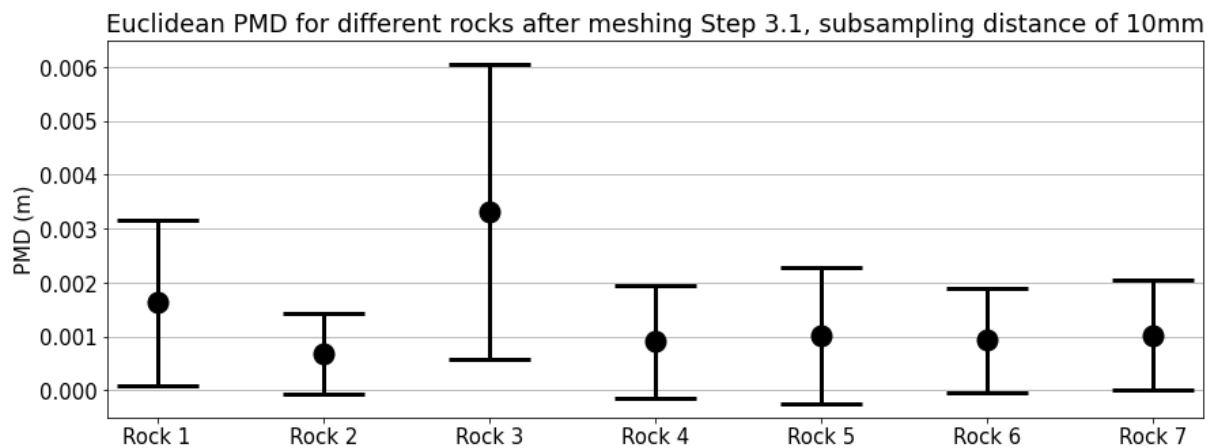


Figure 2.25: Euclidean PMD mean value and range of one standard deviation for all seven rocks after meshing Step 3.1, created from point clouds that were subsampled with a distance of 10 mm.

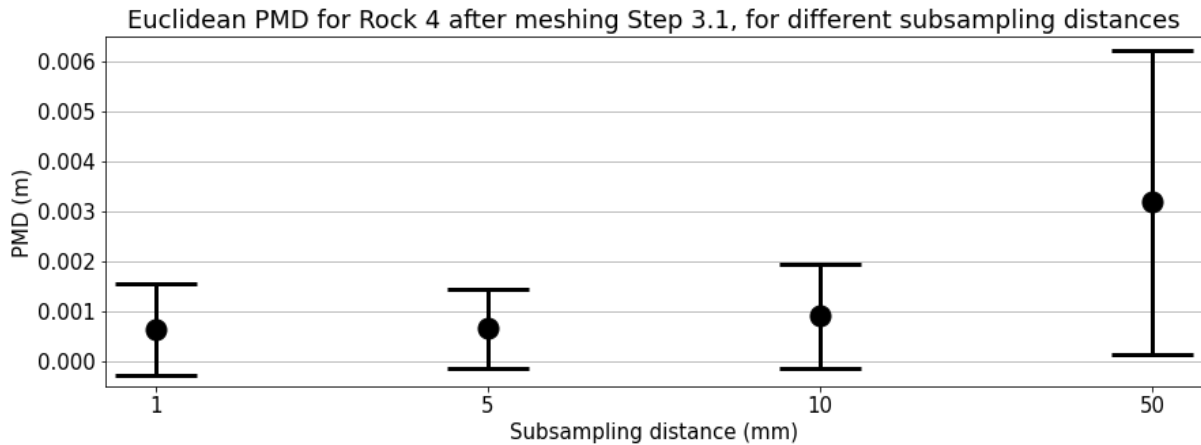


Figure 2.26: Euclidean PMD mean value and range of one standard deviation for Rock 4 after meshing Step 3.1, created from point clouds that were subsampled with different distances.

Apart from the Signed PMD values, the Euclidean values were also calculated. A histogram depicting the PMD range as a function of its number of occurrences can be found in Figure 2.24. It can be seen that the smallest PMD range occurs most. Based on the distribution of the PMD, again, the mean and standard deviation can be calculated for all rocks and subsampling distances. For the Euclidean PMD, the mean PMD and its standard deviation were found to be in the order of 1000 micrometer. Furthermore, the 90<sup>th</sup> percentile of the PMD was calculated to be approximately 1000-6000 micrometer. This means that 90% of the points in the point cloud are within 1-6 mm of the mesh. This means that on average, the points of the point cloud are within millimeters of the mesh surface. The PMD again differs significantly between the rocks (see Figure 2.25). Rock 1 and 3 still have the largest PMD values. The PMD again generally increases with mesh sampling distance (see Figure 2.26).

#### PMD after meshing Step 3.4

The point-to-mesh distance (PMD) from the final (merged TLS and BLK) point cloud was compared to meshes after Step 3.4, made based on subsampled point clouds by space of 1 mm, 5 mm and 10 mm. The main difference between the meshes in Step 3.1 and Step 3.4 is that the meshes were now closed (Step 3.2), remeshed with Griddle so that the elements become of more regular size (Step 3.3) and some small manual adaptations were done in Rhino (Step 3.4). The meshes were compared to the detailed point clouds, without any subsampling. The meshes could not be made in Step 3.4 for subsampled point clouds with a distance of 1 mm, due to a lack of computational power.

### Signed distances

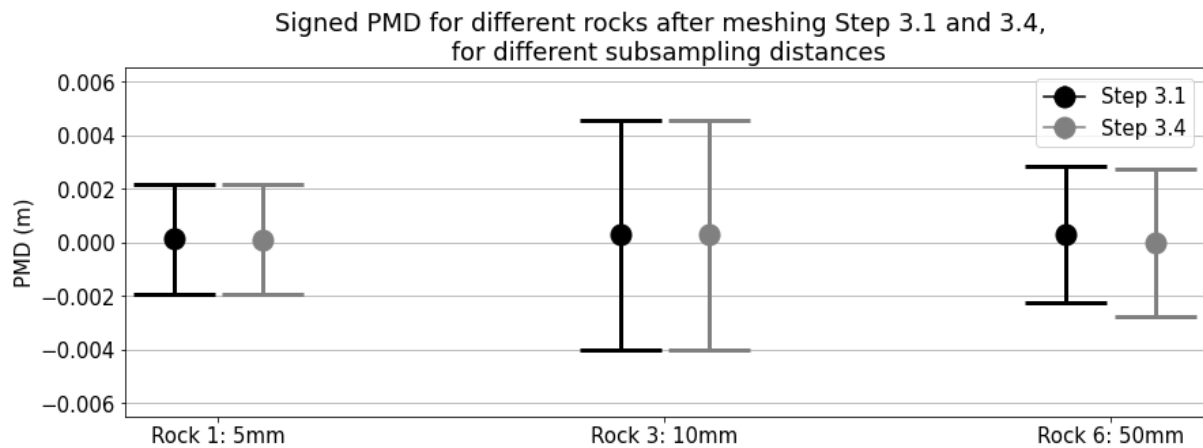


Figure 2.27: Signed PMD mean value and range of one standard deviation for different rocks after meshing Step 3.1 and Step 3.4, created from point clouds that were subsampled with different distances

For the Signed PMD after meshing Step 3.4, it can be found that the mean PMD, as well as its standard deviation, is very similar to the Signed PMD after meshing Step 3.1. This can also be observed in Figure 2.27. Furthermore, the mean PMD is roughly as often negative as positive, greatly differs between different rocks and its absolute value increases with mesh sampling distance.

### Euclidean distances

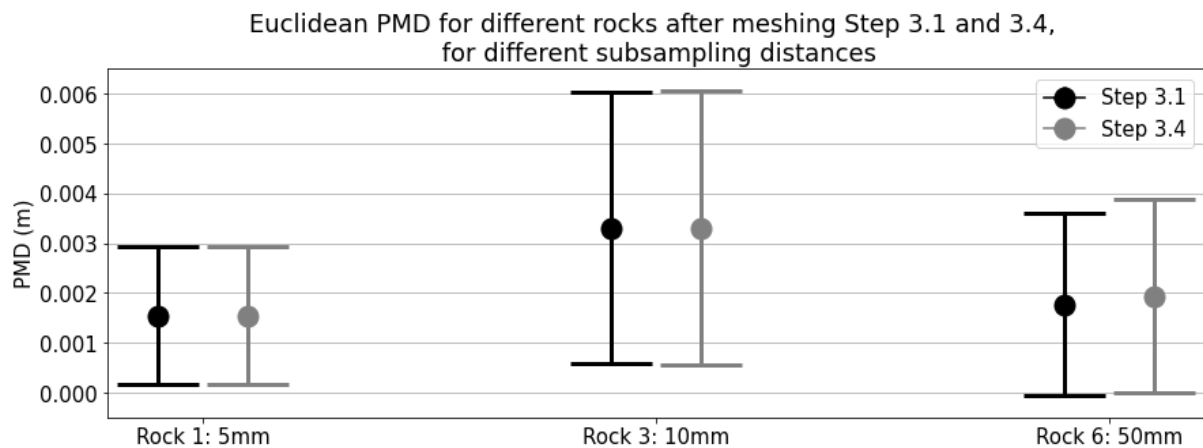


Figure 2.28: Euclidean PMD mean value and range of one standard deviation for different rocks after meshing Step 3.1 and Step 3.4, created from point clouds that were subsampled with different distances.

It was found that the Euclidean PMD values after meshing Step 3.4 are very close to the Euclidean PMD values after meshing Step 3.1, for all rocks. A visualization of the Euclidean PMD comparison for a few rocks between Step 3.1 and Step 3.4 can be found in Figure 2.28. Here, it can again be seen that the differences are really small.

## PMD comparison between TLS data and BLK data

	Number of points (-)
TLS data	4,936,065
BLK data	856,699

Table 2.7: Comparison between the number of points of Rock 4, for TLS and BLK data sets.

The PMD between the meshes (produced with merged datasets) and TLS and BLK point clouds were also analyzed. This was done for Rock 4. The BLK dataset contained approximately 20% of the points of the TLS dataset (Table 2.7), although roughly the same area.

### Signed distances

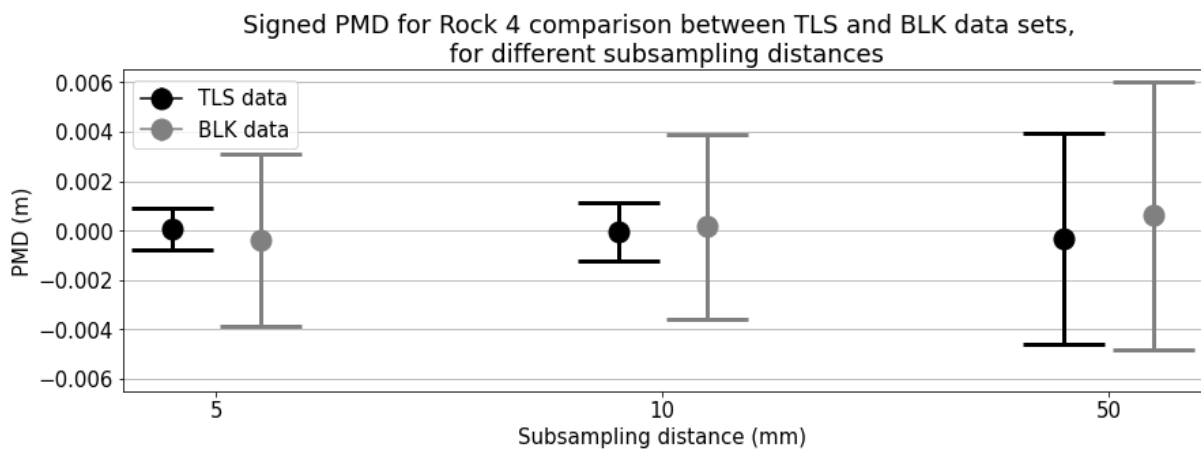


Figure 2.29: Signed PMD mean value and range of one standard deviation for Rock 4 compared to TLS and BLK data sets, created from point clouds that were subsampled with different distances.

The Signed PMD results indicate that the mean PMD is much larger for the BLK data set compared to the TLS data set. This can be a difference up to 300 percent of the TLS PMD. The mean PMD is roughly as often negative as positive, the variation between the rocks is large and its absolute value increases with mesh sampling distance. The plots in Figure 2.29 illustrate the large difference in PMD between the TLS and the BLK datasets. Especially the large difference in standard deviation becomes visible in this comparison.

*Euclidean distances*

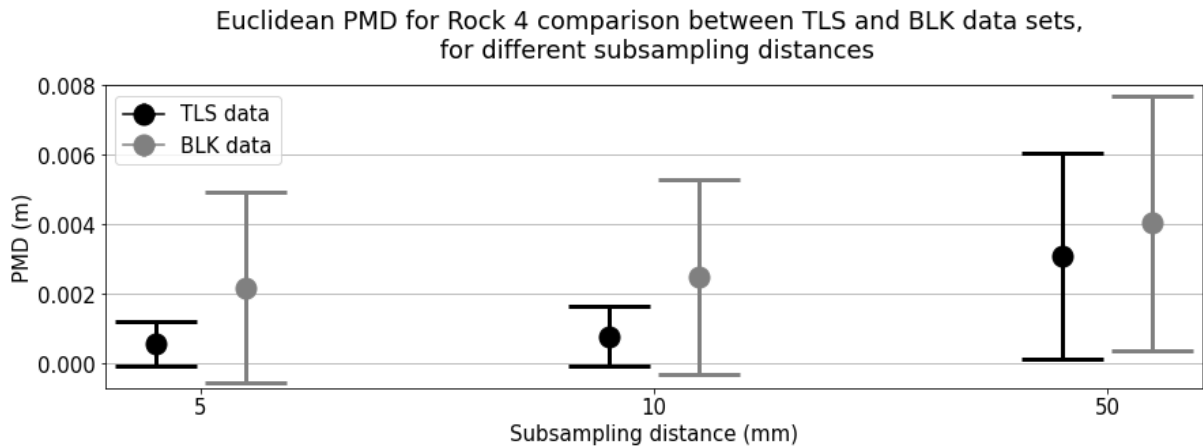


Figure 2.30: Euclidean PMD mean value and range of one standard deviation for Rock 4 compared to TLS and BLK data sets, created from point clouds that were subsampled with different distances

The Euclidean PMD results again indicate that the TLS data results in a much smaller PMD value compared to the BLK data. The plots in Figure 2.30 show the large difference in results for the Euclidean distances of Rock 4. The distribution is much wider for the BLK dataset, meaning a higher variability in results.

**PMD comparison of Rock 3 with and without GIA data**

	Number of points (-)
TLS + BLK + GIA	43,703,363
TLS + BLK	43,705,346

Table 2.8: Comparison between the number of points of Rock 3, with and without GIA data set.

The PMD between the meshes (produced with GIA data) and the point clouds with and without GIA data were also analyzed. This was done for Rock 3. The number of points of the GIA dataset is very small (see Table 2.8).

### Signed distances

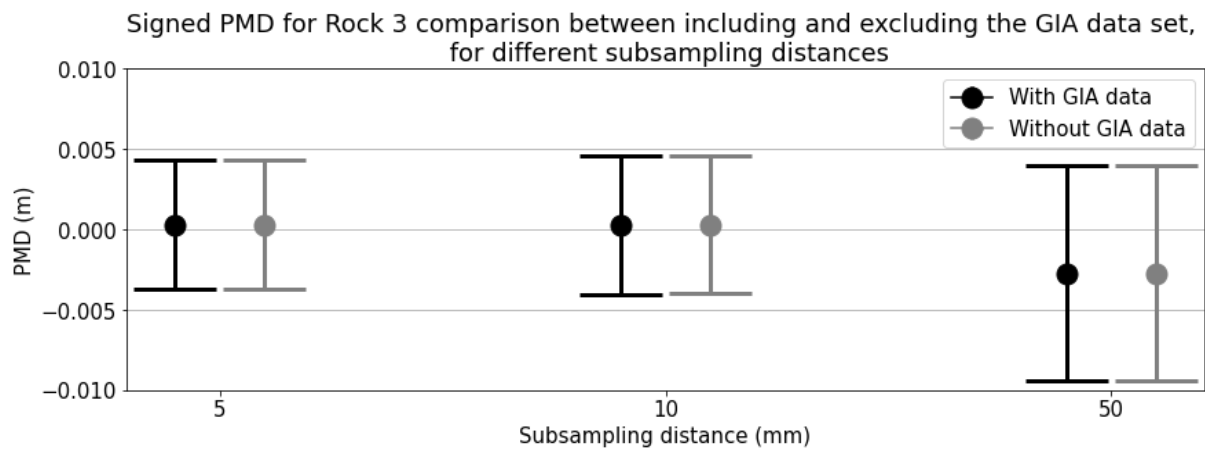


Figure 2.31: Signed PMD mean value and range of one standard deviation for Rock 3 compared for including and excluding the GIA data set, created from point clouds that were subsampled with different distances.

The Signed PMD is very similar for the point cloud containing the GIA data and not containing the GIA data. The plots in Figure 2.31 further illustrate that the differences between the PMD are negligible.

### Euclidean distances

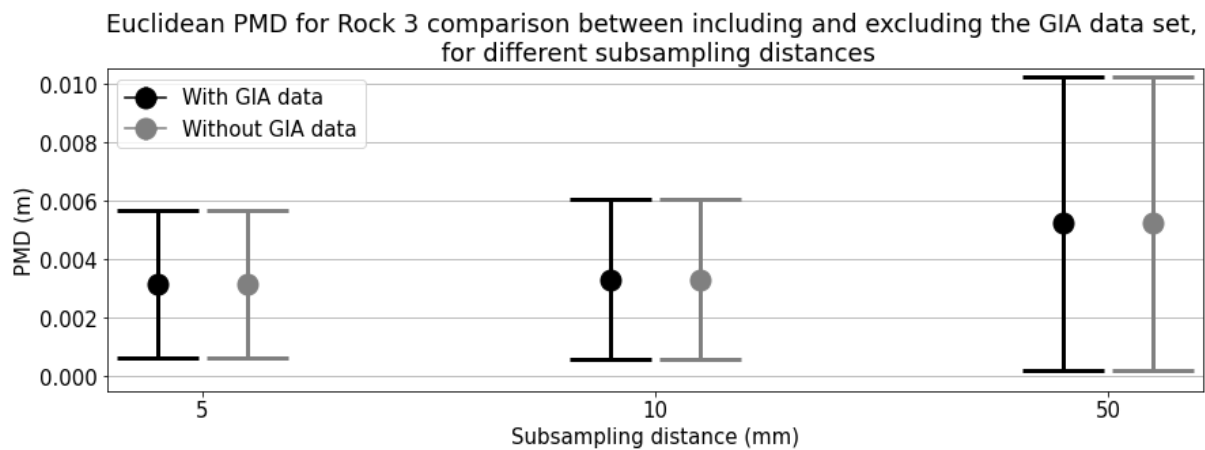


Figure 2.32: Euclidean PMD mean value and range of one standard deviation for Rock 3 compared for including and excluding the GIA data set, created from point clouds that were subsampled with different distances.

For the Euclidean PMD, it was also found that its values were very much the same when comparing the point cloud with and without GIA data. The plots in Figure 2.32 again illustrate the negligible differences between the PMD of Rock 3 with and without GIA data.

## 2.5 Discussion

The discussion section will be split up between the four steps to produce accurate geometrical models: acquiring point cloud data, point cloud-preprocessing, mesh generation and mesh evaluation.

### 2.5.1 Acquiring point cloud data

A total of 51 scanning stations was used to acquire the point cloud data. Especially in the ZOI, a lot of different scanning positions were used. Nonetheless, there are still five parts of rock surfaces with few geometrical data points. These surfaces are generally where rocks are very close to each other or in contact with each other. Also, the surfaces on the inside of the dolmen were hard to reach, since the space was limited to place the scanner and the scanner requires a certain minimum distance between the scanner and the nearest surface. For the TLS scanner, the minimum range was 0.40 m and for the BLK scanner used in the narrow zones, the minimum distance was 0.6 m (Leica Geosystems, 2017a, 2017b). In future research, complementary methods could be used to fill up these areas, such as photogrammetry (Van der Burg, 2021).

The scans resulted in very large data sets consisting of millions of points. These datasets were hard to handle, since the memory of a desktop is limited.

### 2.5.2 Point cloud pre-processing

Creating point cloud models from the raw data was a very time-consuming process, taking almost one month. Several aspects should be considered in this process. First of all, it can be difficult to decide between data coverage and accuracy when deciding on using a slightly less accurate dataset to fill up a surface area with a low point density. This was for example a dilemma when deciding whether GIA data should be used for the point cloud model of Rock 3. A hole in Rock 3 was filled up with GIA data, since no other data was available of this rock surface. Furthermore, it was found that there was a lot more noise in the data of the BLK dataset, compared to the TLS dataset. This data required much more cleaning, and was therefore used less, compared to the TLS data. When creating the point cloud models, it was checked whether a lot of offset between the TLS and BLK data sets was visible. If this was the case, the preference was given to TLS data over BLK data. Another difficulty was deciding on what points should be considered as outliers and noise, and which points constitute the real rock surface. Lastly, the alignment of the different data sets into the same coordinate system was an arduous task. This can only be done with limited accuracy.

In total, 35 point cloud models were pre-processed. The models were made without subsampling and by subsampling distances of 1 mm, 5 mm, 10 mm and 50 mm for all 7 rocks. Subsampling is necessary, since it greatly reduces the number of points and the desktop was only able to handle files of limited file size. Subsampling was done with space, meaning that a minimum distance was specified that was allowed between two adjacent points. Furthermore, it was found that the minimum distance between points in order to create a file that can be used for meshing in Meshlab, was 1 mm. This has to do with computational limitations. Only for a small file size, with few points, Meshlab was able to create a mesh. The smallest subsampling distance with which problems could be run in 3DEC was 50 mm, again due to computational limitations with the memory. Therefore, it was decided to create point cloud models using subsampling distances of 1 mm, 5 mm, 10 mm and 50 mm.

### 2.5.3 Mesh generation

The process of mesh generation is again very time-consuming, a couple of weeks was spent on this step. Meshlab could only process relatively small data files and was unable to mesh point clouds with the number of points of the detailed point clouds. However, after creating subsampled point clouds, the meshing itself could be easily done. Remeshing and volume meshing with Griddle (meshing

Steps 3.3 and 3.5) required a Griddle license for the more detailed meshes. Yet again, it was found that meshing is a process that can encounter computational limitations, as the point cloud that was subsampled by 1 mm space could not be meshed with Griddle. The manual adaptations of meshing Step 3.4 (manual adaptations in Rhino) took a couple of hours for each rock and was especially time-consuming for the detailed meshes. However, it was found that Rhino is a good software to do this, as it offers many built-in options for mesh checking and modifications, such as removing and creating mesh elements.

In total, 21 meshes were created from the 28 subsampled point clouds. It was found that the number of faces decreases linearly with increasing subsampling distance. Further discussion on the mesh fit can be found in the following section.

#### **2.5.4 Mesh evaluation**

The mesh evaluation consisted of qualitative mesh observations and quantitative Point-to-Mesh Distance (PMD) analyses. Regarding the mesh observations, it was found that coarser elements were located in the mesh for the corresponding areas of low point density in the point cloud. Therefore, there was a loss of detail in the mesh when little point cloud data was available. Another observation was that overlapping point cloud surfaces between the TLS and BLK datasets can cause inaccuracies in the mesh. For this reason, overlap between datasets should be prevented. Furthermore, it was found that the meshes created with different subsampling distances would result in meshes of slightly different geometries. Lastly, the normal mesh was compared to the smart mesh and it was found that the outside surface geometries of these rocks were the same, as far as could be observed by the naked eye.

The quantitative analysis showed that the PMD is generally in the range of 100-1000 micrometers. This seems to be reasonable for the goals of the research. Significant differences were found between the different rocks, caused by the quality of the point clouds. Furthermore, the PMD was found to generally increase with an increase in the subsampling distance. This can be explained by that larger elements are used, therefore causing the fit to the point cloud to be less good. The difference between the PMD after meshing Step 3.1 and after Step 3.4 was small. Furthermore, it was found that the TLS point cloud gives a much better fit to the mesh compared to the BLK data for Rock 4. First of all, this could be because the point density is much greater for the TLS point cloud than for the BLK data. The Poisson surface reconstruction bases the mesh on the points of the point cloud. More points from one data set means that the mesh will be more dominated by that data set. Although the TLS data surface is roughly equal to the BLK data surface, it contains a lot more points. Another reason could be that the TLS point cloud was taken as a reference to align the BLK data to, instead of the other way around. There are always small alignment deviations, which could cause a greater deviation in the PMD for the BLK data. Lastly, it could simply be caused by sensor noise. As was already indicated in the product specifications (Appendix A), the BLK data set is likely to be a little less accurate and is thereby assumed to contain more noise. In order to investigate the effect of including the additional GIA dataset on the models, the last PMD analysis focused on Rock 3, with and without GIA data. The mesh fit seems to be very similar between including and not including GIA data to make the mesh. This can be explained by that the number of points of the GIA point cloud used for Rock 3 is less than two thousand, which is very small compared to the number of points of the other two data sets.

## **2.6 Conclusion**

This chapter dealt with the topic of creating models, which (1) accurately document the geometry of all independent rocks and (2) are suitable for digital stability analysis. It was found that the process to create the relevant meshes can be divided into four steps: acquiring point cloud data, point cloud

pre-processing, mesh generation and mesh evaluation.

When acquiring point cloud data, great effort needs to be put into using different scanning positions such that most of the rock surfaces will be captured. Since many scanning stations were used in an effort to fully capture the geometry of the dolmen, there was a lot of overlap between the different scans. This does not need to be a problem, since the alignment of scans from the same scanner is usually good. The geometry of the dolmen was not fully captured, especially near the contact zones of the rocks. Some missing surfaces still remain near the contact areas and on the inside of the dolmen. These surfaces are Rock 1 (North), Rock 1 (South), Rock 2 (South), Rock 5 (South) and Rock 7 (North). Apart from that, Rock 1 (top) showed a circular abnormality. The details of these areas can be found in Section 2.4.2.3. Other techniques, such as photogrammetry, could be used to fill up these holes. For this research, the holes in the point cloud were filled when generating the mesh with the Poisson surface reconstruction method.

During the point cloud pre-processing step, some new difficulties arose. The cleaning of the point clouds proved to bring with it some dilemmas, such as what points should be considered as noise and what data set to use for certain surfaces when making a trade-off between accuracy and point density. Whenever no large offset was observed between the TLS and BLK datasets, overlap between the two datasets was allowed. However, when there was considerable offset between the datasets, the TLS data was preferred as it was considered to contain the most accurate data based on its product specifications and experience during the modelling process.

It was also found that a sufficiently small data file is required for mesh generation. Therefore, it was necessary to subsample the point clouds. The smallest subsampling distance with which calculations could be done in 3DEC was 50 mm. However, when computational capacities would be expanded, this subsampling distance could likely become much smaller.

The mesh was qualitatively and quantitatively evaluated. From observations, it was found that overlap between the TLS and BLK datasets results in inaccuracies in the mesh and that a lack of or low density of data results in a mesh area with larger elements. Furthermore, meshes based on point clouds with different subsampling distances were found to result in slightly different geometries, whereas the surface geometry of normal and smart meshes was found to be the same, as far as could be observed with the naked eye. Quantitatively, the mesh to point cloud fit was evaluated with point-to-mesh distance (PMD) analyses. The PMD could not be determined after meshing Step 3.5, since this file has a format that cannot be opened in other software than 3DEC. However, the PMD after meshing Step 3.4 is in the order of 100-1000 micrometer, which seems reasonable for this type of research. It was found that there is a large variation in mesh fit, depending on the rock. The quality of the point clouds was better for some rocks, such as Rock 4, than others, such as Rock 3. Furthermore, an increasing subsampling distance was found to cause a less good fit between the mesh and the point cloud. The difference between meshing Step 3.1 and 3.4 was found to be very small. When comparing the TLS and BLK data sets to the mesh made with both point clouds of Rock 4, it was found that the mesh fits the TLS dataset much better. Several reasons can be found for this, such as the higher point density of the TLS data, the alignment procedure and sensor noise. The comparison of the PMD of Rock 3 between the data set with and without GIA data showed that the influence of including the GIA dataset is very small. This likely has to do with that it consists of few points.

All in all, it should be concluded that for a model that should only accurately document the geometry of all independent rocks, the most detailed model should be chosen. In this case, that is the mesh based on the point cloud with a subsampling distance of 1 mm. Furthermore, overlap between the different datasets should be minimized, with a preference for the dataset that was obtained with the most accurate laser scanner, in this case, the TLS. When selecting a model that not only accurately documents the geometry of the rocks, but is also suitable for digital stability analysis, one should also pay attention to computational limitations of the digital stability analysis software, in this case, 3DEC. It was found that due to the large file size of detailed geometrical models, the most detailed

meshes that could be used were the meshes created with a point cloud subsampled by a distance of 50 mm. The influence of the mesh coarseness on the model results, as well as the calculation time, will be analyzed in Chapter 5.

## Chapter 3

# Non-destructive examination of rock contact surface parameters

This chapter deals with the determination of the relevant rock contact surface parameters, contributing to the shear strength of the rock contact surfaces. The chapter will start with an introduction (Section 3.1), and then dive into literature on the type of rocks, shear strength models and determination of the rock parameters of the chosen shear strength model (Section 3.2). Then, the methods of the non-destructive field tests and the laboratory tests on rock samples considered as analogs to the rocks of dolmen D14 will be explained (Section 3.3). In Section 3.4, the results will be presented and these will be discussed in Section 3.5. The conclusion can be found in Section 3.6.

### 3.1 Introduction

Not only the geometrical properties of the megalith structure should be known, the parameters of the contact surfaces between the digitally repositioned rocks are also of significance in order to evaluate the stability of the reconstruction scenarios. Rock parameters are often estimated by taking samples from the field and analyzing the parameters of interest in the laboratory. However, these test methods are destructive and the rocks in the field may not be damaged. For this reason, non-destructive test methods should be adopted in order to estimate the rock parameters. Rock parameter values were estimated using three methods: literature study, in-field non-destructive testing and laboratory testing on analog samples to the rocks in the field. A single value was determined for each relevant parameter that could be applied to all rocks and was used as input for the numerical stability analysis. In part 3 (Chapter 4), a sensitivity analysis is conducted to estimate the uncertainty in the stability calculation results caused by the uncertainty and variability in the contact parameters.

### 3.2 Literature

The literature section starts with the determination of the rock types of the rocks in the zone of interest (Section 3.2.1). Then, some shear strength models for rock joints will be discussed and evaluated on their applicability to the rock contact areas in the field (Section 3.2.2). In the last section, the chosen shear strength model is further discussed, as well as its parameters and methods for determining the relevant parameters (Section 3.2.3).

#### 3.2.1 Rock types

All rocks with which dolmen D14 is constructed are glacial erratic rocks. This means that they were transported to the Netherlands by ice sheets. In the second to last ice age in Northern Europe, the

Saale glaciation, the Netherlands was for a substantial part covered with ice. As glaciers can flow, they can also transport materials from one place to another. During this ice age, large quantities of Scandinavian rocks were transported to the Northern part of the Netherlands.

With the help of Harry Huisman, who is a curator of geology at the Hunebed Centrum in Drenthe, the rock types of the rocks of interest were determined (H. Huisman, personal communication, March 10, 2021). Not all rocks could be identified to the same extent, but all identified rocks belong to the granite type. Granite is common for megalithic rocks in the Netherlands. These megalithic rocks are intrusive igneous rocks, often medium or coarse-grained and rich in quartz and feldspar minerals. The specific rock types that were identified can be found in Figure 3.1. The following rock descriptions are based on Zandstra (1988) and (1999).

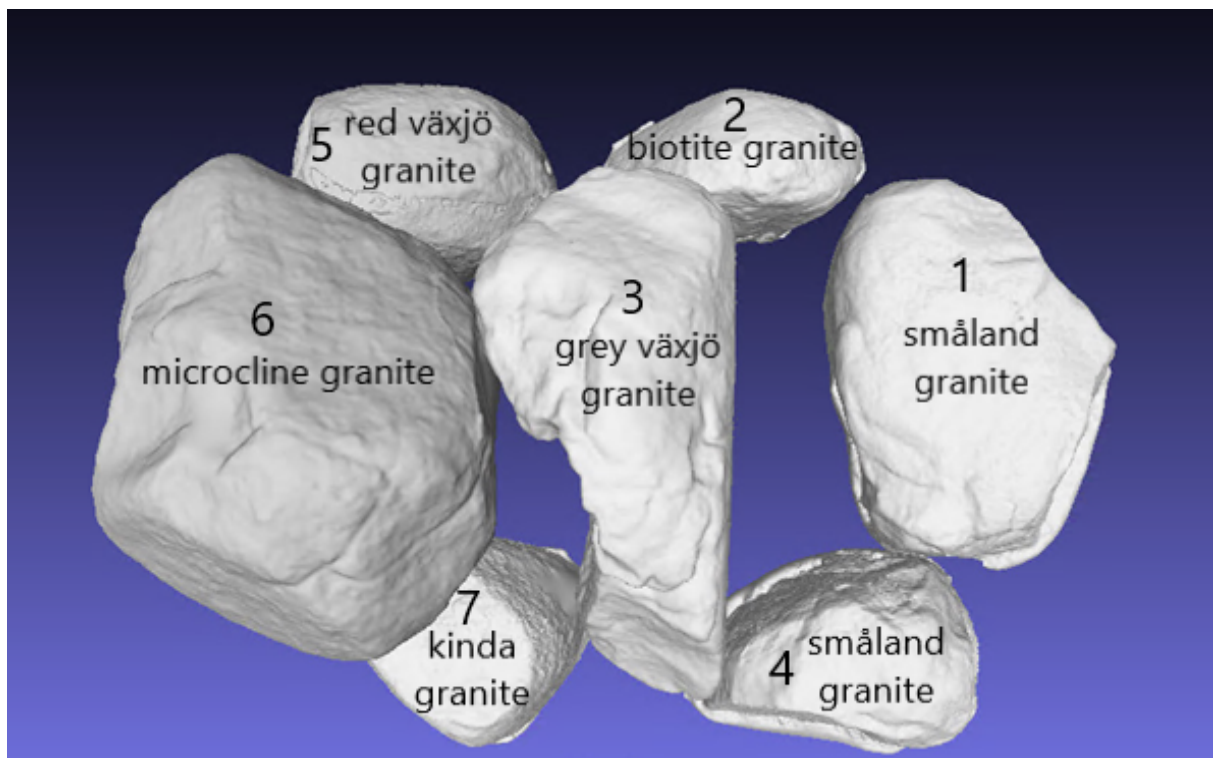


Figure 3.1: Rock types of the rocks in the zone of interest.

Rock 1 is identified as a Småland granite. The Småland granite type refers to a region in the central and Eastern part of the South of Sweden (see Figure 3.3). The region is approximately 14 thousand square kilometers large. Of the crystalline megalithic rocks that have been found in the North of the Netherlands, approximately 20-50% can be traced back to this region. The Kinda and Växjö rocks, respectively Rock 3, 5 and 7, also originate from the Småland region, but can be traced back to even more specific locations. Småland granites are mostly medium to coarse-grained granites, rich in biotite. These granites are often deep red to pink grey of color. The boundaries of grains can be hard to determine with the naked eye. These granites often contain reddish potassium feldspar and smaller amounts of cloudy, yellow plagioclase. The plagioclase can become green when altered. The quartz grains are usually white, grey or blue.

Rock 2 is identified as a biotite granite. Biotite is a group of mica that is often included within igneous rocks. It can be recognized by its dark color and distinct luster. The luster can have a bronze color.

Rock 3 is identified as a grey Växjö granite (see Figure 3.2). This is a special type of rock that can

specifically be traced back to its area of origin, namely the Väjö region in the South of Sweden (see Figure 3.3). This granite is often fine to medium-grained and grey of color, sometimes with a hint of red. Common minerals include plagioclase, alkali feldspar and quartz.

Rock 4 is another Småland granite. This granite is often distinctly red of color and contains blue-greyish quartz minerals. With the limited resources available, no distinct differences could be observed between the rock type of Rock 4 and Rock 1.

Rock 5 is a red Väjö granite (see Figure 3.2). Again, this special type of rock can be traced back to its parent rock in the Väjö area. Red Väjö granite is often medium-grained and red-grey, red or grey-pink of color. The minerals that can be found in this rock are feldspar, quartz and sometimes biotite. Feldspar minerals can be up to 1 or 2cm large. The boundaries of the minerals are often irregular.

Rock 6 is a microcline granite. Microcline is a potassium-rich feldspar mineral that is commonly found in granite and can be recognized from its pink color, although it can occasionally also take other light colors.



Figure 3.2: Grey Väjö granite (left) and red Väjö granite (right). Adopted and modified from (Zandstra, 1999).

Rock 7 is a Kinda granite. The Kinda region in Sweden is 2 thousand square kilometers large. Therefore, it is a common type of rock amongst glacial deposits. Kinda granite belongs to the Filipstad granite type (Smed & Ehlers, 2002). It differs from other Filipstad granites in that Kinda granite always contains blue quartz minerals, feldspar phenocrysts can only be brown, colored stripes in phenocrysts are uncommon, plagioclase rings are usually orange and incomplete and 1-3 mm square, often orange, plagioclase grains can be found in the rock.



Figure 3.3: Map of the origins of the rocks in the zone of interest. Adopted and modified from (Bekkema et al., 2014). The Kinda and Våxjö regions are located within the larger Småland (7) region. The Småland region is classified as the South Baltic area.

### 3.2.2 Shear strength models for rock joints

The shear strength of a rock joint is a key parameter that is of special interest when running stability analyses. Several models exist to characterize the shear strength for rock joints. In order to identify the most suitable shear strength model for the rock contact surfaces in the field, a number of shear strength models were reviewed.

#### Coulomb

One of the simplest shear strength models is the Coulomb model. This is a linear model and is applicable to smooth, clean joints. In this model, the shear strength only depends on the friction between the rocks and the normal stress applied to the rocks.

$$\tau = \sigma_n * \tan(\varphi) \quad (3.1)$$

In this formula,

$\sigma_n$  = normal stress  
 $\varphi$  = friction angle

However, this criterion is not very accurate for natural joints, because these joints are far from smooth. Generally, the Coulomb criterion is regarded to be less realistic and safer than the shear strength criteria that were developed later (Barton, 1971).

#### Patton

Based on fieldwork, Patton (1966) observed that different modes of shear failure take place on non-planar surfaces. A framework was developed to better characterize these different modes of failure. This framework was based on artificially cut rocks with a regularly indented surface with an inclination angle  $i$  (Figure 3.4). Patton recognized that rocks under high normal load behave differently from rocks under low normal load. He formulated a bilinear model, which is applicable to non-planar rock surfaces containing regular and equal teeth (see Figure 3.5). Under low normal stress, there is a significant increase in shear strength with normal stress. The asperities of the rock joint will be overridden and not crushed and therefore dilation is possible. At higher normal stress, the failure envelope becomes less steep. The asperities of the joint will be crushed and dilation is prevented. This model by Patton was one of the first that was not strictly linear. Although Patton proposed this

bi-linear model, Patton also recognized that failure modes often occur simultaneously and therefore the true shear strength behavior is likely to be more curved.

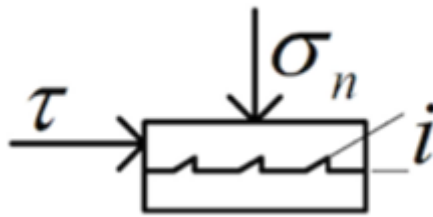


Figure 3.4: The sample shape that Patton used for his bilinear model.

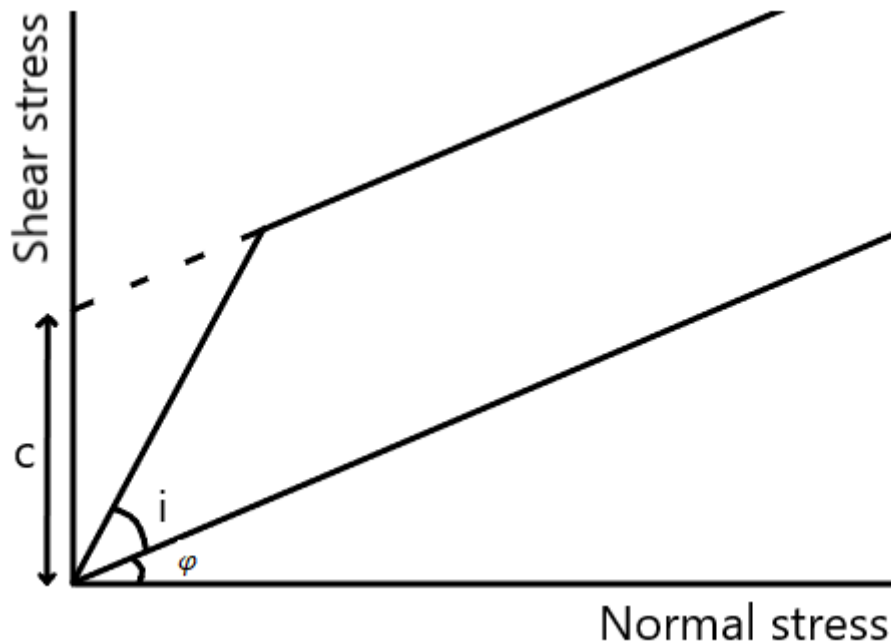


Figure 3.5: Patton's bilinear model for joint shear behavior. Adopted and modified from Patton, 1966.

### Ladanyi & Archambault

The aim of (Ladanyi & Archambault, 1970) was to establish a more general framework for shear behavior than the framework of Patton (1966), which would be related to some more general rock parameters and would take account of previous deformations. The framework was developed based on jointed rock mass in the laboratory scale. Its main addition was that the research of Ladanyi & Archambault does not only focus on regularly indented surfaces such as can be observed in Figure 3.4, but that it should also be applicable to irregular rock surfaces. In reality, different failure modes occur at the same time, since asperities are irregular and crushed at different stresses. Their model is based on a work equation, in which four factors are considered: one factor that accounts for the work done against the external force due to dilation ( $\dot{v}$ ), one factor that accounts for work done due to friction considering dilatancy ( $\varphi_f$ ), one factor that accounts for work done due to internal friction not considering dilatancy ( $\varphi_\mu$ ) and the last factor that accounts for work done due to shearing through

the asperities ( $\varphi_0, s_0$ ). All these factors combined in one equation gives:

$$\tau = \frac{\sigma(1 - a_s)(\dot{v} + \tan(\varphi_\mu)) + a_s(\sigma * \tan(\varphi_0 + s_0))}{1 - (1 - a_s)\dot{v} * \tan(\varphi_f)} \quad (3.2)$$

In this formula,

- $\sigma$  = normal stress
- $a_s$  = shear area ratio
- $\dot{v}$  = ratio of dilation at failure
- $\varphi_\mu$  = angle of frictional sliding resistance along the contact surfaces of the teeth
- $\varphi_0$  = friction similar to the Coulomb shear friction
- $s_0$  = cohesion intercept similar to the Coulomb shear cohesion
- $\varphi_f$  = statistical average value of the friction angle when sliding occurs along the irregularities

The most prevalent critique on the work of Ladanyi & Archambault is that too many parameters need to be determined, which are also relatively hard to determine (Barton, 1971).

### **Barton & Bandis**

In his first studies, Barton (1971) analyzed the relationship between dilatancy, normal stress and shear strength. Based on a number of laboratory shear tests, the following formula was developed for a very rough rock joint:

$$\frac{\tau}{\sigma_n} = \tan[20 \log_{10} \left[ \frac{\sigma_c}{\sigma_n} \right] + 30^\circ] \quad (3.3)$$

In this formula,

- $\sigma_n$  = normal stress
- $\sigma_c$  = compressive strength

In this formula, the  $30^\circ$  refers to the basic friction angle. It is claimed that this formula would be representative for both unweathered and weathered tension joints. In Barton (1973), the influence of weathering on shear strength was analyzed. In this work, the previous formula was adapted to:

$$\frac{\tau}{\sigma_n} = \tan[JRC * \log_{10} \left[ \frac{JCS}{\sigma_n} \right] + \varphi_r] \quad (3.4)$$

In this formula,

- $\sigma_n$  = normal stress
- $JRC$  = Joint Roughness Coefficient
- $JCS$  = Joint wall Compressive Strength
- $\varphi_r$  = residual friction angle

This shear strength criterion, nowadays called the Barton-Bandis shear strength criterion, is the one that is most commonly used (Zhao, 1997b). The differences between both formulas concern the introduction of the effective joint wall compressive strength (JCS), the joint roughness coefficient (JRC) and the residual friction angle ( $\varphi_r$ ). The JCS value should be used instead of the compressive strength ( $\sigma_c$ ) when the rock joint is weathered. The JRC value can range from 0 for very smooth

joints to 20 for very rough joints. The  $\varphi_r$  is a measure of the relationship between the normal stress and shear stress of a rock, at residual strength. This relationship depends on the range of strains that is considered. For rough joints, the shear stress – shear displacement data often shows a peak stress value at low strain, after which a residual value is reached for higher strain (see Figure 3.6). The residual friction angle is determined from the residual shear stress – normal stress data. The residual friction angle for slightly to moderately weathered granite rock joints was previously found to lie between 24 and 36° (Woo, Fleurisson, & Park, 2010).

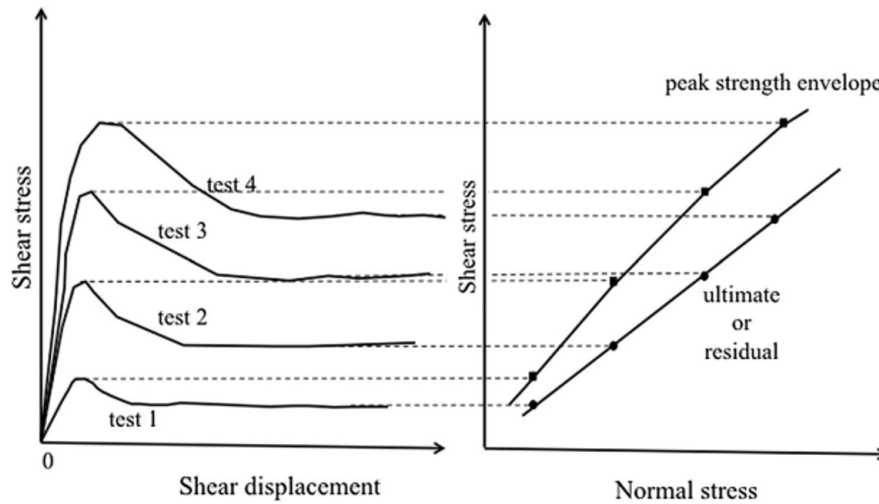


Figure 3.6: Deriving peak and residual shear strength characteristics. Adapted from Hencher & Richards, 2014.

## Zhao

Zhao (1997b) argued on the basis of a series of shear tests on natural joints that when Barton's model is applied to natural joints, the shear strength of less matched surfaces is often overpredicted. Rather, the peak shear strength of a mismatched joint appears to approach the residual shear strength of the joint. Due to this overprediction of the shear strength for natural joints, it is proposed to adapt Barton's criterion to the following formula:

$$\tau = \sigma_n * \tan \left[ JRC * JMC * \log_{10} \frac{JCS}{\sigma_n} + \varphi_r \right] \quad (3.5)$$

In this formula,

- $\sigma_n$  = normal stress
- $JRC$  = Joint Roughness Coefficient
- $JMC$  = Joint Matching Coefficient
- $JCS$  = Joint wall Compressive Strength
- $\varphi_r$  = residual friction angle

This means that an extra factor is added with the JMC, the joint matching coefficient (Zhao, 1997a). The JMC ranges from 0 to 1 and is meant to reflect the degree to which the joint surfaces are matched. It is measured by observing the approximate percentage of contact area between two joint surfaces.

### 3.2.3 Determination of rock parameters

In this research, the parameters of the shear strength criteria of Zhao will be estimated for the rocks in the field. In this section, a description will be provided of all parameters that are required for these criteria and how they are determined. The Zhao failure criterion is as follows:

$$\tau = \sigma_n * \tan[JRC * JMC * \log_{10} \left( \frac{JCS}{\sigma_n} \right) + \varphi_r] \quad (3.6)$$

The required parameters to determine the shear strength based on this failure criterion are: the normal stress ( $\sigma_n$ ), the joint roughness coefficient ( $JRC$ ), the joint matching coefficient ( $JMC$ ), the joint wall compressive strength ( $JCS$ ) and the residual friction angle ( $\varphi_r$ ). In the sections below, more details will be provided on these parameters and how they can be determined in the field and in the lab.

#### Normal stress ( $\sigma_n$ )

The normal stress is the stress that acts perpendicular to, and on the contact area between two rocks. The normal stress is determined with the following formula:

$$\sigma_n = \frac{F_{rock\_3}}{A_{contact}} = V_{rock\_3} * \rho_{rock\_3} * \frac{g}{A_{contact\_surface}} \quad (3.7)$$

In this formula,

$F_{rock\_3}$	= force applied by Rock 3 on the rock contact area
$A_{contact}$	= total contact surface area
$V_{rock\_3}$	= volume of Rock 3
$\rho_{rock\_3}$	= density of Rock 3
$g$	= acceleration due to gravity

The normal stress is a function of the volume and density of Rock 3, since this is the weight that will need to be supported by the bottom rocks (Rock 1, 2 and 4). The volume of Rock 3 can be precisely calculated from the model mesh of Rock 3 and is 1.49 m<sup>3</sup>. For the density, a value can be approximated based on its rock type. For granite, the average density is approximately 2700 kg/m<sup>3</sup>. This gives a total weight of the rock of 4023 kg. Furthermore, the contact surface between the rocks is of importance. This is the area between the rocks that are in contact. Since the rock contact areas consist of non-matching rock surfaces, the contact areas are small. The contact area varies with the reconstruction scenario. If the reconstruction scenario is chosen as it was in 2019, Rock 3 is only supported by Rock 2 and Rock 4. However, if a reconstruction scenario is chosen as it was in 1925, Rock 3 is supported by Rock 1, 2 and 4. Therefore, the contact surface area is likely to differ for each scenario. As a first estimate, a total contact surface of all contact points of 30 cm<sup>2</sup> has been assumed in the calculations. This value is the sum of all contact areas of Rock 3. This is based on field observations of the contact areas between Rock 5 and 6 and between Rock 6 and 7 of the megalithic structure (Figure 3.7 and 3.8), as well as on observations from the point clouds and meshes. The normal stress on the rock contact surfaces will therefore be around 13 MPa.



Figure 3.7: Rock contact zone between Rock 5 and Rock 6. The rock contact zone is indicated with the black marking. Based on visual estimates using CloudCompare, the approximate width of the picture on the left is 2.2m and on the right 0.5m.



Figure 3.8: Rock contact zone between Rock 6 and Rock 7. The rock contact zone is indicated with the black marking. Based on visual estimates using CloudCompare, the approximate width of the picture on the left is 2.1m and on the right 0.6m.

### Joint roughness coefficient (JRC)

The JRC is a value introduced by Barton (1973) and is mostly determined by comparing the roughness profiles taken from a rock with typical roughness profiles (Barton & Choubey, 1977). These roughness profiles can be obtained by using a carpenter's/Barton's comb. The JRC can range from 0 for a completely planar surface, to 20 for a very rough surface.

### Joint matching coefficient (JMC)

The introduction of the JMC parameter is the main addition of Zhao (1997a, 1997b) to the Barton-Bandis shear strength criterion. The Barton-Bandis model mainly accounts for matching rock joints.

However, this is not the case for the megalithic rocks in the field. Since the surfaces are not matching, this greatly reduces the sliding area and thereby the potential friction surface. Therefore, Zhao introduced the JMC in order to account for the effects of surfaces that are not completely matching. For natural joints in granite, Zhao (1997b) proposes a JMC value of 0.3. Also, for non-matching surfaces, it is advised to set the JMC parameter to 0.3.

### Joint wall compressive strength (JCS)

The JCS value is an indication of how strong the material at the contact surface is. For unweathered material, the UCS value can be taken. For weathered material, additional strength tests are required either using a Schmidt hammer or an Equotip. UCS values of granite reported in literature are between 50 and 200 MPa (Basu, Mishra, & Roychowdhury, 2013). For slightly weathered granite, it was found that the UCS is in the range of 55-90 MPa (Irfan & Powell, 1991).

### Residual friction angle ( $\varphi_r$ )

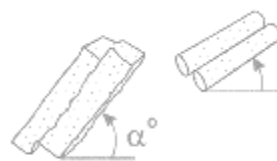
The residual friction angle is a measure of the relationship between the shear and the normal stress at residual shear strength. This parameter can be measured using several methods. First of all, Barton & Choubey (1977) advised using the formula below to calculate the residual friction angle:

$$\varphi_r = \varphi_b - 20 + 20 * \left(\frac{r}{R}\right) \quad (3.8)$$

In this formula,

- $\varphi_b$  = basic friction angle
- $r$  = Schmidt rebound value on wet (weathered surfaces)
- $R$  = Schmidt rebound value on dry, unweathered, sawn surfaces

In this formula,  $\varphi_b$  is a value that can be obtained from tilt tests on dry unweathered, planar, matching surfaces. R denotes the Schmidt rebound value on dry unweathered sawn surfaces and r indicates the Schmidt rebound value on wet (weathered) surfaces. This method has practical limitations in this study, since the Schmidt hammer cannot be used in the field, as it causes damage to the rocks in the form of indentation marks.



TILT TEST

Figure 3.9: Tilt test procedure, determination of  $\varphi_b$ . Adapted from Barton (2013)

The tilt test can also not be done on samples of the megalithic rocks, since it is very destructive to take samples from the rocks in the field. However, analog samples to the ones in the field can be collected to do laboratory experiments on. The basic friction angle of several rocks can also be found in literature. Coulson (1972) reports values for the  $\varphi_b$  between  $31^\circ$  and  $35^\circ$  for unweathered coarse-grained granite. However, the granite in the field is slightly to moderately weathered and therefore the residual friction angle is expected to be lower.

The tilt test can be done on flat, planar joint surfaces, with which the  $\varphi_b$  will be obtained (see Figure 3.9). However, the tilt test can also be done on rough, matching joint samples with which the  $\varphi_r$  can be obtained (Barton, 1999). The roughness can be discounted for with the following formula:

$$JRC_0 = \frac{\alpha^0 - \varphi_r}{\log_{10} \frac{JCS}{\sigma_{no}}} \tag{3.9}$$

In this formula,

- $JRC_0$  = the Joint Roughness Coefficient of the laboratory sample
- $\alpha^0$  = the tilt angle in the laboratory scale, which can be observed in Figure 3.9
- $\varphi_r$  = the residual friction angle of the rock
- $JCS$  = the Joint wall Compressive Strength of the rock
- $\sigma_{no}$  = the normal stress exerted on the sample in the laboratory

The previous sections explain how these five parameters can be obtained.

### 3.3 Methods

The methods to determine the shear strength parameters should be non-destructive to the rocks in the field. Therefore, the methods that were used in this research were either non-destructive field tests (Section 3.3.1) or laboratory tests on analog samples to the field (Section 3.3.2).

#### 3.3.1 Non-destructive field tests

Two non-destructive field tests were conducted. The Barton’s comb was used to determine the JRC and the Equotip was used to determine the JCS. This was done at six locations in the field, at or close to surface areas where contact could be made in potential reconstruction scenarios. The locations where the values were taken can be found in Figure 3.10.

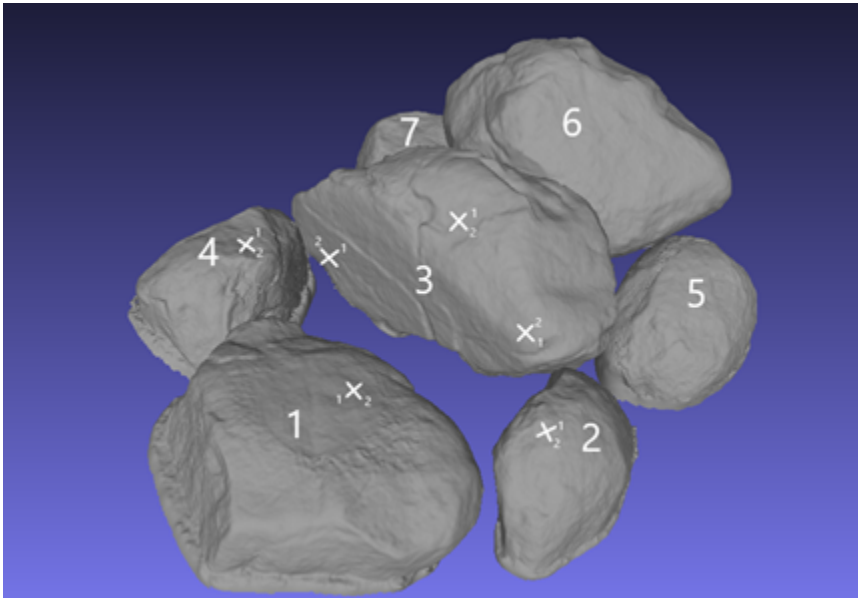


Figure 3.10: Locations in the field where the JRC and JCS were measured.

### JRC determination

The JRC can be determined using a Barton's comb or carpenter's comb. The comb that was used in this research can be found in Figure 3.11. Its length is 15 cm and its height is 8.5 cm. The JRC is determined by sketching roughness profiles and comparing them to typical roughness profiles. These profiles and the determination guide that was used can be found in Appendix H. Roughness profiles were taken at six locations in the field (see Figure 3.10). At all six locations, two profiles were taken which were perpendicular to each other.



Figure 3.11: The Barton's comb that was used to obtain the roughness profiles. The diameter of one pin is approximately 0.8mm and the distance between pins is approximately 1mm.

### JCS determination

The JCS was determined at the same locations as the JRC (see Figure 3.10). Since it was found that the Schmidt hammer leaves indentation marks on the rocks, it could not be used. Instead, the Proceq Equotip with an impact tip of 3 mm diameter and an impact energy of 11 Nm was used to estimate the strength values. At every location, two profiles in perpendicular direction were considered and at each profile 10 Equotip values were recorded. From the 2x10 values per location, the upper ten values were averaged to find the representative Equotip value for that location. Several mathematical relationships exist for the calculation of Equotip values to JCS values. It was decided to adopt the relationship as proposed by Verwaal and Mulder (1993). This relationship used the exact same Equotip, the 3 mm tip Proceq Equotip hardness tester, and is based on granitic rocks (amongst others). Some of the JCS determination locations were on vertical instead of horizontal surfaces. The differences in results due to the application angle of the Equotip were discounted for. This needs to be done, because the Equotip value is based on the rebound distance of the Equotip core, after making contact with the surface that is tested. Due to gravity, this rebound value is different for different application angles.

### 3.3.2 Laboratory tests

Two laboratory tests were conducted, the tilt test and the Golder shear box test. Both tests are used to estimate the residual friction angle of a rock joint sample. It was decided to focus specifically on the residual friction angle determination, because the residual friction angle generally is the most important component of the total shear strength (Singh & Goel, 2011).

## Tilt tests

The tilt test will be discussed by first describing the specifications of the samples that were used for testing and then describing the test methods.

### *Sample specifications*

The samples were cut out of boulders that were collected in Drenthe, a couple of kilometers distance from dolmen D14. These boulders were medium to coarse-grained granite boulders. A study by Alejano, González, and Muralha (2012) showed that the most reliable way to do tilt tests for basic friction angle determination is by using samples that were either of cylindrical shape and longitudinally cut ( $d=54\text{mm}$  and  $h=108\text{mm}$ ) or two square blocks sliding over each other ( $100\times 100\times 40\text{mm}$ ). For the tilt test, one sample of these square dimensions (Figure 3.12) was prepared. The cut between the two square blocks was saw-cut, therefore flat, and afterwards the surfaces were sandblasted. This is done because the surface becomes very smooth when cutting the rock to create the joint. If two really smooth surfaces are sheared over each other, the results will be more of an indication of how smooth the surfaces are cut than of the properties of the rock. With sandblasting, this smoothness is partially counteracted in an effort to reproduce the natural texture of the rock surface. However, a drawback of sandblasting is that this causes microcracks in the surface (Verhoef, Kuipers, & Verwaal, 1984).



Figure 3.12: Tilt test sample.

### *Test methods*

Testing methods were adopted from Alejano et al. (2018). The bottom halves of the samples were secured to the tilt table. Then, the platform was tilted with approximately  $0.5^\circ/\text{s}$ . When the upper block had slid to at least 10% of the sample length, the corresponding tilt angle  $\beta$  was recorded. The test was repeated three times in two positions. The two positions included a repositioning of the blocks by 90 degrees. In Figure 3.13, tilt direction 1 can be seen on the left (the green V-mark is at the left side of the block for the viewer), and tilt direction 2 can be seen on the right (the green V-mark is at the front side of the block for the viewer). For the final value of the tilt angle, the average of the six tests was used. The tilt angle  $\beta$  is equal to the basic friction angle  $\varphi_b$  of the rock.

The  $\varphi_b$  gives an indication of the angle  $\varphi_r$ , since the residual friction angle is usually smaller than the basic friction angle due to weathering.

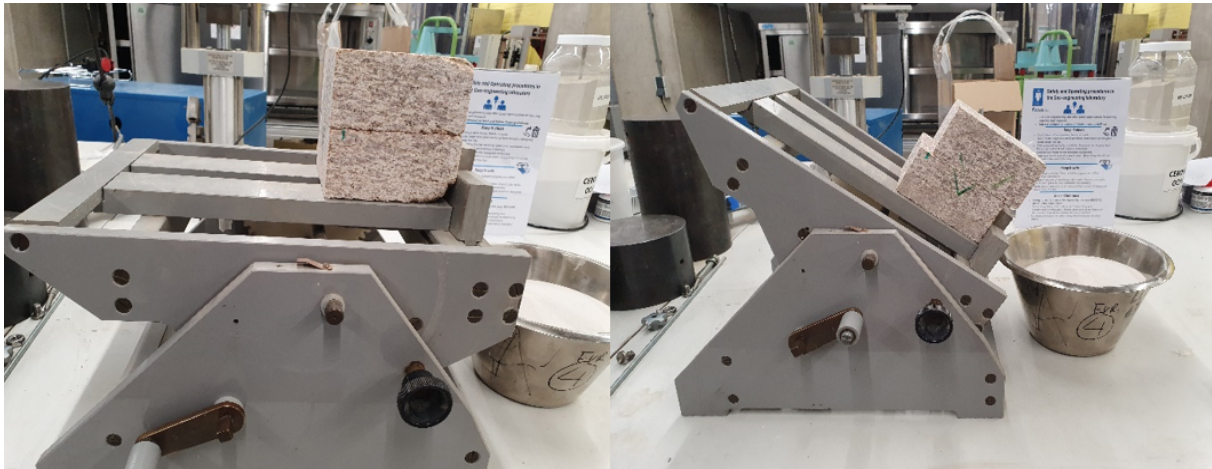


Figure 3.13: Tilt test apparatus.

### **Golder shear box tests**

The Golder shear box test will be discussed by first describing the specifications of the samples that were used for testing and then describing the test methods.

#### *Sample specifications*

The same medium to coarse-grained granite boulders were used for the Golder shear box samples as that were used for the tilt test. From these boulders, two types of samples were cut. There is little literature on how samples should be prepared for rock joint residual friction angle determination. In most cases, either rock cores are taken from the field, or samples with artificially induced cracks according to geometrically consistent patterns, such as saw-tooth surfaces, are produced. In this research, two methods for preparing the samples were explored. The first sample was obtained by cutting the surface and then sandblasting it. Previous research using the Golder shear box has proven that using samples that were sawed, but not sandblasted would give very unreliable results (Bootsma, 2010; Hencher & Richards, 2014). The effect of sandblasting on the sample surface can be observed in Figure 3.14.



Figure 3.14: Sawed surface of the rock sample before (left) and after (right) sandblasting. It can be observed that there are more small cracks along grain boundaries in the surface after sand-blasting.

The second sample was the tensile-split joint. The tensile-split joint was created by placing the rock between two plates with a small bulge (see Figure 3.15). Then, a pushing force is applied from the top, which creates a crack in the rock. Since the surfaces can be rough, but still have to be somewhat planar, the sample area is limited. The roughness of this sample is high compared to the in-situ roughness of the rocks. However, by using the selected shear strength criterion, this can be discounted for with the JRC value. The tensile-split joint can be observed in Figure 3.16.

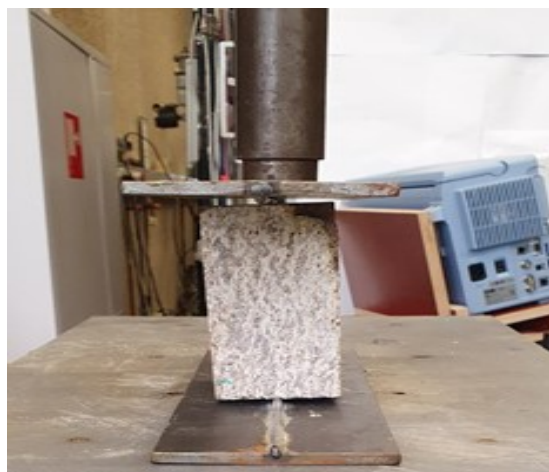


Figure 3.15: Producing a rough joint in the laboratory using steel plates with a bulge.



Figure 3.16: Rough, tensile-split sample as seen from the top (left) and side (right). From these pictures, it can be seen that there is a difference in color between the outside and inside of the material. This is likely caused by weathering of the rock.

The sample preparation does not stop after creating the desired joint type. The samples needed to be prepared further. Firstly, the samples were taped to each other, so that they would remain in place during the sample preparation process. Secondly, the samples were placed within the shear box with their crack parallel to and a couple of millimeters above the shear box. This was done with clay to obtain the exact right position. When the rock was in position, the gypsum could be poured into the shear box and cured. After half an hour of drying time, sample preparation could continue by adding some more clay to separate the already dried gypsum from the top box. Then, the top box was secured to the bottom box and the top box could be filled with gypsum. When the gypsum is dry, the boxes can be detached from each other and the clay can be removed. At the same time, the tape should be cut through so that the samples are completely separated from each other. Pictures of the sample preparation process can be found in Figure 3.17.



Figure 3.17: Sample preparation with clay and gypsum.

### *Test methods*

Before starting the shear test, the sample area, JRC, JCS and JMC should be determined. The outline of the sample was traced on translucent paper, after which the area of the sample can be determined

using graph paper. The JRC was determined by taking the average of three profiles in the direction of shearing for each sample half. The JCS was again determined with the Equotip. On each surface of the laboratory samples, ten Equotip values were recorded. Of these ten values, the lowest five were discarded and the other five were averaged. The final value was obtained by averaging the values of the two halves for each sample. The JMC was determined by looking at the visual contact surface overlap between the matching JRC profiles at the top and bottom of the sample. In total, three pairs of joint surfaces were analyzed. The JMC was determined at the average value of shear displacement between the start of the first test and the end of the last test.

The test setup can be found in Figure 3.18. During the test, the top box is fastened to the apparatus, and thereby it cannot move in the direction of shearing. However, it can become unstable and move in the direction perpendicular to shearing. The bottom box is not fastened and is moved by the hydraulic jack (manufacturer: Enerpac, maximum pushing force of 4.5 ton). This causes the sample to shear. The test can be performed under different normal loading conditions, which can be changed by adding and reducing weights. The weights will produce a load on the sample that is 11 times as large as the weight on the hanger due to the lever arm construction. Horizontal displacement can be measured with an LVDT displacement sensor. Vertical displacement, which is an important indicator of dilatancy, can be measured with another, vertical LVDT displacement sensor. The vertical LVDT had an operating range of 10 mm and the horizontal LVDT had an operating range of 20 mm. The load cell measures the force that is applied by the hydraulic jack to move the specimen. The load cell was the RMP K11 with a maximum force that can be applied of 30 kN.

All tests were performed with four loading stages with an added load of 0, 5, 10 and 15 kg consecutively. This corresponds to added forces of 540, 1079, 1619 and 2158 N, which translates to stresses of 0.1-1.2 MPa for the rough, tensile-split sample and 0.05-0.70 MPa for the flat, sand-blasted sample. These stresses are smaller than the expected normal stress on the rock joint in the field, which is approximately 13 MPa. After obtaining the results for the flat sample, the stresses were discounted for dilatancy.

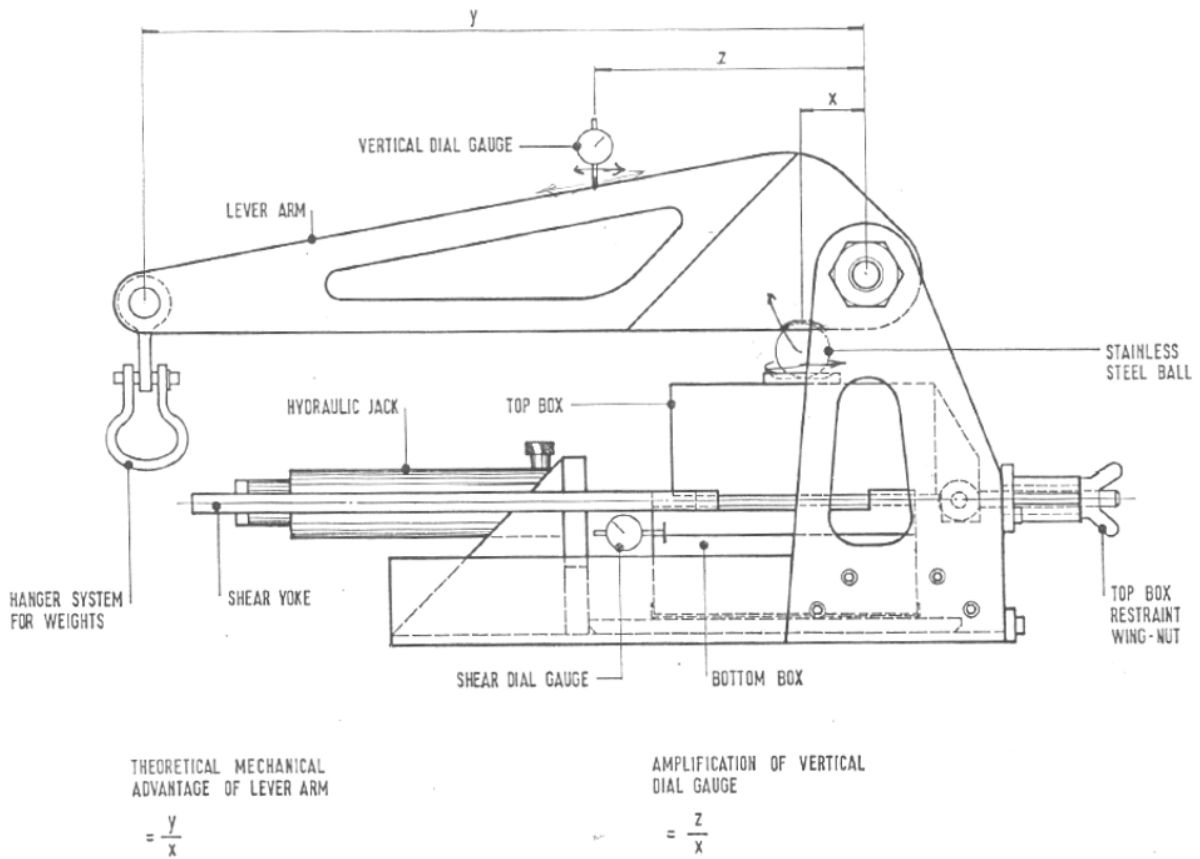


Figure 3.18: Setup of the Golder Shear box. Adopted and modified from Golder Associates 1984.

### 3.4 Results

The results section is split up between the non-destructive field tests (Section 3.4.1) and the destructive laboratory tests on analog samples to the rocks in the field (Section 3.4.2).

#### 3.4.1 Field tests

Two different types of field tests were conducted on Rock 1, 2, 3 and 4 at six locations in the field.

#### JRC

Rock number	Number of measurements for each rock (-)	Average JRC for each rock (-)	Standard deviation (-)	Total average JRC value for all rocks (-)	Standard deviation (-)
Rock 1	2	9.0	1.4	9.2	1.6
Rock 2	2	11.0	1.4		
Rock 3	6	7.7	0.8		
Rock 4	2	9.0	1.4		

Table 3.1: JRC values for each rock and total average JRC value for all rocks.

The range of average JRC values found was between 8 and 11, with a total average of all four rocks of 9.2 (see Table 3.1 and Appendix I). The standard deviation ranges between 0.8 and 1.4 for the

separate rocks and increases to 1.6 for the average JRC value of all rocks.

## JCS

Rock number	Number of measurements (-)	Equotip value (-)	Standard deviation (-)	JCS value (MPa)	Standard deviation (MPa)
Rock 1	20	463.5	136.5	37.0	21.5
Rock 2	20	483.6	141.8	41.1	24.1
Rock 3	60	489.0	158.8	42.3	26.4
Rock 4	20	493.1	190.0	43.2	30.4

Table 3.2: JCS values for each rock.

Total average JCS value for all rocks (MPa)	Standard deviation (MPa)
40.9	25.6

Table 3.3: Average JCS values for all rocks.

In total, 6x2x10 measurements were taken of the JCS in the field. The JCS values of the rocks ranged from 37 to 43 MPa, and the standard deviations from 21.5 MPa to 30.4 MPa (see Table 3.2 and 3.3, and Appendix J). The average JCS value for all rocks is 41, with a standard deviation of 25.6 MPa.

The measurement of the JCS on two rock faces (Rock 3 North and Rock 3 South) was done horizontally, instead of vertically. The difference due to the direction of applying the Equotip was discounted for, following a laboratory comparison between vertically and horizontally applied Equotip values, which in theory, should give the same results. In practice, it was found that the horizontally measured values were slightly larger (see Appendix J.2).

### 3.4.2 Laboratory tests

Laboratory test results were obtained for the tilt test and the Golder shear box test.

#### Tilt tests

Tilt tests were performed in two directions on the tilt test samples. The only difference is that the sample is shifted with 90° horizontally. The results can be found in the table below (and Appendix K).

	Direction 1	Direction 2
	$\beta = \varphi_r$ (°)	$\beta = \varphi_r$ (°)
Test 1	34.0	32.0
Test 2	32.5	32.0
Test 3	33.5	32.0
Average	33.3	32.0
<i>Total average</i>	<b>32.7</b>	

Table 3.4: Tilt test results in two directions.

It can be observed from Table 3.4 that for both directions, the resulting friction angles are very close to each other. For the direction 2, they were even exactly the same. The total average becomes 33°.

### Golder Shear box test

Before testing the samples with the Golder shear box, the JRC, JCS and JMC were determined. The results can be found below and in Appendix L.

Sample type	Number of measurements (-)	Average JRC (-)	Standard deviation (-)
Flat, sand blasted	6	0.0	0.0
Rough, man-made tension crack	6	13.7	2.3

Table 3.5: JRC results for the laboratory samples.

Sample type	Number of measurements (-)	Equotip value (-)	Standard deviation (-)	JCS value (MPa)	Standard deviation (MPa)
Flat, sand blasted	20	679	157	96.3	46.5
Rough, man-made tension crack	20	441	109	32.7	16.6

Table 3.6: JCS results for the laboratory samples.

	JMC after a displacement of 3mm (-)	
	Flat sample	Rough sample
Profile 1 & 6	1	0.7
Profile 2 & 5	1	0.6
Profile 3 & 4	1	0.5
Average	1	0.6

Table 3.7: JMC results for the laboratory samples.

	Test	Residual friction angle (°)		Standard deviation (°)
		Coulomb	Barton	
Flat, sand blasted	1	31.2		1.1
Flat, sand blasted	2	30.5		0.5
Rough, man-made tension crack	1		20.3	0.8
Rough, man-made tension crack	2		30.3	0.6

Table 3.8: Residual friction angle results for the Golder shear box test.

Four tests were conducted with the Golder shear box. Two tests on the flat, sand-blasted sample and two tests on the rough, tensile-split sample. The shear stress against the shear displacement plots of

all four tests can be found in Appendix M. When combining the results of the four loading stages, the residual shear strength - normal stress plots can be drawn up (see Figure 3.19).

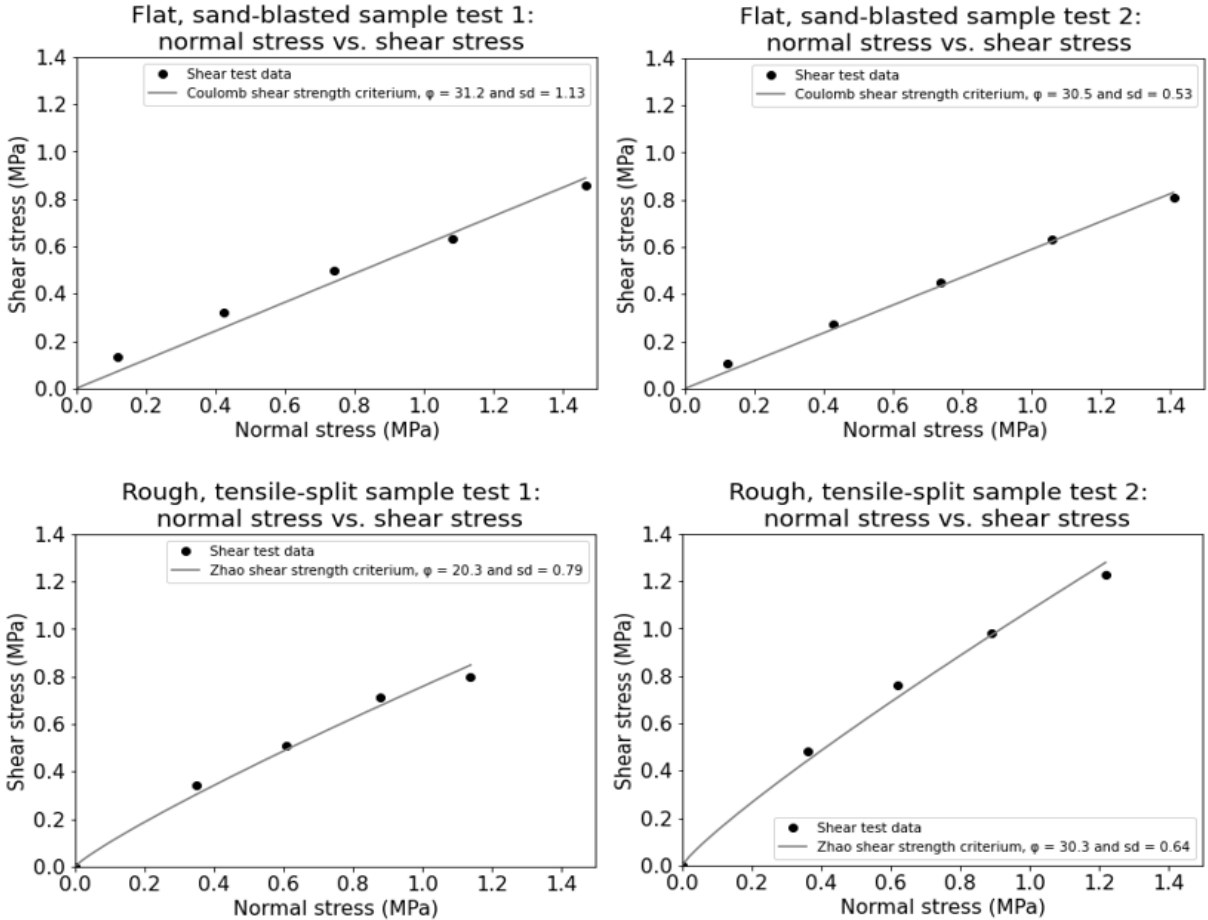


Figure 3.19: Shear stress vs. normal stress plots of flat sand-blasted sample test 1 (upper left corner), flat sand-blasted sample test 2 (upper right corner), rough tensile-split sample test 1 (lower left corner) and rough tensile-split sample test 2 (lower right corner).

The data points of the shear strength and corresponding normal stress are used to fit the failure criterion to. The data was corrected for effective surface area by reducing the effective area by the width of the sample multiplied by the shear displacement of the sample. The residual friction angle can be deduced from the data. The results of the flat sand-blasted sample are interpreted with the Coulomb shear strength criterion and the results of the rough sample were evaluated with Zhao's criterion. For the flat sample, the results were also corrected for dilatancy, because the sample was not completely horizontal with respect to the equipment. For the rough sample, all data points were considered, except the first one. This is because the rock joint halves were matching for the first data points.

For the flat, sand-blasted sample, the residual friction angle results are very close to each other, with a residual friction angle of  $31.2^\circ$  for test 1 and  $30.5^\circ$  for test 2. The results of the rough samples differ significantly from each other, with a residual friction angle of  $20.3^\circ$  and  $30.3^\circ$  for Zhao's criterion.

## 3.5 Discussion

The discussion consists of a discussion on the field test results (Section 3.5.1), laboratory results (Section 3.5.2) and the relative importance of shear strength parameters (Section 3.5.3).

### 3.5.1 Field tests

Non-destructive tests were conducted in the field in order to estimate the JRC and JCS parameters of the rocks.

#### JRC

The JRC values were obtained from 6 different locations on the rocks. At all six locations, two profiles were used. Therefore, 12 values were used to find the total average JRC value for all rocks, which is 9. The corresponding standard deviation of 1.6 seems reasonable. The largest variation between JRC values at one location is 2, the largest variation at one rock is 2 and the overall largest difference is 6. Therefore, there is little anisotropy observed between the measuring locations.

#### JCS

The JCS values were obtained at the same locations as the JRC profiles. A total of twelve profiles was recorded. The resulting total average JCS value is 41 MPa, with a standard deviation of 25.6 MPa. The JCS values are low compared to what would be expected from the literature (Meulenkamp & Alvarez Grima, 1999; Verwaal & Mulder, 1993), and the standard deviation is very high. For slightly weathered granite, the expected JCS values are in the range of 55-90 MPa (Irfan & Powell, 1991). The recorded Equotip values are in the range between 450 and 500, whereas the values reported in the literature are above 800. There can be several reasons for this deviancy. Firstly, it could be because the high Equotip values were found for fresher, less weathered granites. Secondly, it could be caused by the uneven surface on which the tests were conducted. This results in limited lateral rock support around the impact point and the invalidity of the Equotip results (Feal-Pérez & Blanco-Chao, 2013). The standard deviation of the Equotip value is very high. It was found that the value differed significantly between positions that were near to each other. This likely has to do with the rough surface that the tests were performed on. The rocks were medium to coarse-grained, and the Equotip values were very different for tests performed on different positions on the same grain. Alternatively, Schmidt hammer tests could be conducted on analog samples to the rocks in the field.

### 3.5.2 Laboratory tests

Two different laboratory tests were performed, the tilt test and the Golder shear box test.

#### Tilt test

The tilt test was performed on the flat, sand-blasted sample, in two directions with three tests in each direction. The total average basic friction angle based on the tilt tests is 33°, which is in line with values found in the literature for granite rock, between 26 and 40° (Alejano et al., 2012; Coulson, 1972; González, González-Pastoriza, Castro, Alejano, & Muralha, 2014). Therefore, the results seem plausible. This value for the basic friction angle indicates that the residual friction angle is slightly lower. The tilt test samples were made from analog samples to the rocks in the field. However, since the samples were made from the inside of these rocks, the sample rocks that were used for the tilt test are likely to be less weathered compared to the rocks in the field. Weathering reduces the value of the residual friction angle of the rock contact surfaces in the field.

## Golder shear box test

Before conducting tests with the Golder shear box, the JRC, JCS and JMC values had to be determined. The JRC value for the flat surface is 0, and for the rough surface it is 14. This means that the rough laboratory sample is significantly rougher than the in-field surface profiles (JRC 6-12). It can also be observed that the size of the asperities in the joint was larger than the size of the rock crystals. Considering the JCS, it is remarkable to observe that the Equotip and JCS values for the flat surface, 679 (-) and 96 (MPa) respectively, were much higher than the Equotip and JCS values recorded for the rough surface, 441 and 33 MPa respectively. Again, this can be explained by that the Equotip is not applicable to use on very rough surfaces. The values of the flat surface are much closer to the values reported in literature, between 800 and 900 (-) for granites (Aoki & Matsukura, 2008; Meulenkamp & Alvarez Grima, 1999; Verwaal & Mulder, 1993). On the other hand, the strength of the material at the megalith rock surface is likely to be lower than that measured on material located away from the surface exposed to climatic agents. The JMC was determined to be 0.6, which is in line with expectations for a joint that is not very well matched.

For the flat sand-blasted sample, the residual friction angle was obtained by fitting the Coulomb criterion to the shear stress vs. normal stress data since the JRC of the flat sample was equal to zero. The residual friction angle results are both close to each other and also close to values reported in the literature, which are values between 24 and 36° (Woo et al., 2010). Therefore, the results of the flat sample are deemed reasonably reliable.

It was significantly harder to analyze the results of the rough tensile-split sample. This is because of the type of multi-stage testing that was performed. During this testing, the sample was loaded until failure and then a new test was started immediately after, without putting the sample back to the original position. In the case of a non-matching joint, a much smaller contact area of the rock joint exists, which can cause an underestimation of the joint shear strength (Du, Hu, Hu, & Guo, 2011). In the performed tests, the sample joint was matching for the first test, but not matching for the tests after. For this reason, the Zhao failure criterion was used only for the points after the first measurement. Meaning, only for the tests on a non-matching joint. The residual friction angle results are 20.3 and 30.3 degrees. The first value is low compared to what would be expected from the literature, but the second value is in line with what would be expected. Furthermore, the values also significantly differ from each other. This makes these results unreliable. It would be advised not to use rough samples in the future, but instead use a flat sand-blasted sample.

Apart from the considerations of the criteria, some more general aspects of laboratory testing should be considered. The first limitation of laboratory testing is the creep effect. Rocks are significantly less strong under long-term loading compared to instantaneous loading. When strong rocks are loaded at around half of their UCS, they can creep and creep can lead to failure. In the past, significant strength reductions were found for laboratory samples with long-term loading, compared to instantaneous loading. Strength reductions of up to 50% are not uncommon (Barton, 1971). This means that laboratory tests can lead to overestimated shear strength values. Another potential limitation that is often considered is the effect of scale. Generally, the measured strength of a material decreases with an increasing area. This is because asperities can lead to an interlocking effect that has a big influence on the laboratory scale, but a relatively small influence on the field scale. This means that laboratory tests, again, overestimate the shear strength of a material. The JCS and JRC are often overpredicted for in-situ conditions, while the JMC is usually underpredicted (Bandis, Lumsden, & Barton, 1983; Zhao, 1997a). Since in this study, the contact area in the laboratory does not differ too much from the expected contact area between the rocks in the field, the effect of scale is expected to be limited. Lastly, there is the difference between the weathering grade of the rocks in the field and the rocks taken for laboratory testing. The samples were cut from the inside of these analog rocks, and are therefore less weathered compared to the rocks in the field. Weathering has a significant effect on the residual friction angle, which is reduced significantly (Woo et al., 2010).

### 3.5.3 Relative influence of the rock parameters

The relative influence of the rock parameters can be calculated by using Zhao's failure criterion with the parameters as found in this chapter. This gives:

$$\tau = \sigma_n * \tan[JRC * JMC * \log_{10} \left( \frac{JCS}{\sigma_n} \right) + \varphi_r] \quad (3.10)$$

$$\tau = 13 * \tan[9.2 * 0.3 * \log_{10} \left( \frac{50}{13} \right) + 30] \quad (3.11)$$

$$\tau = 13 * \tan[1.6 + 30] \quad (3.12)$$

This means that the effect of the roughness and non-matching of the rock joints (JRC-JMC-JCS term) plays only a little part in the total shear strength of the rock. This justifies that most effort was put into determining the residual friction angle in the laboratory.

## 3.6 Conclusion

This chapter has focused on the determination of the relevant shear strength parameters for the rock contact areas. The goal of the parameter determination was to find a single value for each relevant parameter that could be applied to all rocks, so that it can be used as an input for the numerical stability analyses.

Two tests were performed in the field. The Barton's comb was used to obtain the JRC parameter and the Equotip was used to obtain the JCS. It was found that the JRC value obtained in the field is 9.2. The JCS values taken in the field were low (average of 41 MPa) and varied significantly for locations that were close to each other. The reason for this is that the Equotip is not very suitable for rough, medium to coarse-grained granite, such as examined. For large grains, the Equotip results in widely varying, lower values. For this reason, it should be concluded that the Equotip is not suitable to determine JCS values on rough surfaces. Instead, Schmidt hammer tests could be performed on analog samples to the rocks in the field. The JMC values were not determined in the field, but will be assumed to be 0.3 since all rock contact surface areas are non-matching.

Two laboratory tests were performed. The tilt test was conducted in order to determine the basic friction angle. The basic friction angle for the laboratory sample was found to be 33°. This value is in line with literature, and thereby deemed plausible. The basic friction angle gives an indication of the residual friction angle, as it is expected that the residual friction angle is lower. The Golder shear box was used to determine the residual friction angle of two laboratory samples. For the flat, sand-blasted sample, the results are in line with the literature and therefore deemed reliable. For the rough tensile-split sample, one of the results deviates significantly from the literature and the test is therefore deemed unreliable. It should be concluded that the tilt test and the Golder shear box test with a flat, sand-blasted sample give a good indication of the residual friction angle. The Golder shear box test on a rough sample, however, does not.

Based on the small effect of the JMC-JRC-JCS term of Zhao's failure criterion on the shear strength of the rock contact surface, it was decided to adopt a simple Coulomb failure criterion for the rock joint shear strength in the numerical model. The residual friction angle to be used in the stability analysis is determined to be 30°. This value was chosen, as it is on the low side of the ranges found in the literature, and from the tilt test and Golder shear box test. It was decided to take a slightly lower value, because of the effects of climatic conditions in the field such as the influence of water, which cause laboratory samples to slightly overpredict the value for the residual friction angle, and because

of the potential creep effects that occur as the contact surfaces are subjected to stresses which are large with respect to the UCS. Furthermore, there is the difference in weathering between the analog samples taken for laboratory testing and the rocks in the field. Although the rock samples taken for laboratory testing were not fresh, they were also not as weathered as the outside surfaces of the rocks in the field. A sensitivity analysis will be carried out as a function of the friction angle in order to determine its effect on the results of the numerical simulations.

# Chapter 4

## Numerical stability analyses

This chapter deals with the methods and issues concerned with digitally analyzing potential reconstruction scenarios. A short introduction will be provided in Section 4.1. In Section 4.2, a literature review is presented on stability analyses using limit equilibrium methods, numerical methods and 3DEC, the software that was used in this research. In Section 4.3, the methodology will be discussed, introducing the different stability analyses that have been performed. The results of these analyses will be presented and discussed in Section 4.4. Lastly, a conclusion to this topic will be presented in Section 4.5.

### 4.1 Introduction

The goal of this research is to find out how dolmen D14 can be reconstructed to a stable configuration of rocks, while also conforming to the demands from the relevant dolmen management agencies. Now that the geometrical input and the rock parameters have been produced and determined, it is possible to look at the stability of the structure. The focus of this chapter will be on how potential reconstruction scenarios can be evaluated and what factors influence the stability analyses, and less so on what reconstruction scenario would be most suitable for this specific situation. Determining which reconstruction scenario is the 'best' is a process that does not only involve stability analyses, but also other considerations such as archaeology and aesthetics. For this reason, this chapter will primarily focus on two potential reconstruction scenarios and explain with the help of these scenarios how their stability can be calculated for a destabilizing force and what the influence is of certain model assumptions, such as the number of cycles that can be used for the calculation, the friction angle and the mesh coarseness.

### 4.2 Literature

This literature section will first provide some explanation on the analytical approach for stability analyses. Then, this will be compared to the numerical approach for stability analyses and lastly the numerical software that was used in this research, 3DEC, will be introduced.

#### 4.2.1 Analytical approach

The most commonly used analytical approach for rock stability analysis is the limit equilibrium analysis. This analysis uses analytical methods to calculate the factor of safety for a given situation. A factor of safety greater than 1 means that the situation is stable and a value smaller than 1 means that it is unstable and prone to fail. This method is generally only used in situations when the geometry can be easily quantified. Furthermore, the failure mode has to be specified so that its factor of safety

can be calculated. For a rectangular block on a slope (see Figure 4.1), the factor of safety can be calculated against sliding and toppling for a 2D situation.

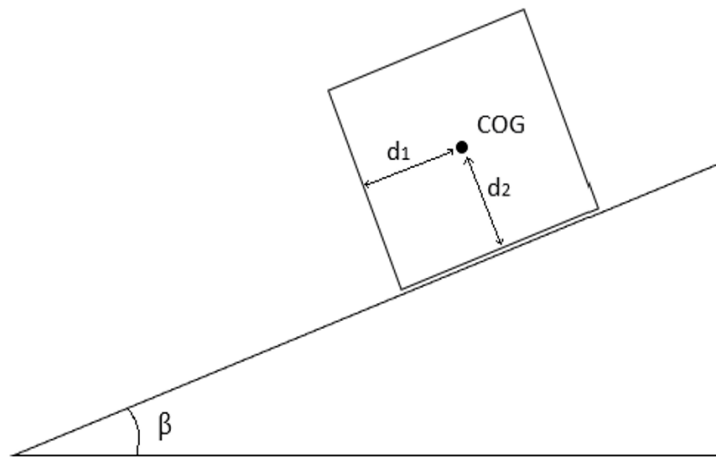


Figure 4.1: Stability of a rectangular block on a slope. The COG denotes the Center Of Gravity of the block.

The factor of safety for the block against sliding can be calculated using:

$$FOS_{sliding} = \frac{\sum F_{stabilizing}}{\sum F_{overturning}} = \frac{\tan(\varphi_b)}{\tan(\beta)} \quad (4.1)$$

In this formula,

- $\varphi_b$  = basic friction angle
- $\beta$  = dip of the plane on which the block rests

For toppling, the following formula should be used:

$$FOS_{toppling} = \frac{\sum M_{stabilizing}}{\sum M_{overturning}} = \frac{W * d_1 * \cos(\beta)}{W * d_2 * \sin(\beta)} \quad (4.2)$$

In this formula,

- $M_{stabilizing}$  = stabilizing moment
- $M_{overturning}$  = overturning moment
- $W$  = weight of the block
- $d_1$  = distance between the center of gravity of the block and the rotation axis, parallel to the dip of the plane on which the block rests
- $\beta$  = dip of the plane on which the block rests
- $d_2$  = distance between the center of gravity of the block and the rotation axis, perpendicular to the dip of the plane on which the block rests

Several studies have compared the analytical methods with data from experiments and concluded that the theory matches practice well (Pérez-Rey et al., 2021). The main drawback of using limit equilibrium methods is that it is best suitable for problems with simple geometries, where it is less easily applicable to problems with more complex, irregular geometries. Nonetheless, this method was used by Pérez-Rey et al. (2019) to calculate the factor of safety on the Pena do Equilibrio, a large boulder with rounded corners lying on an inclined surface. In this research, a stability formula was used to calculate the factor of safety in both static and seismic conditions. A major disadvantage of calculating the factor of safety this way is that it can only be done in 2D, therefore not taking into account the complexity of the 3D geometry.

#### 4.2.2 Numerical approach

Numerical analysis differs from analytical analysis in the way that it solves mathematical problems. Numerical methods are used to approximately solve problems, instead of the exact solutions that are obtained by analytical methods. Numerical methods are mainly used for problems that cannot be solved analytically or would take too much time to do so. Numerical methods use an iterative solving scheme. The way this works when solving an equation for  $x$ , is that an algorithm first takes an initial guess for  $x$  and then uses an algorithm to continually update this value until the guess is sufficiently refined that it meets a specified error requirement.

Numerical methods have been applied to rock stability problems in the past, for example the slope stability of mines (de Bruyn, Coulthard, Baczynski, & Mylvaganam, 2013; Mononen, Kuula, & Lamberg, 2013), the slope stability of bridge abutments (Varughese, Rathod, & Rao, 2010) and slope stability calculations before a landslide occurrence (Brideau et al., 2010). The closest study to the stability analysis of a megalith is that of the stability of a large rounded rock boulder conducted by Muñiz-Menéndez et al. (2020) on the same Pena do Equilibrio boulder as Pérez-Rey et al. (2019), using the same geometrical data as an input for their numerical calculations to analyze the stability of the rock under static and seismic conditions. Comparing their results to the study of Pérez-Rey et al. (2019), showed that their results were very similar. Therefore, it was concluded that their methods were valid and could be used in future research. Nonetheless, a number of simplifications were used for this numerical analysis. The most significant simplification is that the contact area between the rocks was assumed to be flat and planar. In reality, this is not the case and it is one of the critical factors of the stability analysis.

#### 4.2.3 3DEC software

There are several software programs with which numerical analyses can be performed. For rock mechanics, 3DEC is one of the most often used programs (3DEC, version 7.00.141, 2013). 3DEC is a software program, which allows for simulation of the response to loading of discontinuous media. The use of 3DEC is intended for rock engineering projects, and the discontinuous media that are modelled often concern jointed rock mass. 3DEC is the three-dimensional version of the two-dimensional software UDEC, which is a numerical program that can simulate quasi-static and dynamic loading on jointed media.

3DEC is based on the distinct element method for discontinuum modelling. This means that several distinct elements, which are also referred to as blocks, can be part of the model and that all elements have distinct boundary conditions. The blocks can be set to be either rigid or deformable and they behave according to linear or nonlinear force-displacement relations for movement in normal and shear directions. Discontinuities within the rock mass can be established as boundary conditions of blocks. The behavior of the discontinuity, or rock joint, can be specified and it determines the interaction between blocks. The main advantages of distinct element method modelling are that this type of software allows finite displacements and rotations of discrete bodies and recognizes new contacts automatically as the calculation progresses. It is different from limit equilibrium methods, in that

limit equilibrium methods only calculate the static force or moment equilibrium of a body, and do not consider a change in force or moment distributions that causes displacements and rotations to the body.

3DEC employs an explicit in-time solution algorithm, with a defined calculation cycle for each time step. Time steps are calculated based on the mass and stiffnesses in the system. If the stiffness is increased, the time step will be decreased to find the correct results. And for a higher mass associated to a grid point, the time step will be increased. There are two types of mechanical behavior in a discontinuous system, the behavior of the discontinuities and the behavior of the solid material. These components are calculated alternately in 3DEC. At each time step, five calculation steps are performed. At first, the relative velocities of the sub-contact grid points are calculated. Then, the sub-contact displacement increments can be calculated based on the time step and the relative velocities. As a third step, the sub-contact displacement increments are resolved into their normal and shear components and the normal and shear stiffnesses are used to calculate the sub-contact force increments. The force increments are then used to update the total normal and shear forces of the sub-contact, which are then adjusted according to the contact constitutive relations. In step 4, the sub-contact force increments are added to the forces and moments that are acting on the block centroids. Lastly, the new block positions and velocities are calculated using the equations of motion of the blocks, which are integrated using a finite difference procedure. The velocities are then updated for the sub-contacts, and a new time step will begin. The cycle of mechanical calculations is illustrated in Figure 4.2.

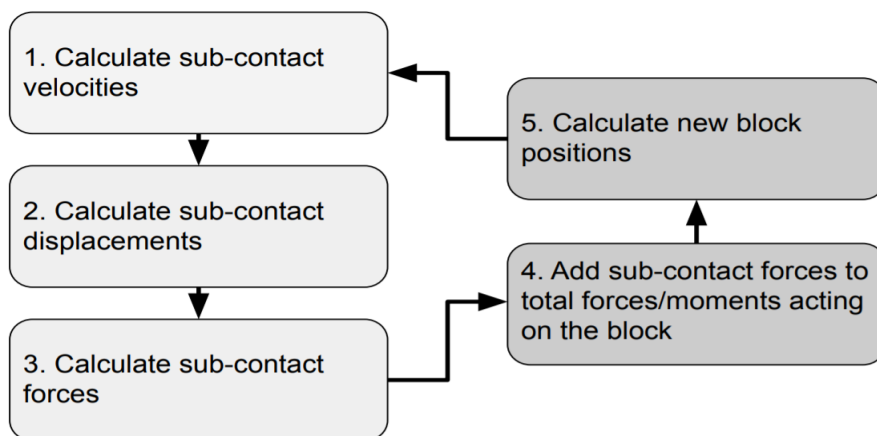


Figure 4.2: Cycle of mechanical calculations. The calculations regarding the discontinuities are displayed in light grey on the left and the calculations regarding the total block are displayed in dark grey on the right. The cycle is stopped when the specified number of cycles is reached or when the model has reached a specified convergence criterium.

3DEC is suitable for the calculation of large displacements, although it should be noted that the displacements are calculated based on arbitrary damping and stiffness values and therefore do not always approximate reality well. Contacts between blocks in the numerical model in 3DEC are handled using the soft-contact approach, which allows for interpenetration of the blocks. Furthermore, both static and dynamic loading is possible in the software. It uses a command-driven interface, which prevents repetition of actions. When combined with the built-in programming language FISH or the python extension, the command-driven approach helps to run many analyses automatically and develop pre- and postprocessing scripts.

There are a few ways in which stability analyses can be conducted in 3DEC. In this research, the mechanical ratio is used as a convergence criterion. Such a criterion means that once convergence is reached, the model is deemed stable. The mechanical ratio that was considered in this research is the average force ratio, which is the sum of all the out-of-balance force components, obtained by summing the forces acting at every grid point, divided by the total forces applied to all grid points (see Equation 4.3). Out-of-balance force components are those components of a force, that are not balanced by a force of equal magnitude in opposite direction. Once the average force ratio is sufficiently small (default parameter of 1e-5), the model is declared as converged. If the model does not converge, it will run until it is manually stopped by the user.

$$\text{Average force ratio} = \frac{\sum_j^n \langle \sum_i f_i \rangle}{\sum_j^n \sum_i \langle f_i \rangle} \quad (4.3)$$

In this formula,

- $i$  = the force vector component at a grid point
- $j$  = the grid point number
- $n$  = the number of grid points in the model

## 4.3 Methods

The methods section is split up into two parts. In the first part, numerical models are compared to analytical solutions for 2D problems (Section 4.3.1). In the second part, the dolmen will be analyzed for stability in 3D (Section 4.3.2).

### 4.3.1 Comparisons between analytical and numerical results

The difference between analytical and numerical methods has been addressed before (in Section 4.2.2). In this section, a comparison will be made for three problems between analytical results calculated by hand and numerical results calculated with 3DEC. The rectangular block on a slope model was investigated as a first effort to compare analytical results to numerical results from 3DEC, for a sliding failure mode. The rectangular block on two rectangular supports was used to compare analytical results to numerical results and to analyze the influence of the mesh coarseness on the model results. The failure mode that was observed was toppling. Lastly, the stability of the dolmen was studied in 2D to obtain a first estimate of the order of magnitude of the minimum force, required for instability of the dolmen. The failure mode considered for the dolmen in 2D was both sliding and toppling.

#### Rectangular block on a slope

The problem of interest is that of a rectangular block on a slope that has a mass  $W$  and a frictional force  $Fr$  (see Figure 4.3). There is a destabilizing force  $F$ , which is applied in order to make the block slide. From this problem, it can be calculated what force  $F$  would be required to make the block slide. This force  $F$  was first calculated analytically, and then compared to the numerical results. The numerical model was programmed as a 2D problem, not allowing any forces or displacement in the out-of-plane direction. The block was 1x1m, resting on a slope with an angle  $\psi = 30^\circ$  and a friction angle of the discontinuity  $\phi = 45^\circ$ . Furthermore, the force was applied at the bottom of the block, in the middle of the edge.

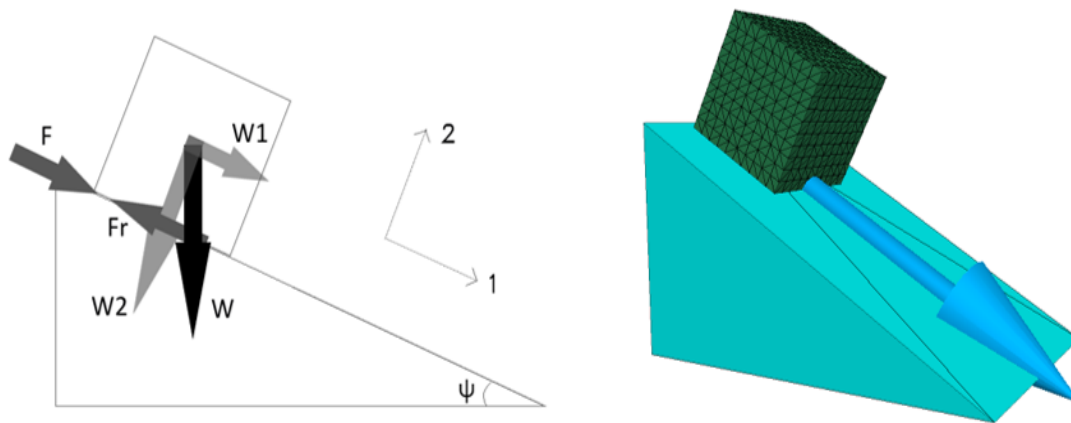


Figure 4.3: Rectangular block on a slope: schematic model used for analytical calculations (left) and numerical model (right).

### Rectangular block on two rectangular supports

The rectangular block on two rectangular supports was analyzed in order to check the numerical results against the analytical results, but also in order to analyze the effect of mesh coarseness on the model results for a simple geometry (see Figure 4.4). The dimensions of the block on the top (2x1m) were in the same order of magnitude as Rock 3 on top of the support, Rock 2 and Rock 4. Only the toppling failure mechanism was analyzed. The analytical results were compared against the numerical result for an average mesh edge length of 0.05, 0.10, 0.15, 0.20 and 0.25 m. The meshes were created in two types for the top block. Normal meshes, with tetrahedral elements of approximately the same size all throughout the block, and smart meshes, with tetrahedral elements that had the same size on the outer surface of the block, but were coarser on the inside of the block. The remeshing was done with Griddle and the remeshing settings can be found in Appendix D. This type of mesh refinement should be considered for large blocks, since it greatly reduces the calculation time for the model. The comparison between a normal mesh and a smart mesh was made in order to analyze whether the type of mesh would have an effect on the model results. All blocks were modelled as rigid bodies and the support blocks were fixed in terms of position, meaning that they could not be moved.

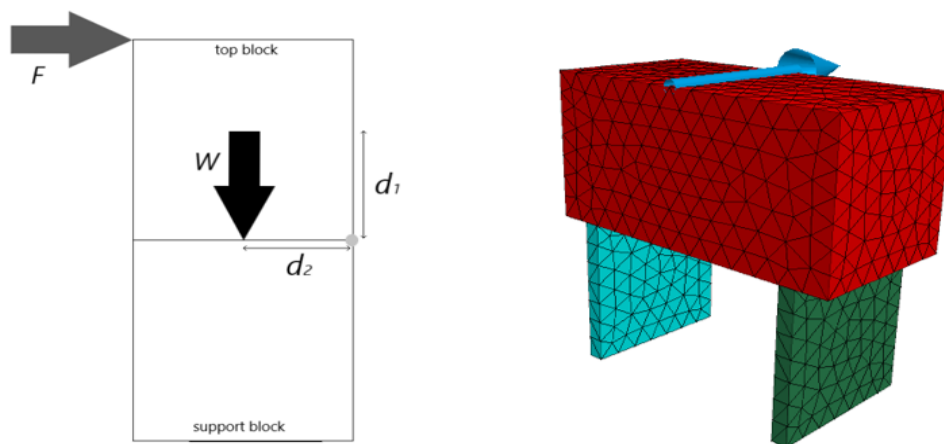


Figure 4.4: Rectangular block on two rectangular supports: schematic model used for analytical calculations (left) and numerical model, with an average mesh edge length of 0.15 m (right).

## Dolmen stability in 2D

The stability of the dolmen was studied in 2D for the failure mechanisms of sliding and toppling. In this case, the block and its supports are not rectangular. Their shapes resemble cross-sections of Rocks 2, 3, and 4. This was done for the scenario when Rock 3 is put back on top of Rock 2 and 4 is put back on top of Rock 3 in the same manner as it was in 2019. The required force to topple Rock 3 depends on the height at which the force was applied. Therefore, the stability was investigated for different heights. The failure force  $F$  was first calculated analytically, and then checked against the values obtained by 3DEC. The outlines of the two 2D megalith profiles can be found in Figures 4.5 and 4.6.



Figure 4.5: Dolmen D14 in 2D at the Northern contact point between Rock 3 and Rock 2: schematic for analytical calculations (left) and numerical model (right).

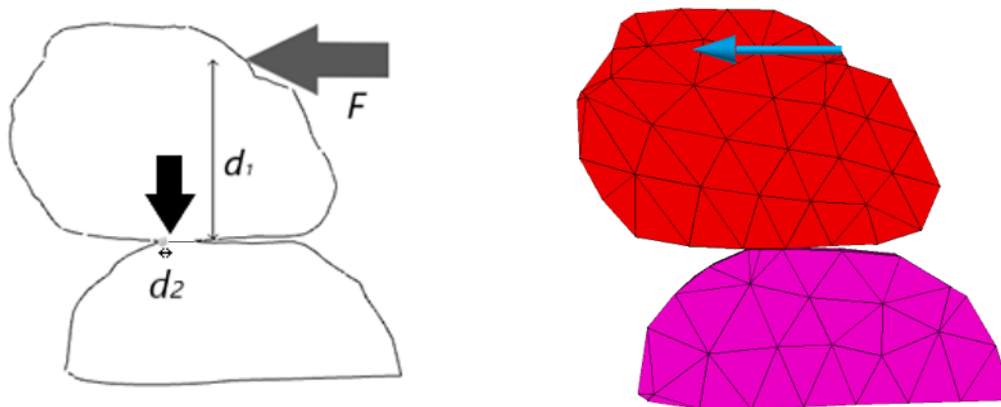


Figure 4.6: Dolmen D14 in 2D at the Southern contact point between Rock 3 and Rock 4: schematic for analytical calculations (left) and numerical model (right).

### 4.3.2 Dolmen stability analysis in 3D

In this section, more information will be provided on how the 3D stability analyses were done for the dolmen. In Section 4.3.2.1, the selected potential reconstruction scenarios will be introduced and in Section 4.3.2.2, the model parameters and assumptions will be discussed.

### Selected reconstruction scenarios

Two different models were investigated for their stability. These models were based on past rock configurations of the dolmen. Model 1 is based on the configuration as it was in 2019 and Model 2 is based on the rock configuration as it was in 1925.

#### Model 1

The first scenario of interest is the configuration of the rocks as they were in 2019. This means that only Rock 3 is moved. It is placed back in the same position as it was in 2019, right before it was dislocated. This scenario is likely to give low stability results, since it proved to be unstable in reality. However, when this configuration failed in 2019, there was a pin inserted between Rock 2 and 3 and mortar was applied between Rock 2 and Rock 3 and between Rock 3 and Rock 4. In this rock configuration, Rock 3 is only supported by Rock 2 and Rock 4 and faces north with its high jut and faces west with its triangular notch. For visual illustrations, see Figure 4.7 and 4.8.



Figure 4.7: Rock 3 as positioned in early 2019. The north is indicated with a grey arrow and the red arrow indicates the high jut of the rock.

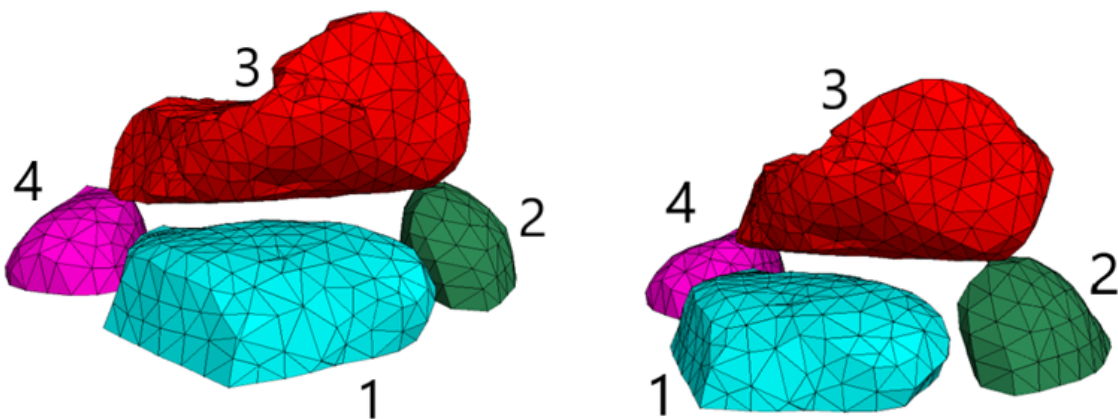


Figure 4.8: Model 1 rock configuration.

#### Model 2

In Model 2, the rocks are placed in a configuration similar to how it was in 1925, before the reconstruction of Van Giffen. Rock 2, 4, 5 and 7 remain in the same position as they currently are, but Rock 1, 3 and 6 are moved. Rock 1 is vertically rotated slightly less than 45 degrees. The face that

is currently on the top, used to face the top/north. This is also illustrated in the Figure 4.9 and 4.10. Rock 3 is turned by 180 degrees and placed back on Rock 1, 2 and 4. The thick jut is now facing south and the triangular notch is now facing east. The orientation of Rock 6 is the same as it was before, however, it is now moved more to the east. It is currently only resting on Rock 5 and 7, but in 1925 it was also touching Rock 3. Thereby, it locks Rock 3 between itself and Rock 1.

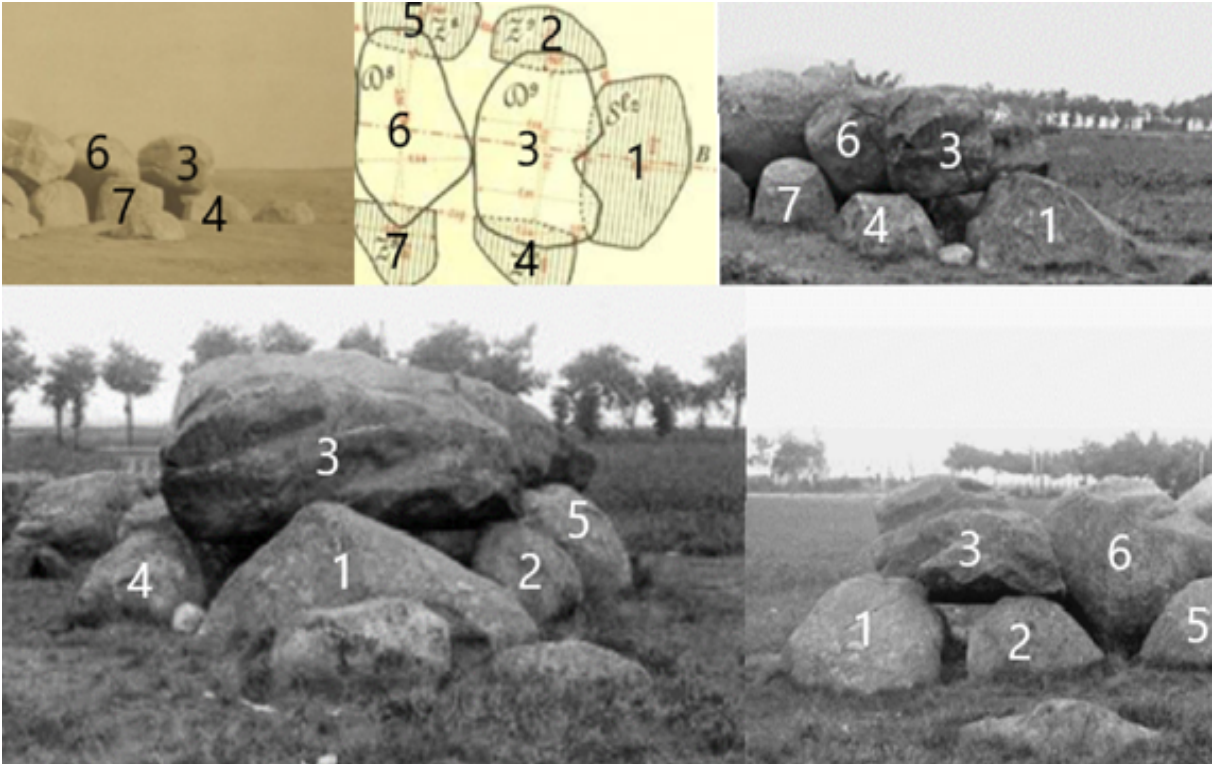


Figure 4.9: The 1925-1927 configuration of the rocks before the reconstruction of Van Giffen.

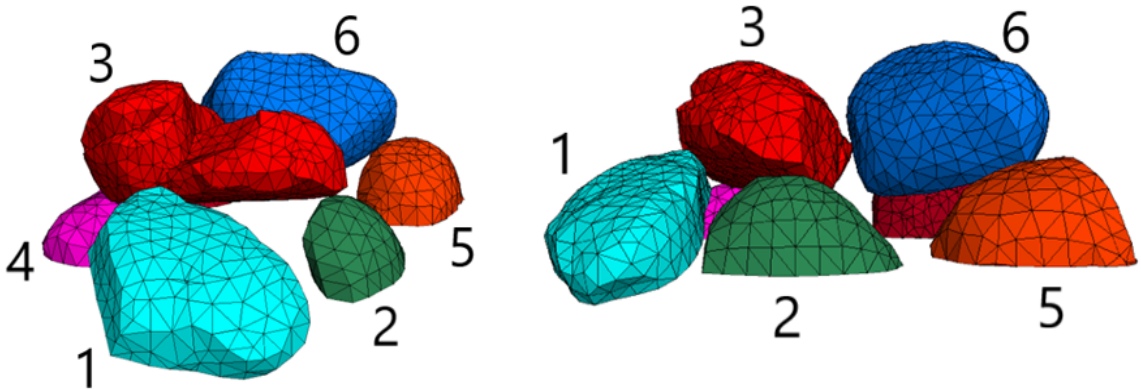


Figure 4.10: Model 2 rock configuration.

**Model parameters and assumptions**

The model parameters used as input for 3DEC can be found in Table 4.1. The density of 2700 kg/m<sup>3</sup> was assumed for granitic rocks. The normal and shear stiffness values were based on the values used by Muñiz-Menéndez et al. (2020). The friction angle of the rock contact surfaces is based on the

values found in the laboratory, as well as the values found in the literature. Lastly, the mesh edge length was set as 0.15 meter, because this is the lowest value that could be used, resulting in the most detailed mesh without having to use a Griddle license. The influence of the model parameters on the model results will be further investigated through a sensitivity analysis.

Parameter	Value	Unit
<i>Block parameters</i>		
Density	2700	kg/m <sup>3</sup>
<i>Joint parameters</i>		
Joint normal stiffness	$1 * 10^{10}$	Pa/m
Joint shear stiffness	$1 * 10^{10}$	Pa/m
Friction angle of the joint	30	°
Residual friction angle of the joint	30	°
Cohesion of the joint	0	Pa
Residual cohesion of the joint	0	Pa
<i>Mesh parameters</i>		
Mesh edge length	0.15	m

Table 4.1: Model parameters used for the sensitivity analysis.

The contact surface between the rocks is modelled as a joint in 3DEC. For the joint model, the Coulomb slip model was chosen. The cohesion, friction angle and shear stiffness determine the linear shear behavior of the joint, see Figure 4.11.

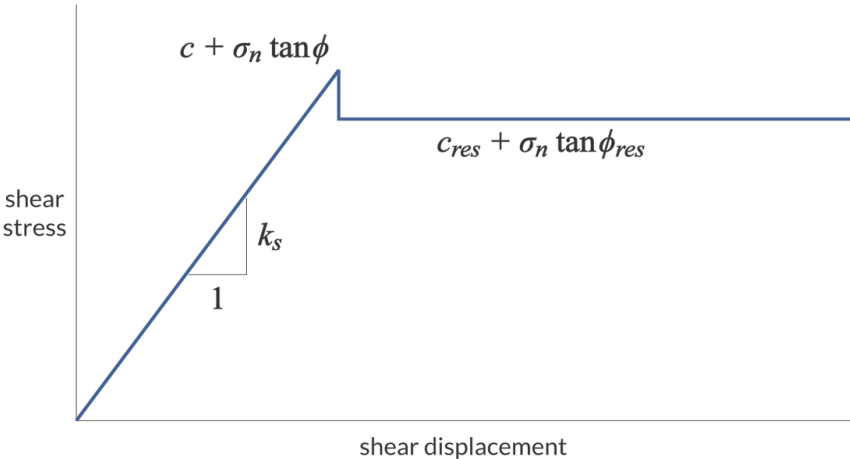


Figure 4.11: Coulomb model in 3DEC. Adopted from (Itasca Consulting Group, Inc., n.d.).

The geometry of the dolmen is represented by tetrahedral elements. These volumetric elements are called blocks in 3DEC. All blocks of which the rock consist, are grouped together. The groups of blocks have been set to be rigid, meaning that they cannot be deformed and keep having the same

shape, all throughout the modelling process. Furthermore, the rocks on the ground floor have been set as fixed, meaning that they cannot move, no matter the force that is exerted on them. This is done, assuming that the foundation of the support rocks prevents movement. In practice, this means that only Rock 3 and 6 are allowed to move in the model.

The results of the model are quantified in terms of the minimum force for non-convergence of the model. It is checked whether the rock configuration remains stable when a force is exerted on Rock 3. In 3DEC, stability can be quantified using a number of markers but in this case it was chosen to use the unbalanced force ratio (see Section 4.2.3). Once this force ratio is sufficiently small, the software will mark the model as 'converged'. Obviously, stability can more easily be achieved for a low force applied on Rock 3, compared to a high force. In this research, it will be investigated what the minimum force is, for which the model is not stable. In other words, the minimum force for which the model does not converge. It was decided not to use displacements as a marker of stability, since the displacements that 3DEC calculates are calculated with an artificial damping constant as well as artificial stiffness values in normal and shear directions.

For this research, one pushing force location and direction was analyzed for each model. The location and direction are arbitrary, but the main principle to determine it was kept the same for the two models. The pushing force direction was set as perpendicular to the 'contact line', the imaginary line between the contact zones of Rock 3 and Rock 2 and between Rock 3 and Rock 4 (see Figure 4.12). The pushing force is located on the line, perpendicular to the 'contact line', where it intersects with the center of gravity. These lines are different for both models, since their contact areas and center of gravity of Rock 3 are at different locations. The pushing direction does not have a vertical component unless specified otherwise.

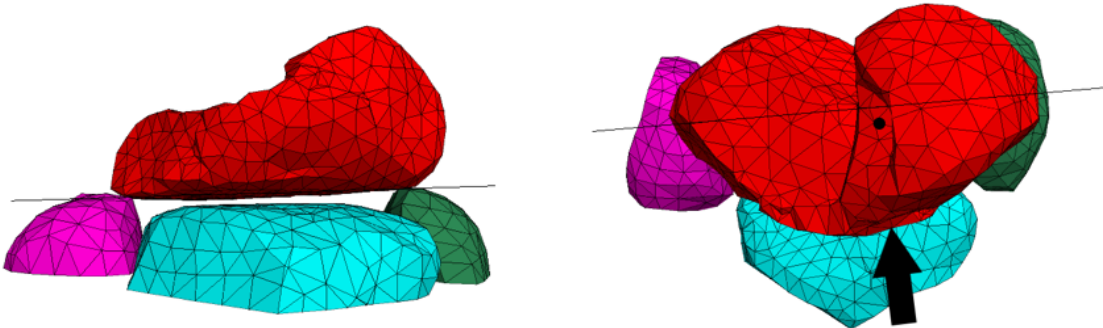


Figure 4.12: Schematic of pushing force location and direction.

Running the model consists of two phases. In the Phase 1, the geometry of the rocks is loaded into 3DEC and the parameters are specified. Then, the gravitational force is applied and the rock is slowly being lowered onto the support stones (see Figure 4.13). Whenever the mechanical ratio is sufficiently small, in this case at a value of  $1e-5$ , the model is deemed 'stable' and is stopped. During Phase 2, a force is applied to Rock 3 and the model is checked for convergence within a specified number of cycles (see Figure 4.14). The 3DEC code to run modelling Phases 1 and 2 can be found in Appendix N.

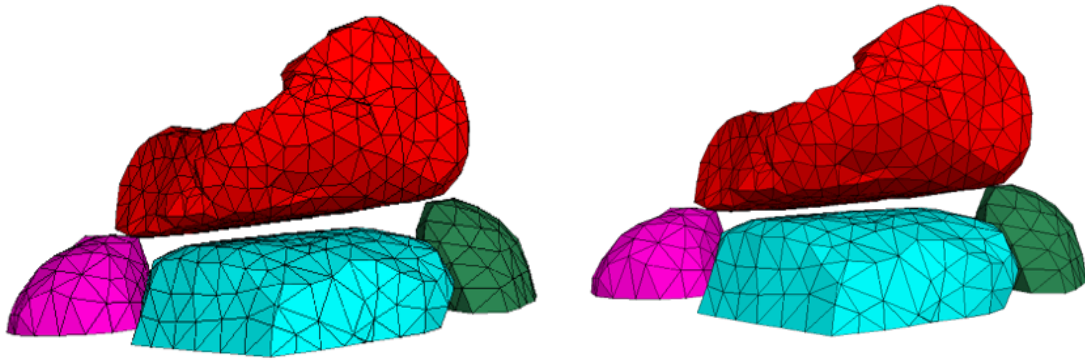


Figure 4.13: Rock configuration before (left) and after (right) modelling Phase 1.

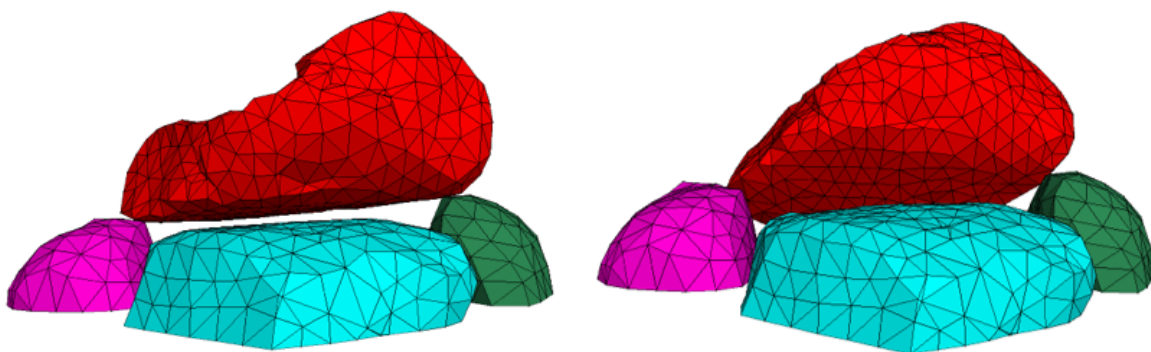


Figure 4.14: Rock configuration before (left) and after (right) modelling Phase 2. The applied force was 30 kN for 100000 cycles.

### 4.3.3 Sensitivity analysis of the model

The influence of the model parameters on the model results is analyzed with a sensitivity analysis. The variables are the number of cycles, the mesh coarseness and the friction angle of the joint. The results have been determined in terms of the minimum force for non-convergence. The parameters were only varied for Model 2. This is because Model 1 has such a low minimum force for non-convergence (very unstable model), that a change in the model parameters will not give very insightful results.

## 4.4 Results and discussion

In this section, the results of the two types of analyses will be presented and discussed. First, the simple 2D models will be discussed (Section 4.4.1). Secondly, the results of the more complex 3D models will be discussed (Section 4.4.2).

### 4.4.1 Comparison between the analytical and numerical results

Three different models were analyzed in order to compare the numerical results to the analytical results. The rectangular block on a slope model was investigated to compare the numerical results to the analytical results. The rectangular block on two rectangular supports model was used for the same reason, as well as to analyze the influence of the mesh coarseness on the model results. The 2D stability analysis of the dolmen was studied in order to obtain a first estimate of the force required for instability of the megalith structure. The maximum number of cycles within which convergence

should be reached was set to 100000 for all 2D models, as this was deemed sufficiently high so that the influence of the number of cycles on the model results was limited.

**Rectangular block on a slope**

Analytically, it was found that the minimum force required for instability is approximately 7.3 kN, when using a friction angle of 45° (for calculations, see Appendix O). Numerical results were obtained using 3DEC. Several analyses were done, with varying values for the force and the friction angle.

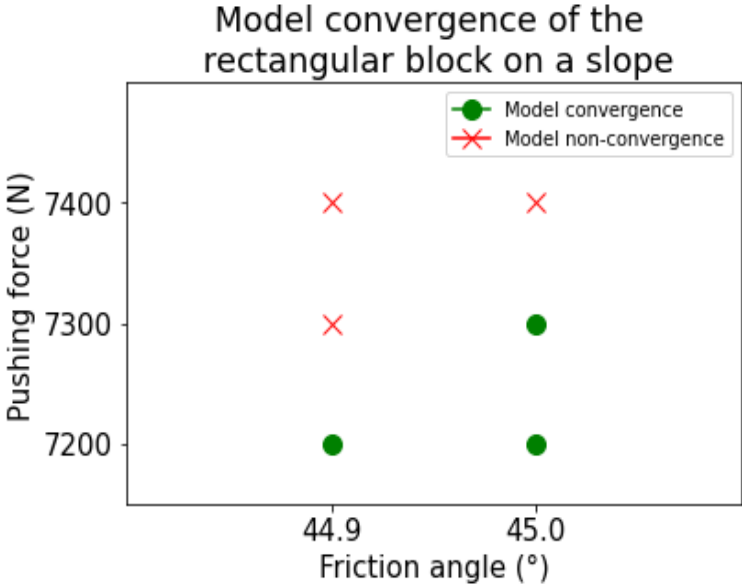


Figure 4.15: Results of the rectangular block on a slope. Model convergence is depicted with a green circle and model non-convergence is depicted with a red cross. Model convergence was checked within 100000 cycles.

When comparing the analytical values to the numerical results for the block model, it can be observed that the numerical results are very much in line with what would be expected (see Figure 4.15). It was analytically calculated that the force required for failure would be 7.3 kN, for a friction angle of 45°. The numerical results show that the model converges for a force lower than 7.3 kN, and a friction angle that is 45°. The model does not converge for a force higher than 7.3 kN, or a friction angle lower than 45°. This means that for an applied force lower than the analytically calculated force, the model would result in a stable situation, as expected. For a higher force than analytically calculated, or a lower resistance to movement (friction angle), the block would start sliding.

**Rectangular block on two rectangular supports**

The analytical minimum force for failure was calculated to be 20 kN (for calculations, see Appendix P). This was only calculated for toppling. Numerical results were obtained in 3DEC. The friction parameter was set to an artificially high value of 80°, in order to prevent sliding and thus force a failure mode of toppling for the block. The minimum force for model non-convergence was determined for meshes with varying average mesh edge lengths (AMEL) and for normal and smart meshes.

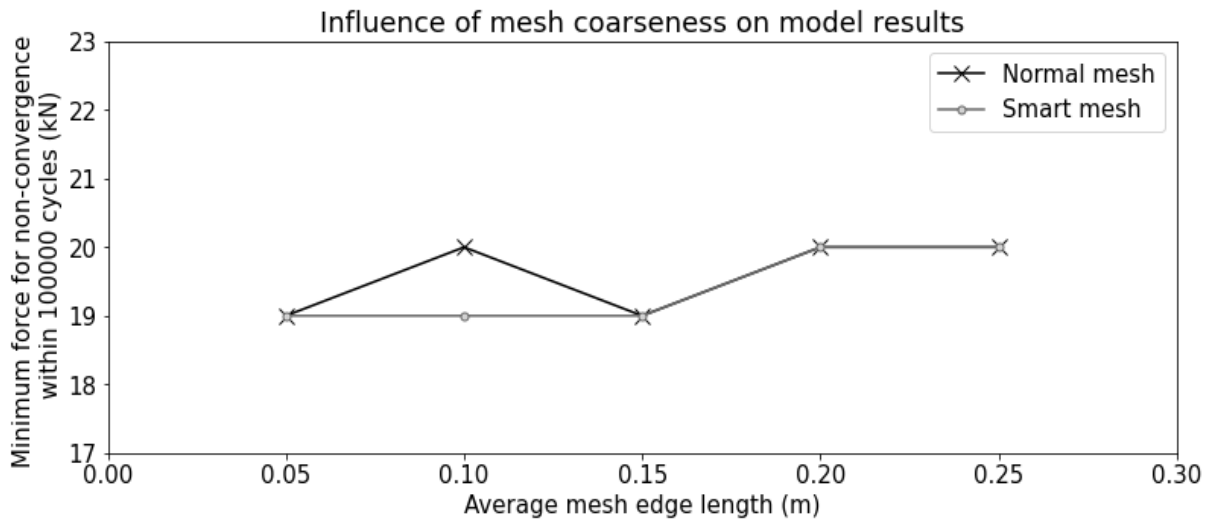


Figure 4.16: Influence of the mesh coarseness on the model results for the rectangular block on two rectangular supports.

The results of the rectangular block on two rectangular supports model indicate that there are only small differences in the stability results when comparing a smart mesh to a normal mesh (see Figure 4.16). Only for the model with an AMEL of 0.10 m, a small difference in model results of 1 kN could be observed. Furthermore, the differences in the model results between the models with different coarseness are small. It was found that the numerical results are close to the analytical result of 20 kN for all meshes.

## 2D megalith model

The force required for failure was first calculated analytically (see Table 4.2 and for calculations see Appendix Q). For sliding, it was found that the destabilizing force should be at least 11.6 kN. For toppling, two 2D profiles were studied, one at the Southern contact point of Rock 3 and 4 and one at the Northern contact point between Rock 3 and 2. The required force therefore ranged from 0.3-10.4 kN, depending on the profile and the height of the applied force. At the Southern contact, the required force for failure is much smaller than the required force for instability at the Northern contact, because the center of gravity is much closer to the point around which the block can topple.

	Southern contact (kN)	Northern contact (kN)
Sliding	11.6	11.6
Toppling, force at top	0.3	5.8
Toppling, force at bottom	0.8	10.4

Table 4.2: Analytical results, required force for instability of the 2D megalith models.

The numerical results obtained with 3DEC can be found in Table 4.3. It can be seen that the numerical results are mostly higher than the analytical results. Deviations between the analytical and numerical calculations can be explained by the complex geometry of the rocks and the fact that sliding did still occur, even though the frictional resistance term was set to an artificially high value. Since the mesh was not very refined, the rotation point could be different for Rock 3 in the numerical model compared to Rock 3 in the analytical model.

	Southern contact (kN)	Northern contact (kN)
Force at top	0.7	6.5
Force at bottom	2.3	12.0

Table 4.3: Numerical results, minimum force for instability of the 2D megalith models.

All in all, the results of the numerical analysis seem in line with the analytical results. Based on these calculations, it can be estimated that the required force for instability of the reconstruction scenario of Model 1 will likely be a couple of kilonewtons, thus, very unstable.

#### 4.4.2 Stability analysis for the dolmen

The stability of the dolmen was analyzed for two potential reconstruction scenarios, Model 1 and Model 2. In both models, the stability of the rock configuration was analyzed for a pushing force applied to Rock 3. Even though the potential reconstruction scenarios were only evaluated for one force in one direction, the minimum force to cause failure that was calculated can give an indication of the order of magnitude of the force that is required to create an imbalance in the megalith structure.

##### Stability analysis for Model 1

It was found that the minimum force for model non-convergence is 2 kN for Model 1. The failure mechanism is dominated by toppling and sliding (see Figure 4.17). This can be expected, since the configuration of Model 1 resembles the rock configuration of a rectangular block on two rectangular supports. A block on two supports is likely to slide and topple, depending on the magnitude of the friction angle.

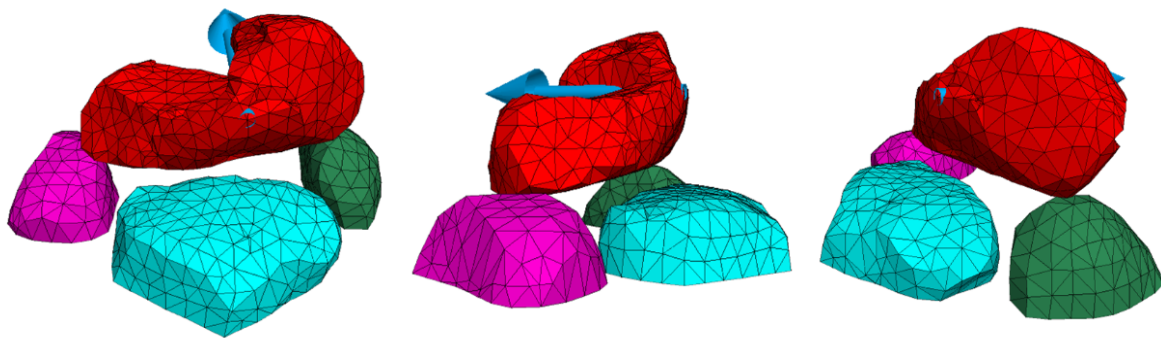


Figure 4.17: Rock configuration of Model 1 after 200000 cycle steps, for a normal mesh and a force of 2 kN. The blue arrow indicates the pushing force direction and location.

##### Stability analysis for Model 2

The minimum force for model non-convergence is 94 kN for Model 2. This means that Model 2 is much more stable than Model 1, which is likely due to the interlocking effect that is created by the positioning of Rock 1 and Rock 6. The failure mechanism of Model 2 is more complicated than for Model 1 (see Figure 4.18). Over time, a couple of observations can be made regarding the failure mechanism. First, Rock 3 loses contact with Rock 1 due to the pushing force. Then, Rock 3 loses contact with Rock 2 as it is lifted upwards. Meanwhile, Rock 3 slides over Rock 4 in the direction of

pushing, but contact remains, and Rock 6 is pushed backward over its supports, Rock 5 and Rock 7. The rotation of Rock 3 in this failure mode is mostly vertical.

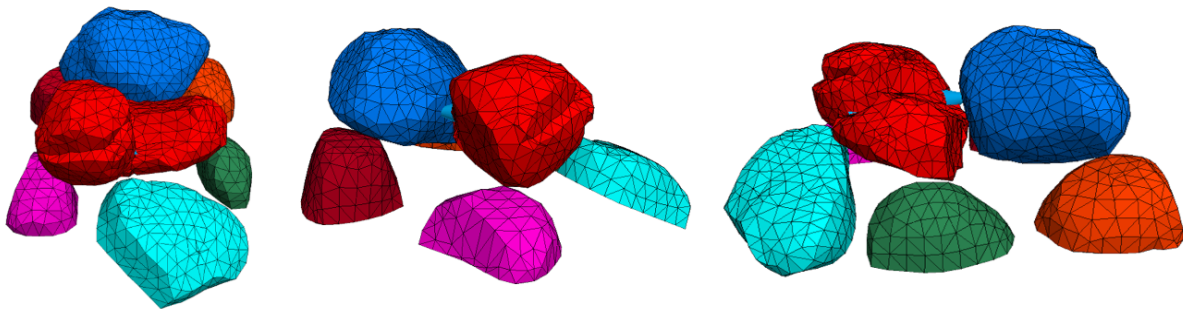


Figure 4.18: Rock configuration of Model 2 after modelling Phase 2, for a normal mesh and a force of 94 kN. The blue arrow indicates the pushing force direction and location. It can be observed that Rock 3 is tilted in the pushing force direction and has lost contact with Rock 2.

#### 4.4.3 Sensitivity analysis for the model

There are many factors that influence the model results. A sensitivity analysis was conducted to analyze the effect of certain parameters. The investigated variables are: the number of cycles, the mesh coarseness and the friction angle of the rock joints. All results are reported in terms of the minimum force for model non-convergence. The sensitivity analysis was only conducted on Model 2, since Model 1 is so unstable that the results are likely to give unreliable trends. All numerical results of the stability analysis can also be found in Appendix R. Although some model assumptions have been researched with the sensitivity analysis, others have not been analyzed. Examples of this include the influence of the destabilization of the supports rocks, such as differential settlement, or the location and direction of the destabilizing pushing force.

##### Number of cycle steps

3DEC works with calculation cycles, in which the forces and displacements of all grid points in the model are calculated (see Section 3.2.4). When doing stability analysis, the unbalanced force ratio is calculated in each cycle. However, when determining whether a model converges, there is the issue of over what time period this is determined. Simply put, how many cycles should be run in order to allow the model to converge. In this analysis, it is investigated what influence the number of cycles, within which convergence should be reached, has on the model results.

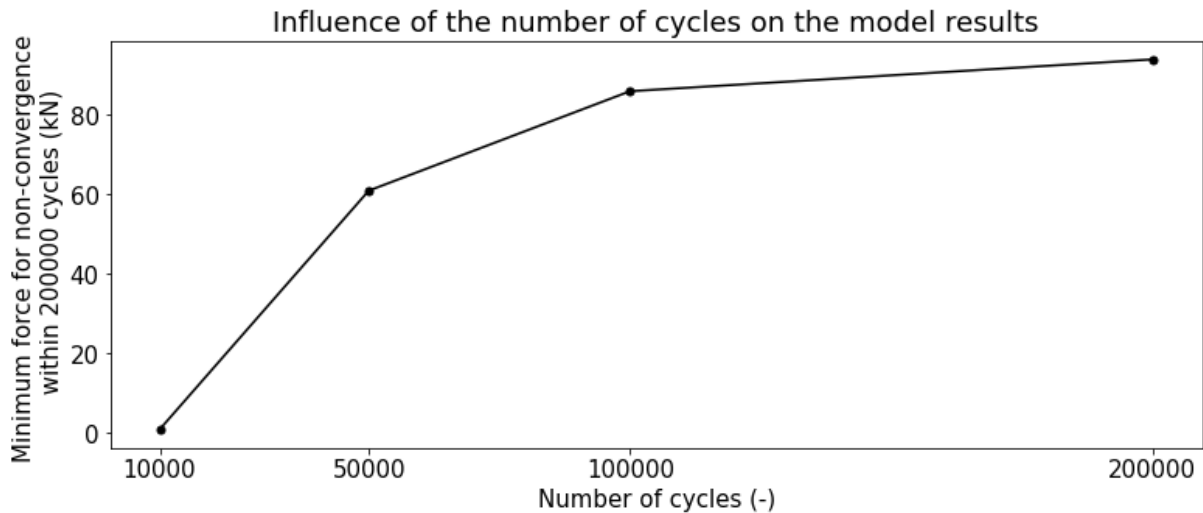


Figure 4.19: Effect of the number of cycles on the minimum force for model non-convergence, for Model 2.

The effect of the number of cycles was evaluated for the minimum force for model non-convergence (see Figure 4.19). It can be seen that the minimum force for model non-convergence rapidly increases with the number of cycles but seems to reach a stable value for a high number of cycles. This is because convergence takes time. It takes a couple of cycles in order for the unbalanced force ratio to become sufficiently small that convergence is reached. When a low force is applied, this convergence is easier reached than for a high force. That being said, if convergence has not been reached, the model can still converge after the specified number of cycles. However, since it was not given the time to do so, it is not documented as a 'converged' scenario. It can also be seen that this does not hold for all number of cycles. At a certain point, the influence of the specified number of cycles becomes smaller. However, the number of cycles in which convergence can be reached remains an arbitrary threshold.

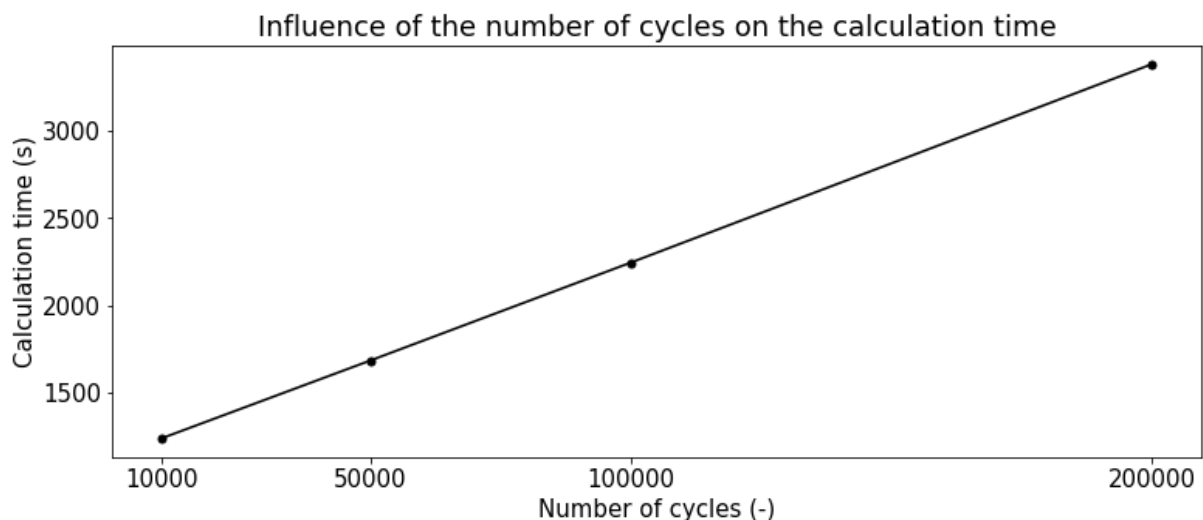


Figure 4.20: Effect of the number of cycles on the calculation time, for Model 2.

When looking at the influence of the number of cycles on the calculation time (Figure 4.20), it can be seen that the calculation time increases roughly linearly with the number of cycles.

## Mesh coarseness

The mesh coarseness has to do with the size of the tetrahedral elements that are used to represent the geometry of the rocks in the field. For very detailed geometry, with a low value for the average mesh edge length (AMEL), the mesh better represents the geometry of the rocks in the field. However, it also takes much more time to calculate the model results. Due to computational limitations, the most detailed model that was run, was the model with an AMEL of 0.05 m. However, even then, the mesh had to be run with a 'smart mesh', meaning that the geometry on the surface of the rocks had the same level of detail, but that the elements on the inside of the mesh were more coarse. Creating bigger elements on the inside of the mesh reduces the number of grid points in the model, and thereby the calculation time.

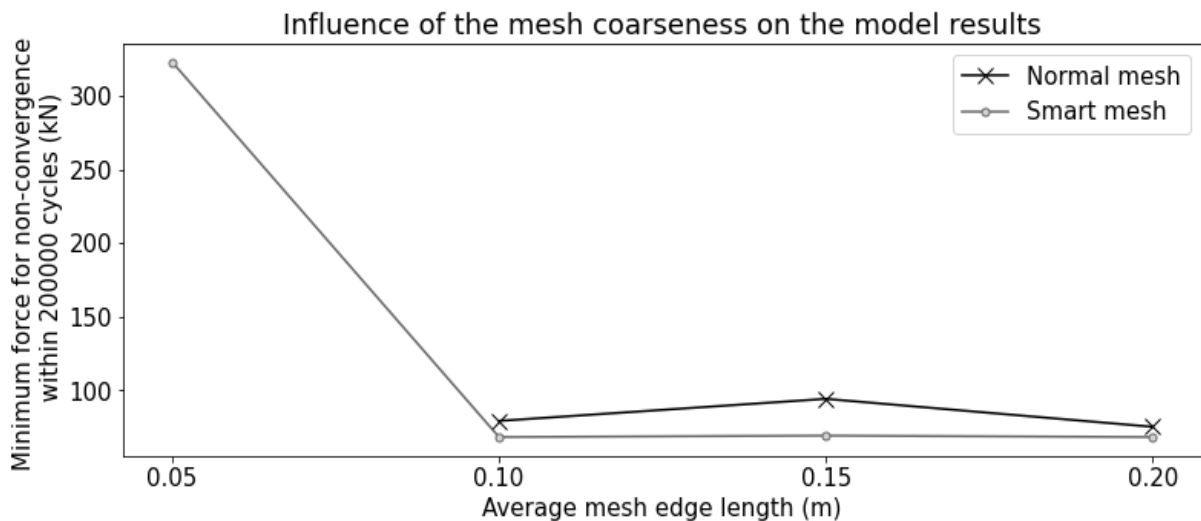


Figure 4.21: Effect of the mesh coarseness on the minimum force for model non-convergence, for Model 2.

First of all, it can be seen in Figure 4.21 that there is a difference between the normal mesh and the smart mesh model results. When using the smart mesh, the results seem to be consistently smaller than for the normal mesh. This means that the smart mesh results in less stable, thus more conservative predictions. This difference is the largest for the mesh with an AMEL of 0.15 m, with a difference of 15 kN. In Section 2.4.4.1, it was found that the geometry of the normal and smart meshes is the same on the outside surface of the rocks. This means that the meshing method should have a limited influence on the model results. However, when observing the rock configuration before and after modelling Phase 1 (equilibrium under gravity, but no additional force), it was visually found that there is little difference between the rocks before modelling Phase 1, but a distance between the meshes of up to centimeters after modelling Phase 1 (see Figure 4.22). This means that the starting position of the rock configurations is different for the two types of meshes, and therefore the model results are likely to be different. It was also observed that the number of cycles of modelling Phase 1 before model convergence is different for the different mesh types (see Table 4.4). The cause of this difference in model results after Phase 1 is not easily determined. One potential explanation could be in the calculation of the unbalanced force ratio. Modelling Phase 1 is run until convergence, meaning that the unbalanced force ratio is lower than a set threshold. The unbalanced force is calculated over all grid points. However, since the smart mesh contains fewer grid points, the calculation results are also likely to be a little different, meaning that the model is stopped after a different number of cycles with a different rock configuration.

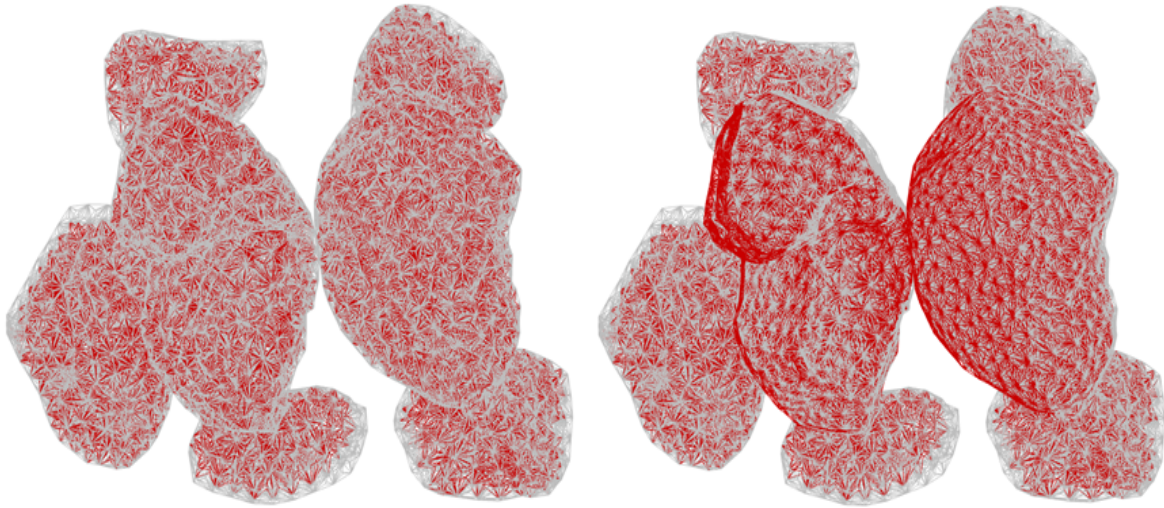


Figure 4.22: Meshes before (left) and after (right) modelling Phase 1, for an AMEL of 0.15 m. The normal mesh is depicted in grey and the smart mesh in red. It can be observed that the locations of Rock 3 and 6 are slightly different for the two mesh types after modelling Phase 1.

Average mesh edge length (m)	Number of cycles before convergence is reached in Phase 1 (-)	
	Normal mesh	Smart mesh
0.05	-	155,101
0.10	167,332	171,131
0.15	114,176	122,350
0.20	130,567	123,946

Table 4.4: Number of cycles before convergence is reached, for different AMELs and mesh types.

The second point in question, based on Figure 4.21, is the very high value for the minimum force for non-convergence for the mesh with an AMEL of 0.05 m. The minimum force for non-convergence is 323 kN for this mesh, while it is 68/69 kN for the other AMELs with smart meshes. It was expected that the value for the mesh with an AMEL of 0.05 m would be much closer to the values of the other meshes. This problem is in a way similar to the rectangular block on two rectangular supports model. In this analysis, it was found that the meshes with an AMEL of 0.05 gave similar results to the meshes with AMELs of 0.10, 0.15 and 0.20 m. For this reason, it could be argued that the cause of the deviancy in the results for the mesh with an AMEL of 0.05 m is in the geometry of the rocks. In light of this observation, two potential causes of this large difference have been identified: the difference in the rock configuration after modelling Phase 1 due to the different geometry of the rocks and the difference in the failure mechanism due to the different rock configurations.

As was found in Section 2.4.4.1, the geometry of the meshes made with different subsampling distances is slightly different. A different geometry can lead to a different model result. This can also be seen in Figure 4.23, in which the difference between the locations of the rocks before and after modelling Phase 1 can be observed for the normal meshes with an AMEL of 0.10 and 0.20 m. It was found that a different mesh coarseness results in a slightly different rock configuration. The rock configuration of the meshes with an AMEL of 0.05 m is also very different after Phase 1 compared to the coarser meshes (see Figure 4.24). This is because Rock 3 does not touch Rock 4 for the meshes with an AMEL of 0.05 m after Phase 1. The reason for the difference in rock configuration after Phase 1 is in all likelihood caused by the difference in geometry, and more specifically, by the geometry near the contact point between Rock 3 and Rock 1, since this is a very irregular geometry.

However, not only the geometry and configuration of the rocks is different for the mesh with an AMEL of 0.05 m. The different rock configuration after Phase 1 also leads to a different failure mode when the force is applied in Phase 2 (see Figure 4.25). The failure mode of the meshes with AMEL 0.05 m can be described as follows. Rock 3 is pushed against Rock 6 while being locked by Rock 1, which causes a vertical rotation of Rock 3 and Rock 6. Rock 3 rotates with its east side downwards and its west side upwards, while Rock 6 is rotated with its east side upwards and its west side downwards. This vertical rotation is similar to what occurs for the other meshes. At a certain point, Rock 3 has sufficiently been moved westwards that it begins to touch Rock 4. Then, it loses contact with Rock 2 after which horizontal rotation is initiated. This horizontal rotation is due to the fact that Rock 6 is a bit rounded on the side of Rock 3. So when Rock 3 is pushed against it, it starts to rotate. This horizontal rotation is observed much less significantly in the failure mechanism for the other models.

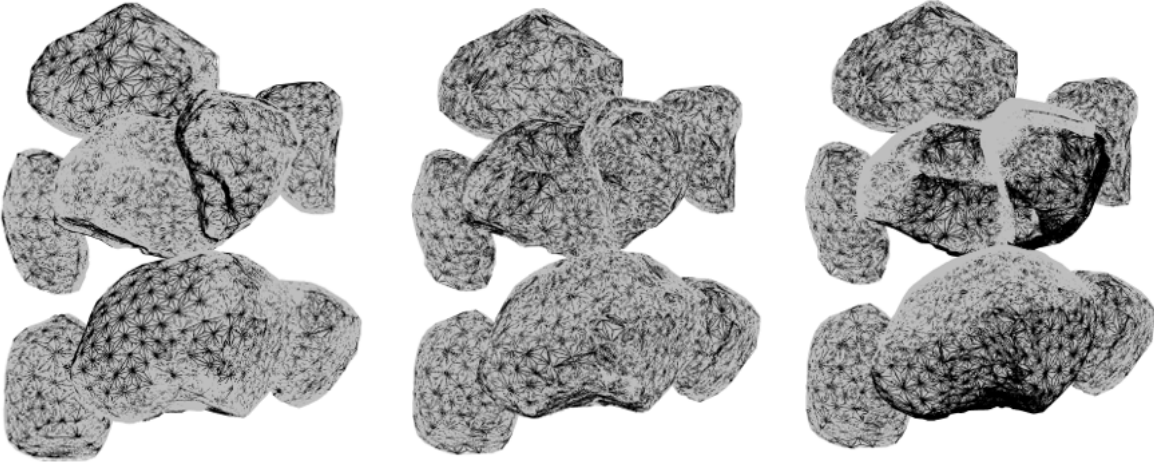


Figure 4.23: Meshes before (left) and after (middle) Phase 1, and after Phase 2 (right). The meshes were made with an AMEL of 0.10 (grey) and 0.20 m (black). The force that was applied was 68 kN for both models. It can be observed that there generally are large differences between the rock configurations, and especially after Phase 2.

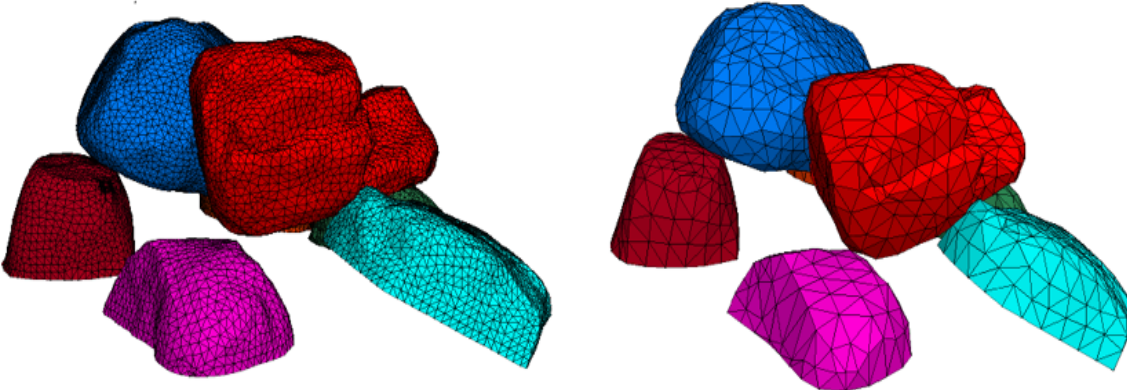


Figure 4.24: Comparison between the rock configuration for the meshes with AMEL 0.05 m (left) and 0.20 m (right) after Phase 1. The main difference is that Rock 3 is not touching Rock 4 for the meshes with an AMEL of 0.05 m.

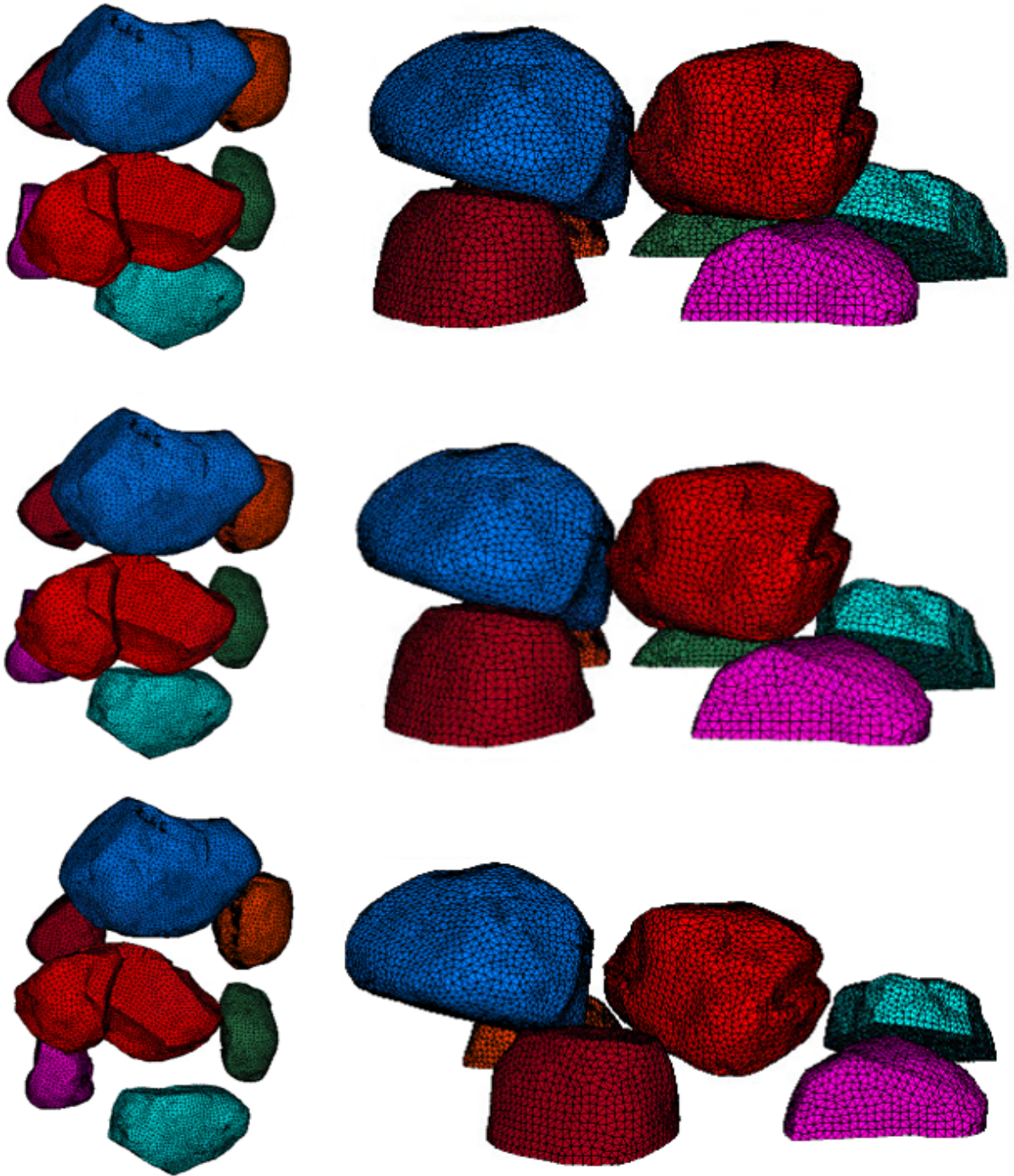


Figure 4.25: Figures of the failure mode of the models with an AMEL of 0.05 m, from different perspectives. The captures were taken at 100000 cycles (top), 125000 cycles (middle) and 150000 cycles (bottom). The pushing force was 323 kN. It can be seen that Rock 3 and 6 move in the direction of pushing. Furthermore, the horizontal rotation of Rock 3 can clearly be observed over time.

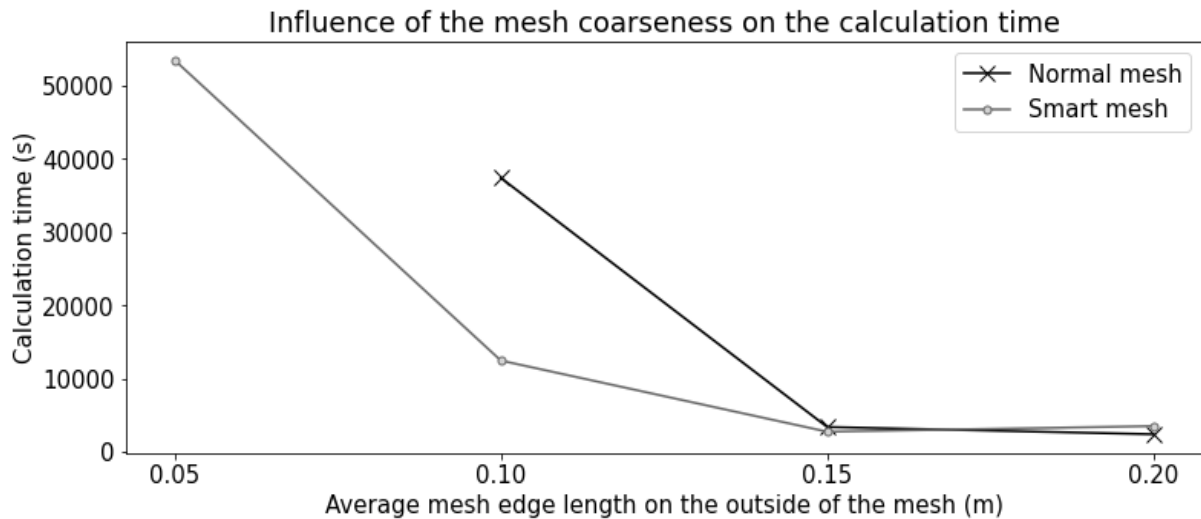


Figure 4.26: Effect of the mesh coarseness on the calculation time, for Model 2.

When comparing the mesh coarseness in terms of calculation time, it can be found that an AMEL of 0.05 m greatly increases the calculation time, compared to an AMEL of 0.10 or 0.20 m (see Figure 4.26). This is mostly because more grid points are used in the models with a more refined mesh, and therefore it takes more time to calculate the forces and displacements in all of these points. Furthermore, it can be observed that the smart mesh saves calculation time for the detailed model with an AMEL of 0.10 m. This is because fewer grid points are present in the smart meshes, which means that fewer points need to be calculated during each time step.

### Friction angle

The friction angle of the interfaces between the rock blocks was elaborately discussed in Chapter 3. The value for the friction angle used to determine the minimum force of non-convergence of Model 2 was  $30^\circ$ , but this value was varied in this sensitivity analysis with steps of  $10^\circ$ .

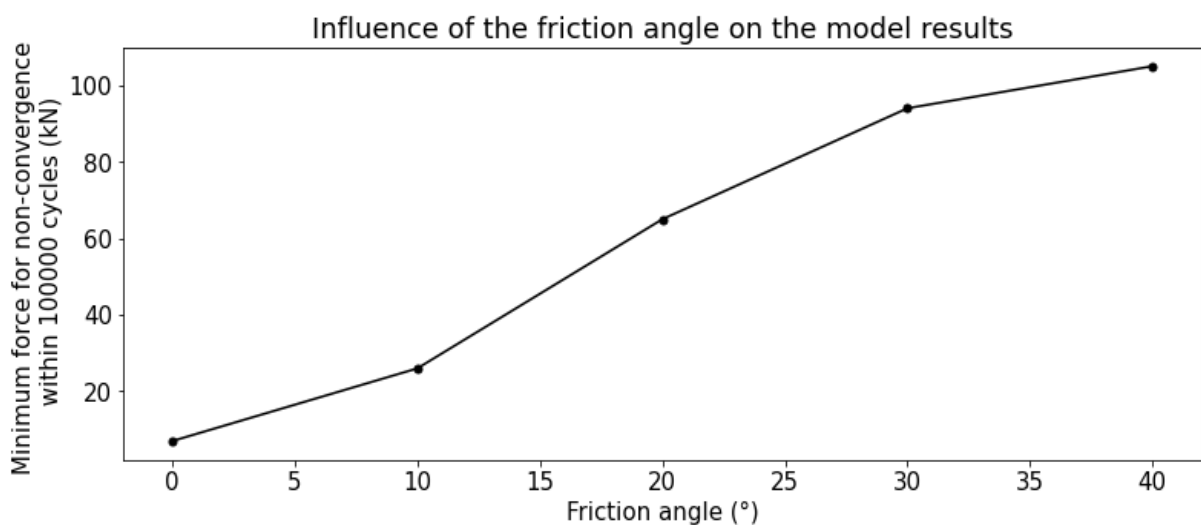


Figure 4.27: Effect of the mesh coarseness on the minimum force for model non-convergence, for Model 2. The AMEL was 0.15 m.

It can be observed in Figure 4.27 that there is a significant increase of the minimum force for model convergence with an increasing friction angle. This is expected since a high friction angle causes more resistance against sliding, and therefore, a higher force can be applied before instability occurs. The failure mode seems to be similar for all values of the friction angle. The friction angle did not have a significant influence on the calculation time of the model.

## 4.5 Conclusion

The goal of this chapter was to find out how potential reconstruction scenarios for dolmen D14 should be digitally analyzed on their stability, while considering the computational limitations of numerical models. Numerical models were analyzed with 3DEC to investigate how this should be done. These models were either in 2D or in 3D, but aimed to investigate the response of a block or rock when a force is applied to it.

The following 2D models were analyzed: a rectangular block on a slope, a rectangular block on two rectangular supports and 2D models of the megalith at the contact between Rock 3 and Rock 2, and between Rock 3 and Rock 4. From the results of the rectangular block on a slope model, it can be concluded that the analytical results are in line with the numerical results as calculated with 3DEC. The rectangular block on two rectangular supports was analyzed in order to investigate the influence of the type of mesh (normal/smart mesh) and mesh size (average mesh edge length (AMEL) of 0.05, 0.10, 0.15, 0.20 or 0.25m) on the model results. It was found that the mesh type, as well as the AMEL, does not influence the model results much. The 2D dolmen models were investigated in order to find a first range of values for the minimum force to cause failure, being between 0.7 and 12.0 kN.

When looking at the 3D megalith analysis, the most important values are those found for the required force for model non-convergence. It was decided not to use displacements as a marker of stability, since the displacements that 3DEC calculates are calculated with artificial damping constant as well as artificial stiffness values in normal and shear directions. It was found that the required force for failure was 2 kilonewtons for Model 1, and 94 kilonewtons for Model 2, when using a coarse mesh with an average mesh edge length of 0.15 m. This shows that Model 2 is much more stable than Model 1 for the conditions under research. This was expected based on the different rock configurations, due to the interlocking effect that is created by the repositioning of Rock 1 and Rock 6 in Model 2.

A sensitivity analysis was performed for Model 2 to analyze the effect of the model parameters on the model results. This was done for the number of cycles within which convergence should be reached, the mesh coarseness and the friction angle. It was found that for a higher number of cycles, within which convergence should be reached, the minimum force for non-convergence within the specified number of cycles increases. This is because convergence takes time and for a high force, more time is required for convergence. However, the results seemed to flatten out, which indicates that there is a number of cycles for which the minimum force for model convergence does not increase. Furthermore, a greater number of cycles increases the calculation time approximately linearly.

The mesh coarseness is quantified by the average mesh edge length (AMEL). Furthermore, smart meshes were created in order to decrease the calculation time of the model. It was found that for a normal mesh, the minimum force for model non-convergence was slightly higher compared to the smart mesh. This can likely be explained by the way in which the unbalanced force ratio is calculated. A different number of grid points at different locations will lead to a different unbalanced force ratio for the model, since this is an average value of all grid points in the model. Furthermore, it was found that the model results were very different for the model with an AMEL of 0.05 m (323 kN), compared to the models with an AMEL of 0.10, 0.15 or 0.20 m (68/69 kN). Two potential causes for this have been identified: the difference in the rock configuration after modelling Phase 1 due to the different geometry of the rocks, and the difference in the failure mechanism due to the different rock configurations. This implies that it is crucial to work with the most refined mesh as possible

when conducting the numerical analyses, to best represent the geometry of the rocks in the field. Furthermore, it means that when repositioning the rocks in the field, small deviations in the rock position can have a large effect on the stability of the rocks. Additionally, it was found that a coarser mesh greatly reduces the calculation time. Doubling the AMEL of a mesh, can lead to a decrease in the calculation time of approximately 75%.

Lastly, the friction angle was found to have a significant impact on the model results. For a higher friction angle value, the minimum force for non-convergence becomes larger and the model thus becomes more stable. This can be explained by that the friction angle is an important parameter contributing to the shear strength of the rock joint. The failure mode was found to be very similar for different values of the friction angle.

The previous findings give more insight into how potential reconstruction scenarios should be assessed on their stability. Some parameters were found to have a significant impact on the model results. Nonetheless, it should be clear that more research is necessary to be able to analyze what the most optimal potential reconstruction scenario would be for dolmen D14.

## Chapter 5

# Conclusion

The goal of this research was to investigate how potential reconstruction scenarios for dolmen D14 could be evaluated on their stability. This was done in response to the dislocation of capstone Rock 3 in the spring of 2019, after which the Rijksdienst Cultureel Erfgoed asked TU Delft to investigate new (digital) techniques to assess potential reconstruction scenarios. On the basis of this request, the following research question was formulated:

*How can dolmen D14, focusing around the dislocated capstone Rock 3, be reconstructed to a stable configuration of rocks while also conforming to the demands from the relevant dolmen management agencies?*

The research was split up into three parts: the development of a geometrically accurate 3D model, the non-destructive examination of rock parameters and the digital stability analysis. The conclusion will be split up accordingly.

### 5.1 Creating geometrically accurate 3D meshes

The first step in order to be able to numerically analyze potential reconstruction scenarios for the dolmen is to develop models that accurately represent the geometry of the rocks. Therefore, this part of the thesis aimed at answering the following research sub-question:

*How can a model be created, which (1) accurately documents the geometry of all individual rocks in the zone of interest and (2) is suitable for digital stability analysis?*

This research question contains two elements, and different models are most suitable to fit either of these requirements. For the accurate documentation of the geometry, it was found that a detailed mesh based on a subsampling distance of the point cloud of 1 mm is most suitable, while a model that is best suitable for digital stability analyses should be made with a subsampling distance of 50 mm. This larger subsampling distance is required because of the computational limitations in terms of memory that are inherent to using a common desktop when conducting numerical analyses. A larger subsampling distance results in a coarser mesh, and thereby in a smaller file size. Nonetheless, the creation of the geometrical models that satisfy either requirement generally follows the same four steps: the acquisition of point cloud data, point cloud pre-processing, mesh generation and mesh evaluation. These four steps, and the findings from these steps will be further illustrated below.

The point cloud data was acquired with a large, accurate TLS scanner and a smaller, slightly less

accurate BLK scanner. The BLK scanner was mostly put to use in the narrow spaces, which the TLS scanner could not capture due to its large size. It turned out to be difficult to check whether all surfaces of the dolmen have been captured and the level of accuracy with which this was done in the field. This was difficult, because some of the rock surfaces were so close to each other that the laser scanner could not reach them. Apart from the point cloud data that was acquired in the field, additional data was used from GIA (2017). This point cloud data was collected before the dislocation of Rock 3, and is therefore able to describe the rock surface of Rock 3 that is currently lying on the ground.

The second step in creating a 3D model is pre-processing point cloud models so that a mesh can be generated in the next step. The pre-processing step should be approached with consideration, since it involves decisions about which data source to use and also what data can be deemed reliable, and what data should be considered to be noise. The main take-away of this step is that it was found that it is best to prevent overlap in the point cloud surfaces of different sources, such as the TLS and BLK. There is generally a small offset between two different point clouds, and this creates inaccuracies in the final meshes, especially for detailed point clouds. Although alignment algorithms can be very good, it remains hard to avoid all offset between point clouds.

The third step in creating the 3D models is to actually generate the meshes on the basis of the pre-processed point clouds and modify the meshes in such a way that they can be imported into 3DEC. The biggest take-away from this step was that there are significant computational limitations as to the size of the files that meshing software can handle. It was found that subsampling of the point clouds is required to be able to create 3D meshes. For the purpose of structural stability calculations, a subsampling distance of the points below 1 mm is not needed. Small scale surface roughness can be captured in contact surface models such as the Zhao (1997a; 1997b) model. The maximum coarseness of the meshes is thought to depend on the sensitivity of the results of the stability analysis.

Mesh evaluation was the last step in creating the models. Mesh evaluation was done both qualitatively, by observations, and quantitatively, through point-to-mesh distance (PMD) analyses. Several anomaly zones have been detected in the point clouds: the circular mark on top of Rock 1 and surfaces with missing data on Rock 1 (North), Rock 1 (South), Rock 2 (South), Rock 5 (South) and Rock 7 (North). These anomalies in the point clouds, may or may not have a significant impact on the meshes of the rocks, but their impact is most profound for the refined meshes. Furthermore, it was found that the mean Euclidean PMD is in the order of 0.1-1 mm for all rocks after meshing Step 3.4, which is deemed sufficiently accurate for the stability calculations. Also, it was found that the fit of the meshes to the original point clouds become less good when the meshes become more coarse.

## **5.2 Non-destructive examination of rock contact surface parameters**

The second step in order to be able to do digital stability analysis is to estimate the required rock parameters for the rocks in the field. To this end, the following research sub-question was formulated:

*How can the relevant rock parameters, contributing to the shear strength of the rock contact surfaces between the rocks, be determined?*

Numerical analyses only work when they are performed with values that represent the reality in the field. It was determined, based on a literature study, that the shear strength model of Zhao (1997a; 1997b) could best be used to represent the non-matching rock contact areas. In this research part, the focus was on determining the parameters that were required for this criterion. It is common practice to take samples from the field and then test these in the laboratory to obtain the values for rock

parameters. However, this is a destructive method and would bring great harm to the rocks under analysis, which was not allowed by the relevant dolmen management agencies. Therefore, the focus has been on non-destructive methods in this examination of the rock parameters. Tests have been performed in the field with non-destructive methods and in the laboratory on samples with assumed similar characteristics.

In the field, it was found that the JRC parameter could be determined easily with a carpenter's comb. On the contrary, the JCS parameter was much harder to determine. The JCS is usually obtained with a Schmidt hammer. However, this was found to leave indentation marks on the rocks, and therefore, this method was deemed too destructive. Another way of obtaining the JCS value is by means of the Equotip. The Equotip was found to give results that were low compared to literature, and very variable. Based on these results, it should be concluded that the Equotip should not be used on such rough surfaces as the rock surfaces in the field. Instead, JCS values could be obtained with a Schmidt hammer on analog samples to the rocks in the field or by taking values from the literature.

In the laboratory, two different tests were performed in order to get an estimate of the residual friction angle of the rocks in the field. The tilt test was found to give a reliable result for the basic friction angle of  $33^\circ$ , in line with literature. The basic friction angle is usually higher than the residual friction angle. The second test was the Golder shear box test. This test was performed on a flat sand-blasted sample and on a rough, tensile-split sample. Both samples were internally weathered to some extent. It was found that only the flat sample results in reliable results, in line with literature. The test indicated a residual friction angle of  $30^\circ$ . This value is assumed to be representative for the friction angle of the non-matching partially weathered contact surfaces between the caprocks and their support rocks in the field. A sensitivity analysis was conducted to analyze the effect of variations of the interface friction angle on the magnitude of the minimum force that can destabilize Rock 3.

### 5.3 Numerical stability analyses

The last part of this study combines the previous two parts to conduct analyses that assess the stability of potential reconstruction scenarios for the dolmen. In this part, the focus was more on how stability analysis should be conducted, and what factors influence the model results, and less so on what potential reconstruction scenario would provide the most 'optimal' solution. The following research sub-question was formulated:

*How can potential reconstruction scenarios be digitally assessed on their stability, while considering the limitations inherent to digital analyses?*

Several analyses were performed with 3DEC in order to analyze the stability of the dolmen. This was done in 2D and 3D. Three 2D analyses were performed. From the rectangular block on a slope model, it was concluded that the analytical model results are in line with the numerical model results as calculated with 3DEC. The rectangular block on two supports model was used to investigate the effect of the mesh type (normal/smart) and average mesh edge length (AMEL) on the model results. A smart mesh has the exact same geometry as a normal mesh on the outside of the mesh, but has coarser elements on the inside of the mesh, which saves calculation time. The AMEL ranged from 0.05 m to 0.25 m. It was found that both model assumptions have little impact on the model results. Lastly, 2D dolmen models were investigated to get a first impression of the minimum force that is required to create an imbalance in the model. This was found to be between 0.7 and 12.0 kN for the scenario in which Rock 3 was placed back in the same position as it was in 2019.

Stability analyses were also done in 3D for two different reconstruction scenarios. Model 1, based on the configuration of the rocks as it was in 2019, was compared to Model 2, which configuration was based on the rocks as they were around 1925. The results were expressed in terms of the minimum

force for model non-convergence, with convergence calculated based on the unbalanced force ratio in all grid points in the model. It was found that the minimum force for non-convergence was 2 kN for Model 1, and 94 kN for Model 2, which indicates that the first model was significantly less stable than the second model. This can be explained by the interlocking effect due to the repositioning of Rock 1 and Rock 6 in Model 2.

Since many assumptions were made to arrive at this observation, a sensitivity analysis was performed for Model 2 to analyze the influence of these assumptions on the model results. This was done for the number of cycles within which convergence should be reached, the mesh coarseness and the friction angle of the rock discontinuities. It was found that an increase in the number of calculation cycles also results in an increase in the minimum force for model non-convergence. For a high number of cycles of up to 200000 cycles, the minimum force for model non-convergence stabilizes. Simultaneously, for an increase in the number of cycles, the calculation time increases almost linearly. From the mesh coarseness analysis, it was found that the minimum force for model non-convergence was generally higher for the normal mesh compared to the smart mesh. This difference is caused by the calculation of the unbalanced force ratio, which occurs in all grid points. When the grid points are different, the average unbalance force ratio will be different too. Furthermore, the mesh with an AMEL of 0.05 m was found to have a much larger minimum force for model non-convergence (323 kN) compared to the coarser meshes (68/69 kN). Two potential reasons have been identified: the different geometry of the rocks causes a different rock configuration, and the different rock configuration, in turn, leads to a different failure mechanism. Lastly, it was found that an increase in the friction angle causes an increase in the minimum force for model non-convergence.

## Chapter 6

# Recommendations

This study is a first step in analyzing non-destructive, digital methods for assessing the stability of potential reconstruction scenarios for dolmens. It is hoped that this research can provide guidance for future research into the non-destructive, digital assessment of the stability of megalithic monuments. Some recommendations for future research can be found below.

### 6.1 Creating geometrically accurate 3D meshes

With the help of laser scanners, point clouds and 3D meshes were developed that could be used as an input for the stability analyses. However, this was only done for the visible surface areas of the rocks. In future studies of (this) dolmen, it would be useful to include more geometrical information on the buried parts of the rocks, as this, too, is part of the stability of the structure (see for example Zijlstra, 2022). Furthermore, some anomalies have been identified in the geometrical models. These should be corrected for, which could be done by going back to the field. Another key point that was found during this research is that it is best to only use one dataset for each rock surface and prevent overlap between datasets, as potential misalignment can create inaccuracies in the meshes. The best procedure is to check for each surface what data is available and use the data with the highest accuracy first and only include data from other scanners to fill up areas with a low point density. This strategy was implemented for most rocks in this research, but some surfaces still had overlap of data, for example on top of Rock 1. For rock surfaces with missing point cloud data, other techniques such as photogrammetry could be used (see for example Van der Burg, 2021). Another way to better capture the rock surfaces could be to do data acquisition twice, the second time after checking the results of the first data acquisition round. Lastly, it is highly recommended to use a computer with large capacity in terms of memory for data handling. When working with point clouds, it is of essence that the computer is able to handle large data files, as this is required for point-cloud pre-processing and mesh generation.

### 6.2 Non-destructive examination of rock contact surface parameters

The relevant parameters for the Zhao (1997b) shear strength criterion were estimated using non-destructive methods to the rocks in the field. The JRC could be easily determined with a carpenter's comb in the field. However, it could also be interesting to look at whether this would be possible using the point cloud data or 3D meshes and if this would bear similar results, following an update of the approach of Khoshelham et al. (2011). Then, high resolution point clouds, with a subsampling distance in the order of 1 mm, would be required. The JCS parameter found in the field was low compared to the literature. This is because the impact point of the Equotip is not surrounded

with enough material, due to the roughness and the large size of the crystals. Another method to determine the JCS parameter is the Schmidt hammer test. Even though this test is too destructive to be performed on the rocks in the field, it could be performed on analog samples. Regarding the residual friction angle, it would be advised to use flat, sand-blasted samples and not rough, tensile-split samples for the Golder shear box test in future research. Furthermore, the rock samples that are tested in the laboratory and the rocks in the field should ideally be similar, especially considering the rock mineralogy, crystal sizes and degree of weathering. Since the residual friction angle is of most influence on the shear strength of the rock contact surfaces, it is best to focus most attention on the correct determination of this parameter.

### **6.3 Numerical stability analyses**

Using the geometrical models that were developed from point cloud data and the shear strength parameters that were found in the field and the laboratory, digital stability analyses could be conducted. The stability of the structure was evaluated based on the force required for non-convergence (instability) of the model. The displacements were not used as a measure of instability, because the displacements are calculated in 3DEC based on arbitrary stiffness and damping values. Since the reconstruction scenarios were only tested for one pushing force location and direction, it would also be highly recommended to expand this analysis to include different pushing force scenarios in order to be able to say what reconstruction scenario is truly the most stable. Additionally, it can be insightful to perform other calculations, such as finding out how humans can dislocate Rock 3. Other adaptations could include the (in)stability of the support stones or the effect of exfoliation surfaces and asperity crushing. Furthermore, it would be advised to use a more refined mesh in future research. In this study, the most refined mesh was based on a subsampled point cloud with a distance of 50 mm. A refinement of this subsampling distance up to 1 mm could greatly help in making the results closer to reality. However, it should be investigated whether a more refined mesh really has a great influence on the model results. In line with refining the meshes overall, it would be useful to refine the meshes mainly near the contact surfaces. This could save a lot of computational time. However, the impact of partial mesh refinement on the model results should also be checked. With coarse meshes, contact surfaces count a very limited number of elements. This might cause greater instability compared to refined meshes. Lastly, it was found that smart meshes, with an equal refinement on the outside of the mesh but more coarse elements on the inside of the mesh, have a limited effect on the model results. Therefore, it would be strongly recommended to use this type of meshes for future research in order to save computation time.

# References

- Alejano, L., González, J., & Muralha, J. (2012). Comparison of different techniques of tilt testing and basic friction angle variability assessment. *Rock Mechanics and Rock Engineering*, 45, 1023–1035.
- Alejano, L., Muralha, J., Ulusay, R., Li, C., Pérez-Ray, I., Karakul, H., ... Aydan, (2018). Isrm suggested method for determining the basic friction angle of planar rock surfaces by means of tilt tests. *Rock Mechanics and Rock Engineering*, 51, 3853–3859.
- Alshawabkeh, Y., Bal'awi, F., & Haala, N. (2010). 3d digital documentation, assessment, and damage quantification of the al-deir monument in the ancient city of petra, jordan. *Conservation and management of archaeological sites*, 12(2), 124–145.
- Aoki, H., & Matsukura, Y. (2008). Estimating the unconfined compressive strength of intact rocks from equotip hardness. *Bulletin of Engineering Geology and the Environment*, 67, 23–29.
- Bakker, J. (2010). *Megalithic research in the netherlands, 1547-1911*. Leiden: Sidestone Press.
- Bandis, S., Lumsden, A., & Barton, N. (1983). Fundamentals of rock joint deformation. *International Journal of Rock Mechanics, Mineral Science & Geomechanics*, 20(6), 249-268.
- Barton, N. (1971). A relationship between joint roughness and joint shear strength. In *Proceedings of symposium for rock fracture* (p. 1–8). Nancy, France.
- Barton, N. (1973). Review of a new shear-strength criterion for rock joints. *Engineering Geology*, 7(4), 287–332.
- Barton, N. (1999). General report concerning some 20th century lessons and 21st century challenges in applied rock mechanics, safety and control of the environment. In *Proceedings of the 9th isrm congress* (Vol. 3, p. 1659–1679,). Paris.
- Barton, N. (2013). Shear strength criteria for rock, rock joints, rockfill and rock masses: Problems and some solutions. *Journal of Rock Mechanics and Geotechnical Engineering*, 5, 249–261.
- Barton, N., & Choubey, V. (1977). The shear strength of rock joints in theory and practice. *Rock Mechanics Felsmechanik Mecanique des Roches*, 10, 1–54.
- Basu, A., Mishra, D., & Roychowdhury, K. (2013). Rock failure modes under uniaxial compression, brazilian, and point load tests. *Bulletin of Engineering Geology and the Environment*, 72(3), 457–475.
- Bayram, B., Nemli, G., Özkan, T., Oflaz, O., Kankotan, B., & Çetin, I. (2015). Comparison of laser scanning and photogrammetry and their use for digital recording of cultural monument case study: Byzantine land walls-istanbul. *ISPRS Annals of the Photogrammetry, Remote Sensing and Spatial Information Sciences*, 2(5), 17–24.

- Bekkema, M., Huisman, H., Balen, R., & Kluiving, S. (2014). Gidsgesteenten in hunebedden published. *Grondboor & Hamer: Nederlandsche Geologische Vereniging*, 68(4), 93–99.
- Bootsma, M. (2010). *Shear strength of the bremanger sandstone: Determining the basic friction angle using a golder direct shear box* (Bachelor thesis, TU Delft, Delft, the Netherlands). Retrieved from <http://resolver.tudelft.nl/uuid:10f1516c-2282-41f9-9f00-4eed1bcd8add>
- Brideau, M., Stead, D., Lipovsky, P., Jaboyedoff, M., Hopkinson, C., Demuth, M., ... Delaney, K. (2010). Preliminary description and slope stability analyses of the 2008 little salmon lake and 2007 mt. steele landslides, yukon. In K. MacFarlane, L. Weston, & L. Blackburn (Eds.), *Yukon exploration and geology* (p. 119–133).
- Clerinx, H. (2017). *Een paleis voor de doden*. Athenaeum - Polak & Van Genneep.
- Cloudcompare (version 2.11.3) [GPL software]. (2021). Retrieved from <http://www.cloudcompare.org/>
- Cloudcompare (version 2.12.alpha) [GPL software]. (2021). Retrieved from <http://www.cloudcompare.org/>
- Coulson, J. (1972). Shear strength of flat surfaces in rock. In E. Cording (Ed.), *Proceedings of the 13th symposium on rock mechanics* (p. 77–105). Urbana, Illinois.
- de Bruyn, I., Coulthard, M., Baczynski, N., & Mylvaganam, J. (2013). Two-dimensional and three-dimensional distinct element numerical stability analyses for assessment of the west wall cutback design at ok tedi mine, papua new guinea. In *Proceedings of the 2013 international symposium on slope stability in open pit mining and civil engineering* (p. 653–668). Perth.
- Du, S., Hu, Y., Hu, X., & Guo, X. (2011). Comparison between empirical estimation by jrc-jcs model and direct shear test for joint shear strength. *Journal of Earth Sciences*, 22(3), 411–420.
- Eberly, D. (1999). Distance between point and triangle in 3d. Retrieved from <https://www.geometrictools.com/Documentation/DistancePoint3Triangle3.pdf>.
- Feal-Pérez, A., & Blanco-Chao, R. (2013). Characterization of abrasion surfaces in rock shore environments of NW Spain. *Geo-Marine Letters*, 33, 173–181.
- Georgopoulos, A. (2014). 3d virtual reconstruction of archaeological monuments. *Mediterranean Archaeology & Archaeometry*, 14(4), 155–164.
- Golder Associates. (1984). *Instruction manual for golder associates direct shear box*. Berkshire, England.
- González, J., González-Pastoriza, N., Castro, U., Alejano, L., & Muralha, J. (2014). Considerations on the laboratory estimate of the basic friction angle of rock joints. In *Conference: Rock engineering and rock mechanics: Structures in and on rock masses - proceedings of eurock 2014* (p. 199–204). ISRM European Regional Symposium.
- Groningen Institute of Archaeology (GIA). (2017). *D14 - Eexterhalte* [3D model]. Retrieved from <https://sketchfab.com/3d-models/d14-eexterhalte-1c9b0754c219453393b9fd58409782e2>
- Hencher, S., & Richards, L. (2014). Assessing the shear strength of rock discontinuities at laboratory and field scales. *Rock Mechanics and Rock Engineering*, 48, 883–905.
- Hoppe, H., DeRose, T., Duchamp, T., McDonald, J., & Stuetzle, W. (1992). Surface reconstruction

- from unorganized points. In *Proceedings of the 19th annual conference on computer graphics and interactive techniques* (p. 71–78).
- Hunebeddencentrum. (2018). *Hunebed d26 reconstructie* [Photograph]. Retrieved from <https://www.hunebeddencentrum.eu/wp-content/uploads/2018/03/Hunebed-D26-reconstructie.jpg>
- Irfan, T., & Powell, G. (1991). *Georeport no. 8: Foundation design of caissons on granitic and volcanic rocks*. Hong Kong: Geotechnical Engineering Office, Civil Engineering Dept., Hong Kong.
- Itasca Consulting Group, Inc. (n.d.). *Mohr-Coulomb Joint model in 3DEC* [Figure]. Retrieved from <http://docs.itascacg.com/3dec700/3dec/docproject/source/theory/mohrcoulomb/mohrcoulomb.html?node2094>.
- Itasca Consulting Group, Inc. (2013). *3DEC version (7.00.141)* [software].
- Itasca Consulting Group, Inc. (2020). *Griddle version (2.00.8)* [software].
- Kazhdan, M., Bolitho, M., & Hoppe, H. (2006). Poisson surface reconstruction. In *Proceedings of the fourth eurographics symposium on geometry processing* (Vol. 7).
- Kazhdan, M., & Hoppe, H. (2013). Screened poisson surface reconstruction. *ACM Transactions on Graphics*, 32(3), 1–13.
- Khoshelham, K., Altundag, D., Ngan-Tillard, D., & Menenti, M. (2011). Influence of range measurement noise on roughness characterization of rock surfaces using terrestrial laser scanning. *International Journal of Rock Mechanics and Mining Sciences*, 48, 1215–1223. doi: 10.1016/j.ijrmms.2011.09.007
- Ladanyi, B., & Archambault, G. (1970). Simulation of shear behaviour of a jointed rock mass. In *Proceedings of the 11th u.s. symposium for rock mechanics* (p. 105–125). New York.
- Leica Geosystems. (2017a). *Blk 360 product specifications*. Retrieved from [https://shop.leica-geosystems.com/sites/default/files/2019-04/blk360\\_spec\\_sheet\\_2\\_0.pdf](https://shop.leica-geosystems.com/sites/default/files/2019-04/blk360_spec_sheet_2_0.pdf)
- Leica Geosystems. (2017b). *Leica scanstation p30/p40 product specifications*. Retrieved from [https://w3.leica-geosystems.com/downloads123/hds/hds/general/brochures-datasheet/Leica\\_ScanStation\\_P30-P40\\_Plant\\_DS\\_en.pdf](https://w3.leica-geosystems.com/downloads123/hds/hds/general/brochures-datasheet/Leica_ScanStation_P30-P40_Plant_DS_en.pdf)
- Lim, S., & Haron, H. (2014). Surface reconstruction techniques: a review. *Artificial Intelligence Review*, 42(1), 59–78.
- McNeel, R. & Associates. (2021). *Rhinoceros 3D version (6.34.21034.7001)*. [software].
- Meshlab (version 2020.12)* [GPL software]. (2020). Retrieved from <https://www.meshlab.net/>
- Meulenkamp, F., & Alvarez Grima, M. (1999). Application of neural networks for the prediction of the unconfined compressive strength (ucs) from equotip hardness. *International Journal of Rock Mechanics and Mining Sciences*, 36, 29–39.
- Mononen, S., Kuula, H., & Lamberg, M. (2013). Slope stability analysis at siilinjärvi mine. In *Proceedings of the 2013 international symposium on slope stability in open pit mining and civil engineering, australian centre for geomechanics* (p. 707–718). Perth.
- Motsa, S., Drosopoulos, G., Stavroulaki, M., Maravelakis, E., Borg, R., Galea, P., ... Stavroulakis,

- G. (2020). Structural investigation of Mnajdra megalithic monument in Malta. *Journal of Cultural Heritage*, 41, 96-105.
- Muñiz-Menéndez, M., González-Gallego, J., Moreno-Robles, J., Pérez-Rey, I., Alejano, L., & Riquelme, A. (2020). Stability analysis of balanced boulders: Methodology and case study. In *ISRM International Symposium - EUROCK*.
- Neubauer, W., Doneus, M., Studnicka, N., & Riegl, J. (2005). Combined high resolution laser scanning and photogrammetrical documentation of the pyramids at giza. In *CIPA XX International Symposium* (p. 470–475).
- Nurunnabi, A., West, G., & Belton, D. (2015). Robust methods for feature extraction from mobile laser scanning 3d point clouds. *Research@ Locate*, 15, 109–120.
- Patton, F. (1966). Multiple modes of shear failure in rock. In *Proceedings of the first ISRM Congress* (p. 509–513). Lisbon.
- Pérez-Rey, I., Alejano, L. R., Riquelme, A., & González-deSantos, L. (2019). Failure mechanism and stability analyses of granitic boulders focusing a case study in Galicia (Spain). *International Journal of Rock Mechanics and Mining Sciences*, 119, 58–71.
- Pérez-Rey, I., Muñiz Menéndez, M., González, J., Vagnon, F., Walton, G., & Alejano, L. (2021). Laboratory physical modelling of block toppling instability by means of tilt tests. *Engineering Geology*, 282, 1-16.
- Rodríguez-Miranda, A., Pérez-Vidiella, P., Fernández-Eraso, J., Mujika-Alustiza, J., & Valle-Melón, J. (2017). 3d modelling in the registration and restoration of a megalithic tomb. In *ISPRS - International Archives of the Photogrammetry, Remote Sensing and Spatial Information Sciences* (Vol. 42, p. 297–304).
- RTV Drenthe. (2019). *De achterste deksteen is van het hunebed* [Photograph]. Retrieved from <https://www.rtvdrenthe.nl/nieuws/146769/Deksteen-van-Hunebed-D14-bij-Eexterhalte-gevallen>
- Singh, B., & Goel, R. (2011). *Engineering rock mass classification: Tunneling, foundations, and landslides*. Burlington, MA: Butterworth-Heinemann.
- Smed, P., & Ehlers, J. (2002). *Steine aus dem norden: Geschiebe als zeugen der eiszeit in nord-deutschland* (2nd ed.). Stuttgart: Borntraeger.
- Tapete, D., Casagli, N., Luzi, G., Fanti, R., Gigli, G., & Leva, D. (2013). Integrating radar and laser-based remote sensing techniques for monitoring structural deformation of archaeological monuments. *Journal of Archaeological Science*, 40(1), 176–189.
- Ten Anscher, T. (2020). *Hunebed d14-eexterhalte, een aanzet voor een hunebedbiografie met speciale aandacht voor deksteen d9*. [RAAP 4112].
- Van der Burg, L. (2021). *Combining point clouds from different sensors to create a 3d mesh of a rock surface* (Bachelor thesis). TU Delft, Delft, the Netherlands.
- Varughese, A., Rathod, G., & Rao, S. (2010). 3d stability analysis of chenab bridge abutments. In *Indian geotechnical conference* (p. 775–778).
- Verhoef, P., Kuipers, T., & Verwaal, W. (1984). The use of the sand-blast test to determine rock durability. *Bulletin of the International Association of Engineering Geology*, 29, 457–461.

- Verwaal, W., & Mulder, A. (1993). Estimating rock strength with the equotip hardness tester. *International Journal of Rock Mechanics and Mining Sciences & Geomechanics Abstracts*, 30(6), 659–662.
- Vosselman, G., & Maas, H. (2010). *Airborne and terrestrial laser scanning*. Whittles Publishing. Retrieved from <https://app.knovel.com/hotlink/pdf/id:kt00BRXVN3/airborne-terrestrial/laser-scanning-technology>
- Wei, O., Chin, C., Majid, Z., & Setan, H. (2010). 3d documentation and preservation of historical monument using terrestrial laser scanning. *Geoinformation Science Journal*, 10(1), 73–90.
- Woo, I., Fleurisson, J., & Park, H. (2010). Influence of weathering on shear strength of joints in a porphyritic granite rock mass in jechon area, south korea. *Geosciences Journal*, 14, 289–299.
- Zandstra, J. (1988). *Noordelijke kristallijne gidsgesteenten*. Leiden: E.J. Brill.
- Zandstra, J. (1999). *Platenatlas van noordelijke kristallijne gidsgesteenten*. Leiden: Backhuys Publishers.
- Zhao, J. (1997a). Joint surface matching and shear strength. part a: Joint matching coefficient (jmc). *International Journal of Rock Mechanics, Mineral Science*, 34(2), 173–178.
- Zhao, J. (1997b). Joint surface matching and shear strength. part b: Jrc-jmc shear strength criterion. *International Journal of Rock Mechanics, Mineral Science*, 34(2), 179–185.
- Zijlstra, M. (2022). *Assessment of the burial depth of a megalithic structure by means of geophysical models* (Master thesis, under preparation). TU Delft, Delft, the Netherlands.

## Appendix A

# Leica scanners product specifications

	Leica P40 terrestrial laser scanner (Leica Geosystems, 2017a)	Leica BLK360 scanner (Leica Geosystems, 2017b)
Range	Up to 270 m	0.6 – 60 m
3D point accuracy	3mm @ 50m / 6mm @ 100m	6mm @ 10m / 8mm @ 20m
Point measurement rate	Up to 1,000,000 points/second	360,000 points/second
Wavelength	1550 nm / 658 nm	830 nm

Table A.1: Characteristics of the Leica scanners that were used to capture point cloud data.

## Appendix B

# Figures of modelling Step 2: Point cloud pre-processing

In this appendix, the steps for creating point cloud models will be illustrated. For an explanation of the steps, see Section 3.2: Point cloud pre-processing.

### 2.1 Crop TLS and BLK data to the zone of interest (ZOI).

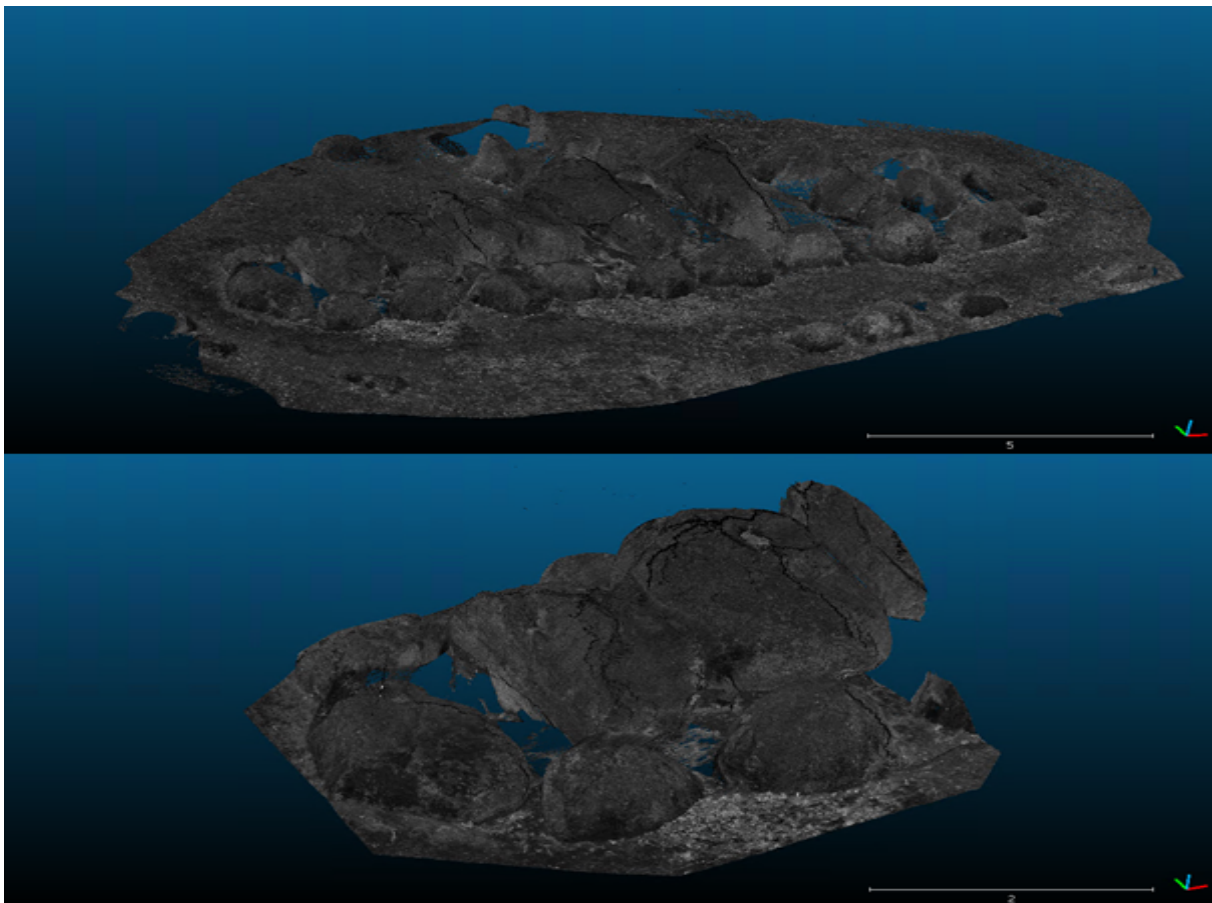


Figure B.1: Illustration of point cloud modelling Step 2.1: cut the TLS and BLK data to the ZOI. The scale of the figure is indicated in meters.

## 2.2 Align BLK data to TLS data set.



Figure B.2: Illustration of point cloud modelling Step 2.2: Align BLK data to TLS data set. The scale of the figure is indicated in meters.

### 2.3 Clean the data sets.

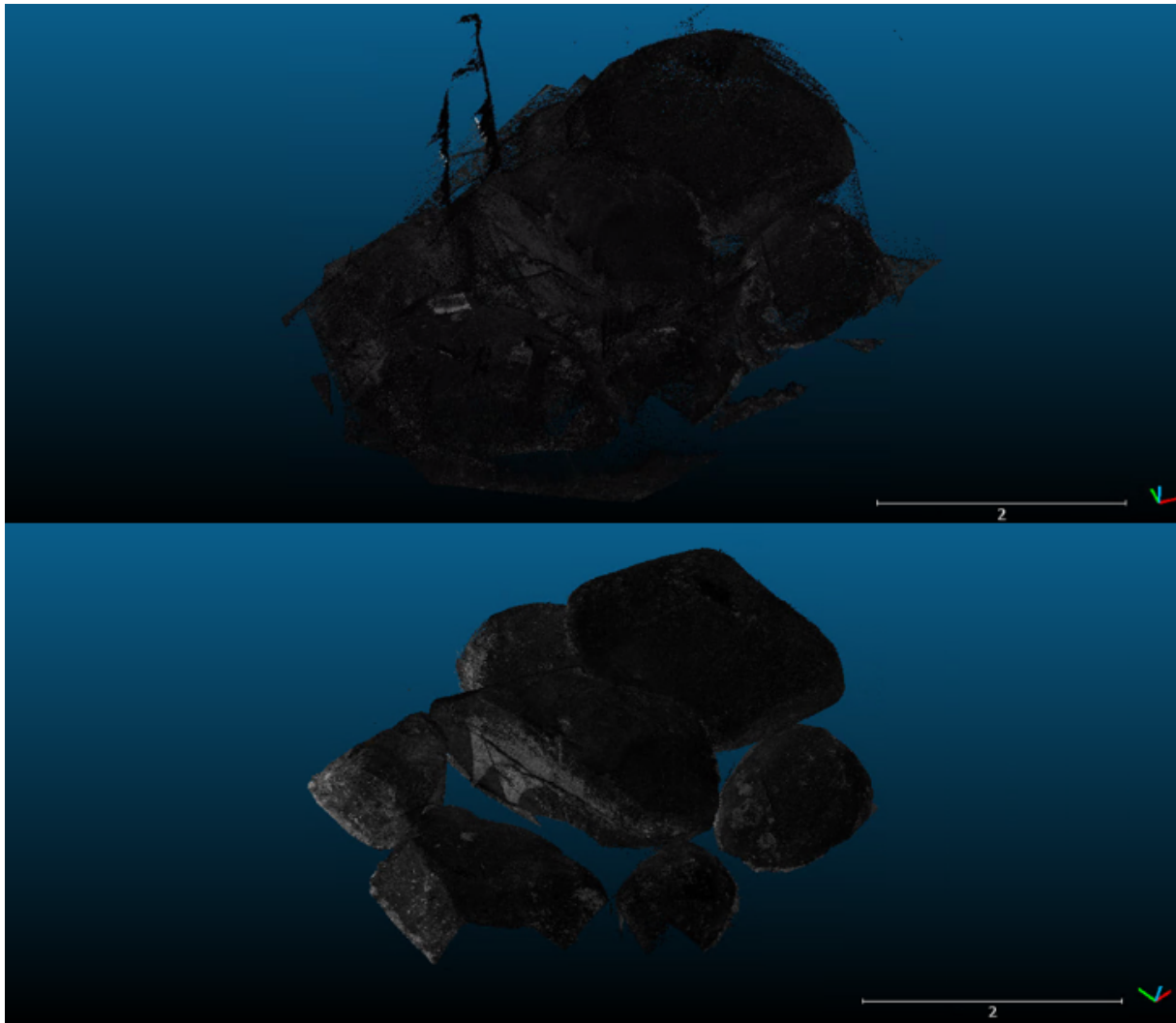


Figure B.3: Illustration of point cloud modelling Step 2.3: Clean the data sets. The scale of the figure is indicated in meters.

2.4 *Make separate models for the rocks.*

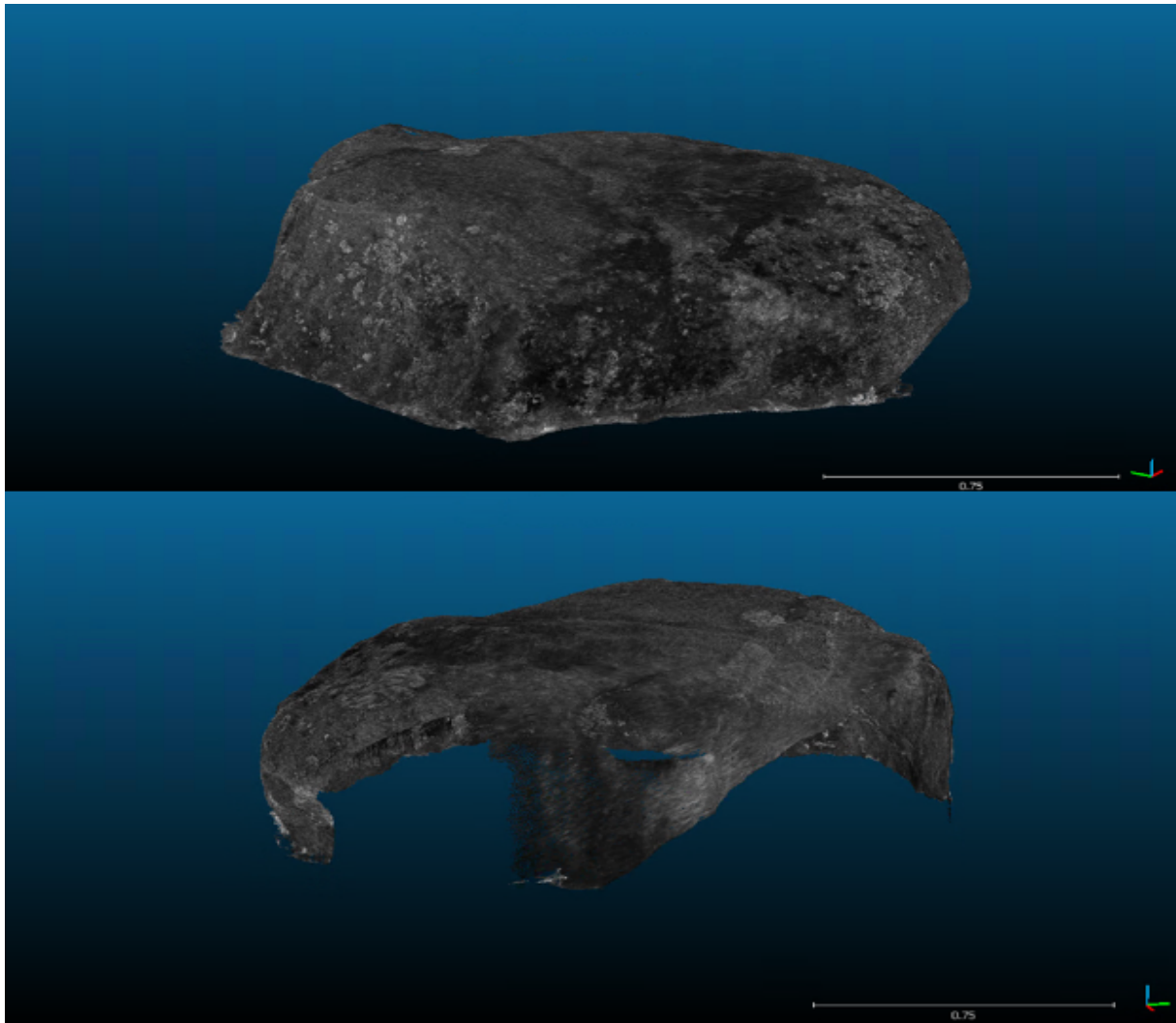


Figure B.4: Illustration of point cloud modelling Step 2.4: Make separate models for the rocks. The scale of the figure is indicated in meters.

2.5 *Align again.*

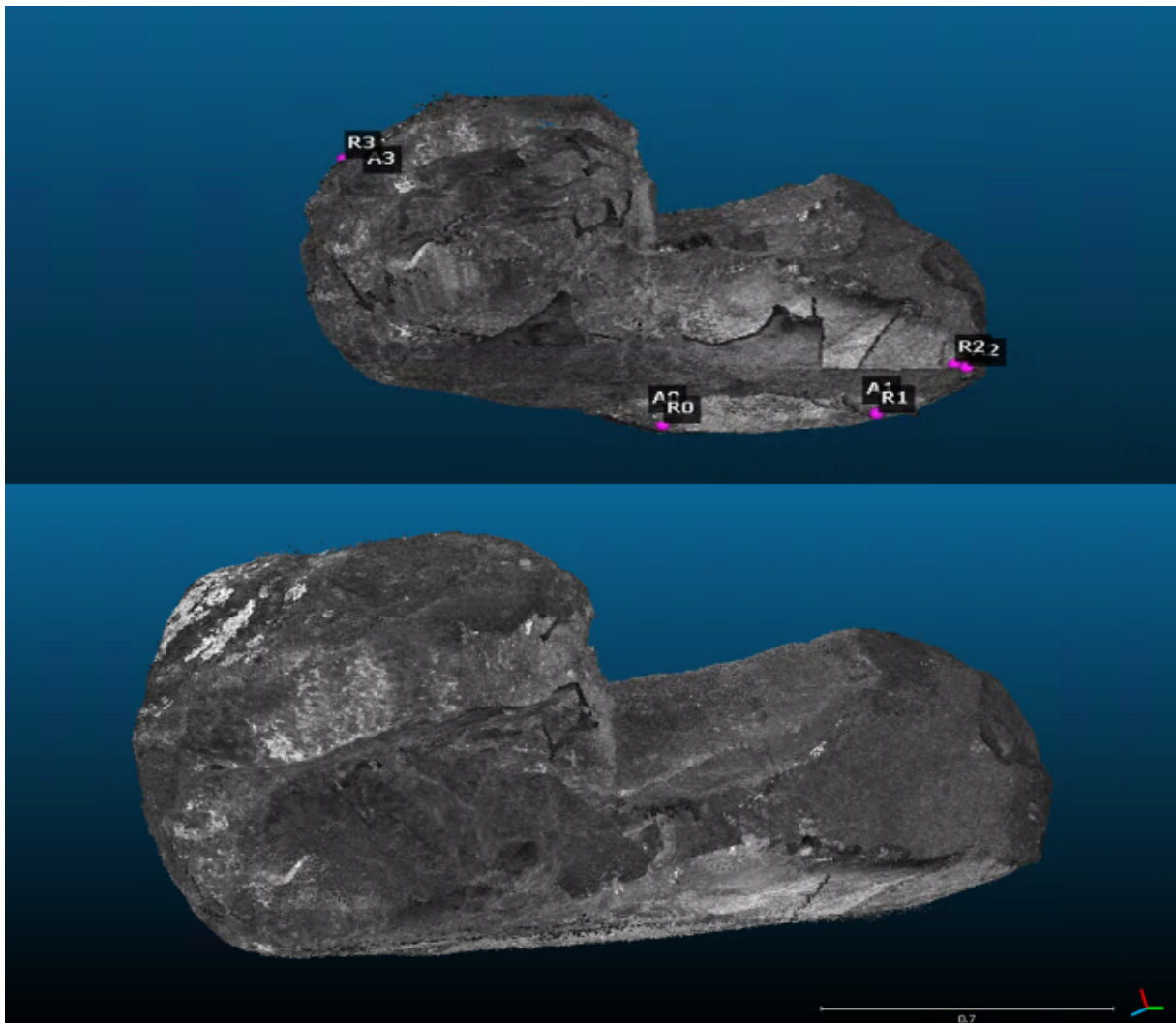


Figure B.5: Illustration of point cloud modelling Step 2.5: Align again. The scale of the figure is indicated in meters.

2.6 Fill the holes in the TLS data set with BLK data.

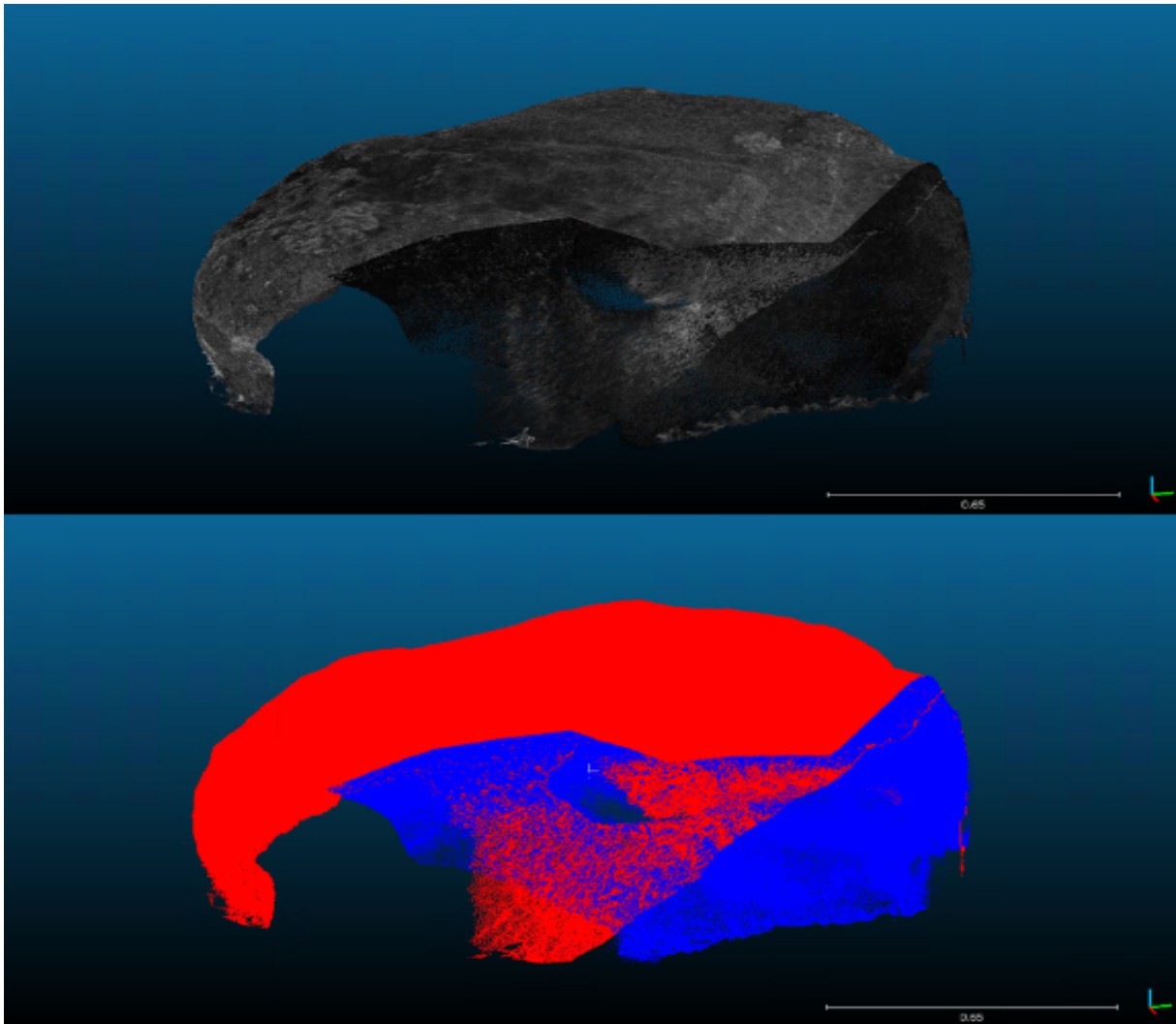


Figure B.6: Illustration of point cloud modelling Step 2.6: Fill the holes in the TLS data set with BLK data. The final result of this step can be observed at the top, and the origins of the points below. The red points come from the TLS data set and the blue dots come from the BLK data set. The scale of the figure is indicated in meters.

2.7 *Clean the data set.*



Figure B.7: Illustration of point cloud modelling Step 2.7: Clean the data set. The scale of the figure is indicated in meters.

2.8 *Subsample.*



Figure B.8: Illustration of point cloud modelling Step 2.8: Subsample. The scale of the figure is indicated in meters.

## Appendix C

# Figures of modelling Step 3: Mesh generation

In this appendix, the steps for generating the meshes will be illustrated. For an explanation of the steps, see Section 3.3: Mesh generation.

### 3.1 *Initial meshing in MeshLab.*

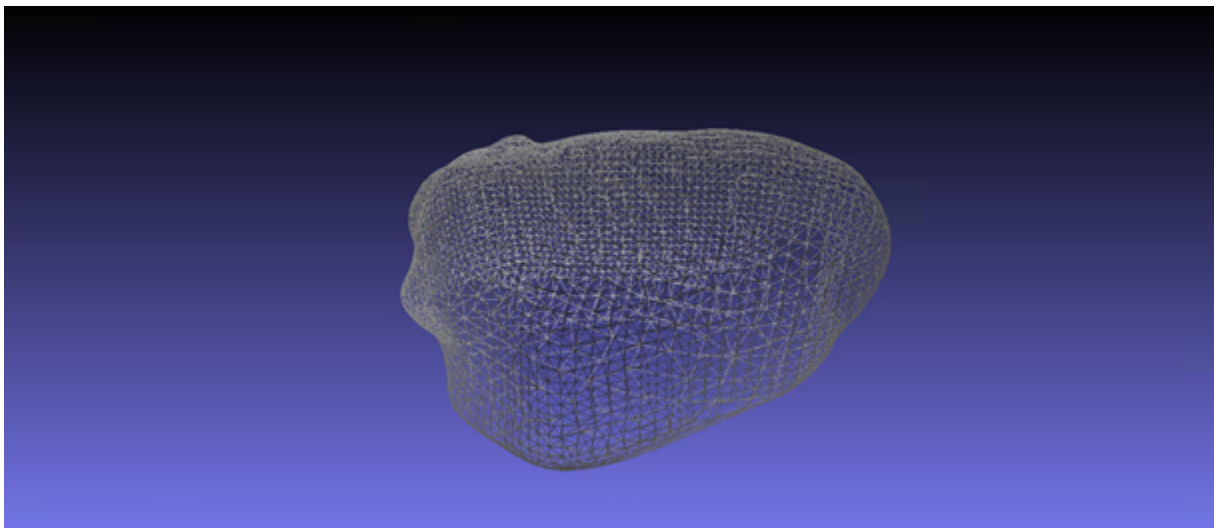


Figure C.1: Illustration of meshing Step 3.1: Initial meshing in Meshlab.

3.2 Filling holes in the meshes and levelling in Rhino.

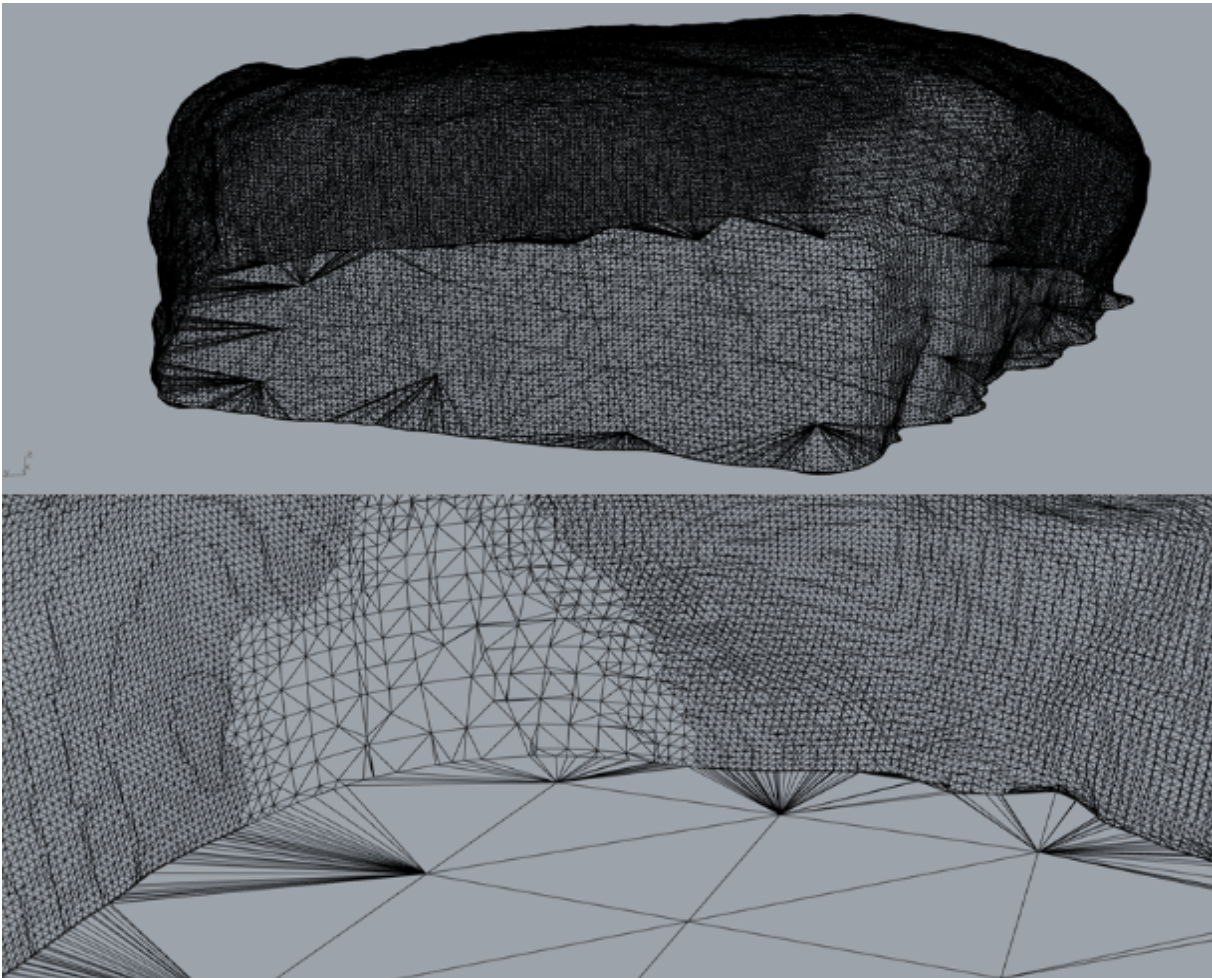


Figure C.2: Illustration of meshing Step 3.2: Closing the meshes and levelling in Rhino.

3.3 Griddle remeshing in Rhino.

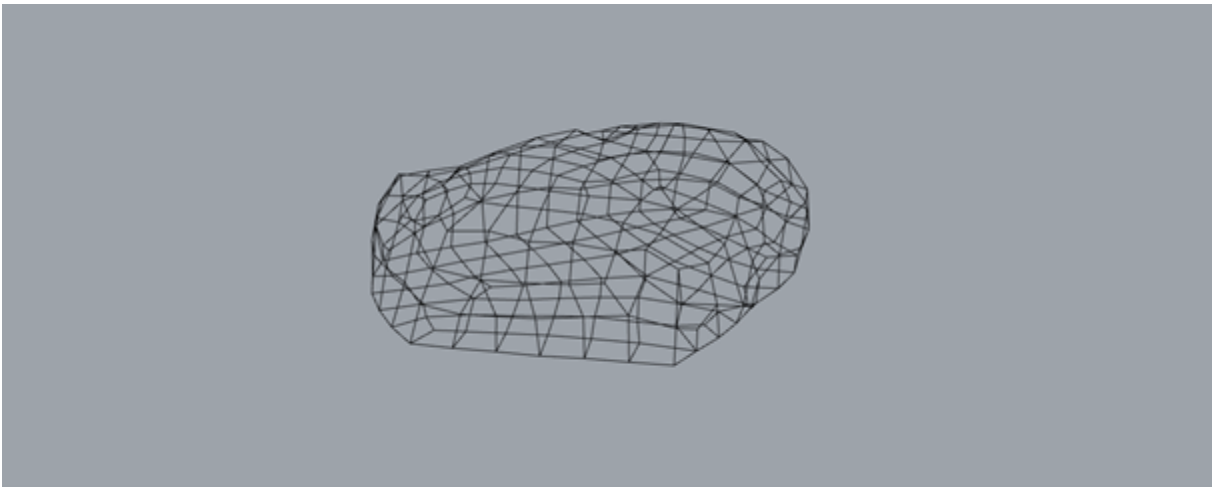


Figure C.3: Illustration of meshing Step 3.3: Griddle remeshing in Rhino.

3.4 *Manual adaptations in Rhino.*

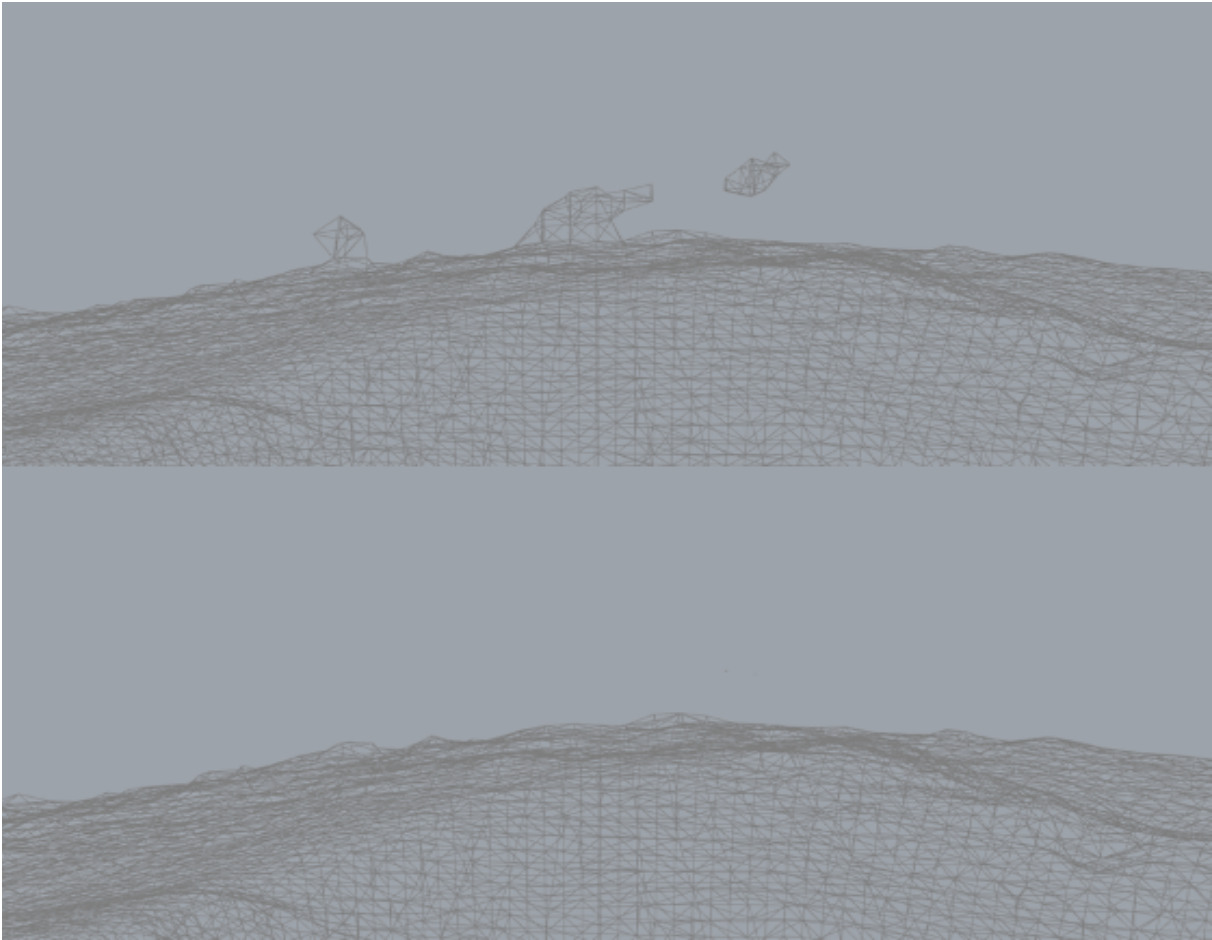


Figure C.4: Illustration of meshing Step 3.4: Manual adaptations in Rhino.

3.5 *Converting Rhino to 3DEC files.*

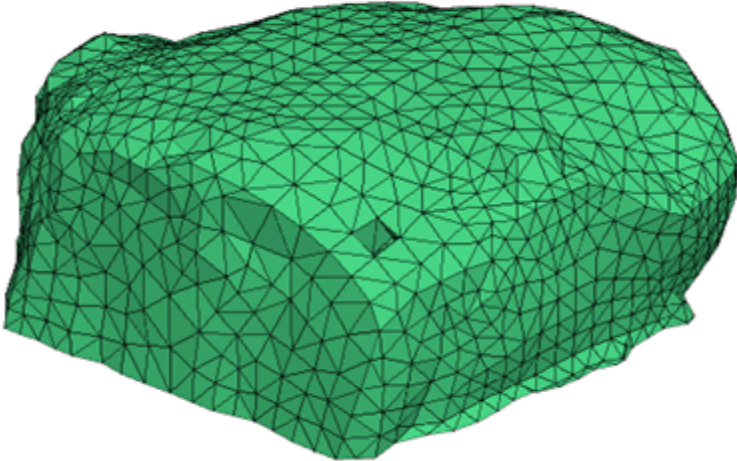


Figure C.5: Illustration of meshing Step 3.5: Converting Rhino to 3DEC files.

## Appendix D

# Griddle meshing settings

Parameter	Value	Unit	Default?
Mode	QuadDom	-	No
MinEdgeLength	0.15	m	No
MaxEdgeLength	0.15	m	No
RidgeAngle	20	-	Yes
MaxGradation	0.1	-	Yes
Optimization	5	-	Yes
QuadWeight	0.75	-	Yes
ShapeQuality	0.7	-	Yes
OutputMesh	Separated	-	Yes
DeletelInput	Yes	-	Yes

Table D.1: Griddle meshing settings for GSurf, for the default mesh.

Parameter	Value	Unit	Default?
Mode	Tet	-	Yes
MaxGradation	0.5 (default mesh) / 5 (smart mesh)	-	Yes
TargetSize	0 (default mesh) / 0.3 (smart mesh)	m	Yes
Optimization	5	-	Yes
ShapeQuality	0.75	-	Yes
IniErrorCheck	Yes	-	Yes

Table D.2: Griddle meshing settings for GVol, for the default and smart mesh.

## Appendix E

### Areas with sparse point density in the point cloud models

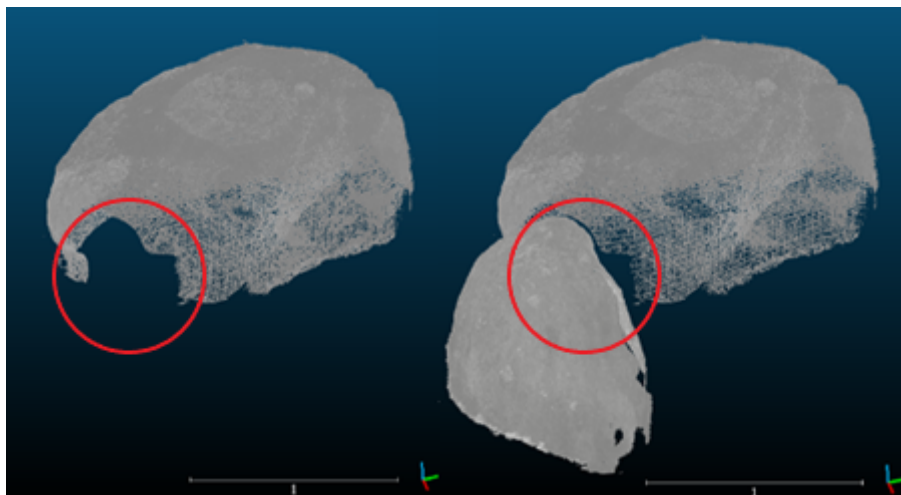


Figure E.1: Rock 1 (left) and Rock 1 and Rock 2 (right). There is little data on the North side of Rock 1 near Rock 2. The scale of the figure is indicated in meters.

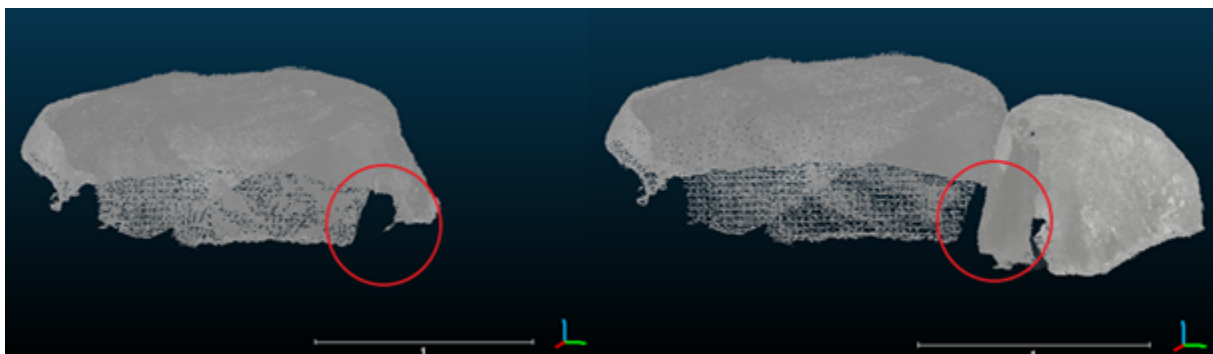


Figure E.2: Rock 1 (left) and Rock 1 and Rock 4 (right). There is little data on the South side of Rock 1 near Rock 4. The scale of the figure is indicated in meters.

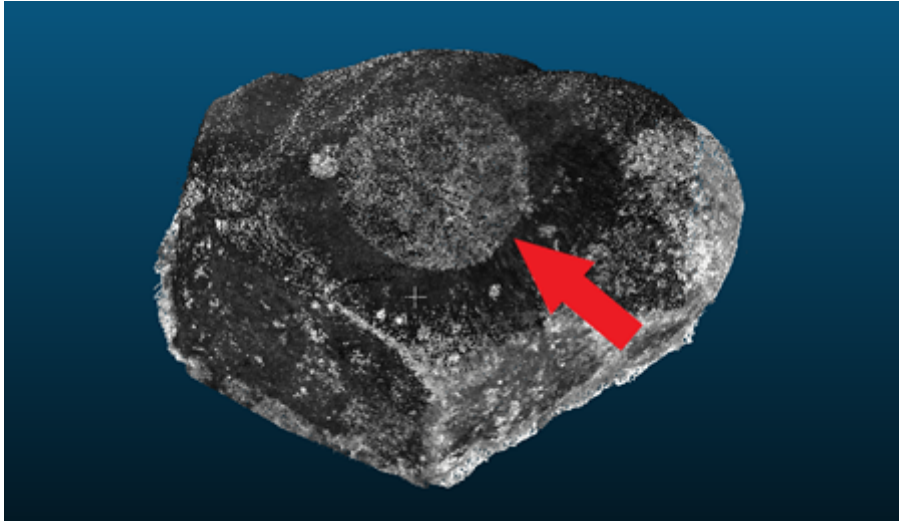


Figure E.3: Rock 1 as seen from the top. It can be seen that there is a circle on the top of the point cloud.

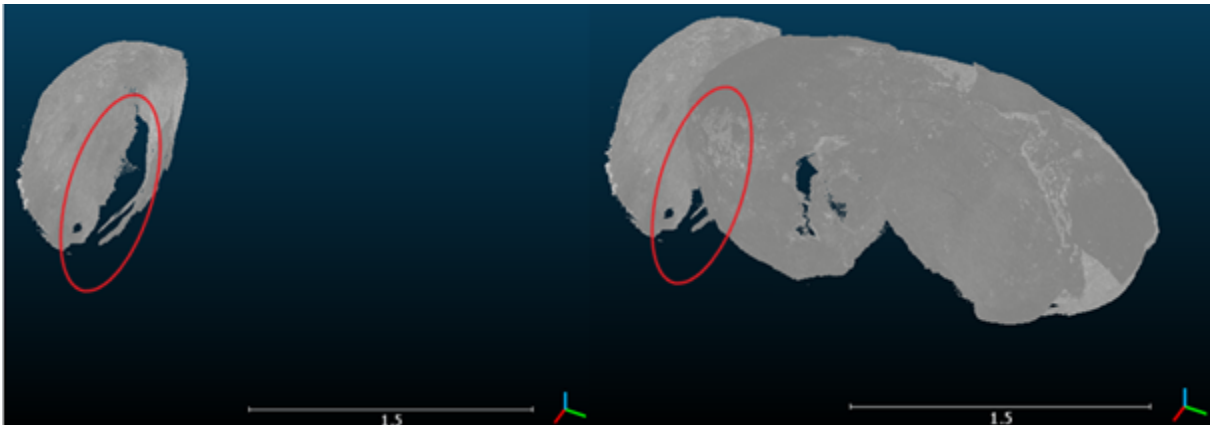


Figure E.4: Rock 2 (left) and Rock 2 and Rock 3 (right). There is little data on the South side of Rock 2 near Rock 3. The scale of the figure is indicated in meters.

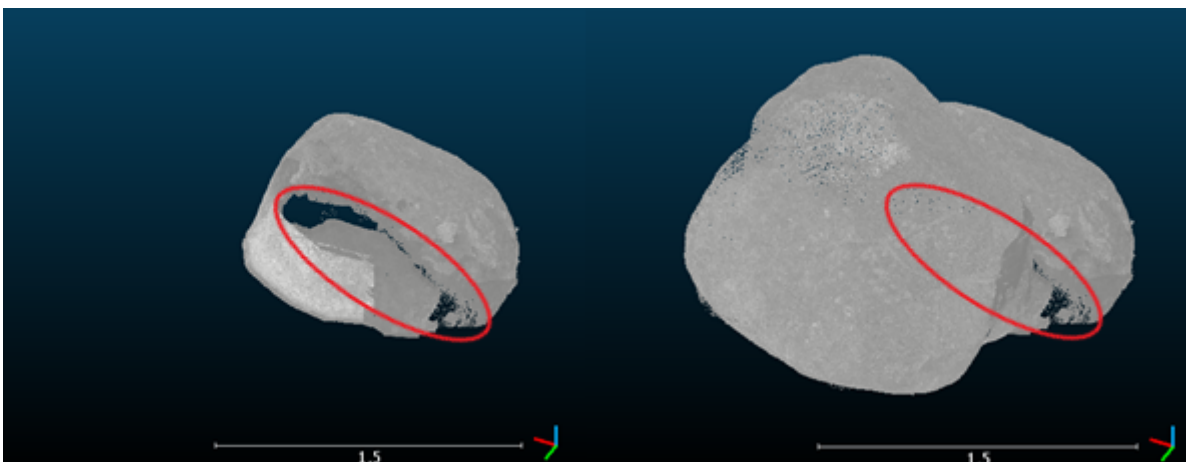


Figure E.5: Rock 5 (left) and Rock 5 and Rock 6 (right). There is little data on the South side of Rock 5 near Rock 6. The scale of the figure is indicated in meters.

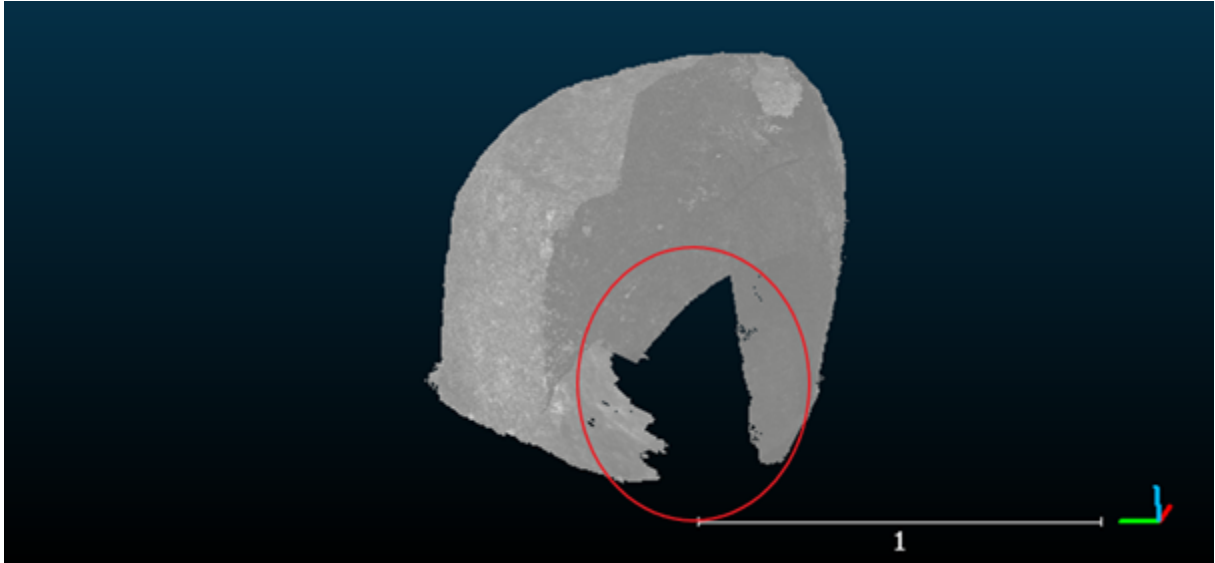


Figure E.6: Rock 7, little data on the North side. The scale of the figure is indicated in meters.

## Appendix F

# Mesh faces and sampling distance

	Number of mesh faces (-)			
	Sampling distance 1 mm	Sampling distance 5 mm	Sampling distance 10 mm	Sampling distance 50 mm
Rock 1	NA	140,687	42,870	1,736
Rock 2	NA	80,710	20,052	988
Rock 3	NA	343,806	108,348	3,900
Rock 4	NA	80,977	20,018	1,013
Rock 5	NA	121,885	34,444	1,331
Rock 6	NA	347,310	99,860	3,836
Rock 7	NA	121,471	27,617	1,259

Table F.1: Number of mesh faces for meshes created with subsampled point clouds.

# Appendix G

## PMD analyses

### G.1 Signed distance, after meshing Step 3.1

	Mean distance (mm)			
	Sampling distance 1 mm	Sampling distance 5 mm	Sampling distance 10 mm	Sampling distance 50 mm
Rock 1	-2.59E-04	1.10E-04	-5.19E-04	-1.05E-04
Rock 2	-3.94E-05	-7.49E-05	-8.13E-05	5.31E-04
Rock 3	2.93E-05	2.71E-04	2.69E-04	-2.74E-03
Rock 4	8.55E-06	7.40E-05	-8.51E-05	-1.30E-04
Rock 5	-5.12E-05	-4.10E-05	5.80E-05	5.67E-04
Rock 6	5.12E-05	-9.69E-05	1.60E-04	2.92E-04
Rock 7	3.20E-06	1.55E-04	1.68E-04	-5.52E-05

Table G.1: Signed PMD mean distance after meshing Step 3.1.

	Standard deviation (mm)			
	Sampling distance 1 mm	Sampling distance 5 mm	Sampling distance 10 mm	Sampling distance 50 mm
Rock 1	3.24E-03	2.06E-03	2.18E-03	3.81E-03
Rock 2	7.80E-04	7.18E-04	1.01E-03	2.95E-03
Rock 3	4.33E-03	4.02E-03	4.28E-03	6.69E-03
Rock 4	1.11E-03	1.02E-03	1.38E-03	4.40E-03
Rock 5	1.34E-03	1.16E-03	1.62E-03	3.53E-03
Rock 6	1.19E-03	1.26E-03	1.33E-03	2.54E-03
Rock 7	1.20E-03	1.11E-03	1.44E-03	3.44E-03

Table G.2: Signed PMD standard deviation after meshing Step 3.1.G.2 Euclidean distance, after meshing Step 3.1

## G.2 Euclidean distance, after meshing Step 3.1

	Mean distance (mm)			
	Sampling distance 1 mm	Sampling distance 5 mm	Sampling distance 10 mm	Sampling distance 50 mm
Rock 1	2.26E-03	1.54E-03	1.63E-03	2.79E-03
Rock 2	4.78E-04	4.97E-04	6.78E-04	2.16E-03
Rock 3	3.20E-03	3.14E-03	3.31E-03	5.22E-03
Rock 4	6.32E-04	6.52E-04	9.03E-04	3.18E-03
Rock 5	7.17E-04	7.20E-04	1.01E-03	2.54E-03
Rock 6	7.52E-04	8.70E-04	9.29E-04	1.77E-03
Rock 7	7.59E-04	7.73E-04	1.03E-03	2.51E-03

Table G.3: Euclidean PMD mean distance after meshing Step 3.1.

	Standard deviation (mm)			
	Sampling distance 1 mm	Sampling distance 5 mm	Sampling distance 10 mm	Sampling distance 50 mm
Rock 1	2.34E-03	1.38E-03	1.53E-03	2.59E-03
Rock 2	6.18E-04	5.24E-04	7.51E-04	2.08E-03
Rock 3	2.93E-03	2.52E-03	2.73E-03	5.01E-03
Rock 4	9.12E-04	7.84E-04	1.04E-03	3.04E-03
Rock 5	1.13E-03	9.16E-04	1.26E-03	2.52E-03
Rock 6	9.27E-04	9.20E-04	9.67E-04	1.84E-03
Rock 7	9.26E-04	8.16E-04	1.02E-03	2.35E-03

Table G.4: Euclidean PMD standard deviation after meshing Step 3.1.

	90 <sup>th</sup> percentile (mm)			
	Sampling distance 1 mm	Sampling distance 5 mm	Sampling distance 10 mm	Sampling distance 50 mm
Rock 1	5.35E-03	3.31E-03	3.70E-03	6.13E-03
Rock 2	9.45E-04	1.04E-03	1.39E-03	4.70E-03
Rock 3	6.88E-03	6.55E-03	6.84E-03	1.25E-02
Rock 4	1.29E-03	1.42E-03	1.96E-03	7.12E-03
Rock 5	1.46E-03	1.57E-03	2.23E-03	5.60E-03
Rock 6	1.51E-03	1.80E-03	1.95E-03	3.74E-03
Rock 7	1.64E-03	1.68E-03	2.19E-03	5.34E-03

Table G.5: Euclidean PMD 90<sup>th</sup> percentile after meshing Step 3.1. G.3 Signed distance, after meshing Step 3.4

### G.3 Signed distance, after meshing Step 3.4

	Mean distance (mm)			
	Sampling distance 1 mm	Sampling distance 5 mm	Sampling distance 10 mm	Sampling distance 50 mm
Rock 1	NA	1.08E-04	-5.11E-04	2.07E-04
Rock 2	NA	-7.87E-05	-9.73E-05	9.87E-04
Rock 3	NA	2.68E-04	2.66E-04	-3.01E-03
Rock 4	NA	6.96E-05	-6.92E-05	-1.30E-03
Rock 5	NA	-3.80E-05	4.26E-05	2.81E-03
Rock 6	NA	-6.37E-05	1.42E-04	-4.38E-05
Rock 7	NA	1.53E-04	1.54E-04	4.33E-04

Table G.6: Signed PMD mean distance after meshing Step 3.4.

	Standard deviation (mm)			
	Sampling distance 1 mm	Sampling distance 5 mm	Sampling distance 10 mm	Sampling distance 50 mm
Rock 1	NA	2.06E-03	2.18E-03	4.15E-03
Rock 2	NA	7.24E-04	1.03E-03	3.22E-03
Rock 3	NA	4.02E-03	4.28E-03	6.91E-03
Rock 4	NA	1.03E-03	1.40E-03	4.72E-03
Rock 5	NA	1.17E-03	1.63E-03	3.73E-03
Rock 6	NA	1.27E-03	1.32E-03	2.75E-03
Rock 7	NA	1.12E-03	1.46E-03	3.69E-03

Table G.7: Signed PMD standard deviation after meshing Step 3.4.

### G.4 Euclidean distance, after meshing Step 3.4

	Mean distance (mm)			
	Sampling distance 1 mm	Sampling distance 5 mm	Sampling distance 10 mm	Sampling distance 50 mm
Rock 1	NA	1.54E-03	1.64E-03	3.09E-03
Rock 2	NA	5.04E-04	7.00E-04	2.48E-03
Rock 3	NA	3.14E-03	3.31E-03	5.48E-03
Rock 4	NA	6.61E-04	9.30E-04	3.53E-03
Rock 5	NA	7.28E-04	1.03E-03	2.81E-03
Rock 6	NA	8.77E-04	9.31E-04	1.94E-03
Rock 7	NA	7.84E-04	1.05E-03	2.76E-03

Table G.8: Euclidean PMD mean distance after meshing Step 3.4.

	Standard deviation (mm)			
	Sampling distance 1 mm	Sampling distance 5 mm	Sampling distance 10 mm	Sampling distance 50 mm
Rock 1	NA	1.38E-03	1.53E-03	2.78E-03
Rock 2	NA	5.27E-04	7.62E-04	2.28E-03
Rock 3	NA	2.52E-03	2.74E-03	5.17E-03
Rock 4	NA	7.86E-03	1.05E-03	3.16E-03
Rock 5	NA	9.17E-04	1.27E-03	2.65E-03
Rock 6	NA	9.25E-04	9.49E-04	1.95E-03
Rock 7	NA	8.18E-04	1.03E-03	2.48E-03

Table G.9: Euclidean PMD standard deviation after meshing Step 3.4.

	90 <sup>th</sup> percentile (mm)			
	Sampling distance 1 mm	Sampling distance 5 mm	Sampling distance 10 mm	Sampling distance 50 mm
Rock 1	NA	3.31E-03	3.71E-03	6.76E-03
Rock 2	NA	1.05E-03	1.44E-03	5.37E-03
Rock 3	NA	6.56E-03	6.84E-03	1.30E-02
Rock 4	NA	1.43E-03	2.01E-03	7.73E-03
Rock 5	NA	1.58E-03	2.26E-03	6.13E-03
Rock 6	NA	1.82E-03	1.95E-03	4.24E-03
Rock 7	NA	1.69E-03	2.23E-03	5.89E-03

Table G.10: Euclidean PMD 90<sup>th</sup> percentile after meshing Step 3.4.G.5 Signed distance, TLS and BLK comparison

## G.5 Signed distance, TLS and BLK comparison

	Mean distance (mm)			
	Sampling distance 1 mm	Sampling distance 5 mm	Sampling distance 10 mm	Sampling distance 50 mm
TLS data	-8.35E-06	6.93E-05	-3.91E-05	-3.32E-04
BLK data	5.99E-04	-4.06E-04	1.57E-04	6.10E-04

Table G.11: Signed PMD mean distance comparison for Rock 4 between TLS and BLK data.

	Standard deviation (mm)			
	Sampling distance 1 mm	Sampling distance 5 mm	Sampling distance 10 mm	Sampling distance 50 mm
TLS data	8.20E-04	8.46E-04	1.17E-03	4.28E-03
BLK data	3.73E-03	3.49E-03	3.74E-03	5.42E-03

Table G.12: Signed PMD standard deviation comparison for Rock 4 between TLS and BLK data. G.6 Euclidean distance, TLS and BLK comparison

## G.6 Euclidean distance, TLS and BLK comparison

	Mean distance (mm)			
	Sampling distance 1 mm	Sampling distance 5 mm	Sampling distance 10 mm	Sampling distance 50 mm
TLS data	5.10E-04	5.57E-04	7.86E-04	3.10E-03
BLK data	2.33E-03	2.19E-03	2.48E-03	4.04E-03

Table G.13: Euclidean PMD mean distance comparison for Rock 4 between TLS and BLK data.

	Standard deviation (mm)			
	Sampling distance 1 mm	Sampling distance 5 mm	Sampling distance 10 mm	Sampling distance 50 mm
TLS data	6.42E-04	6.40E-04	8.72E-04	2.97E-03
BLK data	2.98E-03	2.75E-03	2.80E-03	3.66E-03

Table G.14: Euclidean PMD standard deviation comparison for Rock 4 between TLS and BLK data.

	90 <sup>th</sup> percentile (mm)			
	Sampling distance 1 mm	Sampling distance 5 mm	Sampling distance 10 mm	Sampling distance 50 mm
TLS data	1.01E-03	1.16E-03	1.62E-03	6.99E-03
BLK data	5.24E-03	4.84E-03	5.41E-03	8.58E-03

Table G.15: Euclidean PMD 90<sup>th</sup> percentile comparison for Rock 4 between TLS and BLK data. G.7 Signed distance, comparison with and without GIA data

## G.7 Signed distance, comparison with and without GIA data

	Mean distance (mm)			
	Sampling distance 1 mm	Sampling distance 5 mm	Sampling distance 10 mm	Sampling distance 50 mm
Rock 3 with GIA data	2.93E-05	2.71E-04	2.69E-04	-2.74E-03
Rock 3 without GIA data	2.95E-05	2.71E-04	2.71E-04	-2.74E-03

Table G.16: Signed PMD mean distance comparison for Rock 3, with and without GIA data.

	Standard deviation (mm)			
	Sampling distance 1 mm	Sampling distance 5 mm	Sampling distance 10 mm	Sampling distance 50 mm
Rock 3 with GIA data	4.33E-03	4.02E-03	4.28E-03	6.69E-03
Rock 3 without GIA data	4.34E-03	4.02E-03	4.28E-03	6.69E-03

Table G.17: Signed PMD standard deviation comparison for Rock 3, with and without GIA data.

## G.8 Euclidean distance, comparison with and without GIA data

	Mean distance (mm)			
	Sampling distance 1 mm	Sampling distance 5 mm	Sampling distance 10 mm	Sampling distance 50 mm
Rock 3 with GIA data	3.20E-03	3.14E-03	3.31E-03	5.22E-03
Rock 3 without GIA data	3.20E-03	3.14E-03	3.31E-03	5.22E-03

Table G.18: Euclidean PMD mean distance comparison for Rock 3, with and without GIA data.

	Standard deviation (mm)			
	Sampling distance 1 mm	Sampling distance 5 mm	Sampling distance 10 mm	Sampling distance 50 mm
Rock 3 with GIA data	2.93E-03	2.52E-03	2.73E-03	5.01E-03
Rock 3 without GIA data	2.93E-03	2.53E-03	2.73E-03	5.01E-03

Table G.19: Euclidean PMD standard deviation comparison for Rock 3, with and without GIA data.

	90 <sup>th</sup> percentile (mm)			
	Sampling distance 1 mm	Sampling distance 5 mm	Sampling distance 10 mm	Sampling distance 50 mm
Rock 3 with GIA data	6.88E-03	6.55E-03	6.84E-03	1.25E-02
Rock 3 without GIA data	6.88E-03	6.46E-03	6.83E-03	1.25E-02

Table G.20: Euclidean PMD 90<sup>th</sup> percentile comparison for Rock 3, with and without GIA data.

# Appendix H

## JRC determination guidelines

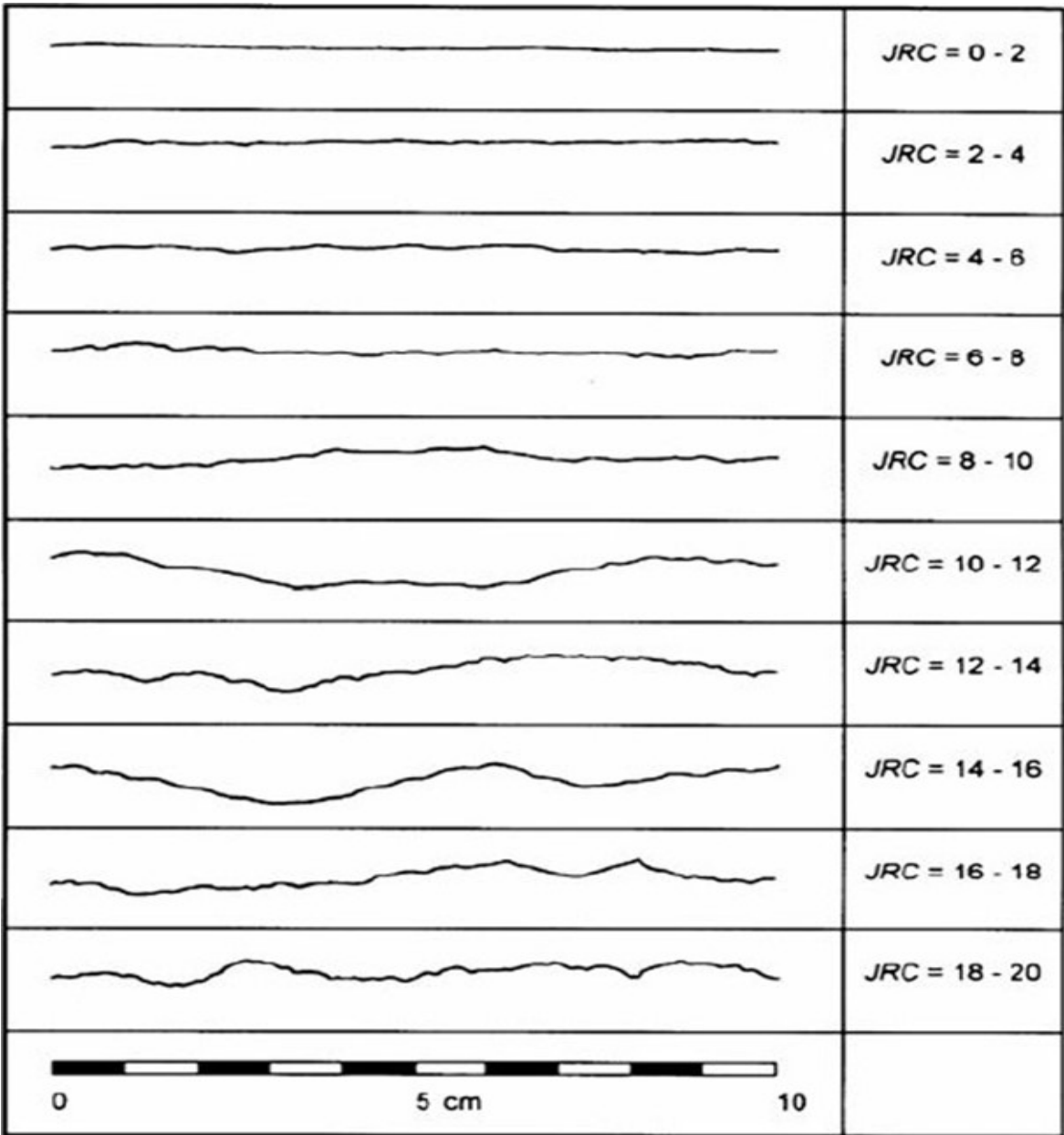


Figure H.1: Typical roughness profiles. Adopted from Barton & Choubey, 1977.

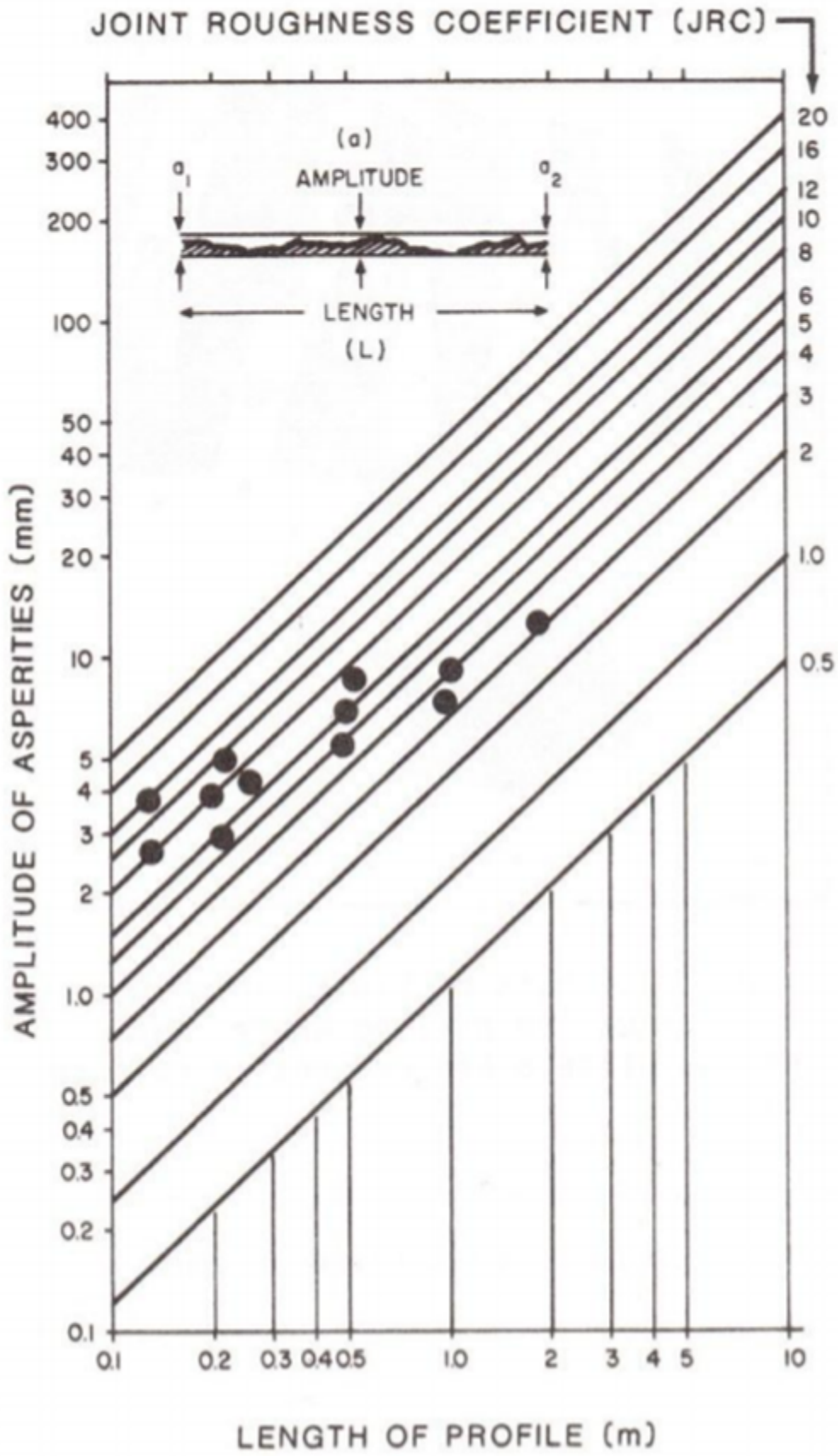


Figure H.2: JRC determination guide. Adopted from Barton & Bandis, 1990.

## Appendix I

# JRC values in the field

### I.1 Locations in the field

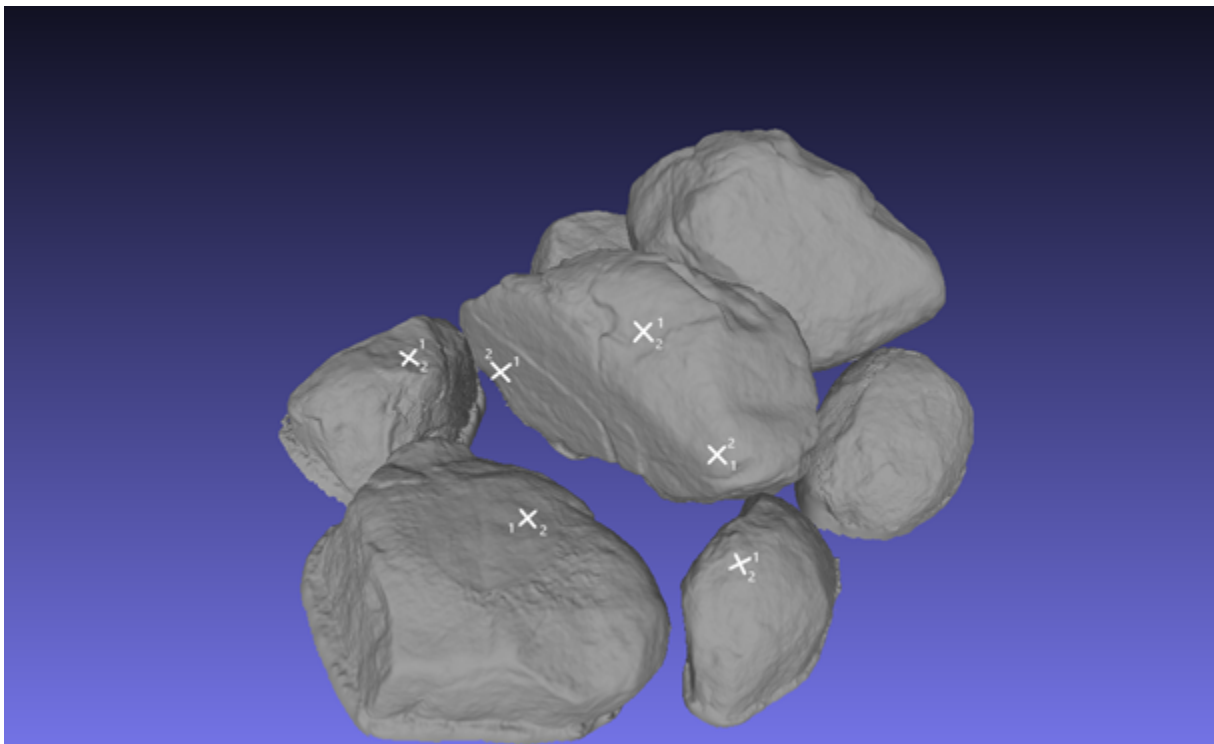


Figure I.1: Locations in the field where the JRC and equotip values were measured.

## I.2 JRC values for different locations

	Line	JRC (-)	JRC for each location (-)	JRC for each rock (-)
Rock 1	1	10	9	9
	2	8		
Rock 2	1	10	11	11
	2	12		
Rock 3 North	1	8	8	8
	2	8		
Rock 3 top	1	8	8	
	2	8		
Rock 3 South	1	8	7	
	2	6		
Rock 4	1	8	9	
	2	10		

Table I.1: JRC values for different locations in the field.

Rock 1

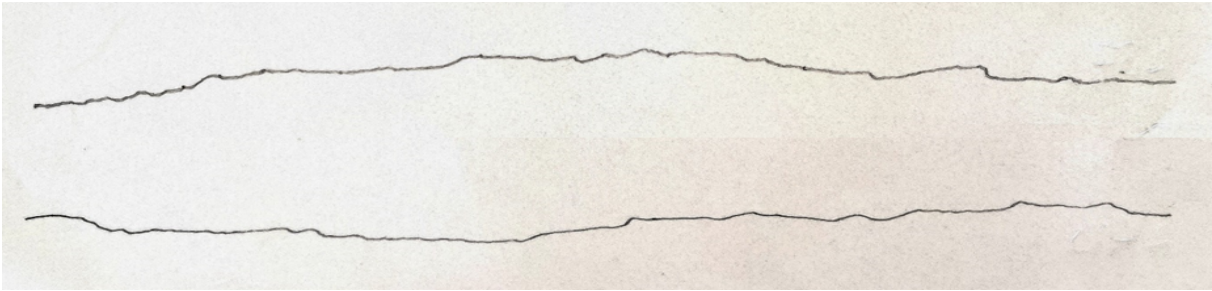


Figure I.2: Roughness profile Rock 1. Profile 1 (top) and profile 2 (bottom).

Rock 2

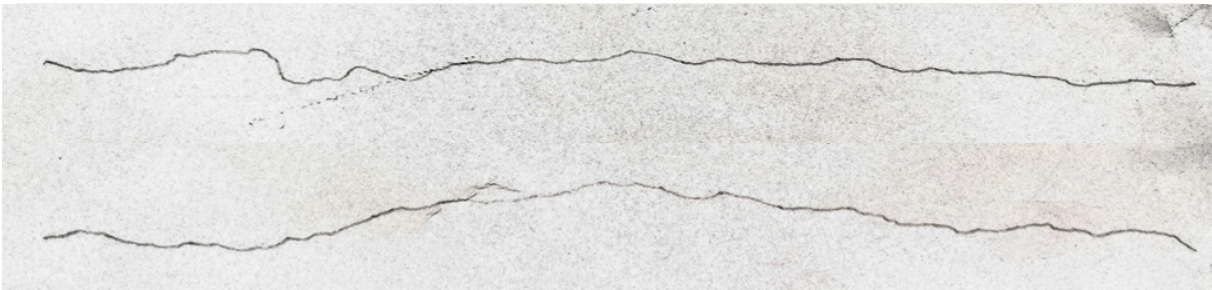


Figure I.3: Roughness profile Rock 2. Profile 1 (top) and profile 2 (bottom).

Rock 3 North

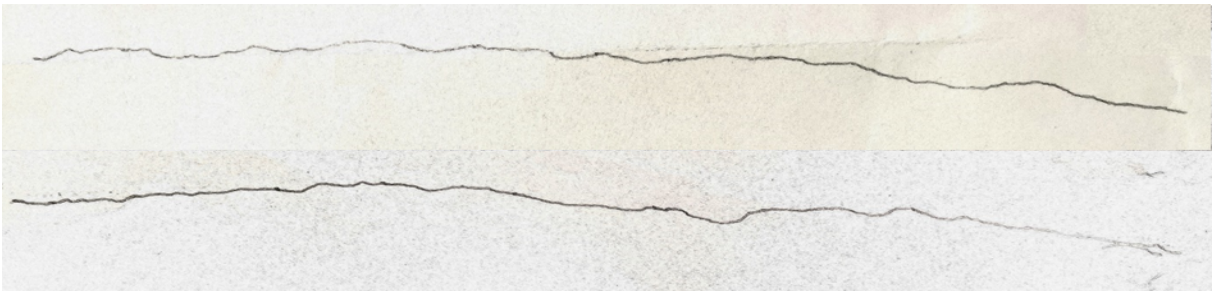


Figure I.4: Roughness profile Rock 3 North. Profile 1 (top) and profile 2 (bottom).

Rock 3 top



Figure I.5: Roughness profile Rock 3 top. Profile 1 (top) and profile 2 (bottom).

Rock 3 South



Figure I.6: Roughness profile Rock 3 South. Profile 1 (top) and profile 2 (bottom).

Rock 4



Figure I.7: Roughness profile Rock 4. Profile 1 (top) and profile 2 (bottom).

## Appendix J

# JCS values in the field

### J.1 JCS values in the field

Rock 1										
1	504	642	407	397	554	407	372	240	263	240
2	247	237	218	276	372	382	213	260	598	187
Rock 2										
1	253	468	382	393	67	562	197	296	494	235
2	499	246	305	243	299	500	551	212	491	496
Rock 3 north										
1	262	445	264	452	376	197	261	393	365	538
2	296	516	390	480	600	238	650	487	480	671
Rock 3 top										
1	296	616	393	383	74	427	181	342	382	483
2	160	193	135	477	229	677	465	185	186	401
Rock 3 south										
1	582	509	519	460	112	342	125	136	482	403
2	164	105	278	156	282	220	230	398	561	377
Rock 4										
1	64	536	136	221	396	309	244	212	559	178
2	606	186	444	143	583	55	673	440	267	385

Table J.1: Equotip values for each location in the field. The rejected values are displayed in red.

	Average for each line (-)	Average for each line after correction, if applicable (-)	Average for each location (-)	Average for each location after correction, if applicable (-)	Average for each rock (-)	
Rock 1						
1	502.8		463.5		463.5	Rock 1
2	377.6					
Rock 2						
1	459.8		483.6		483.6	Rock 2
2	507.4					
Rock 3 north						
1	440.8	416.1	502.1	474.0		
2	584.8	552.1				
Rock 3 top						
1	536.8		470.4		452.4	Rock 3
2	449.8					
Rock 3 south						
1	510.4	481.8	437.4	412.9		
2	379.2	358.0				
Rock 4						
1	408.8		493.1		493.1	Rock 4
2	549.2					

Table J.2: Equotip values for each rock in the field. Corrections were applied for tests that were taken in horizontal, instead of vertical direction (see Appendix I.2)

Rock number	Equotip value (-)	Standard deviation (-)	JCS value (MPa)	Standard deviation (MPa)	Total average JCS value for all rocks (MPa)	Standard deviation (MPa)
Rock 1	463.5	136.5	37.0	21.5	40.9	25.6
Rock 2	483.6	141.8	41.1	24.1		
Rock 3	489.0	152.4	42.3	26.4		
Rock 4	493.1	190.0	43.2	30.4		

Table J.3: JCS values for each rock and total average JCS value, as calculated based on the Equotip values of Table J.2

## J.2 Influence of equotip test direction

Small analysis of the influence of the direction of the equotip on the equotip results.

											Average for each direction (-)	Standard deviation (-)	
Vertical													
1	637	695	754	781	730	665	704	567	801	741	767.7	101.4	
2	685	749	742	631	408	522	765	787	772	785			
Horizontal													
1	797	734	793	848	775	607	736	702	797	778	810.9	66.6	
2	707	825	618	819	816	769	848	775	719	788			

Table J.4: Comparison between the vertical and horizontal Equotip values obtained on the same sample. Rejected values are displayed in red.

It was found that there is a small influence of the test direction on the equotip test results. Therefore all test results that were obtained in the horizontal direction (Rock 3 North and Rock 3 South), have been multiplied by the correction factor of 0.944 (see equation J.1).

$$correction\ factor = 767.7/810.9 = 0.944 \quad (J.1)$$

# Appendix K

## Tilt test results

	Direction 1	Direction 2
	$\beta$ ( $^{\circ}$ )	$\beta$ ( $^{\circ}$ )
Test 1	34	32
Test 2	32.5	32
Test 3	33.5	32
Average for each direction	33.3	32
<i>Total average for both directions</i>	<b>33</b>	

Table K.1: Tilt test results for two directions.



Figure K.1: Tilt test performed on the flat, sand-blasted granite sample in direction 1 (left) and direction 2 (right).

## Appendix L

# JCS, JRC and JMC values in the lab

### L.1 JCS values in the lab

<i>Tensile-split sample</i>										
Bottom sample	295	518	250	184	119	540	217	575	525	169
Top sample	165	142	245	401	433	284	523	319	127	203
<b>Total</b>	<b>441</b>									
<i>Flat, sand-blasted sample</i>										
Bottom sample	654	580	633	641	725	653	605	497	602	621
Top sample	504	259	772	603	573	712	731	598	547	652
<b>Total</b>	<b>679</b>									

Table L.1: Equotip values for the samples that were used in the laboratory. Rejected values are displayed in red.

	JCS (MPa), calculated using Verwaal & Mulder (1993)
Tensile-split sample	<b>32.7</b>
Flat, sand-blasted sample	<b>96.3</b>

Table L.2: JCS values for the samples that were used in the laboratory, based on the Equotip values as found in Table L.1

## L.2 JRC values in the lab

<i>Rough sample</i>		JRC (-)	<i>Flat sample</i>		JRC (-)
Bottom sample	1	12	Bottom sample	1	0
	2	10		2	0
	3	14		3	0
<i>Average</i>	12		<i>Average</i>	0	
Top sample	4	16	Top sample	4	0
	5	16		5	0
	6	14		6	0
<i>Average</i>	15		<i>Average</i>	0	
<i>Combined average</i>	14		<i>Combined average</i>	0	

Table L.3: JRC values in the lab L.2.1 JRC values JRC values for the laboratory samples.

Roughness profiles of the rough sample, bottom

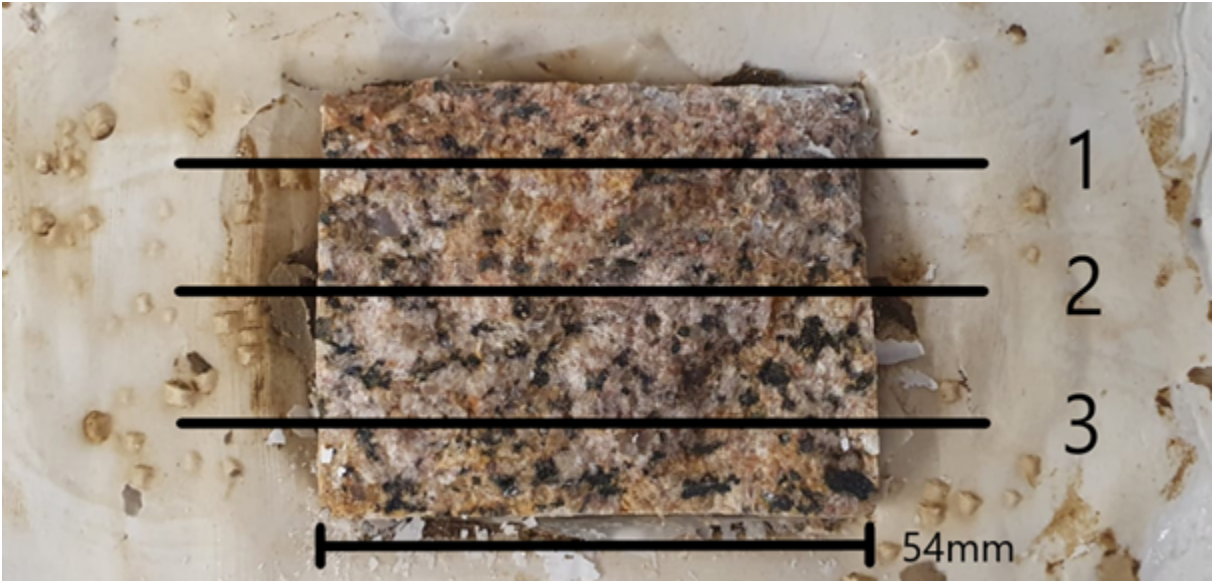


Figure L.1: Overview of the roughness profiles on the rough bottom sample.

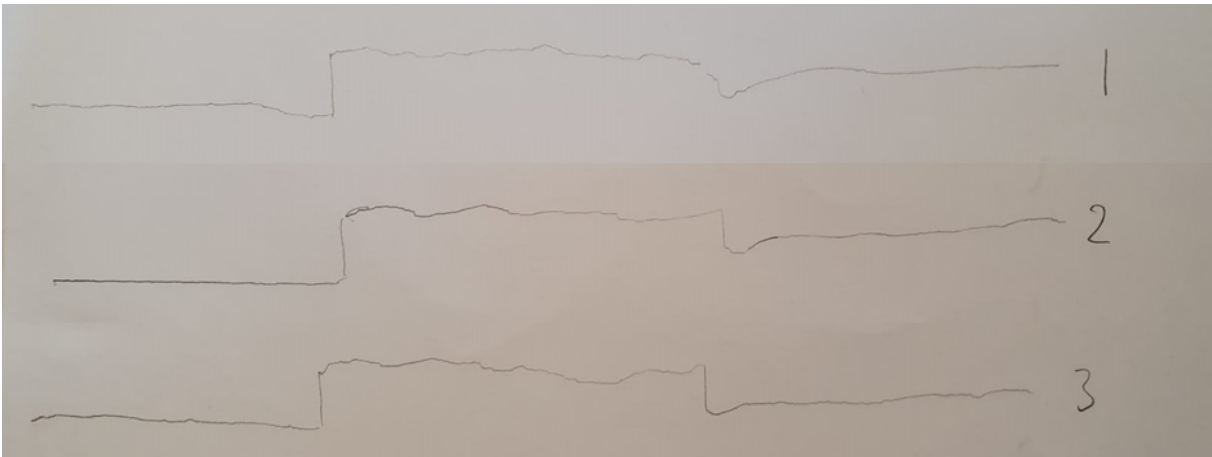


Figure L.2: Roughness profiles of the rough bottom sample. The width of the rock sample is 54mm.

Roughness profiles of the rough sample, top

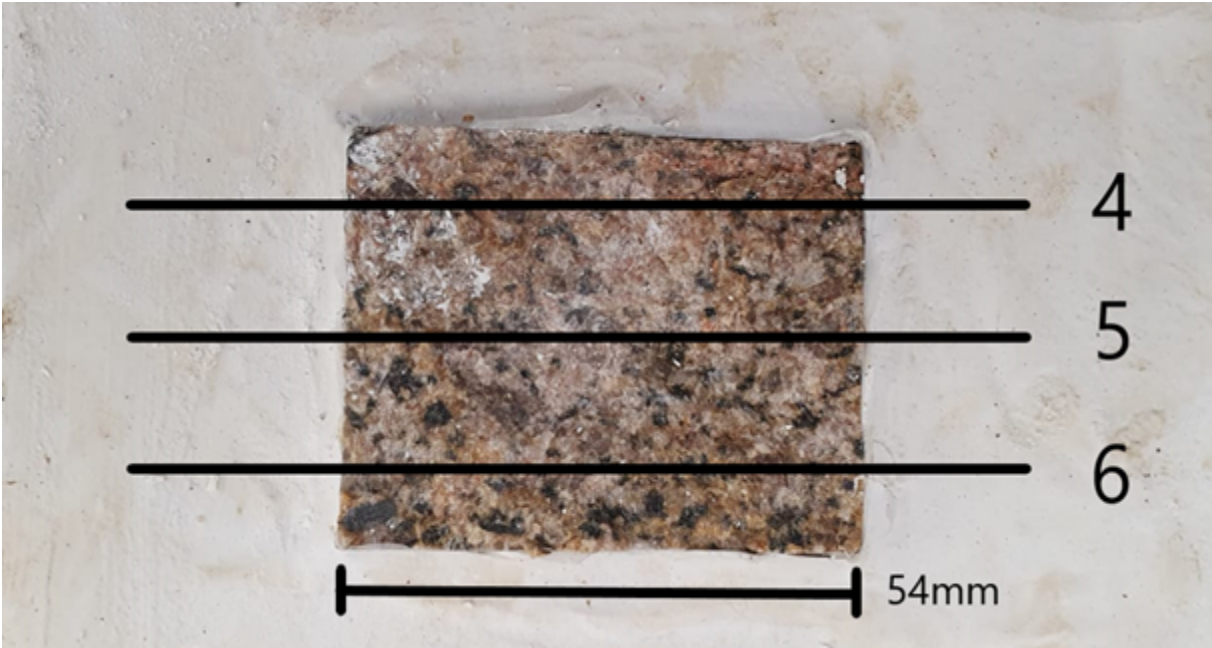


Figure L.3: Overview of the roughness profiles on the rough top sample.

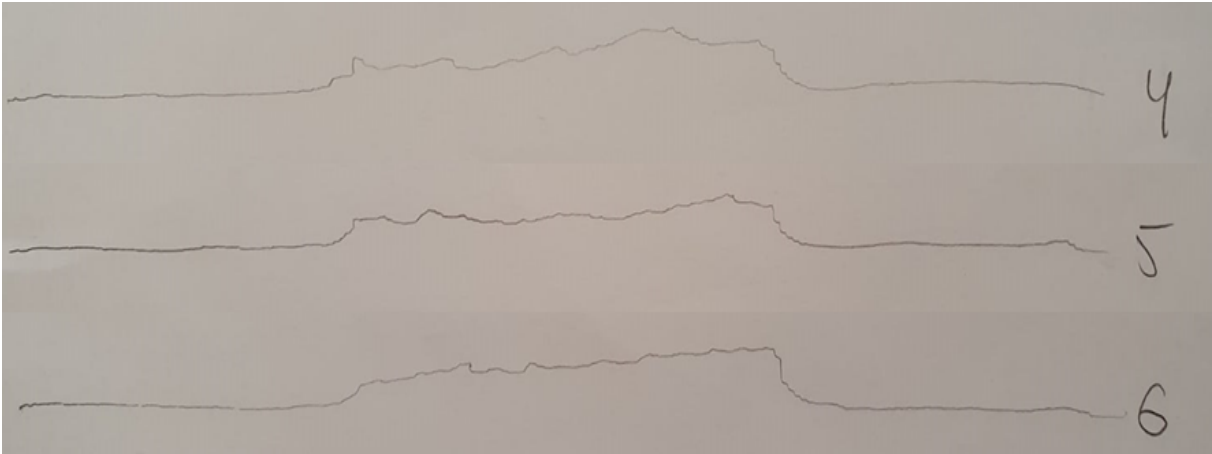


Figure L.4: Roughness profiles of the rough top sample. The width of the rock sample is 54mm.

Roughness profiles of flat sample, bottom

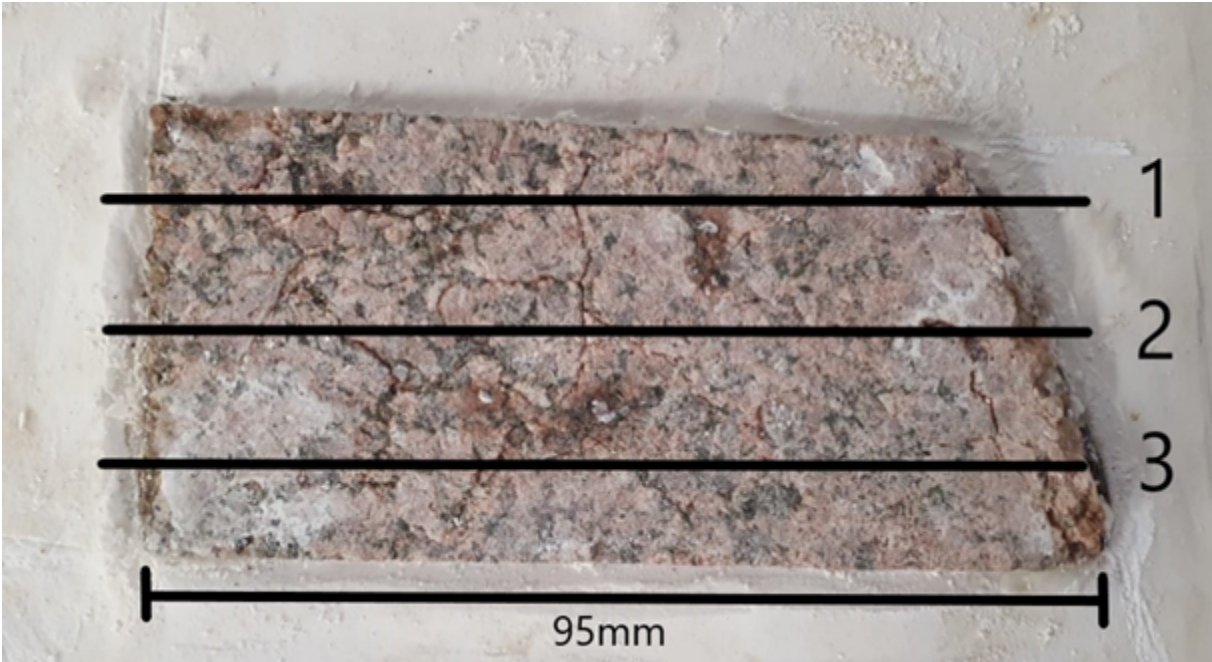


Figure L.5: Overview of the roughness profiles on the flat bottom sample.

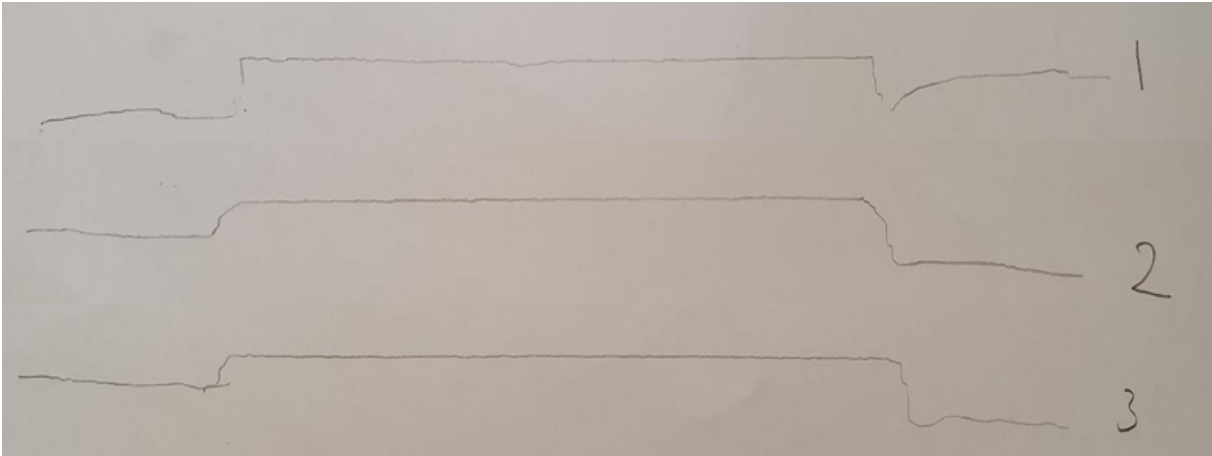


Figure L.6: Roughness profiles of the flat bottom sample. The width of the rock sample is 95mm at the bottom near profile 3.

**Roughness profiles of flat sample, top**



Figure L.7: Overview of the roughness profiles on the flat top sample.

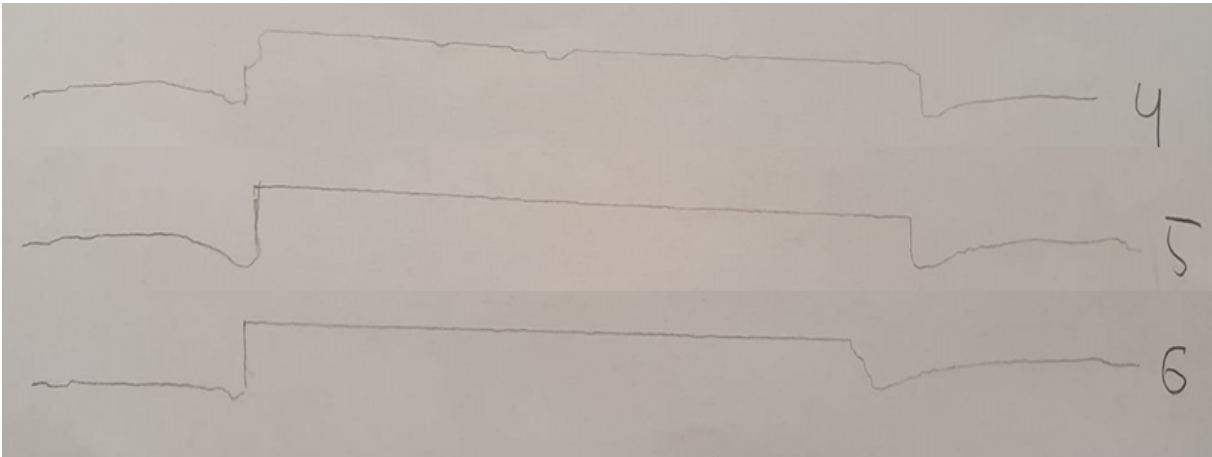


Figure L.8: Roughness profiles of the flat top sample. The width of the rock sample is 73 mm at the bottom near profile 6.

**L.3 JMC values in the lab**

	JMC after a displacement of 3mm (-)
Profile 1 & 6	0.7
Profile 2 & 5	0.6
Profile 3 & 4	0.5
Average	0.6

Table L.4: JMC results for the rough, tensile-split laboratory sample.

# Appendix M

## Golder shear box results

### M.1 Table of residual friction angle values

	Test	Residual friction angle (°)		Standard deviation (°)
		Coulomb	Barton	
Flat sample	1	31.2		1.1
Flat sample	2	30.5		0.5
Rough sample	1		20.3	0.8
Rough sample	2		30.3	0.6

Table M.1: Residual friction angle results for the Golder shear box test on a flat, sand-blasted sample and a rough, tensile-split sample.

### M.2 Graphs of normal stress vs. shear stress

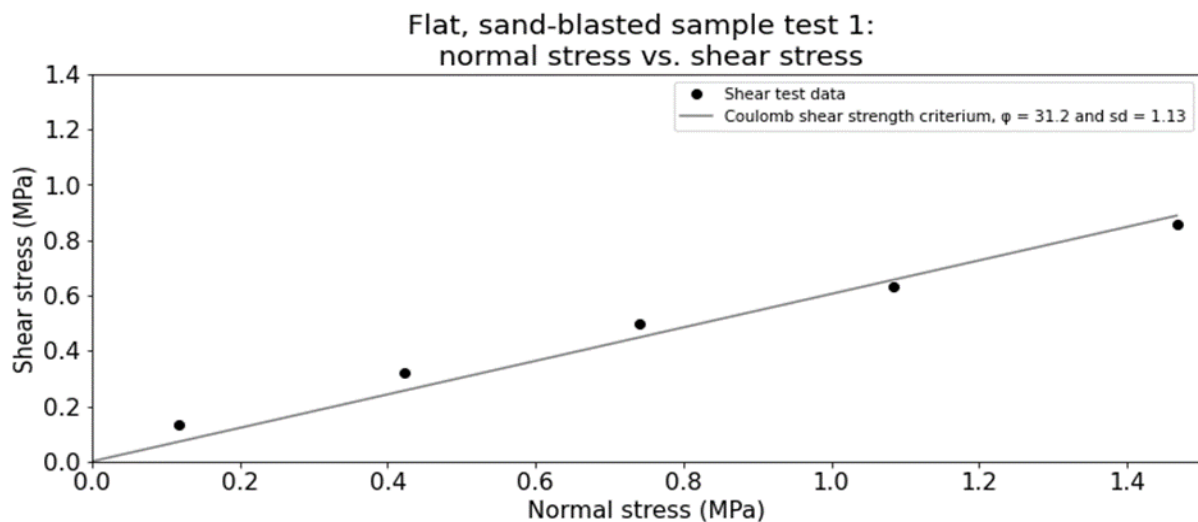


Figure M.1: Shear stress vs. normal stress for the flat sample, test 1. The stresses were corrected for dilation and effective surface area.

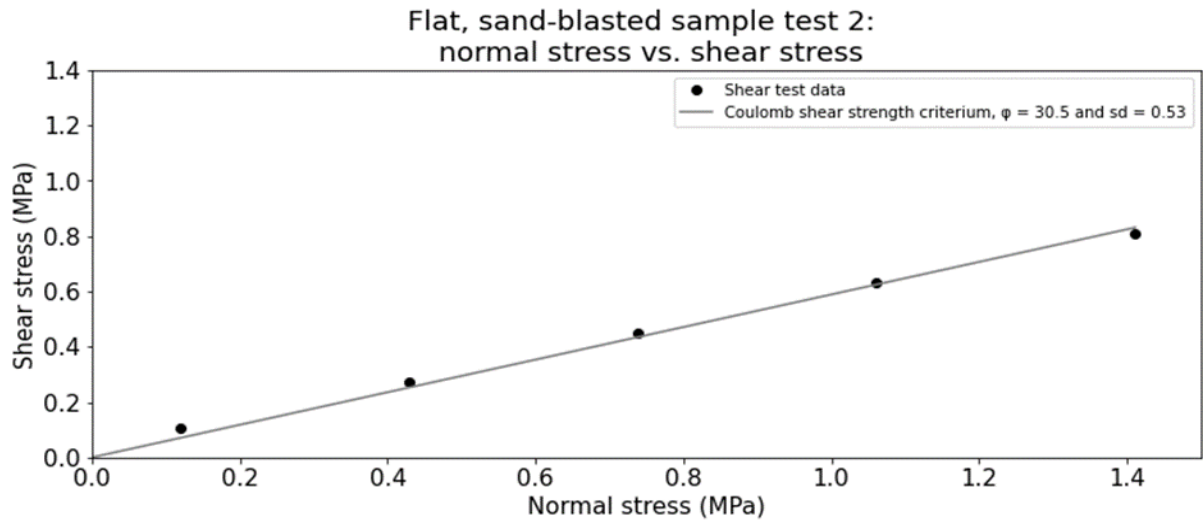


Figure M.2: Shear stress vs. normal stress for the flat sample, test 2. The stresses were corrected for dilation and effective surface area.

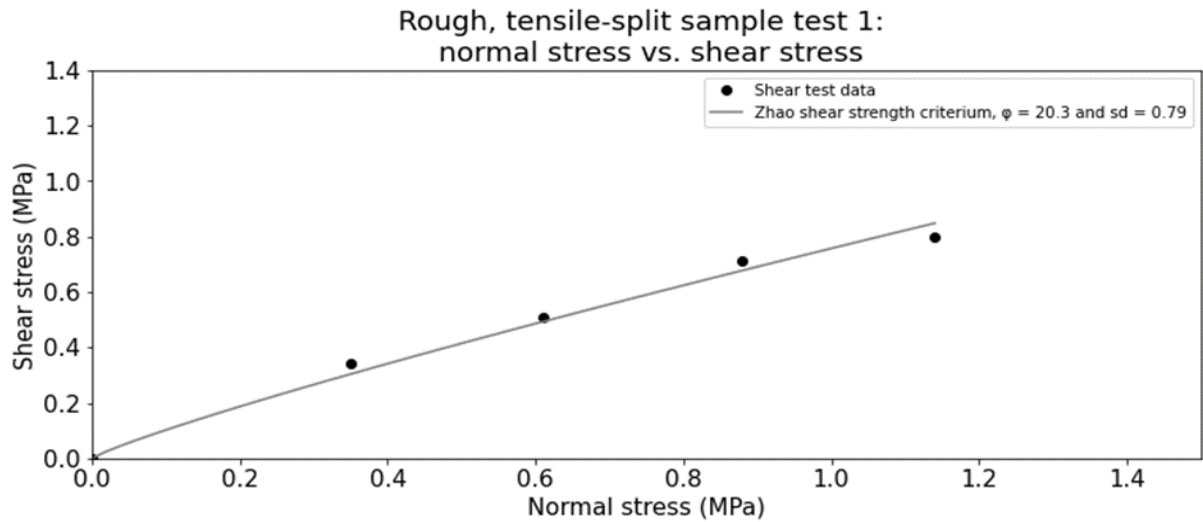


Figure M.3: Shear stress vs. normal stress for the rough, tensile-split sample, test 1. The stresses were corrected for the effective surface area.

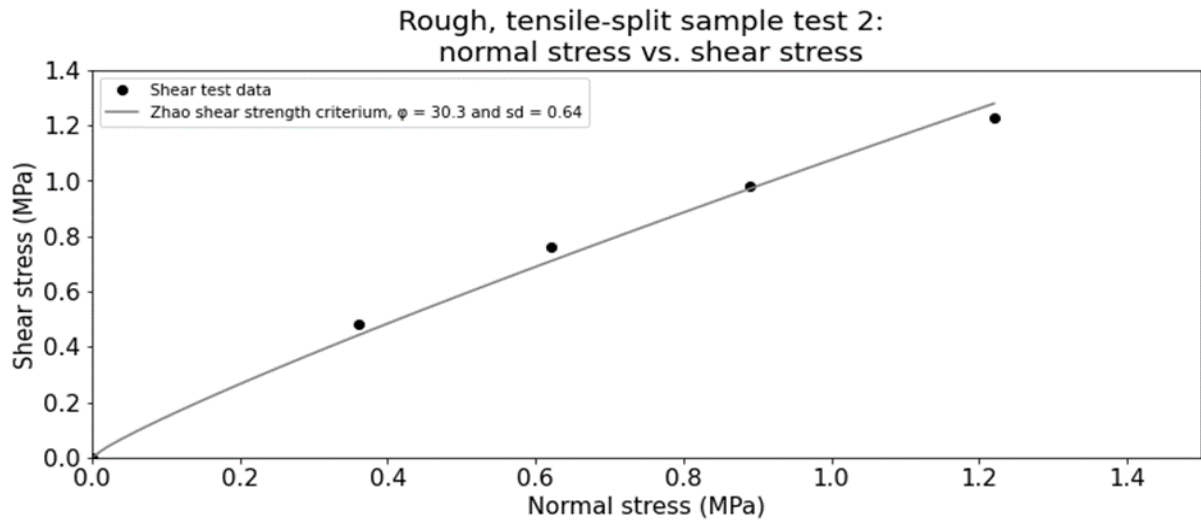


Figure M.4: Shear stress vs. normal stress for rough, tensile-split sample, test 2. The stresses were corrected for the effective surface area.

### M.3 Graphs of horizontal displacement

#### M.3.1 Results for flat, sand-blasted sample, test 1

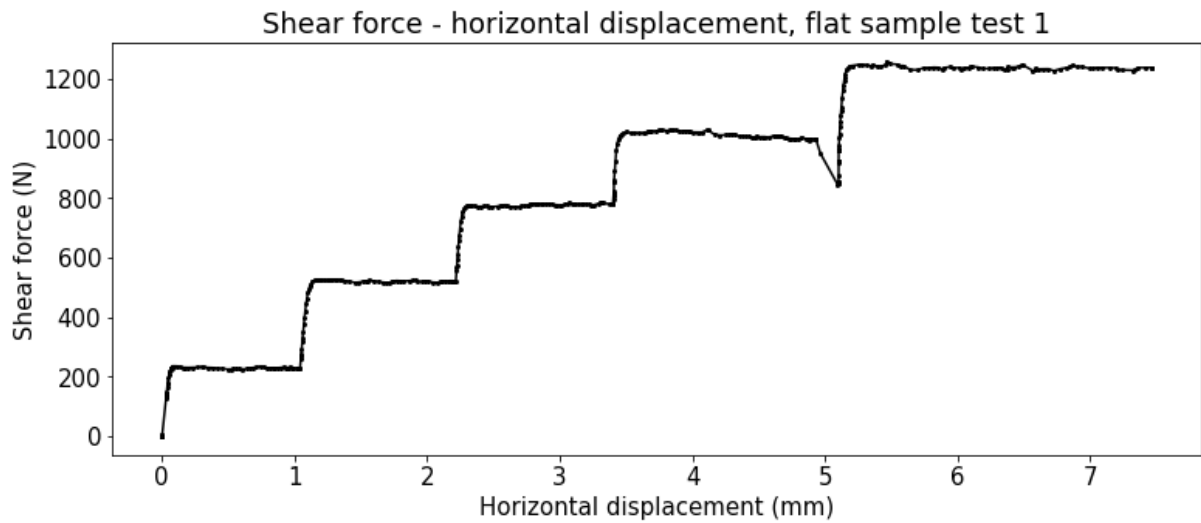


Figure M.5: Shear force vs. horizontal displacement for the flat, sand-blasted sample, test 1.

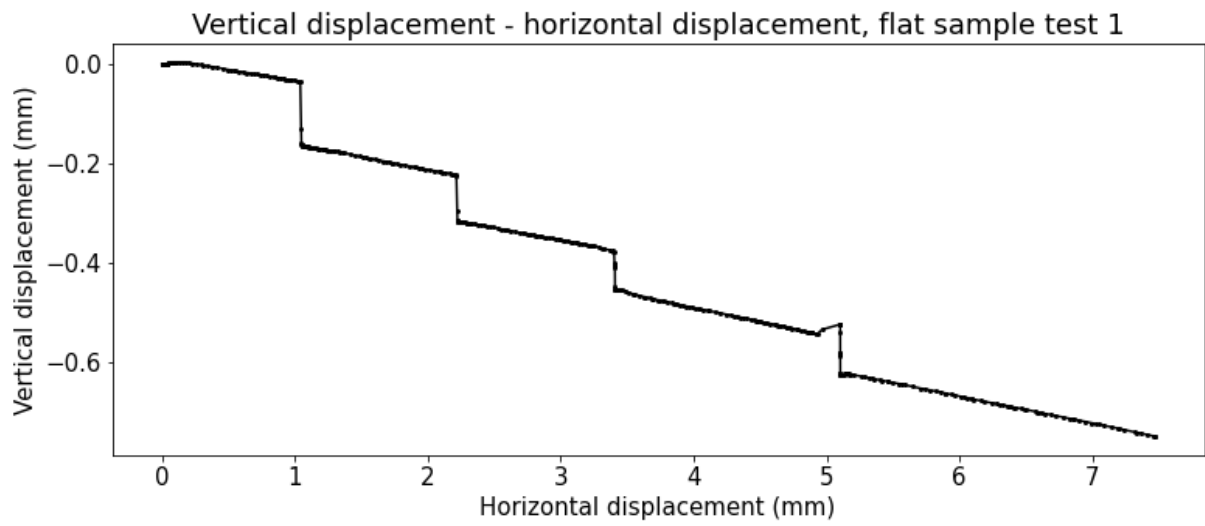


Figure M.6: Vertical vs. horizontal displacement for the flat, sand-blasted sample, test 1.

### M.3.2 Results for flat, sand-blasted sample, test 2

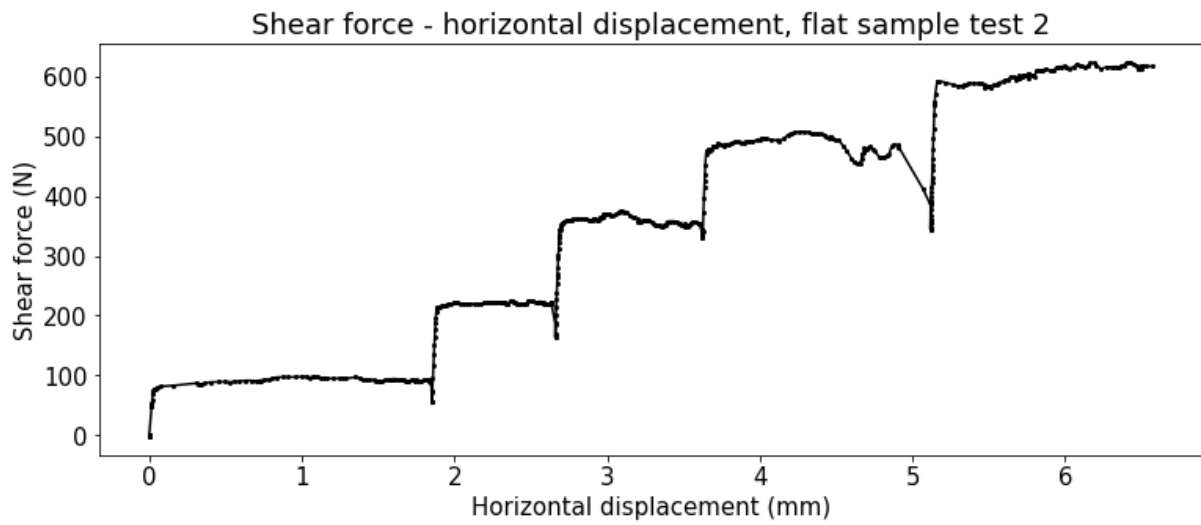


Figure M.7: Shear force vs. horizontal displacement for the flat, sand-blasted sample, test 2.

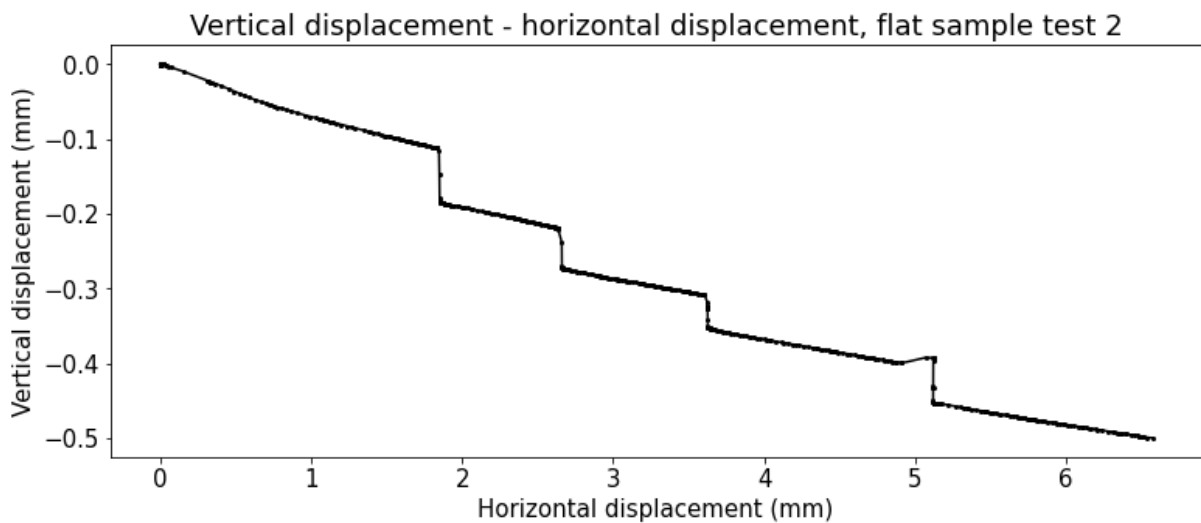


Figure M.8: Vertical vs. horizontal displacement for the flat, sand-blasted sample, test 2.

### M.3.3 Results for rough, tensile-split sample, test 1

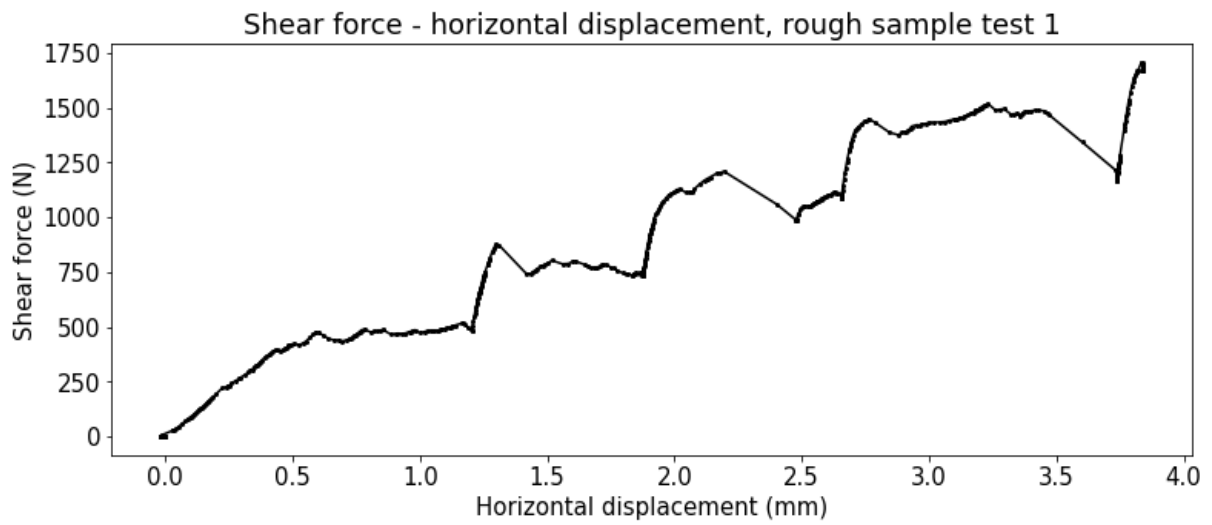


Figure M.9: Shear force vs. horizontal displacement for the rough, tensile-split sample, test 1.

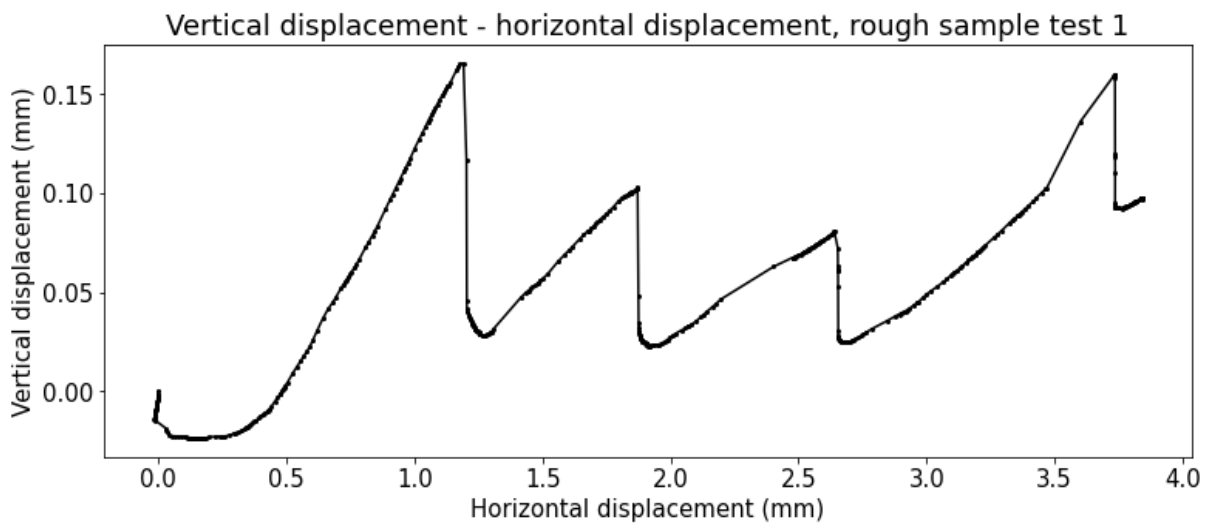


Figure M.10: Vertical vs. horizontal displacement for the rough, tensile-split sample, test 1.

### M.3.4 Results for rough, tensile-split sample, test 2

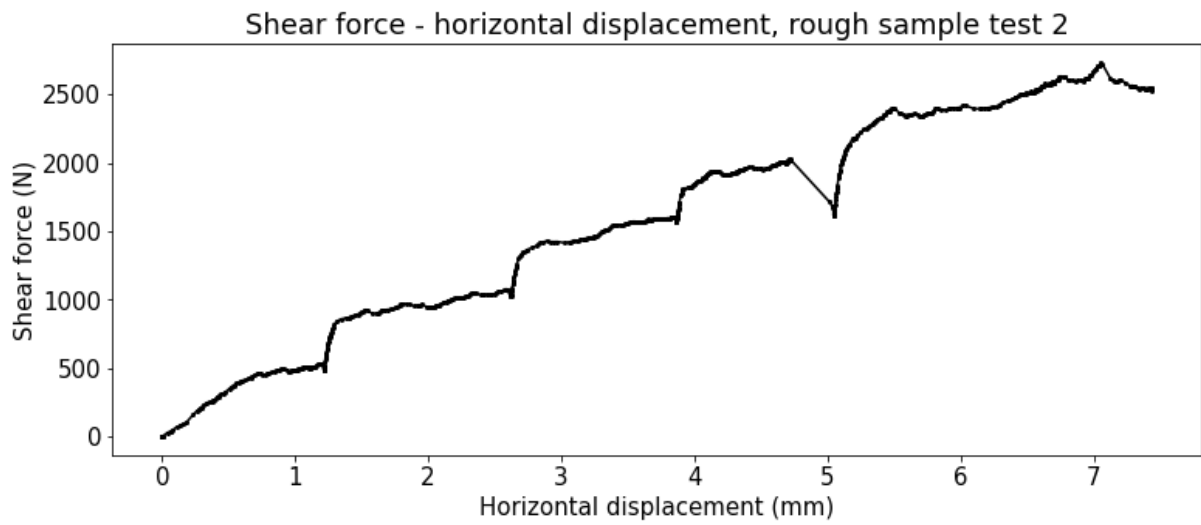


Figure M.11: Shear force vs. horizontal displacement for the rough, tensile-split sample, test 2.

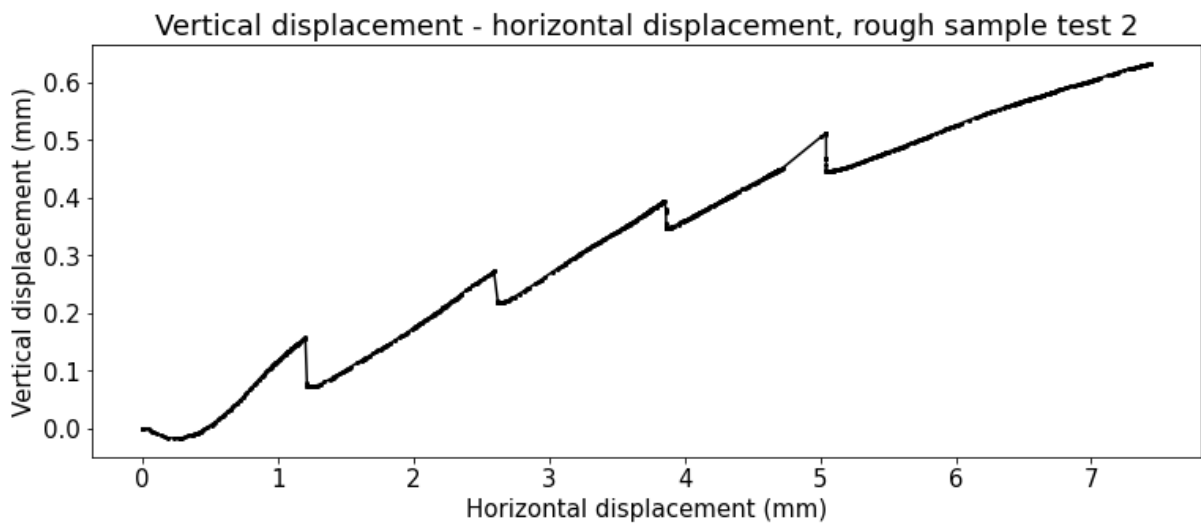


Figure M.12: Vertical vs. horizontal displacement for the rough, tensile-split sample, test 2.

# Appendix N

## 3DEC scripts

### N.1 Script for modelling Phase 1

```
1 model new
2 model large-strain on
3
4 ; IMPORTING THE BLOCKS
5
6 block import filename 'Rock_1.3dgrid'
7 block group 'BL_1'
8 block join
9 block hide on
10
11 block import filename 'Rock_2.3dgrid'
12 block group 'BL_2'
13 block join
14 block hide on
15
16 block import filename 'Rock_3.3dgrid'
17 block group 'BL_3'
18 block join
19 block hide on
20
21 block import filename 'Rock_4.3dgrid'
22 block group 'BL_4'
23 block join
24 block hide on
25
26 block import filename 'Rock_5.3dgrid'
27 block group 'BL_5'
28 block join
29 block hide on
30
31 block import filename 'Rock_6.3dgrid'
32 block group 'BL_6'
33 block join
34 block hide on
35
36 block import filename 'Rock_7.3dgrid'
37 block group 'BL_7'
38 block join
39 block hide on
40
41 ; FIXING THE BLOCKS THAT REST ON THE GROUND
42
43 block hide off
```

```

44 block hide range group 'BL_3'
45 block hide range group 'BL_6'
46 block fix
47
48 ; ASSIGNING THE ROCK PARAMETERS
49
50 block hide off
51 block property density 2700.0
52 block contact generate-subcontacts
53 block contact jmodel assign mohr
54 block contact property stiffness-normal 10e10 stiffness-shear 10e10 friction
    30.0
55
56 ; CREATING THE PLOTS
57
58 model history name 'mech ratio' mechanical ratio
59
60 plot create 'Plot-1'
61 plot item create block active on ...
62     label group-block slot 'Default'
63 plot item create axes
64 plot item create chart-history active on ...
65     history 'mech ratio' name "his-unbal mechanical ratio limit" style line
        reversed-x off reversed-y off
66 plot view projection perspective magnification 1 ...
67     center (-12.2416,-9.29396,-0.74357) eye (-17.5065,-9.96076,0.288934) roll
        358.1372 ...
68     clip-front -1e+10 clip-back 1e+10
69 plot item create block-vector active on ...
70     scale target 0.05 value 10.8382 automatic ...
71     color 'black'
72 plot item create block-vector ...
73     legend active on ...
74     title active on text "" value fap ...
75     scale target 0.05 value 10e-04 ...
76     color 'skyblue'
77
78 ; RUN THE MODEL
79
80 model gravity 0 0 -10
81 block mech damp local 0.8
82
83 model solve
84 model save 'Model_import.sav'

```

Listing N.1: 3DEC code for modelling Phase 1

## N.2 Script for modelling Phase 2

```
1 ; RESTORE PHASE 1
2
3 model restore 'Model_import.sav'
4
5 block gridpoint initialize displacement-x 0.0
6 block gridpoint initialize displacement-y 0.0
7 block gridpoint initialize displacement-z 0.0
8
9 ; APPLY THE FORCE
10
11 block gridpoint apply force-x 470 range id 11058
12 block gridpoint apply force-y 172 range id 11058
13
14 ; CREATING THE PLOTS
15
16 block hide off
17 block hide range group 'BL3' not
18 block history displacement gridpointid 7756 label 'dis'
19 block history velocity gridpointid 7756 label 'vel'
20 block hide off
21 model history name 'ratio' mechanical ratio
22
23 plot create 'Plot_1'
24 plot item create block active on ...
25     label group-block slot 'Default'
26 plot item create axes
27 plot view projection perspective magnification 1 ...
28     center (-12.0076,-9.23845,-0.967338) eye (-15.5245,-10.6665,-0.181553) roll
29     359.5236
30 plot item create block-vector active on ...
31     scale target 0.05 value 10.8382 automatic ...
32     color 'black'
33 plot item create block-vector ...
34     legend active on ...
35     title active on text "" value fap ...
36     scale target 0.05 value 10e-04 ...
37 color 'skyblue'
38
39 plot create 'Plot_2'
40 plot item create chart-history active on ...
41     history 1 name "Displacement magnitude at gp 7756"
42
43 plot create 'Plot_3'
44 plot item create chart-history active on ...
45     history 2 name "Velocity magnitude at gp 7756"
46
47 plot create 'Plot_4'
48 plot item create block active on ...
49     label group-block slot 'Default'
50 plot item create axes
51 plot item create chart-history active on ...
52     history 'ratio' name "his-unbal mechanical ratio limit" style line reversed-
53     x off reversed-y off
54 plot view projection perspective magnification 1 ...
55     center (-12.2416,-9.29396,-0.74357) eye (-17.5065,-9.96076,0.288934) roll
56     358.1372 ...
57     clip-front -1e+10 clip-back 1e+10
58
59 ; RUN THE MODEL
60
```

```
58 model solve mechanical cycles 200000
```

Listing N.2: 3DEC code for modelling Phase 2

## Appendix O

# Comparison analytical and numerical results, rectangular block on slope

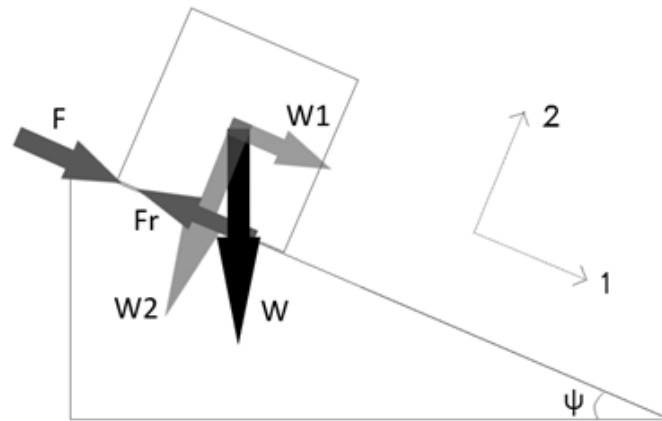


Figure O.1: Block model with analytical forces used in calculations.

### O.1 Analytical approach

The force required to start sliding the block is calculated below. This force is dependent on the frictional resistance and the weight of the block.

$$W = 1 * 1 * 1 * 2000 * 10 = 20kN \quad (O.1)$$

$$W_1 = W * \cos(\psi) = 20 * \cos(30) = 10kN \quad (O.2)$$

$$W_2 = W * \sin(\psi) = 20 * \sin(30) = 17.3kN \quad (O.3)$$

$$F_r = W_2 * \tan(\varphi) = W_2 * \tan(45) = 10kN \quad (O.4)$$

$$\sum F_1 = 0 = F + W_1 - F_r = 0 \quad (0.5)$$

$$F = F_r - W_1 = 17.3 - 10 = 7.3kN \quad (0.6)$$

## O.2 Numerical approach

The numerical approach uses a number of assumptions to get to its results.

### O.2.1 Numerical assumptions

Parameter	Value	Unit
<i>Block parameters</i>		
Density	2000	kg/m <sup>3</sup>
<i>Joint parameters</i>		
Joint normal stiffness	1 * 10 <sup>10</sup>	Pa/m
Joint shear stiffness	1 * 10 <sup>10</sup>	Pa/m
Friction angle of the joint	45	°
Residual friction angle of the joint	45	°
Cohesion of the joint	0	Pa
Residual cohesion of the joint	0	Pa
<i>Mesh parameters</i>		
Mesh edge length	0.1	m

Table O.1: Numerical assumptions for the block on a slope.

### Numerical results

Force (N)	Friction angle (°)	Model converged?
7200	45.0	Yes
7200	44.9	Yes
7300	45.0	Yes
7300	44.9	No
7400	45.0	No
7400	44.9	No

Table O.2: Results for the block on a slope, in terms of convergence.

## Appendix P

# Comparison analytical and numerical results, rectangular block on two rectangular supports

The following problem has been solved analytically for  $F$ , the minimum force for instability of the block on two supports (Figure P.1). The calculation was also done in 3DEC to verify that the model results are similar to what would be expected from an analytical solution. The analytical results was compared to numerical results for meshes of different mesh edge lengths and normal as well as smart meshes.

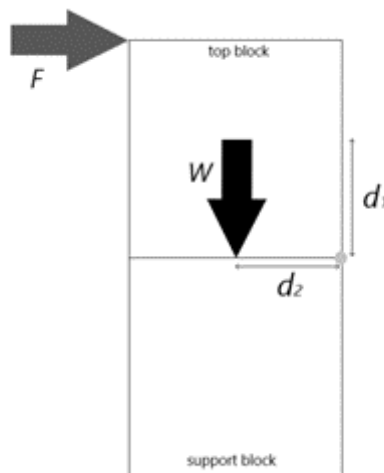


Figure P.1: Block on two supports with forces used in the analytical calculations.

### P.1 Analytical approach

The problem was only analyzed for the toppling failure mode.

$$W = 2 * 1 * 1 * 2000 * 10 = 40kN \quad (P.1)$$

$$F = W * \frac{d}{a} = 40 * \frac{0.5}{1} = 20kN \quad (P.2)$$

## P.2 Numerical approach

The numerical approach uses a number of assumptions to get to its results.

### P.2.1 Numerical assumptions

Parameter	Value	Unit
<i>Block parameters</i>		
Density	2000	kg/m <sup>3</sup>
<i>Joint parameters</i>		
Joint normal stiffness	$1 * 10^{10}$	Pa/m
Joint shear stiffness	$1 * 10^{10}$	Pa/m
Friction angle of the joint	80	°
Residual friction angle of the joint	80	°
Cohesion of the joint	0	Pa
Residual cohesion of the joint	0	Pa
<i>Mesh parameters</i>		
Mesh edge length	0.05, 0.10, 0.15, 0.20	m

Table P.1: Numerical assumptions for the block on two supports.

### P.2.2 Numerical results

Average mesh edge length (m)	Minimum force for model non-convergence (kN)	
	Normal mesh	Smart mesh
0.05	-	35
0.10	20	19
0.15	19	19
0.20	20	20
0.25	39	39

Table P.2: Numerical results for the block on two supports.

The following problem has been solved analytically for F, the minimum force for instability of the block on the slope. The calculation was also done in 3DEC to verify that the model results are similar to what would be expected from an analytical solution.

## Appendix Q

# Comparison analytical and numerical results, dolmen in 2D

The following problem has been solved analytically for  $F$ , the minimum force for instability of the megalith in 2D. The calculation was also done in 3DEC to verify that the model results are similar to what would be expected from an analytical solution. This calculation was done for the Northern contact and the Southern contact.

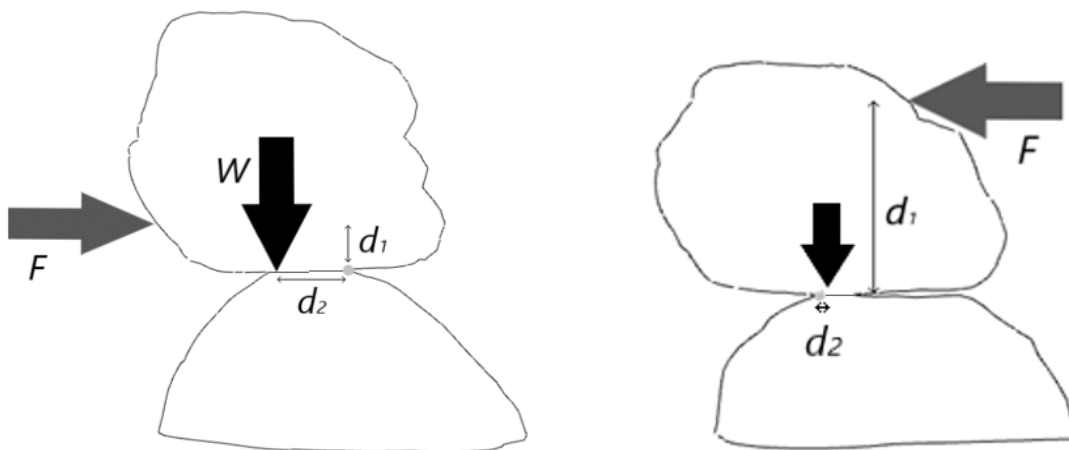


Figure Q.1: Dolmen in 2D at the Northern contact point between Rock 3 and Rock 2 (left) and at the Southern contact point between Rock 3 and Rock 4 (right).

### Q.1 Analytical approach

In this appendix, it will be calculated what force is required to achieve an unstable configuration of two rocks, Rock 3 and either Rock 2 or Rock 4. This will be done for sliding and for toppling.

First, the force  $W$  will be calculated, as this is necessary for both failure mechanisms.  $W$  represents the force from the weight of Rock 3. This can be calculated by multiplying the volume, density and acceleration of gravity.

$$W = 1.49 * 2700 * 10/2 \approx 20120N \quad (Q.1)$$

### Q.1.1 Sliding

The force equilibrium with respect to sliding consists of the destabilizing force  $F$  and the stabilizing force  $F_{fr}$ . The friction force is a function of the normal force and the friction angle.

$$\sum F_{horizontal} = 0 = F - F_{fr} = F - W * \tan(30) \quad (Q.2)$$

$$F = W * \tan(30) = 20120 * \tan(30) = 11620N \quad (Q.3)$$

### Q.1.2 Toppling

For toppling, the location at which the force is applied, is also of interest. Three variations have been investigated. Again, the force  $F$  is calculated, for which the rock configuration becomes unstable. Pictures of the rock outlines can be found below.

$$\sum M_R = 0 = F * d_1 - W * d_2 \quad (Q.4)$$

$$F = W * \frac{d_2}{d_1} \quad (Q.5)$$

For scenario North top:

$$F = 20120 * \frac{0.28}{0.97} = 5810N \quad (Q.6)$$

For scenario North bottom:

$$F = 20120 * \frac{0.28}{0.54} = 10430N \quad (Q.7)$$

The Southern outline is a particular case, since the center of mass is located almost exactly above the rotation point R. Therefore, the horizontal force can be very small to create an unstable situation.

For scenario South top:

$$F = 20120 * \frac{0.01}{0.77} = 260N \quad (Q.8)$$

For scenario South bottom:

$$F = 20120 * \frac{0.01}{0.24} = 830N \quad (Q.9)$$

## Q.2 Numerical approach

The numerical approach uses a number of assumptions to get to its results.

### Q.2.1 Numerical assumptions

Parameter	Value	Unit
<i>Block parameters</i>		
Density	2000	kg/m <sup>3</sup>
<i>Joint parameters</i>		
Joint normal stiffness	$1 * 10^{10}$	Pa/m
Joint shear stiffness	$1 * 10^{10}$	Pa/m
Friction angle of the joint	45	°
Residual friction angle of the joint	45	°
Cohesion of the joint	0	Pa
Residual cohesion of the joint	0	Pa
<i>Mesh parameters</i>		
Mesh edge length	0.1	m

Table Q.1: Numerical assumptions for dolmen in 2D.

### Q.2.2 Numerical results

Contact location	Force location	Minimum force for non-convergence (kN)
North	Top	6.5
	Bottom	12.0
South	Top	0.7
	Bottom	2.3

Table Q.2: Numerical results for dolmen in 2D.

## Appendix R

# Numerical results for dolmen stability analysis

### R.1 Minimum force to cause failure

Calculate the required force for the rock to 'fail'. Failure is defined as non-convergence of the model within the specified number of cycles.

	Minimum force required for non-convergence of the model within 200000 cycles (kN)
Model 1	2
Model 2	94

Table R.1: The minimum force required for model non-convergence for Model 1 and 2.

### R.2 Cycle steps analysis

The influence of the number of cycle steps, within which convergence should be reached, on the minimum force for non-convergence of the model was analyzed for Model 2.

Number of cycles (-)	Minimum force for model non-convergence within 200000 cycles (kN)	Calculation time for Phase 1 and 2 (s)
10	1	1239
50	61	1684
100	86	2245
200	94	3381

Table R.2: The minimum force for model non-convergence and corresponding calculation time for different numbers of cycles for Model 2.

### R.3 Mesh coarseness analysis

The influence of the mesh coarseness, in terms of the average mesh edge length (AMEL), on the minimum force for non-convergence of the model was analyzed for Model 2.

Average mesh edge length (m)	Minimum force for model non-convergence within 200000 cycles (kN)	
	Normal mesh	Normal mesh
0.05	-	323
0.10	79	68
0.15	94	69
0.20	75	68

Table R.3: The minimum force for model non-convergence for different AMELs for Model 2.

Average mesh edge length (m)	Calculation time for modelling Phase 1 and 2 (s)	
	Normal mesh	Smart mesh
0.05	-	53483
0.10	37392	12453
0.15	3381	2737
0.20	2388	3505

Table R.4: The calculation time for different AMELs for Model 2.

### R.4 Friction angle

The influence of the friction angle of the joint on the minimum force for non-convergence of the model was analyzed for Model 2.

Friction angle (°)	Minimum force for model non-convergence within 200000 cycles (kN)
0	7
10	26
20	65
30	94
40	105

Table R.5: The minimum force for model non-convergence for different joint friction angles for Model 2.